Physical and Computation Modelling of Turbidity Currents: The Role of Turbulence-Particles Interactions and Interfacial Forces

Ke San Yam

Submitted in accordance with the requirements for the degree of
Doctor of Philosophy

The University of Leeds
School of Earth & Environment,

December 2012

The candidate confirms that the work submitted is his own, except where work which has formed part of jointly-authored publications has been included. The contribution of the candidate and the other authors to this work has been explicitly indicated below. The candidate confirms that appropriate credit has been given within the thesis where reference has been made to the work of others.

Chapter 3 is based on the following paper:

Yam, K; McCaffrey, WD; Ingham, DB; Burns, AD CFD modelling of selected laboratory turbidity currents. *Journal of Hydraulic Research*, vol. 49, pp. 657-666.

The candidate is the primary author of the paper.

Abstract

Experimental and numerical investigations have been conducted in order to evaluate the accuracy of the Mixture Model, a depth-resolved and time-averaged multiphase numerical model, in predicting the behaviour of dilute surge-type turbidity currents. The effects of turbulent dispersion and turbulence modulation upon sediment transport within turbidity currents are directly modelled via their incorporation into the Mixture Model. Modelled predictions of flow front propagation and deposit density are compared against both experimental data and refined two-fluids model from previous studies. When modelled using the formulation of Chen & Wood (1985), turbulence modulation does not affect on the propagation of dilute turbidity currents significantly. Turbulent dispersion can be modelled by incorporating the formulation of Simonin (1991) into the slip equation of the Mixture Model. Its effect is strongest in dilute flows carrying fine particles and diminishes when either grain size or flow concentration increases. Modelled turbulent dispersion effects are too strong in simulations of flows carrying silicon carbide particles; Mixture Model simulations agree poorly with both experimental data or refined two-fluids model results of the deposit mass profile. Yet turbulent dispersion is essential to ensure that model predictions of flows carrying glass beads compare well with experimental data. The reasons for the discrepancy between modelling approaches best suited to each of these flow types remains poorly understood.

A new analytical approach is developed to evaluate the effect of the lift force on particles of small, intermediate and large particle Reynolds number immersed in two-dimensional shear flows. The lift force always reduces the magnitude of the particle settling velocity and may push particles forward or backward, depending on the sign of both the lift coefficient and the flow vorticity. Given plausible velocity profiles within natural turbidity currents, the effect of lift force on the sand-like particles immersed in such turbidity currents is negligible. It may become significant when the ratio of the particle density to the flow density approaches unity.

New experiments are presented for flows over the flow concentration range 0.25 – 5% and grain size range 58 - 115μm. The data are used to facilitate a more complete validation of the Mixture Model, based on flow front propagation rates, deposit mass density and deposit grain characteristics. Modelling results for first two variables are in good agreement with the experimental data, when turbulent dispersion effects are incorporated. For reasons which remain unclear, the model cannot simulate the unexpected experimental result that deposit grain size is largely unfractionated if the standard deviation of the source material is less than 11 but significantly fractionated if it exceeds 18. This discrepancy requires further work.

Acknowledgements

I would like to express my gratitude to my supervisors, Profs. Bill McCaffrey, Derek Ingham and Dr. Alan Burns for the guidance and support they have given during the progress of this project. Without their constant encouragement and sound advice, I would have never been able to complete this work. Their diligent proof reading has significantly improved the text of this thesis, and the prompt return of chapters was much appreciated.

I also would like to thank Turbidite Research Group (TRG) for sponsoring this project. Without the financial supports from TRG, I would never had the opportunity to undertake this research.

Thanks to Gareth, Russ and Kat in assisting me in setting-up and develop a proper methodology for the lock-release experiments.

Thanks to my office mates Nic Yin, Ya Dong, Tao Wei, Andy, Chris, Kieran, and Lindsey.

Finally, I would like to thank my families for their unwavering love and supports throughout my life.

Table of Contents

List of Tables

List of Figures

Nomenclature

Roman Upper Case

Symbol	Unit	Description
A	-	Constant for linear function of lift coefficient
B_R	-	Constant for function of particle rotation
A_p	m^2	Projected area of the particle in the direction of relative flow velocity
B_k	$kgms^{-2}$	Body forces
C	%	Concentration
C^+	-	Law of wall constant
$C_{1\epsilon}$, $C_{2\epsilon}$, $C_{3\epsilon}$	-	Turbulence model $k-\epsilon$ constants
C_D	-	Aerodynamic drag coefficient
C_{DS}	-	Stoke drag coefficient
C_{DO}	-	Oseen drag coefficient
C_{DN}	-	Newton drag coefficient
C_{LA}	-	Aerodynamic lift coefficient
C_L	-	Shear-induced lift coefficient
C_{LS}	-	Stoke lift coefficient
C_{LN}	-	Newton lift coefficient
C_R	-	Magnus lift coefficient
C_f	-	Darcy friction factor
C_{TD}	-	Eddy viscosity modifier
D_t	m^2s^{-1}	Turbulent diffusivity
$\vec{F}_{D,Stoke}$	$kgms^{-2}$	Stoke drag force
F_D	$kgms^{-2}$	Drag force
F_L	$kgms^{-2}$	Lift force
F_D^*	-	Non-dimensional drag force

F_L^*	-	Non-dimensional lift force
Fr	-	Froude number
G	s^{-1}	Velocity gradient
Ga	-	Galileo number
G_{km}	$kgm^{-1}s^{-2}$	Mixture turbulent shear production
G_{bm}	$kgm^{-1}s^{-2}$	Mixture turbulence buoyancy
G_{mm}	$kgm^{-1}s^{-2}$	Mixture turbulence modulation
H	m	Height of the ambient fluid
I	%	Turbulent intensity
M_{fk}	ms^{-1}	Fluid momentum interaction
M_{pk}	ms^{-1}	Particle momentum interaction
M_{mk}	ms^{-1}	Mixture momentum interaction
$\vec{M}_p^{TD}$	$kgms^{-2}$	Turbulent dispersion force
$M_{pi}^{'}$	ms^{-1}	Turbulent dispersion effect on slip velocity
P	Pa	Favre-averaged pressure
Pa	-	Particle momentum number
Re_f	-	Flow Reynolds number
Re_s	-	Particle Reynolds number
Re_p	-	Reynolds number based on particle translational velocity
Re_R	-	Reynolds number based on particle angular velocity
Re_s	-	Reynolds number based on slip velocity
Re_∞	-	Reynolds number based on u_∞
Re_ω	-	Reynolds number based on fluid vorticity
S_{ij}	s^{-1}	Mean strain rate tensor
U_i	ms^{-1}	Favre-averaged velocity
U_{fi}	ms^{-1}	Favre-averaged fluid velocity
U_{pi}	ms^{-1}	Favre-averaged particle velocity
U_{mi}	ms^{-1}	Favre-averaged mixture velocity

U_{Mi}	ms^{-1}	Diffusion velocity
V_p	-	Particle Volume

Roman Lower Case

Symbol	Unit	Description
c_b	%	Reference concentration near boundary
d_p	m	Particle diameter
g'	ms^{-1}	Flow Reduced gravitational acceleration
g_R	ms	Reduced gravity in Galileo number
h	m	Flow height
h_{max}	m	Height where the maximum velocity is located
g	ms^{-2}	the magnitude of gravitational acceleration
g_i	ms^{-2}	Vectorial gravitational acceleration
r_ρ	-	$(\rho_s - \rho_f)/\rho_f$
l_f^t	m	Fluid turbulent length
t_p	s	Particle relaxation time
t_f^t	s	Eddy time scale
C_p	kgs^{-1}	Turbulent dispersion function, $\frac{1}{8}C_D A_p \rho_f \left\vert \vec{U}_p - \vec{U}_f \right\vert$
h_t	m	Bed elevation
m_{dep}	kgm^{-2}	Deposit mass areal density
$\widetilde{m}_{dep}$	-	Dimensionless deposit mass areal density
n	-	Power law constant for velocity profile in jet region
h_0	m	Initial Suspension height
h_t	m	Thickness of the viscous sublayer
k	m^2s^{-2}	Turbulent kinetic energy
k_f	m^2s^{-2}	Fluid turbulent kinetic energy
k_m	m^2s^{-2}	Mixture turbulent kinetic energy
p	Pa	Local instantaneous pressure
q_s	$kgm^{-3}s^{-1}$	Sediment flux

r_{Re}	-	Ratio of $\mathrm{Re_s}/\mathrm{Re_\infty}$
t	s	Time
$\tilde{t}$	-	Dimensionless time
t'	-	Non-dimensional time scale
t_{fd}^{t}	s	Eddy-particle interaction time
t_{f}^{t}	s	Eddy time scale
t_{vis}	s	Viscous time scale
u	$\mathrm{ms^{-1}}$	Downstream velocity
u_∞	$\mathrm{ms^{-1}}$	Settling velocity derived based balance of drag and gravity
u_τ	$\mathrm{ms^{-1}}$	Shear velocity
u^+	-	Dimensionless wall velocity
u_f'	$\mathrm{ms^{-1}}$	Fluctuating component fluid velocity
u_f'	$\mathrm{ms^{-1}}$	Fluctuating component particle velocity
u_b	$\mathrm{ms^{-1}}$	Flow buoyancy velocity
u_f	$\mathrm{ms^{-1}}$	Flow velocity
u_{max}	$\mathrm{ms^{-1}}$	Maximum downstream velocity
u_m	$\mathrm{ms^{-1}}$	Mixture downstream velocity
u_N	$\mathrm{ms^{-1}}$	Velocity of the front of gravity current
u_p	$\mathrm{ms^{-1}}$	Particle velocity
u_r	$\mathrm{ms^{-1}}$	Particle slip/relative velocity
u_s	$\mathrm{ms^{-1}}$	Particle settling velocity
u_i	$\mathrm{ms^{-1}}$	Local instantaneous velocity
u_τ	$\mathrm{ms^{-1}}$	Shear velocity
v_m	$\mathrm{ms^{-1}}$	Mixture vertical velocity
$\tilde{x}$	-	Dimensionless downstream distance
x	m	Downstream distance
x_i	m	Cartesian coordinates
$\tilde{y}$	-	Dimensionless vertical distance
y^+	-	Dimensionless wall coordinate

Greek Symbols

Symbol	Unit	Description
α_c	-	Concentration profile model constant
α_v	-	Velocity profile model constant
α_G	-	Dimensionless shear rate (check again where)
α_f	-	Fluid volume fraction
α_{max}	-	Maximum particle volume fraction
α_p	-	Particle volume fraction
α_{pm}	-	Particle maximum packing limit
$\nabla\alpha_p$	-	Particle volume fraction gradient
$\nabla\alpha_f$	-	Fluid volume fraction gradient
Λ	-	Lift Number
β_c	-	Concentration profile model constant
β_v	-	Velocity profile model constant
$\beta_k, \beta_\epsilon, \sigma_t$	-	Turbulence model $k-\epsilon$ constant
δ_{ij}	-	Kronecker delta
ϵ_s	s^{-1}	Strain rate
ϵ	m^2s^{-3}	Turbulent dissipation energy
ϵ_m	m^2s^{-3}	Mixture turbulent dissipation energy
η	-	Rouse exponent
κ	-	Model constant
κ_w	-	Law of wall constant
λ	-	Deposit mass goodness of fit parameter
λ_p	-	Bed porosity
μ_f	$kgm^{-1}s^{-1}$	Fluid dynamic viscosity
μ_t	$kgm^{-1}s^{-1}$	Eddy viscosity
μ_m	$kgm^{-1}s^{-1}$	Mixture dynamic viscosity
μ_{eff}	$kgm^{-1}s^{-1}$	Effective dynamic viscosity
ν	m^2s^{-1}	kinematic viscosity

ν_f	m^2s^{-1}	Fluid kinematic viscosity
ω	s^{-1}	Turbulence specific dissipation rate
ω_f	s^{-1}	Fluid vorticity
ω_p	s^{-1}	Particle vorticity
ρ	kgm^{-3}	Density
ρ_m	kgm^{-3}	Mixture density
ρ_f	kgm^{-3}	Fluid density
ρ_p	kgm^{-3}	Particle density
ϕ	degree/rad	Angle of incidence
$\Delta\rho$	kgm^{-3}	Density difference between the flow and the ambient
σ_{TD}^t, C_β	-	Simonin model constants
τ	Pa	Shear
τ_{ik}	Pa	Viscous stress tensor
τ_{fik}	Pa	Fluid viscous stress tensor
τ_{mik}	Pa	Mixture viscous stress tensor
τ_{fik}^t	Pa	Fluid Reynolds stresses
τ_{pik}^t	Pa	Particle Reynolds stresses
τ_{mik}^t	Pa	Mixture Reynolds stresses
τ_{Dik}	Pa	Turbulent dispersion stresses
τ_{ij}	Pa	Stress tensor
τ_b	Pa	Boundary shear stress
τ_c	Pa	Critical boundary shear stress
θ	degree/rad	Angular deflection
ζ	-	Simonin model functions

Abbreviation

BB	Bagchi & Balachandar (2002)
BL	Bluemink et al. (2009)
DNS	Direct Numerical Simulations
FVM	Finite Volume Methods

LES	Large Eddy Simulation
RANS	Reynolds Averaged Navier Stokes
SWM	Shallow Water Models
TD	Turbulent dispersion
UDF	User-Defined Functions

Chapter 1

Introduction

1.1 Research Rationale

Turbidity currents and their deposits have been a subject of research interest to academia and industry for well over 60 years (e.g., Meiburg and Kneller, 2010 and references therein). They are academically important because they are complex multiphase phenomena that play a major role in sculpting the continental margins. They are commercially important because their deposits (turbidites) may host significant hydrocarbon reserves (Weimer and Slatt, 2007). Therefore, developing a better understanding the flow processes of turbidity currents can significantly aid accurate prediction regarding the location and structure of turbidites, with important consequences for understanding the development of an important class of land form, and for cost reduction in hydrocarbon extraction.

Three kinds of approach are generally employed to study the behaviour of turbidity currents, viz. field observation, laboratory experiments and theoretical approaches. From a cost perspective, field observation is restrictive because the natural phenomenon is generally both rare and destructive. Laboratory experiments allow scaled-down versions of turbidity currents to be modelled under controlled boundary conditions. With modern instrumentation, high resolution information on the flow behaviour (velocity and concentration) can be acquired (e..g, Keevil, 2005). The disadvantage of physical modelling arises in scaling the flows. It has been argued before that the dynamics of laboratory flows cannot be scaled straightforwardly such that they capture the dynamics of natural flows (Peakall et al., 1996). Theoretical modelling represents another approach to understanding the dynamics of turbidity currents. An advantage of theoretical models is that they can be scaled-up to predict the behaviours of natural turbidity currents. A range of approaches can be followed. Simple models describe macroscopic behaviour of the turbidity currents such as the evolution of the shape of flows (e.g., Box Models such as those of Dade & Huppert,

1995). More complex models describe the internal dynamics of the flows (multiphase models) at varying degrees of complexity. Theoretical models constantly evolve as our understanding of flow dynamics improves. Measurement data from laboratory flows are generally used to verify the accuracy of the prediction from theoretical models. Comparing the prediction from theoretical models against detailed and accurate experimental measurement can reveal what essential physical mechanisms should be incorporated into the models. Thus theoretical and experimental approaches can work well in parallel to achieve a better understanding of the dynamics of turbidity currents.

Natural turbidity currents occur in a range of complex settings, i.e. confined to unconfined, with different bed slopes, roughness and where channelised, experiencing varying degrees of sinuosity in the channel, different channel widths and heights, etc.; additionally they may carry a wide range of different grain sizes at different concentrations (Meiburg & Kneller, 2010). Because of this diversity in the natural setting and the multitude of physical interactions that may be invoked within the flows, it can be posited that the interplay between the various key mechanisms within turbidity currents is best studied via numerical modelling. Yet any numerical model must also be simple, robust, and practical enough for it to be employed to describe large-scale flows. In the past, depth-averaged numerical models have been favoured because of their computational efficiency. However, such models do not take into account gradients in flow properties with the flows, a restriction which significantly affects their accuracy. With advances in computer power, it is now feasible to resolve internal flow variation within turbidity currents. However, resolving turbulence of the flow is still computationally expensive. Therefore a key challenge is to understand the role that turbulence plays in the different physical mechanisms such as particle entrainment and flow-particle interaction so that its effect upon flow averaged quantities can be modelled.

1.2 Aims of Thesis

The aims of this thesis are to:

i. Build a practical numerical model for predicting the behaviour of surge-type turbidity currents.

ii. Identify the key physical mechanisms governing the settling motion of particles within turbidity currents.

1.3 Thesis Structure

Chapter 2 reviews current understanding of the behaviour of turbidity currents. The detail of the theoretical model here employed (the Mixture Model) and the important fluid-particle interactions that are the subject of analysis within this thesis are discussed. A review is also given on the type of theoretical models that have been employed in the past to investigate turbidity currents.

Chapter 3 presents the two-dimensional modelling results of the Mixture Model in simulating lock-release dilute turbidity currents of various concentration and grain size. The numerical predictions on the propagation and the deposit mass profile of flows are compared against experimental and direct numerical simulations results produced by other workers. The effects of turbulence dispersion in turbidity currents are investigated by comparing the prediction on the evolution on the concentration distribution within flows from the Mixture Model with or without a turbulence dispersion model. The effect of turbulence modulations in the flows is also investigated.

Chapter 4 presents the derivations of simple analytical expressions for the lift force on particles suspended within shear flows based on the force balance equation. Simple expressions are derived for small, intermediate and large particle Reynolds number. The expressions are evaluated to determine the effect of the lift force on the particle settling characteristics in turbidity currents.

Chapter 5 presents a combined physical and numerical experimental investigation of lock release turbidity currents. The propagation, deposit mass profile and grain size characteristics of a total 15 flows of different concentration and grain sizes are presented and discussed. These flows are simulated using the Mixture Model and the results are compared against experimental prediction. The effect of turbulent dispersion in these flows is compared with that of the flows investigated in Chapter 3.

Chapter 6 summarises the key findings in each chapter and provide an overall conclusions to the thesis. Suggestions are given for possible future work.

Chapter 2

Literature Review

2.1 Introduction

The aim of this chapter is to give a brief review of turbidity currents, the important physics within them and the numerical models that have been used to study them.

2.2 Origins of Turbidity Currents

Turbidity currents are a type of subaqueous particulate gravity currents that are responsible for transporting sediment from the shallow water settings, depositing it in the deep sea ocean. In physics, it is known as a dilute form of gravity current (or density current) whose motion is induced by the pressure difference, or the excess density which is provided by the sediment suspended within the flows. Other forms of gravity currents that are commonly observed in nature are atmospheric fronts which flow due to temperature-induced density differences, katabatic winds (temperature), dense gas dispersion from chimnies (gaseous density) and watery discharging from factories (solute density). In these examples, the motion of the flows are instigated by the either temperature difference or the difference in the solution density. Full-scale turbidity currents have rarely been observed since they are inaccessible to direct observation and are destructive enough to destroy any deployed observation equipment. The concept of turbidity currents was expanded by Kuenen & Menard (1952) who produced laboratory turbidity currents and observed that the deposit from such flows grade throughout their entire thickness from relatively coarse-grained at the bottom to fine-grained at the top, which resembles that of natural graded sandstones. Another classic example piece of evidence for turbidity currents is the sequence in which transatlantic undersea cables were destroyed during the Grand Banks earthquake that occurred in 1929. Heezen & Ewing (1952) studied these cables and postulated that the earthquake had triggered an underwater slide that transformed into turbidity currents which travelled for hundreds of kilometres and destroyed the cables in sequence along their path. Since

then, numerous researches have conducted investigations on the mechanics of the sediment transport of turbidity currents and its relationship with the formation or structure of turbidites (deposits of turbidity currents).

Generally speaking, there are two types of turbidity currents which are known to result in different types of turbidites, namely a surged-typed turbidity current and a sustained turbidity current. In deep sea, the former is postulated to be triggered by the catastrophic sediment failures on the slope which results in a submarine landslide or slump or debris flow that transforms into a turbidity current through dilution by mixing with seawater (Normark & Piper, 1991). Hence, the former has a fixed volume of suspension and relatively short life if erosion does not occur. As a result, such a flow is unsteady (the structure within the flows constantly changes) and deposits thin and graded turbidites. On the other hand, sustained turbidity currents typically are postulated to originate from hyperpycnal flows (highly concentrated sediment underflows in a fluvial system) that travel from the rivers into the ocean and transforms into turbidity currents. Hence, a current can have a very long life if it continues to be fed with sediment from the rivers. As a result, the current may possess a uniform and quasi-steady body (the flow does not change significantly in a short time) and is likely to deposit a large amount of ungraded turbidites.

2.3 Laboratory Turbidity Currents

Since it is expensive or problematical to conduct a direct observation on natural turbidity currents, researchers resort to re-produce them at a smaller-scale in a laboratory and to run the flow with simple boundary conditions such as straight and smooth channels and without an erodible bed in order to study the basic behaviour of the turbidity currents. Clearly the way the turbidity currents are initiated in the natural system are complex and it is difficult to emulate in the laboratory. Therefore, simple configurations for producing turbidity currents have been proposed in the past. We can review some of the configurations used in the past. The commonly used configuration to produce a surged-type turbidity current is called the Lock-Release system. In this configuration, a box containing a suspension mixture (called the lock box) is prepared at one of end of a flume and the suspension is separated from the flume by inserting a lock gate between, see Fig. 2.1(a). A surge-typed turbidity current is triggered by removing the lock gate from the flume. Once the

lock gate is released, a flow exchange occurs whereby the heavier mixture propagates into the lower half of the main flume by virtue of the excess density whereas the lighter ambient fluid from the main flume propagates into the upper half of the lockbox. The heavy mixture quickly develops into a turbidity current and propagates until all sediments have settled on the bed of the flume. Without a significant slope or additional input of sediment from the erosion or the source, a fixed volume current dies out relatively quick. Therefore, researchers had designed a configuration that produce a surge-typed turbidity currents that sustains for a longer period of time. The configuration is to feed the mixture suspension from an external tank into the flume through a pipe at an adjustable rate as shown in Fig. 2.1(b). The speed, size and duration of the flows can thus be controlled by adjusting the feed rate. However, it should be noted that the mixture first enters the flume as a jet flow. Through turbulent mixing and dispersion, the flow expands quickly and hence loses the momentum it inherited from the initial condition. At some distance from the inlet where the mixture enters the flume, the mixture starts to flow as a turbidity current. Such a configuration allows a longer duration and hence a more accurate measurement on the internal structure of the flow and thus has been used to study velocity, concentration and turbulence profiles.

In addition, there is a kind of configuration devised specifically for studying the only dynamics of the head of the turbidity currents. The idea of this configuration is to create a stationary and steady turbidity current with respect to the observer so that a longer duration of measurement can be taken on the flow. Such flows can be achieved by injecting the ambient fluid and the mixture from two opposite sides of a flume. At the bottom of the flume, a conveyor belt is fitted onto the bottom of the flume in order to create a moving bed. Figure 2.1(c) shows an example of a setup used to produce steady and stationary saline flows (Simpson & Britter (1979)). A limitation of this setup is that can only be employed for saline gravity currents.

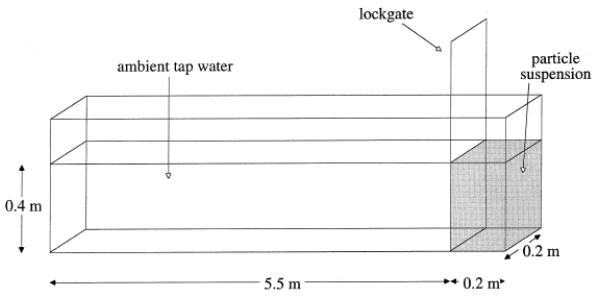

(a)

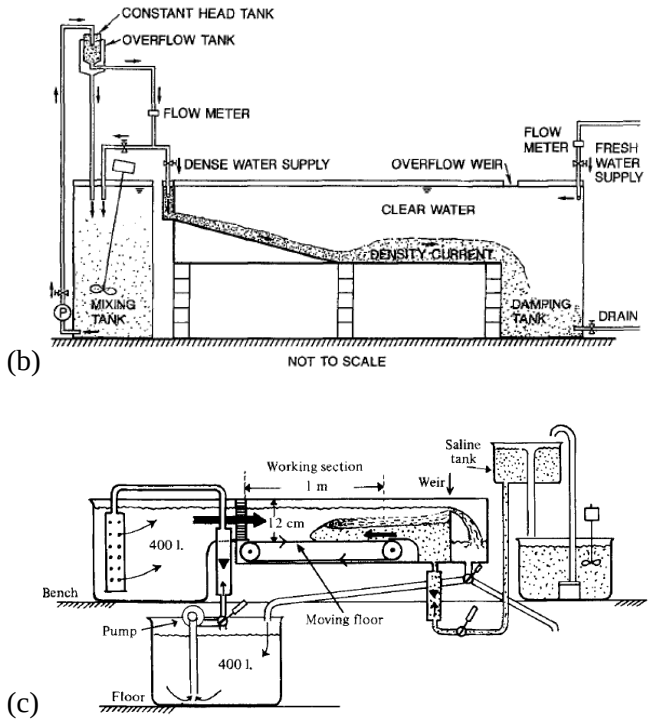

Figure 2.1 Schematic diagram showing (a) a lock box configuration for producing a fixed volume turbidity currents employed in Gladstone et al. (1998), (b) a configuration for producing a quasi-steady turbidity current employed in Garcia (1994), and (c) a configuration for producing a stationary head of a turbidity current employed in Simpson & Britter (1979).

Table 2.1 Measurements performed on the 'sustained' surged-typed particulate density currents conducted in the past.

Authors	Excess Density	Measurement
Altinakar et al. (1996)	Particulate	Velocity and concentration profile
Garcia (1994)	Particulate	Velocity and concentration profile
McCaffrey et al. (2003)	Particulate	Velocity, concentration, grain size and turbulence stresses distribution
Leeder et al. (2005)	Particulate	Velocity, concentration, grain size and turbulence profile
Hosseini et al. (2006)	Particulate	Velocity and concentration profile
Sequeiros et al. (2010)	Particulate	Velocity and concentration profile

Many experimental investigations have been performed on both surge-typed and sustained turbidity currents in order to understand the propagation, the flow structure and the deposit characteristics of a turbidity current. Tables 2.1 and 2.2 lists several

examples of experimental investigations on sustained and surge-typed turbidity currents conducted in the past and the type of measurements that were performed in each investigation.

Table 2.2 Measurements performed on the 'lock-release' surge-typed saline or particulate density currents conducted in the past.

Author	Excess Density	Measurement
Huppert & Simpson (1980)	Saline	Front Propagation
Laval et al. (1988)	Particulate	Deposit Thickness
Bonnecaze et al. (1993)	Particulate	Front Propagation, Deposit Thickness
Hacker et al. (1995)	Saline	Concentration distribution
Middleton & Neal (1989)	Particulate	Deposit Thickness and Grain size
Gladstone et al. (1998)	Particulate	Front Propagation, Deposit Thickness
Kneller et al. (1999)	Saline	Velocity and turbulence profile
Rooij & Dalziel (2001)	Particulate	Deposit Thickness
Gladstone & Woods (2000)	Particulate	Front Propagation
Choux et al. (2002)	Particulate	Front Propagation, deposit thickness and Grain size
Gladstone & Pritchard (2010)	Particulate	Deposit Thickness
Hodson & Alexander (2010)	Particulate	Front Propagation, Deposit Thickness, Velocity and Turbulence Profile

2.4 Dynamics of Turbidity Currents

2.4.1 General Description

A turbidity current is described to possess a characteristic longitudinal anatomy of head, neck, body and tail as illustrated in Figure 2.2 (here a saline gravity current is used because it shows each part of the flow clearly). The head has a clear 'nose' as a result of the no-slip condition at the lower boundary and frictional resistance or shear at the upper boundary. The head constantly displaces the ambient fluid, overrides the ambient fluid near the bottom boundary and at the same time ingests some ambient fluid into the body of the flows. This complex interaction results in the formation of the lobe and cleft features (see Figure 2.3) at the base of the head of

the current. Simpson (1972) studied in detail the structure of lobes and clefts and postulated that they are formed from the convective instability produced by the light liquid which has been overrun by the denser liquid in the gravity current. This study also suggested that the lower boundary plays an essential role in determining the substructure of the head. More recently, Härtel et al. (2000) have investigated the structure of the lobe and cleft by simulating a saline gravity current using a Direct Numerical Simulations as shown in Fig. 2.3. A series of billows, known as the Kelvin-Helmholtz vortices, can be observed near the upper boundary of the head. This instability is due to the velocity difference across the interface, or the shear between the saline currents and the ambient fluids. The vortices or billows are the dense fluid being detraining out from the back of the head. Therefore intense mixing between the current and the ambient fluid occurs along this interface.

(a)

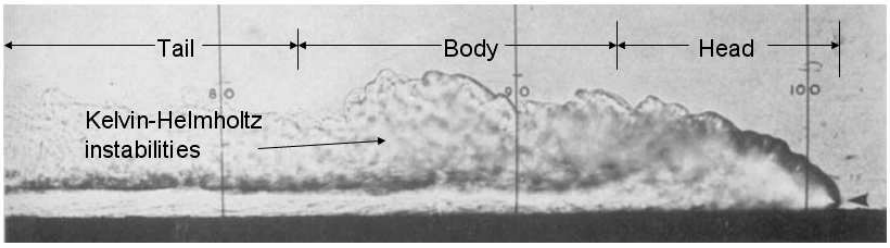

(b)

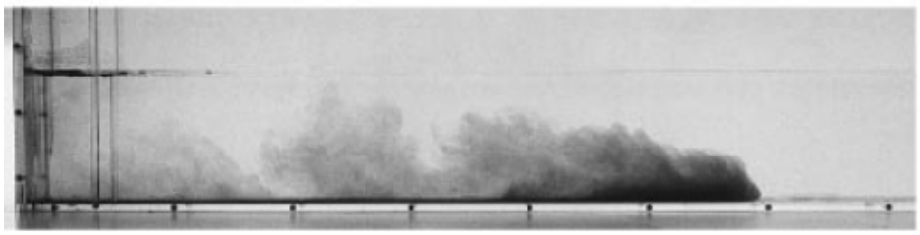

Figure 2.2 Photograph showing (a) the structure of a compositional gravity current, reproduced from Simpson and Britter (1979), and (b) a turbidity currents, reproduced from Gladstone & Woods (2000). Both flows are produced using the lock-release configuration.

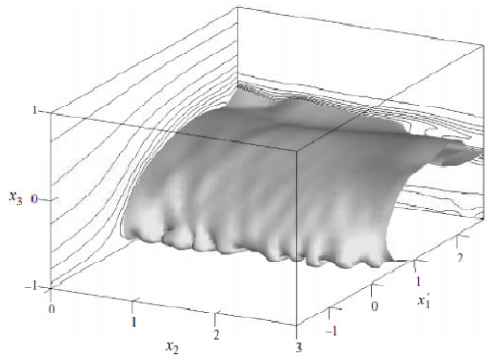

Figure 2.3 A Direct Numerical Simulation of a lock-release generated saline gravity current showing the structure of lobe breakdown and cleft formation at an advancing gravity current head, reproduced from H Härtel et al. (2000).

2.4.2 Front Propagation

Benjamin (1968) drew an analogy between the propagation of a steady gravity current and an empty cavity advancing along the upper boundary of a liquid. Assuming no energy loss, Benjamin (1968) showed that the Bernoulli principle can be applied and this leads to the following equation:

$$u_N = Fr\sqrt{g'h}$$

where Fr is the Froude number and has a value of $\sqrt{2}$, h is the flow height, and g' is the reduced gravitational acceleration. Huppert & Simpson (1980) showed that Fr = 1.19 for flows propagating in very deep water, i.e., for $h/H < 0.075$, where H is the height of the ambient fluid. The derivation of equation (2.1) has a significant discovery since it indicates that the propagation of the flow depends only on the concentration of the flow and the flow height. Expression (2.1) can be easily extended to include the effect of the slope. Equation (2.1) is valid for a steady–state flow. For a surge-typed turbidity current, the speed of the flow reduces due to the decrease in concentration and the turbulence. The effect of the concentration and particle deposition on the propagation was studied by Riddell (1969).

2.4.3 Velocity Profiles

Experimental investigations on sustained turbidity currents (Altinakar et al., 1996; Sequeiros et al., 2010) shows that the velocity profile of a body of a turbidity current is characteristically similar to that of saline gravity currents (Kneller et al, 1999, Hosseini et al., 2006). Essentially the body of a sustained turbidity current possess a maximum velocity which is located at about one third of the height of the flow and hence separates the velocity profile into two parts: a region below the velocity maximum is known as the wall region and a region above the maximum velocity which is known as the jet region. The wall region can be described using the logarithmic relation which is defined as follows:

$$\frac{u}{u_\tau} = \frac{1}{\kappa} ln\left(\frac{y}{y_0}\right) \qquad (2.2)$$

where κ is the von Karman constant, u_τ is the shear velocity, y is the vertical coordinate (or the flow height), and k_s denotes a bed roughness length. For

hydraulically smooth flows, $\frac{u_\tau y_0}{\nu} \leq 5$; for hydraulically transitional, $5 \leq \frac{u_\tau y_0}{\nu} \leq 70$; and $\frac{u_\tau y_0}{\nu} \geq 5$ based on the study conducted by Nikurase (1932) for pipe flows. Alternatively, it can be described using an empirical power relation (Altinakar et al., 1996):

$$\frac{u}{u_m} = \left(\frac{y}{h_m}\right)^n \tag{2.3}$$

It should be noted that this expression is normalized, or made dimensionless, by dividing the velocity by the maximum velocity and the flow height by the height where the maximum velocity is located h_m. The value of *n* is determined by fitting the power-law expression against the experimental data. For low concentration flows, $n = 1/6$ according to Altinakar et al (1996). On the other hand, the velocity profile in the jet region ($y > h_m$) can be described using a Gaussian relation defined as follows:

$$\frac{u}{u_m} = \exp\left[-\alpha_v X^{\beta_v}\right] \tag{2.4}$$

where α_v and β_v are empirical constants whose value depend on how X is normalized. Altinakar et al. (1996) suggested a normalization in a similar way to that used in equation (2.3) being normalized on (u/u_m, y/h_m), whereas Garcia (1994) suggested a normalization using depth-averaged quantity where U is the depth-averaged velocity and Y is the depth averaged height (see the definition in Fig. 2.4 (Ellison & Turner, 1959)):

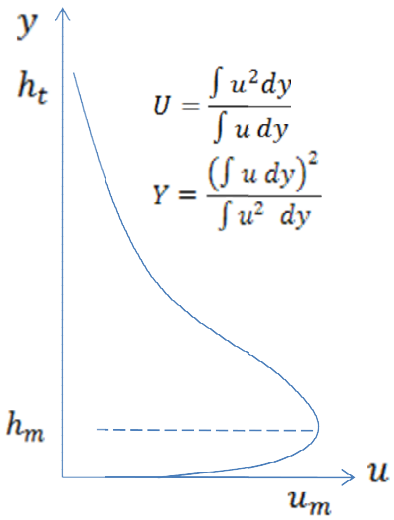

Figure 2.4 Schematic diagram on the definitions of a typical turbidity current velocity profile of the Ellison & Turner (1959).

A velocity profile may vary depending on the regime that a flow falls into, which is either subcritical or supercritical. The parameter that decides the regime of the flow is the Froude number which is defined as follows:

$$Fr = \frac{U}{\sqrt{g\,\Delta\rho/\rho_m h}} \tag{2.5}$$

The flow is subcritical if $Fr < 1$ or otherwise the flow is supercritical. Here U is the depth-averaged velocity, h is the depth averaged flow height, $\Delta\rho$ is the density difference between the flow and the ambient, ρ_m is the density of the flow. From equation (2.5), we can deduce that a subcritical flow, in general, corresponds to lower slopes, thicker flows and lower than velocities in supercritical flows.

In addition, the condition of the bed has an effect on the velocity profile. Experimental investigations conducted by Sequeiros et al. (2010) have shown that a turbidity current flowing on a smooth plane bed tends to have a greater maximum velocity and it is located at a lower height as shown in Fig. 2.5. The details of how the roughness and the characteristics of the bed form influences the velocity profile of the flows is beyond the scope of this work and therefore is not further discussed.

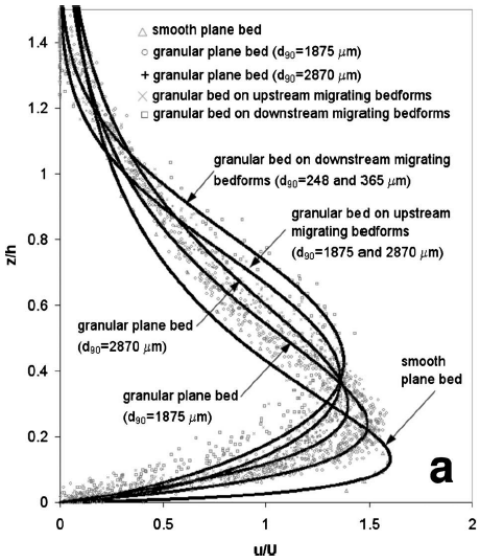

Figure 2.5 Dimensionless velocity profile of a turbidity currents flowing on different beds (reproduced from Sequeiros et al., 2010).

2.4.4 Concentrations Profiles

For a depositing sustained turbidity current flowing in a smooth channel, the experimental investigations performed by Altinakar et al. (1996) have shown that the concentration profile in the body of such flows can be described using a Rouse relation in the wall region and a Gaussian relation in the jet region where the Rouse relation is defined as follows:

$$\frac{C}{C_b} = \left(\frac{h_{max}-y}{y}\,\frac{b}{h_{max}-b}\right)^{\eta} \tag{2.6}$$

where $\eta = u_s/(\kappa u_\tau)$ is the Rouse exponent, c_b is the reference concentration at a distance $b = 0.05h_t$ from the bed, κ is a constant and u_τ is a shear velocity. In the jet-region, the concentration profile can be described using an exponential function defined as follows:

$$\frac{C}{C_m} = \exp\left[-\alpha_c \left(\frac{y-h_m}{h-h_m}\right)^{\beta_c}\right] \tag{2.7}$$

where α_c and β_c are constant values, C_m is the concentration where the maximum velocity is located, and h_m is the height where the maximum velocity is located. Figure 2.6 shows the data that they obtained from their experiment and the equations (2.5 – 2.6) that are fitted onto the data. It can observed that their experimental data has significant amount of scattering in the jet region and this increases the uncertainty in the accuracy of their data. On the other hand, more consistent experimental data were obtained by Garcia (1994) in a separate experimental investigation as shown in Fig. 2.6(a). Their concentration profile fitted well with an exponential function in similar form as equation (2.7), and this suggests an exponential function is sufficient to completely describe the concentration profile of the body of the turbidity current. In a more recent experimental investigation performed by Sequeiros et al. (2010), sustained turbidity currents propagating in a smooth plane exhibit Gaussian-like concentration profiles as shown in Fig 2.6(b). Also shown in Fig. 2.6(b) are the concentrations of a turbidity current flowing on a rough bed which exhibit markedly different kind of profile, i.e. the concentration becomes a constant instead of continually increasing as it approaches the bottom boundary.

The discussion so far has been on the body of a sustained turbidity currents. The concentration distribution of a surge-typed turbidity current may deviate from that of a sustained turbidity current. McCaffrey et al. (2003), Choux et al. (2004) recorded snapshots of the concentration field of surged-typed turbidity currents at different downstream locations. They observed that the head is thicker and has a greater concentration than the body of the flows as shown in Figure 2.7 (the thickness of the flows gradually decreases towards the rear of the flows). However, the head exhibits equally strong concentration stratification as the body of the flows and this indicates

that the concentration profile of the head of the flow can be estimated using a Gaussian relation. Similar kinds of concentration distributions were predicted in the two-dimensional numerical simulation performed by Felix (2002) as shown in Fig. 2.8.

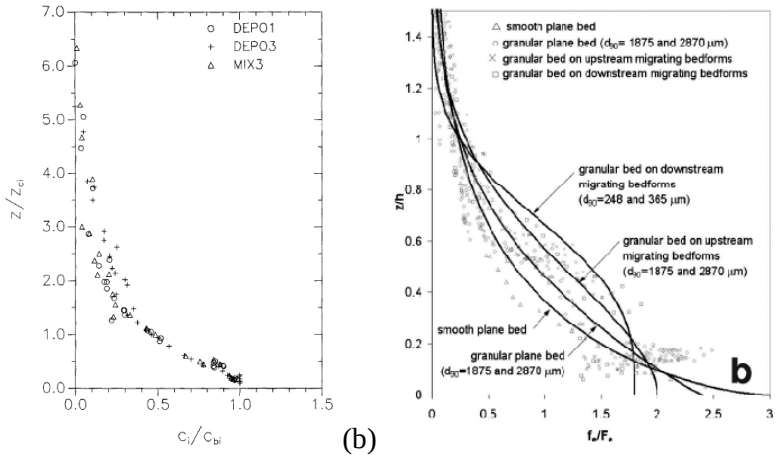

(a) (b)

Figure 2.6 Experimental predictions on the concentration profile of a turbidity current flow in (a) flat bed, reproduced from Garcia (1994), and (b) different bed roughness, reproduced from Sequeiros et al. (2010).

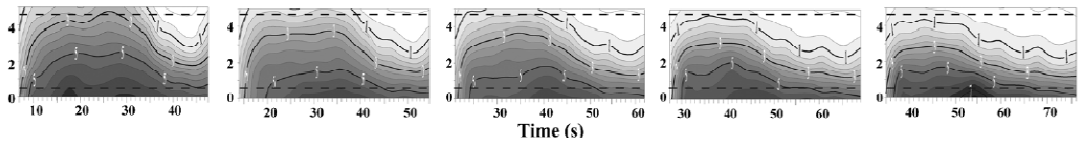

Figure 2.7 A measurement on the concentration distribution within a turbidity current at five different downstream locations, for flows with a 14% initial concentration, reproduced from Choux et al. (2004).

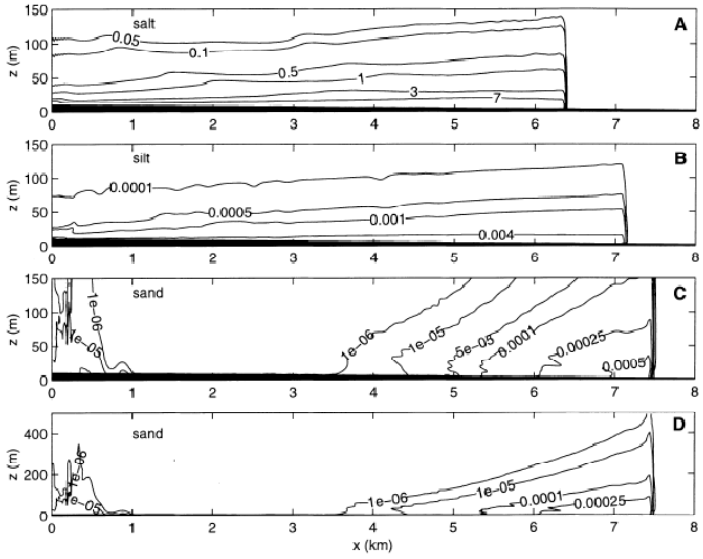

Figure 2.8 Numerical predictions on the concentration distribution of gravity currents carrying (a) salt, (b) silt, (c) fine sand, and (d) coarse sand, reproduced from Felix (2002).

2.4.5 Flow Turbulence

The turbulence structure is an important feature in turbidity currents as it influences the suspension of the grains it carries as well as the movement of the current itself. Kneller et al. (1997, 1999) presented the turbulence structure of a turbulent and sub critical saline gravity current. It was observed that the instantaneous velocities can exceed the mean downstream velocities by up to 50%. In addition, the maximum Reynolds stress was found to occur within the head which also has the highest turbulence intensities. Large Reynolds stresses were found at the top of the head and beneath the nose of the current due to the shear along the boundary of the current. Figure 2.9(a) shows that the arrival of the head is immediately preceded by a rapid increase in the displaced ambient fluid, followed by a large fluctuation in the velocities due to the large eddies flowing inside the current. Negative vertical

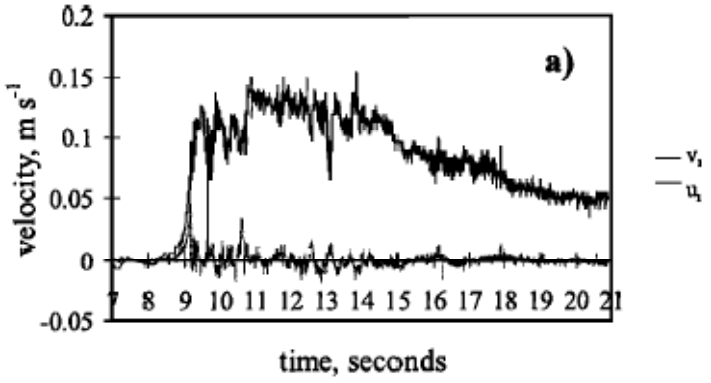

(a)

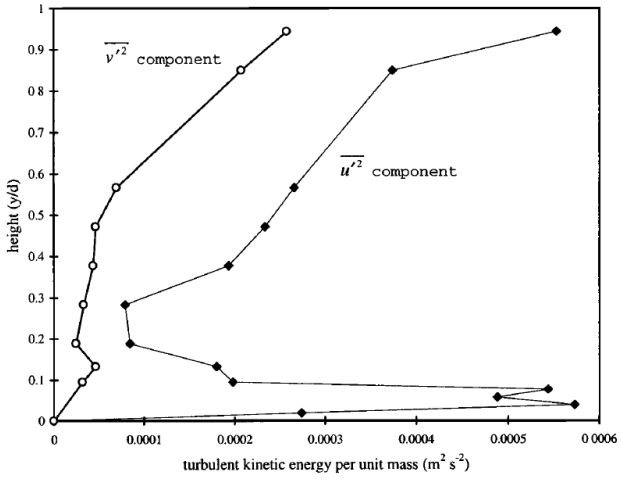

(b)

Figure 2.9 (a) Measurements on the time-series downstream and vertical velocities of a lock-release saline gravity currents at downstream 800mm and height 7mm. (b) Streamwise and vertical components of the turbulent kinetic energy per unit mass as a function of height within the current, reproduced from Kneller *et al.* (1997).

velocities were observed due to the intense mixing of the current with the ambient fluid and the downwards motion of the mixed flow. Kneller *et al.* (1999) showed both vertical and horizontal components of turbulent kinetic energy of density currents are minima around the level of the downstream velocity maximum and maximum at the top and bottom boundary due to the high shear rate (see Figure 2.9(b)).

2.4.6 Deposit Characteristics

The deposit characteristics of a turbidity current represents the thickness and the length of the deposit and the grain structure within it. The initial and the boundary conditions play an important role in influencing the deposit characteristics. The sediment concentrations, the grain characteristics (size, density and shape, and the initial volume of the flows, can affect the deposit characteristics. In addition, the boundary condition such as the channel slope, and the surface condition (type of sediment that overlain the surface and the surface roughness) can affect deposition.

Generally, it is difficult to gain a full understanding of the relation of these parameters and the final deposit characteristics, since these parameters are correlated. Changing one parameter can affect the dynamics of the flow, e.g. for a flow with a fixed concentration travelling down a slope. Hence, the best way is to start with flow with the simplest dynamics and then slowly increase the complexity of the problem. Alternatively, research may be divided into studying a specific dynamics by changing just one specific parameter. Here a brief review is given on the important findings from the previous investigations in order to gain some understanding on how the initial conditions can affect the bed characteristics.

Middleton & Neal (1989) investigated the effect of the flow initial concentration, initial suspension volume and grain size lock release flow on the bed thickness and length. They showed that flows with high concentration (40%), low settling velocity (fine particles), and large volume of suspension (large lock volume in the experiment) tend to exhibit uniform bed thickness and only in distal parts is there a rapid decrease in the bed thickness. On the other hand, flows with a low concentration (20%) and large settling particles (coarser particles) tend to exhibit a wedged shaped deposit thickness. Using dimensional analysis, Middleton & Neal (1989) derived the following functional relationship:

$$\frac{t}{(HL)^{0.5}} = f\left[\left(\frac{u_s}{u_f}\right), C\right] \tag{2.8a}$$

where u_f is the speed of the front of the flow, u_s is the settling velocity of the particle, and H and L are the height and the length, respectively, of the mixture in the lock box. Middleton & Neal (1989) plotted $\log(u_s/u_f)$ vs $\log(t/(HL)^{0.5})$ and showed that the data for a concentration of 20% can be fitted by the line:

$$\log\left(\frac{u_s}{u_f}\right) = 1.75 + 2\log\left[\frac{t}{(HL)^{0.5}}\right] \tag{2.8b}$$

This equation is useful for estimating the velocity of the head of the current (u_f) from observable properties of the bed, if an assumption is made about the concentration of the suspension. Further, Gladstone et al. (1998) showed that the run-out distance of surged typed flows is significantly extended if a small amount of fine material is added into the flow. They show that the fine particles have a low particle settling velocity and hence have lower rate of sedimentation.

2.5 Physics within Turbidity Currents

In a clear flow, the motion of a fluid is governed by the Navier-Stokes equations which comprises of a set of equations that expresses the conservation of mass and momentum as follows in Cartesian coordinates:

$$\frac{\partial \rho}{\partial t} + \frac{\partial \rho u_i}{\partial x_i} = 0 \tag{2.9}$$

$$\frac{\partial}{\partial t}(\rho u_k) + \frac{\partial}{\partial x_i}(\rho u_i u_k - \tau_{ik}) = -\frac{\partial p}{\partial x_k} + B_k \tag{2.10}$$

where ρ and u_i denote the density and velocity fields, and τ_{ij} denotes the viscous stress tensor, and p and B_k denote the pressure and volumetric body forces, respectively. Since particles and fluid co-exist in turbidity currents, it is necessary to describe the physics of the particle motions as well as the interaction between the fluid and the particles. If the Knudsen number is close to or greater than unity, the mean free path of a molecule is comparable to the length scale of the problem under investigation and therefore the continuum assumption of fluid mechanics is no longer a good approximation. For flows with small Knudsen number, it is convenient to treat the particle phase as a continuum which can be described using another set of transport equations that has similar form to equation (2.9) (e.g. see Drew (1983)). Thus, the particle phase has its own density, velocity and pressure

fields but shares the same pressure field with the fluid phase. To distinguish the particle from that of the fluid, we denote the fluid phase by the subscript *f* and the particle phase by *p*.

In turbulent flow, the turbulence causes the flow to fluctuate with time, which means that the instantaneous quantities of the flows such as velocity, concentration and pressure fields, randomly deviate from their average values. In order to determine the effect of the turbulence on the flow, it is necessary to apply an averaging procedure on the governing equations (2.9) & (2.10). The possible choices for the averaging procedure can be either ensemble-, time- or space-averaging. Applying either of these averaging procedures on equations (2.9) & (2.10) leads to the phase averaged equations for the fluid phase which takes the following form:

$$\frac{\partial}{\partial t}(\alpha\rho) + \frac{\partial}{\partial x_i}\left(\alpha_f \rho_f U_{fi}\right) = 0 \tag{2.11}$$

$$\frac{\partial}{\partial t}\left(\alpha_f \rho_f U_{fk}\right) + \frac{\partial}{\partial x_i}\left(\alpha_f \left(\rho_f U_{fi} U_{fk} - \left(\tau_{fik} + \tau^t_{fik}\right)\right)\right) = -\alpha_f \frac{\partial P}{\partial x_k} + \alpha_f B_k + \rho_f M_{fk} \tag{2.12}$$

Here a new variable α which denotes the volume fraction of the fluid appears in both equations. Two new terms τ^t_{fik} and M_{fk} appear in equation (2.12) and these denote Reynolds stresses and the interfacial forces acting on the fluid phase due to the presence of the particle phases, respectively. The interfacial forces for a particle generally consist of drag, lift, virtual forces etc. The detail of these forces is discussed in section 2.4.1. The phase averaged equations for the particle phase has a similar form to those given in equations (2.11) & (2.12).

In the literature for multiphase flow, it is common practice to apply a second averaging procedure on the governing equations (2.11) & (2.12) in order to achieve a more physically intuitive model of the turbulent multiphase phenomena (see Bernard & Harlow, 1988; Burns et al. 2004). Such averaging procedures can be either time-averaging or Favre-averaging. Generally the latter is favoured because it entails no extra term in equation (2.11) whereas the latter leads to an extra term appearing in this equation. As for equation (2.11), both averaging procedures entail an extra term that is known as turbulent dispersion, which describes the effects of

the fluid turbulence on the particle phase. The details of this term are further discussed in section 2.4.3.

In the continuum theory of mixtures, the constituents of a mixture may be modelled as the superimposed continua, so that each point in the mixture may be simultaneously occupied by a material point of each constituent. The transport equations for the Mixture phase can be derived by summing the transport equations for the particles and the fluid which take the form (e.g. Manninen et al. 1995):

$$\frac{\partial}{\partial t}(\rho_m) + \frac{\partial}{\partial x_i}(\rho_m U_{mi}) = 0 \tag{2.13}$$

$$\frac{\partial}{\partial t}(\rho_m U_{mk}) + \frac{\partial}{\partial x_i}(\rho_m U_{mi} U_{mk} - (\tau_{mik} + \tau_{mik}^t)) + \frac{\partial}{\partial x_i}(\tau_{Dik}) = -\frac{\partial P}{\partial x_k} + \rho_m B_k + \rho_m M_{mk} \tag{2.14}$$

Here the mixture phase is denoted by the subscript *m* to distinguish the variables from the fluid and particle phases. The mixture density ρ_m is defined as $\rho_m = \alpha_f \rho_f + \sum \alpha_p \rho_p$ and the mixture velocity is defined as $U_{mi} = 1/\rho_m(\alpha_f \rho_f U_{mi} + \alpha_p \rho_p U_{pi})$. Turbidity currents may carry more than one type of particle and thus the mixture phase represents the summation of the fluid and all the particles carried by the flows. The definition of the convection term of the mixture momentum equation (2.14) is defined as follows:

$$\frac{\partial}{\partial x_i}(\rho_m U_{mi} U_{mk}) = \frac{\partial}{\partial x_i}\left(\alpha_f \rho_f U_{fi} + \sum \alpha_p \rho_p U_{pi}\right) - \frac{\partial}{\partial x_i}\left(\alpha_f \rho_f U_{Mi} U_{Mi} + \sum \alpha_p \rho_p U_{Mi} U_{Mi}\right) \tag{2.15}$$

where U_{Mi} is the diffusion velocity which represents the velocity of each phase relative to the mixture velocity, i.e. $U_{Mi} = U_{fi} - U_{mi}$ for the fluid phase and $U_{Mi} = U_{pi} - U_{mi}$ for the particle phase. Note that a new stress tensor τ_{Dik} appears in equation (2.14) which is the diffusion stress due to the phase slip and it is defined as

$$\tau_{Dik} = \alpha_f \rho_f U_{Mi} U_{Mi} + \sum \alpha_p \rho_p U_{Mi} U_{Mi} \tag{2.16}$$

The mixture viscous stress tensor is defined as $\tau_{mik} = \alpha_f \tau_{fik} + \sum \alpha_p \tau_{pik}$ and the Reynold stress-like stress tensor is defined as $\tau_{mik}^t = \alpha_f \tau_{fik}^t + \sum \alpha_p \tau_{pik}^t$. Further, M_{mk} represents the summation of the interfacial forces $M_{mk} = M_{fk} + \sum M_{pk}$.

2.5.1 Particle Interfacial Forces

2.5.1.1 Drag Force

For a solid particle immersed in a fluid, the primary interfacial force is the balance of the drag force and gravity. If the density of the particle ρ_p is greater than that of the fluid ρ_f, the particle is pulled downwards by the gravity force and is resisted by the drag force that arises from the pressure and viscous stresses applied on the particle surface. Consequently, there is a difference between the velocity of the particle and that of the ambient fluid and this difference is known as the relative velocity $\vec{u}_r$, which is also known as the slip velocity in some literature. For consistency, the former term is adopted in this thesis. If the particle is settling in a quiescent flow (ambient fluid has zero velocity), the terminal velocity of the particle is generally known as the particle settling velocity and is denoted by u_s here. The general interest is the theory that is used to determine the magnitude of the particle settling velocity. For a spherical particle, an analytical solution for u_s is only available when the convection of the flow is assumed to be zero and this solution was first derived by Stokes (1851). Stokes determined that the drag force on a particle in such a limit is given by:

$$\vec{F}_{D,Stoke} = 3\pi d_p \mu_f |\vec{u}_r| \tag{2.17}$$

where d_p is the particle diameter, and μ_f is fluid dynamic viscosity. This expression can be expressed in a more general form as follows:

$$\vec{F}_D = -\frac{1}{2} A_p \rho_f C_D u_r |\vec{u}_r| \tag{2.18}$$

Here A_p is the surface area of the particle ($A_p = \pi d^2/4$), C_D is the aerodynamic drag coefficient and takes a value of $24/Re_s$, and Re_s is the particle Reynolds number that is defined as

$$Re_s = \frac{d|\vec{u}_r|}{\nu_f} \tag{2.19}$$

Equating equation (2.17) to the gravity force results in an expression for the Stokes settling velocity that is widely used in the sedimentology literature:

$$u_s = \frac{(\rho_p - \rho_f) g d^2}{18 \mu_f} \quad (2.20)$$

However, the assumption that convection is negligible limits equation (2.17) to very small particle Reynolds number ($Re_s \ll 1$). For Re_s greater than about 1, the flow structure around the particle changes and the assumption of negligible convection no longer holds. Thus, there is no analytical solution available to describe the drag on a particle in this regime and either numerical simulations or experiments are used to determine the drag force. It should be noted that the drag force expression (2.18) is unchanged but the drag coefficient changes with different values of Re_s. For a sphere, with a particle Reynolds number less than 800, the drag coefficient can be accurately estimated using the correlation suggested by Schiller & Naumann (1935) which is defined as

$$C_D = \frac{24}{Re_s}(1 + 0.15 Re_s^{0.687}) \quad (2.21)$$

Equation (2.21) describes a decrease in C_D with an increase in the value of Re_s. At Re_s = 800, the value of C_D has dropped to about 0.44 and changes remarkably little for 800 < Re_s < 3.5 x 10^5. This regime is known as the Newton regime whereas the regime where C_D is decreasing is known as the intermediate regime.

2.5.1.2 Lift Force

When a particle is immersed in a shear flow, it experiences an additional force that acts on the particle, and this is known as the shear-induced lift force. The shear flow results in a velocity difference around the surface of the particle which consequently results in a pressure difference around the particle. Since a higher velocity results in a lower pressure and vice versa, a particle immersed in a shear flow experiences a push away from the low-velocity region. Early theoretical predictions on the lift force on a particle immersed in a shear flow was derived by Saffman (1964). However, his analysis is restricted to only small Particle Reynolds number (Re_p << 1) and small shear Reynolds number (Re_ω << 1) (see Chapter 4 for the definition). McLaughlin (1991) extended the analysis of Saffman to higher particle and shear Reynolds number ($Re_p \leq 1$). For $Re_p > 1$, accurate results can be obtained via experimental or numerical studies and these studies generally expresses the prediction on the lift force in terms of the lift coefficient C_L. (Kurose & Kumari,

1999; Bagchi & Balachandar, 2002; Kim, 2006). It should be noted that the lift on a stationary particle in a shear flow and that on a particle is allowed to rotate freely in a shear flow are different. According to Bagchi & Balanchandar, the latter has a lower value of lift coefficient. Furthermore, it is possible for a particle to experience a lift force in the absence of shear. This occurs on a rotating particle with a significant slip between the fluid and the particle rotational velocity. Such a lift force is known as the rotation-induced lift force. The physic behind such a lift force has similarities with that of the shear-induced lift force, i.e. the rotational slip results in a velocity difference and hence a pressure difference across the particle.

The significance of the lift force is known in many industrial applications. For instance, the distribution of the bubbles flowing up a pipe is influenced by both the shear in the flow and the physical characteristics (size and shape) of the bubbles (e.g. Frank et al. (2004, 2008). In vertical pipe flow, small bubbles tend to drift towards the wall, whilst larger bubbles drift towards the axis of the pipe. For particles flowing in an air duct, the shear-induced lift force has been postulated to be responsible for the lifting of particles that have deposited on the surface of the duct back into the main flow (e.g. Zeng & Michaelides, 2002). In a centrifugate (a process that involves the use of the centrifugal force for the sedimentation of mixtures within a centrifuge) where particle rotation is significance, the rotation-induced lift force is important for an accurate prediction on the particle distribution within the flows. In the laboratory, the shear-induced lift force can be observed on spherical particles suspended in a Poiseuille flow (Segre & Silberberg, 1962).

2.5.2 Turbulence

2.5.2.1 Single-phase flow

A flow experiences random fluctuations in the velocity and fields when the Reynolds number of the flow reaches a value in order of magnitude O(10^5)). Consequently, time-averaging the transport equation of the fluids, namely equations (2.9) and (2.10) give raises to an extra unknown in the equations which is commonly known as the Reynolds-stresses tensor (denoted as $< u_i u_j >$). The appearance of the new unknown results in a so-called closure problem because the number of unknowns in the transport equations exceeds the number of equations available to be solved. To overcome such limitations, the Reynolds stresses have to be modelled.

The commonly accepted assumption is the Boussinesq approximation which assumes that Reynolds stresses can be treated in the same way as the viscous shear stress based on the fact that they both have the same mathematical form. Using the Boussinesq approximation, the Reynolds stresses take the form (e.g. Wilcox, 1993):

$$< u_i u_j >= \tau_{ij} = 2\mu_t S_{ij} - \frac{2}{3}\rho k \delta_{ij} \quad (2.22)$$

Here μ_t is the eddy viscosity, S_{ij} is the mean strain rate tensor, δ_{ij} is kronecker delta and $k$is the turbulent kinetic energy. The key to successfully modelling the turbulence is the accurate prescription on the value of μ_t which describes the state of the turbulence. How μ_t is determined is not straightforward because further assumptions have to be made (see below) and the accuracy of the predictions on the value of μ_t relies on the validity of these assumptions. The approach or assumptions taken on predicting μ_t is commonly known as the RANS turbulence model. In the past, numerous turbulence models have been proposed for resolving μ_t. Some investigations have built model specifically tailored to specific applications. For instance, Mellor & Yamada (1982) developed a multi-level turbulence closure model for a Geophysical Fluid Model and the turbulence model of Spalart & Allmaras (1992) is built in predicting aerodynamic flows. On the other hand, there are general purpose turbulence models that are built without tailoring to any type of flows. The widely used models are the $k-\epsilon$ turbulence model suggested by Jones & Launder (1972) and the $k-\omega$ turbulence model suggested by Wilcox (1993). In the $k-\epsilon$ model, the μ_t is computed as follows:

$$\mu_t = c_\mu \rho k^2/\epsilon \quad (2.23)$$

Here ϵ is the rate of dissipation of turbulence and $c_\mu = 0.09$. A transport equation for the each turbulent kinetic energy and the rate of dissipation of turbulence is derived from the RANS transport equation. These are given as follows:

$$\frac{\partial(\rho k)}{\partial t} + \frac{\partial(\rho u^i k)}{\partial x^j} = \frac{\partial}{\partial x^j}\left[\beta_k \mu_{eff}\frac{\partial k}{\partial x^i}\right] + G_k - \rho\epsilon \quad (2.24)$$

$$\frac{\partial(\rho \epsilon)}{\partial t} + \frac{\partial(\rho u^i \epsilon)}{\partial x^j} = \frac{\partial}{\partial x^j}\left[\beta_\epsilon \mu_{eff}\frac{\partial \epsilon}{\partial x^i}\right] + C_{1\epsilon}\frac{\epsilon}{k}G_k - C_{2\epsilon}\rho\frac{\epsilon^2}{k} \quad (2.25)$$

Here there are the usual time derivative and the convective terms on the left hand side of the equations. The symbol μ_{eff} is the combination of the molecular viscosity

and the eddy viscosity $\mu_{eff} = \mu_f + \mu_t$. The first term on the right hand side of the equations describes the diffusion of either the turbulent kinetic energy or the rate of dissipation of turbulence. G_k represents the production of the turbulence due to shear, and the closure coefficients are $C_{1\epsilon} = 1.44$ and $C_{2\epsilon}$ = 1.92. The quantities β_k and β_ϵ represent the inverse effective Prandtl numbers, which have a value of 1.393 in the high-Reynolds number limit. It should be noted that these quantities are the consequence of the k-ϵ model that is derived using a rigorous statistical technique called the Renormalization Group Theory and hence they do not appear in the standard k- ϵ model.

2.5.2.2 Multiphase flow

The modelling of turbulence in multiphase flows is more complex than for single phase flows because both the fluid and the particle turbulence and the interactions between them need to be taken into account. Three kinds of treatment, which vary in complexity, have been suggested in the literature (e.g. FLUENT, 2009). The simplest approach is known as the mixture turbulence models which treat the turbulence of the particle and the fluid together as a single phase. In this approach, the turbulence of the mixture is modelled using a RANS turbulence model that is extended from the single-phase model. The mixture turbulence model is only suitable for flows where the fluid and particles are very well mixed and their density ratio is close to unity. In these cases, the turbulence characteristics of the fluid and particles are almost the same and hence can be accurately represented by the mixture turbulence. In the second and more advanced approach called dispersed phase turbulence, the turbulence of the continuous phase and that of the dispersed phase are treated separately. The former is modelled using a modified RANS turbulence model whereas the latter is modelled using an algebraic model (e.g. Simonin 1991). The algebraic model predicts the turbulence of the particle based on the turbulence characteristics of the fluid phase. The interaction between the turbulence of the fluid and that of the particle is also taken into account. The dispersed phase turbulence approach is applicable for flows where the turbulence characteristics of the particles are distinctively different from that of the fluid. In the most advanced approach which is known as the dispersed RANS model, the turbulence of each phase is resolved using the RANS turbulence model.

The choice on the approach depends on the type of the flows. Ideally, the dispersed RANS model is suitable for solving any kind of multiphase flow. However, the model is more complex and may achieve greater difficulty in achieving solution convergence due to the need to resolve two additional transport equations. Thus, it is prudent to opt for a simpler approach if it is possible. In turbidity currents, where the particles are well mixed within the flows and the particles settle slowly in the flows (particles are strongly coupled with the fluid flow), it is safe to use the mixture turbulence model approach.

The Mixture $k-\epsilon$ turbulence model is derived in a similar way as that for the single phase $k-\epsilon$ model. Deriving from the mixture momentum equation (2.14), the transport equations for $k-\epsilon$ take the form:

$$\frac{\partial(\rho k_m)}{\partial t}+\frac{\partial(\rho u_{mi} k_m)}{\partial x_j}=\frac{\partial}{\partial x_j}\left[\beta_k \mu_{eff}\frac{\partial k_m}{\partial x_i}\right]+G_{km}+G_{bm}+G_{mm}-\rho_m \epsilon_m \qquad (2.26)$$

$$\frac{\partial(\rho_m \epsilon_m)}{\partial t}+\frac{\partial(\rho_m u_{mi} \epsilon_m)}{\partial x^j}=\frac{\partial}{\partial x^j}\left[\beta_\epsilon \mu_{eff}\frac{\partial \epsilon_m}{\partial x^i}\right]+C_{1\epsilon}\frac{\epsilon_m}{k_m}(G_k+C_{3\epsilon}G_b)+G_m-C_{2\epsilon}\rho\frac{\epsilon^2}{k} \qquad (2.27)$$

Here each symbol is denoted with a subscript *m* to indicate that the phase is mixture, and k_m and ϵ_m are the mixture turbulent kinetic energy and rate of dissipation. Note that two additional terms G_b and G_m appear in both equations, and these terms are known as the turbulence buoyancy and turbulence modulation, respectively. The turbulence buoyancy is modelled using the standard Boussinesq gradient diffusion approach:

$$G_b=-\frac{\mu_{tm}}{\sigma_t \rho_m} g_i \frac{\partial \rho_m}{\partial x_i} \qquad (2.28)$$

Here σ_t is a constant and typically takes a value between 0.75 and 1. A stable stratification (negative concentration gradient) reduces the strength of the mixture turbulence while an unstable stratification (positive concentration gradient) enhances the mixture turbulence. The flux Richardson number is generally used to quantify the extent to which the turbulent mixing is damped by the turbulent buoyancy. It is defined as the ratio of the turbulent buoyancy (damp turbulence) to the turbulent shear production (generate turbulence), namely,

$$Ri_f = -\frac{G_b}{G_k} \tag{2.29}$$

For $Ri_f > 0.25$, the flow is dynamically stable (suppression of turbulence by stable stratification overcomes production by shear). Further, for $Ri_f < 0.25$, the flow is dynamically unstable (turbulent). Neglecting the downstream component of the flows, Smith & McLean (1977) derived an analytical expression that directly expresses the effect of stable density stratification on the eddy viscosity of the flow which is as follows:

$$\mu_t = \frac{\mu_{tm}}{1+10M} \tag{2.30}$$

where M is related to the Richardson number as follows:

$$M = \frac{1.35Ri_f}{1-13.5Ri_f} \tag{2.31}$$

Equation (2.28) can also be expressed in terms of the particle volume fraction α_p as follows:

$$G_b = -r_\rho \rho_f \frac{\mu_{tm}}{\sigma_t \rho_m} g_i \frac{\partial \alpha_p}{\partial x_i} \tag{2.32}$$

where $r_\rho = (\rho_s - \rho_f)/\rho_f$. The constant $C_{3\epsilon}$ in equation (2.27) controls the degree of the effect of G_b on ϵ_m. Rodi (1980) has suggested the values of the coefficient $C_{3\epsilon}$ to be close to 1 in vertical boundary layers and close to 0 in horizontal boundary layers. Henkes et al. (1991) suggested the following expression for $C_{3\epsilon}$ that satisfies both limits, namely

$$C_{3\epsilon} = \tanh\left|\frac{v_m}{u_m}\right| \tag{2.33}$$

where v_m is the component of the flow velocity parallel to the gravitational vector and u_m is the component of the flow velocity perpendicular to the gravitational vector. Thus $C_{3\epsilon}$ is 1 if the main flow direction is aligned with the direction of gravity. For buoyant shear layers that are perpendicular to the gravitational vector, $C_{3\epsilon}$ is zero. Equation (2.32) have been employed in many previous studies (e.g. Jha & Bombardelli, 2009) for predicting the velocity and concentration profiles of sediment laden, open channel flows using two-equations turbulence models. The significance of the turbulence buoyancy in an open channel was demonstrated in the

numerical results of Toorman (2003). The results show that the flux Richardson number for open channel flows carrying small particles (low settling velocity) tend to reach an asymptotic value of 0.25, which is the critical value for transition from laminar to turbulent flow in non-buoyant stratified flow. Recently, Bahari and Hejazi (2009) simulated a stratified gravity current using the k-ϵ turbulence model and showed that the flows are largely inclined to a stable stratified situation. They also compared equation (2.29) with the Algebraic Stress Model of Davidson (1990) (which considers the additional non-isotropic turbulent stress in the production term) and showed that the former tends to predict a higher value of eddy viscosity at the current head and consequently a slightly greater spreading rate. However, no experimental data was employed to validate the accuracy of either model.

Turbulent modulations describe the reduction or enhancement of the fluid turbulent kinetic energy due to the presence of the particles in the fluid. The known mechanism responsible for the reduction of the fluid turbulent kinetic energy is the acceleration of the particles whereas the mechanism responsible for the enhancement of the fluid turbulent kinetic energy is the flow velocity disturbance created by the wake or the vortices shed from the particles. Clear evidence of turbulence modulation was first demonstrated by Gore & Crowe (1989) who synthesized data from various sources that investigated the change of flow turbulence intensity due to the presence of the particles in the flow. Gore & Crowe (1989) successfully categorized the turbulence modification into reduction and enhancement by proposing an intuitive parameter,d_p/l_e, which is the ratio of the particle diameter to a characteristic size of the large eddies. They noted that d_p/l_e = 0.1 represents a demarcation point where at larger values of $d_p/l_f^t$the addition of particles will increase the carrier phase turbulent intensity and at lower values cause a decrease as shown in Fig. 2.10. However, there is a concern on the generality of this classification given that most of the results are based on gas-solid/gas-liquid flows and whose dynamics are different from that liquid-solid flows. More recently Tanaka & Eaton (2008) have improved the classification of turbulence modulation, as introduced by Gore & Crowe (1989) by taking into account the mass loading of the particles (ratio of the total mass flow rate of the particles to the total mass flow rate of the fluid phase) or the particle Reynolds number, which are important factors in controlling the magnitude of the turbulence modulation. Performing a

dimensional analysis on the particle-laden Navier-Stokes equations, they derived a new dimensionless parameter so-called the “particle momentum number” Pa which effectively separates the cases into enhancement and reduction groups as shown in Fig 2.11. Particles with large values of Pa result in turbulence enhancement while particles with a smaller value of Pa decrease the turbulence. However, the classification is not monotonic because the range of Pa for turbulence enhancement in gas-solid flows and liquid-solid flow is not similar and this suggests that the mechanics behind turbulence modulations for gas-solid and liquid-solid flows are characteristically different. However, the actual reason is not clear and further analysis is needed to understand it.

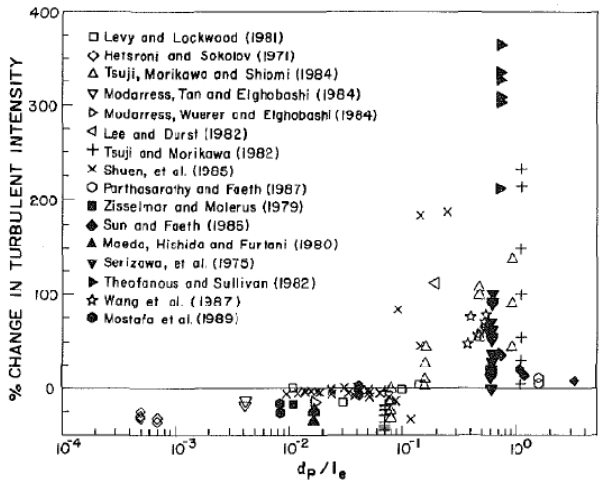

Figure 2.10 Percentage change in turbulent intensity of flows carrying particles as function of the ratio o the particle size to eddy length scale, reproduced from Gore & Crowe (1989).

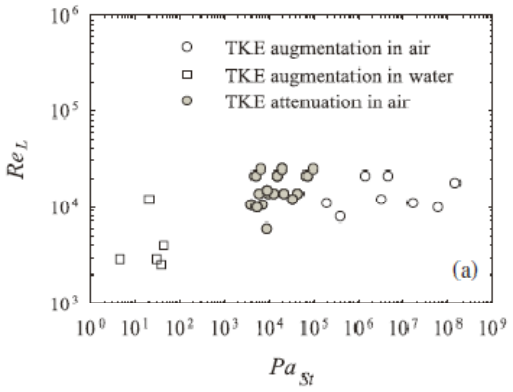

Figure 2.11 Plot of Re_L as a function of Pa (reproduced from Tanaka & Eaton, 2008).

We have illustrated that turbulence modulation may be important in a solid-fluid flow. In the following, we present the approach proposed in the past for modelling turbulence modulation. Chen & Wood (1985) were among the earliest to successfully implement the turbulent modulation (reduction only) function into the $k-\epsilon$ turbulence model. They demonstrated that the turbulent modulation function is given by

$$G_m = \overline{F_D u_p^{'}} = \frac{\alpha_p \rho_p}{t_p}\left(\overline{u_f^{'} u_p^{'}} - \overline{u_p^{'} u_p^{'}}\right) \tag{2.34}$$

where $u_p^{'}$ is the fluctuating component of the particle velocity, F_D is the hydrodynamic drag force and it is given by the Stokes law for small particle, i.e. $F_D = \alpha_p \rho_p (u_p - u_f)/t_p$, and t_p is the Stoke particle relaxation time. The unknown $\overline{u_f^{'} u_p^{'}}$ needs to be modelled and Chen & Wood modelled it as follows:

$$\overline{u_f^{'} u_p^{'}} = 2k_f \exp(-\frac{0.0825 t_p}{t_f^t}) \tag{2.35}$$

This equation was suggested by Chen and Woods (1985) to model the fluid velocity fluctuation-particle velocity fluctuation cross-correlation for a gas-solid flow. Alternative models are those of Tu & Fletcher (1994), Mostafa & Mongia (1988) and Lightsone & Hodgson (2004). Lightstone & Hodgson (2004) compared the predictions of the aforementioned models against the experimental predictions of gas-solid flows of Tsuji et al. (1984) and concluded that these models are effectively predictors for cases where the particles affect the gas-phase turbulence mainly through the drag force. Their observations verified that the models are applicable for gas-solid flows and therefore their validity in liquid-solid flows is not known. Due to the lack of experimental data on measuring the reduction of turbulence in liquid-solid flows, a new experimental investigation is required, but this is outside of the scope of this thesis. For this reason, equation (2.35) is assumed to be valid for the class of problems investigated in this thesis. A more detailed description on the mathematical forms of the turbulence modulation in $k - \epsilon$ turbulence model is given in appendix A1.

2.5.3 Turbulent Dispersion

As discussed in section 2.3, double averaging the multiphase transport equation of momentum results in an additional term M^{TD} known as the turbulent dispersion. The following equation show that Favre-averaging the interfacial force M_p of the particle transport equation results in two terms, the original interfacial force term and the turbulent dispersion term M^{TD} which contains the fluctuating component of the interfacial force (Burns et al., 2004):

$$\overline{\vec{M}_p} = \vec{M}_p + \vec{M}_p^{TD} \tag{2.36}$$

The overbar denotes the Favre-averaging procedure. Physically, this term represents the particle acceleration due to the interaction between the continuous phase velocity fluctuations and the interphase momentum transfer. If only drag force is considered in the interfacial term, the modelled form of the turbulent dispersion is given by (Burns et al., 2004):

$$\vec{M}_p^{TD} = C_p \frac{\nu_t}{\sigma_t}\left(\frac{\nabla\alpha_p}{\alpha_p} - \frac{\nabla\alpha_f}{\alpha_f}\right) \tag{2.37}$$

Where $C_p = \frac{1}{8} C_D A_p \rho_f \left|\vec{U}_p - \vec{U}_f\right|$, $\nu_t$is the fluid kinematic eddy viscosity, $\nabla\alpha_p$ is the gradient of the particle volume fraction and $\nabla\alpha_f$ is the gradient of the fluid concentration. In the limit of very small particle, particle has zero volume fraction α_p = 1 and $C_p = 1$, which reduces equation (2.37) to be equivalent to Fick's law of diffusion.

An alternative way to model the turbulence dispersion was suggested by Simonin (1991) who derived several models in the general framework of the probability density function (PDF) approach, each of which uses a different level of sophistication to capture the various mechanisms of interaction between particles and the gas-flow turbulence, and hence to determine the fluctuating motions of the particles. His most basic model is based on the turbulence theory of Tchen (1947), which describes the behaviour of particles in a steady, homogeneous turbulent flow. The model relies on an algebraic formulation to relate the particle and fluid-particle quantities via inertial drag expressions to the fluid flow turbulence. Thus no transport equation is needed to model the turbulence of the particle and the particle-fluid correlation. The model is applicable to dilute flows of particles with low inertia (or particle having small Stoke number). For particle with large Stoke number, higher order closure models will be needed in order for the prediction to be accurate. The model has similar form of equation to equation (2.37) but instead of fluid eddy viscosity, it is computed using the following diffusivity function:

$$D_t = \frac{1}{3}\,\overline{u_f' u_p'}\; t_{fp}^t \tag{2.38}$$

where $\overline{u_f' u_p'}$ is the particle-fluid fluctuating velocity correlation and t_{fp}^t is the eddy-particle interaction time and they are modelled as follows

$$\overline{u_f^{'}u_p^{'}} = \frac{2t_{fp}^t}{t_p + t_{fp}^t} k_f \tag{2.39}$$

$$t_{fp}^t = \frac{t_f^t}{\sigma_{TD}^t}\left[1 + C_\beta \zeta^2\right]^{-\frac{1}{2}} \tag{2.40}$$

The term in the bracket term of Equation (2.40) was first developed by Csanady (1963), and accounts for the cross-trajectory effect when large droplets pass through eddy due to their high relative inertia. Constant σ_{TD}^t is a coefficient used to ensure that the gas-droplet coefficient D_t approaches the value for the diffusive transport of a scalar as the particle relaxation time approaches zero with respect to the eddy-droplet interaction time. In such a limiting case, the gas-droplet velocity correlation $\overline{u_f^{'}u_p^{'}}$ approaches the values of the fluid's turbulent KE $2k_f$, and the eddy-droplet interaction time t_{fp}^t approaches t_f^t/σ_{TD}^t.

The turbulent time scale t_f^t is computed using the following equation:

$$t_f^t = \frac{3}{2} C_\mu \frac{k_f}{\epsilon_f} \tag{2.41}$$

Where C_μ is a turbulence model constant and has a value of 0.09, k is turbulent kinetic energy and ϵ is the turbulence dissipation rate. The particle relaxation time is determined using the following equation

$$t_p = \frac{4}{3}\frac{\rho_p}{\rho_f}\frac{d_p}{C_D|u_r|} \tag{2.42}$$

Where C_D is the particle aerodynamic drag coefficient, and $|u_r|$ is the magnitude of the slip velocity.

The cross trajectory effect arises in the dispersion of large particles in a turbulent flow field because large particles do not follow the fluid motion due to their inertia. Large particles possess the velocity non-equilibrium characteristic which enables these particles to interact with several turbulent eddies. This results in a reduction in the particle residence time in each eddy and mitigates the influence of the eddy on the particle trajectory. The effect of cross-trajectories is taken into account in the Simonin model through the parameter C_β. Further, LES simulations performed by Deutsch & Simonin (1991) have showed that C_β takes a value of 0.45 in the direction parallel to the mean relative velocity and 1.8 in the orthogonal direction. In

FLUENT, C_β is modelled by the expression $C_\beta = 1.8 - 1.35\,cos^2\,\theta$ where $cos\,\theta = \frac{\vec{v}_{pq}\cdot\vec{v}_p}{|\vec{v}_{pq}||\vec{v}_p|}$.

The parameter ζ is defined as

$$\zeta = \frac{|u_r|}{\sqrt{\frac{2}{3}k_f}} \tag{2.43}$$

Therefore, equation (2.38) can be expressed as follows:

$$D_{t,Sim} = \left(\frac{\gamma}{1+\gamma}\right)\left(1 + C_\beta\,\zeta^2\right)^{-0.5}\mu_t \tag{2.44}$$

where γ is the ratio between the time scale of the energetic turbulent eddies affected by the crossing-trajectories effect t_{fp} and the particle relaxation time t_p, $\gamma = t_{fp}/t_p$.

D_t controls the rate of the diffusivity of the sediment. In turbulent solute flow, it is equivalent to the fluid eddy viscosity μ_t (e.g. Fick's law of diffusion). In sediment laden flows, its value could be different from that of fluid eddy viscosity. Generally, the different is taken into account by multiplying the μ_t by an additional modifying term C_{TD} as follows:

$$D_t = \mu_t C_{TD} \tag{2.45}$$

In some of the Bousinesq-based models, it is treated as a constant (e.g. Choi et al. (2002)), which is a crude approximation. However, the value of D_t may vary depending on the characteristics of the particle and the flows. Hence, in a more generalised M_{TD} should be treated as a non-constant. In the Simonin model, C_{TD} is equivalent to

$$C_{TD} = D_{t,Sim}/\mu_t \tag{2.46}$$

2.5.4 Mixture Model and Slip Equation

Manninen et al. (1995) introduced a major simplification to the multiphase transport equation which significantly improves the robustness of the model in numerical calculating. Manninen et al. derived the so-called 'slip equation' which replace the original particle momentum transport equation in determining the particle velocity field. The advantage of the slip equation is that it is de-coupled from the multiphase

transport equations. Hence using it instead of the original transport equations reduces one transport equation in the numerical solver. The limitation of this equation is that it assumes the particle phase velocity reaches an equilibrium level with the mixture phase instantaneously. In order to satisfy this assumption, the particle must be strongly coupled with the fluid flow, which also means that the particle must be small enough to only need short period of time to fully respond to the flow.

The slip equation can be derived by subtracting the mixture momentum equation from the particle transport equation, which results in the following expression:

$$M_{pk} = \alpha_p \left[\rho_p \frac{\partial U_{Mpk}}{\partial t} + \left(\rho_p - \rho_m\right)\frac{\partial U_{mk}}{\partial t}\right] + \alpha_p\left[\rho_p\left(U_{pi}\cdot\nabla\right)U_{pk} - \rho_m(U_{mi}\cdot \nabla)U_{mk}\right] - \nabla\cdot\left[\alpha_p\left(\tau_{pik} + \tau_{pik}^t\right)\right] + \alpha_p\nabla\cdot(\tau_{mik} + \tau_{mik}^t + \tau_{Dik}) - \alpha_p\left(\rho_p - \rho_m\right)g_i \quad (2.44)$$

Further, the following assumptions have been made:

(i) The particle phase instantaneously reaches an equilibrium state with the mixture phase, i.e. $\frac{\partial U_{Mp}}{\partial t} = 0$. This assumption limits the equation to only strongly-coupled flows where the dispersed and the continuous phases reach an equilibrium state in a short time scale.

(ii) The dispersed phase convection term is equal to the mixture convection term, i.e $\left(U_p\cdot\nabla\right)U_p \approx (u_m\cdot\nabla)U_m$.

(iii) The viscous stress (τ_{mik}, τ_{pik}) and the diffusion stress (τ_{Dik}) are neglected since they are small in comparison to the other effects.

Further, it should be noted that the particle (τ_{pik}^t) and mixture turbulent stresses (τ_{mik}^t) cannot be neglected. The assumptions (i), (ii), and (iii) result in the following equation, which is known as the slip equation (Manninen et al., 1995):

$$U_{si} = \frac{(\rho_p - \rho_m)d_p^2}{18\mu_f C_D}\left(\frac{\partial U_{mi}}{\partial t} + U_{mj}\frac{\partial U_{mi}}{\partial x_j} - g_i\right) + M_{pi}' \quad (2.47)$$

where the term M_{pi}' represents the effect of the turbulence on the particle slip velocity and the approach adopted for determining this value is explained in Section 2.4.3. It should be noted that the slip equation takes into account only the drag force, but it can be easily modified to take into account additional forces, such as the lift

force into account. The mixture transport equations (2.13) & (2.14), together with the particle volume fraction equation, the particle slip equation given above, and the mixture RANS turbulence model equations (2.26 – 2.27) form a complete model which is commonly known as the Mixture Model. Also the particle volume fraction is slightly more complex than the Mixture continuity equation as it contains an extra term that arises due to the diffusion velocity as follows (see equation (2.15) for the definition of the diffusion velocity)

$$\frac{\partial}{\partial t}\left(\alpha_p \rho_p\right) + \frac{\partial}{\partial x_i}\left(\alpha_p \rho_p U_{mi}\right) = -\frac{\partial}{\partial x_i}\left(\alpha_p \rho_p U_{Mi}\right) \tag{2.48}$$

2.5.5 Near Wall Dynamics

The flow near the wall is retarded by the presence of the wall. Towards the wall, the velocity of the flow progressively decreases until it has zero velocity at the wall. Such a condition is known as the 'no-slip' condition. The region where the flow experiences an effect due to the presence of the wall is known as the boundary layer. For a clear-water flow, a sound understanding on the dynamics of the flow within the boundary layer has been achieved after several years of research. A concise description on the boundary layer of clear fluid can be found in the textbook by Nezu (1993) and brief description is presented here. We start from the flow closest to the wall where the flow turbulence is absent and only the fluid viscous stresses are present. In this case, the fluid velocity increases linearly with the flow height. This region is known as the viscous sublayer. The equation for the velocity in this region can be expressed, in general, in the following form:

$$y^+ = u^+ \qquad \text{for} \quad y^+ < 5 \tag{2.49}$$

where $y^+ = y\, u_\tau/\nu$ and $u^+ = u/u_\tau$. Further away than the viscous sublayer (y^+> 30), there exists a region with constant shear stress and negligible viscous effects and the velocity can be expressed as follows:

$$u^+ = \frac{1}{\kappa}\ln y^+ + C^+ \tag{2.50}$$

Equation (2.50) is also known as the "law of the wall" and the region where this equation is applicable is called the 'log-law' region. The value of the constant κ and C^+ are determined by fitting equation (2.50) against experimental predictions. For smooth wall, κ is 0.4 and C^+ is 5.5. The law of the wall is applicable up to 20% of

the height of the flow from the wall. Between the viscous sublayer and the log wall region ($5 < y^+ < 30$), the viscous stresses and the turbulence are equally important. Van Driest (1956)'s mixing length model is commonly used to predict the flow behaviour in this region because it fits well with the experimental observations.

In a solid-fluid flow, the dynamics within the boundary layer is considerably more complex due to the presence of the particles which influences the behaviour of the fluid flow. Thus the boundary layer theory of clear fluids needs to be modified/extended in order to accurately describe the physics. It should be noted that the behaviour of the fluid flow and the particle in the boundary layer is different, and hence they need to be modelled separately. For convenience, the problem is treated at the mixture level. Consequently, the theory of boundary layers of clear fluids is retained, except that all the variables are replaced by the mixture variables. The value of the mixture viscosity coefficient μ_m depends on the concentration of the flows and it can be accurately determined using a power-law expression derived by Ishii & Mashima (1984) which takes the form:

$$\mu_m = \mu_f \left(1 - \frac{\alpha_p}{\alpha_{pm}}\right)^{-2.5\alpha_{pm}} \tag{2.51}$$

where α_{pm} is the maximum packing limit of the solid particles (there are always void spaces between the particles). If the particle concentration is very high within the flows, then the particle-particle collisions become more important. However, the mechanics behind these phenomena not well understood and hence further detail is not given here in this thesis. For dilute flows, it is likely that the particle concentration is very high only in the viscous sub-layer and therefore ignoring this mechanism should not significantly affect the accuracy of the models proposed in this thesis.

There are two kinds of treatment of the boundary condition for a turbulent flow that is employed in the $k - \epsilon$ model. The first approach does not resolve the boundary layer profile but instead predicts only the mean velocity in the log layer using the following law-of-the-wall equation:

$$U^* = \frac{1}{\kappa} ln(E y^*) \tag{2.52}$$

where

$$U^* = U_p C_\mu^{0.25} \tag{2.53}$$

Using this approach, the mesh near the boundary must have an acceptable value of y_p so that the parameter y^* falls in the range 30<y^*<300. This approach was known as the Standard Wall Function approach and was first introduced by Launder & Spalding (1974) and it is known as the Wall Function. However, the wall function is inaccurate and requires modification.

The second approach resolves both the viscosity-affected region and the fully turbulent region. This approach is known as the Enhanced Wall Function. The demarcation of these two regions is determined by a wall-distance-based Reynolds number that is defined as follows:

$$Re_y = \rho y \sqrt{k}/\mu \tag{2.54}$$

where y is the wall-normal distance. When Re_y < 200, the region is viscosity-affected and the one-equation model of Wolfstein (1969) model is employed.

The linear and logarithmic laws-of-the-wall are blended using the following function, as suggested by Kader (1981):

$$\frac{du^+}{dy^+} = e^{\Gamma} \frac{du_{lam}^+}{dy^+} + e^{\frac{1}{\Gamma}} \frac{du_{turb}^+}{dy^+} \tag{2.55}$$

where Γ is a blending function and is given by:

$$\Gamma = -\frac{a(y^+)^4}{1+by^+} \tag{2.56}$$

Where a = 0.01 and b = 5. This formula guarantees the correct asymptotic behaviour for large and small values y^+ and reasonable representation of velocity profiles in the cases where y^+ falls inside the wall buffer region (3 < y^+ < 10). The laminar law-of-the wall is determined from the following expressions:-

$$\frac{du_{lam}^+}{dy^+} = 1 + \alpha y^+ \tag{2.57}$$

$$\frac{du_{turb}^+}{dy^+} = \frac{\sqrt{S'}}{\kappa y^+} \tag{2.58}$$

where

$$S' = \begin{cases} 1 + \alpha\, y^+ & for\ y^+ < y_s^+ \\ 1 + \alpha\, y_s^+ & for\ y^+ \geq y_s^+ \end{cases} \tag{2.59}$$

For turbulent fluid flows travelling on a bed of particles, the flow may entrain (or ‘pick up’) the particles from the bed and suspended them into the main flow. This phenomenon is known as “particle entrainment” (or particle re-suspension). In order

to predict this phenomenon, a great deal of research has been invested into the understanding of how particles are entrained into a flow and how the physics vary with different particle characteristics and flow conditions. The subject is complex because the interactions between the flow and a bed of particles could cause a formation of bed forms or topography on the surface of the particle bed, and different bed forms may affect the rate of particle entrainment in a flow. However, bed form is not discussed in this work because the flow in the current research is a small scale flow that does not develop any well-defined bed forms. Here a discussion is given on some of the theories that have been developed on explaining particle entrainment in sediment-laden, open channel flows. It should be noted that particle entrainment is a common process in gas-solid flows, e.g. aerosol particles in turbulent duct flows (Zhang and Ahmadi, 2000), and has been a subject of much research. Basically, there are two kinds of theories that have been developed on particle entrainment. The more detailed one relies on statistical methods in order to understand the instantaneous characteristics of the turbulence of the flow near the bed (known as the coherent structure of the flow) and its relation with particle entrainment. Basically, a turbulent flow near a boundary is characterized by four different events, i.e. the sweep event, ejection event, outward interaction event and inward interaction event. These four bursting events have different effects on the mode and rate of sediment transport (Bridge & Bennett, 1992). The second approach is a macroscopic approach that is based on the concept that particle entrainment is initiated by a threshold bed shear stress. Shields (1936) was among the earliest researchers to suggest this concept.

In order to predict this phenomenon, a great deal of research has been invested into the understanding of how particles are entrained into a flow and how the physics vary with different particle characteristics. In the early investigations, it was postulated that the shear in the boundary layer is responsible for initiating the particle entrainment. Large shear leads to greater pressure differences across the particle and hence a greater upwards force to be exerted on the particle and a greater likelihood for the particle to be entrained. For particle immersed within the viscous sublayer of the boundary layer, the mechanism is equivalent to the lift force exerted on particles immersed in an unbounded shear flow which has been discussed in detail in Section 2.4.1.2 although the effect of the wall must be taken into account in the latter (e.g. Leighton & Acrivos, 1985). For particles with a size greater than the

thickness of the viscous sublayer, the lifting of the particle is postulated to be due to a local, high instantaneous value of the Reynolds stress (e.g. Robinson, 1991; Niño et al., 2003).

In a steady flow (e.g. open channel flows), the shear in the boundary layer is generally described by the shear velocity or the boundary shear stress since they can be conveniently related to the velocity of the main flow through the following relationship:

$$\tau_b = \rho_f C_f \left(u_f\right)^2 \qquad \text{and} \qquad u_\tau = \sqrt{\tau_b/\rho_f} \tag{2.60}$$

Where C_f is a Darcy friction factor which is a dimensionless coefficient describing the roughness of the bed. The value of the shear velocity can be determined experimentally and hence the experimental prediction has been used to verify equation (2.48). The minimum value of τ_b needed to initiate a particle entrainment is known as the critical boundary shear stress τ_c. A key to a successful prediction on particle entrainment is obtaining the correct value of τ_c for particles of any kind. One of the earliest, and widely used, prediction for τ_c was the Shield diagram as proposed by Shields (1936). The diagram shows the value of τ_c required for a wide range of particle Reynolds number Re_p. Van Rijn (1984) re-investigated the problem and suggested that τ_c is not a single value but rather is a range. More recently, Niño et al. (2003) proposed an alternative criterion based on their experimental observations. Figure 2.12 illustrates a comparison between the predictions of Shields (1936), Van Rijn (1984) and Niño et al. (2003) taken from Niño et al. (2003).

In most numerical modelling of turbidity currents, it is often too computationally demanding and complex to simulate the exact mechanisms that initiate particle entrainment, which requires the modelling of the physical appearance of a sediment bed as well as the fluid flow that passes through the bed. Hence, in most numerical investigations, particle entrainment is modelled using particle entrainment criteria. The criterion is also useful for assessing the likelihood for particle entrainment to occur. In numerical modelling, particle entrainment is often used in conjunction with the Exner equation in order to model a decrease in the bed elevation due to the loss of the sediment through particle entrainment or an increase in bed elevation due to the particle deposition from the flow (the Exner equation is a transport equation that

expresses the conservation of mass between sediment in the bed and sediment that is being transported). The Exner equation can be defined as follows:

$$\frac{\partial h_t}{\partial t} = -\frac{1}{1-\lambda_p} \nabla \cdot q_s \tag{2.61}$$

where h_t the bed elevation, q_s is the sediment flux, and λ_p is the bed porosity.

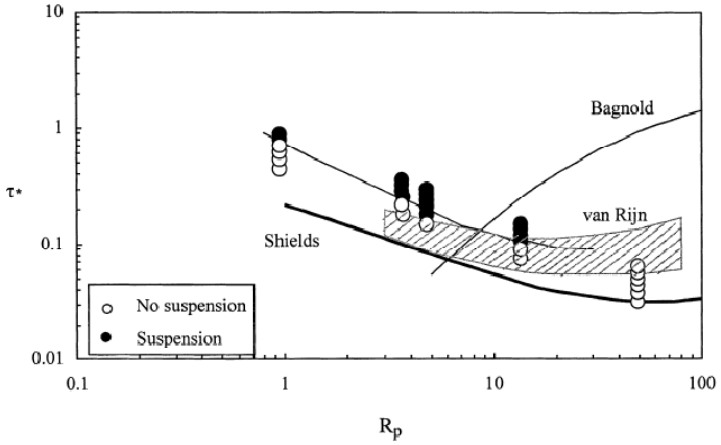

Figure 2.12 Plot of τ^* as a function of the particle Reynolds number R_p with experimental data (circle) and the criteria proposed by Shields (1936), Van Rijn (1984), and Bagnold (1966), reproduced from Niño et al. (2003).

Close to the bed (the actual height of the region is not well defined), particles may moves by rolling, sliding, or saltating (hopping) along the bed. Collectively, these sorts of motion are known as the bed load. Rolling and sliding particles are postulated to be dragged by the fluid flow while saltating has been linked to the turbulence coherent structure near the bottom boundary of the bed (Garcia et al., 1996; Nezu & Nakagawa, 1993). However, since understanding these sorts of physical process is still poor, the modelling of it is not discussed further here.

2.6 Theoretical Model for Turbidity Currents

Numerous numerical investigations on turbidity currents have been performed in the past and many different models have developed or used. Here a review is given on the types of the models and their advantages and limitations.

2.6.1 Integral Box Models

Huppert & Simpson (1980) introduced box models to reproduce the spreading of a fixed volume two dimensional saline gravity surges released using a classical lock-

release configuration. The basis assumption of the model is that the shape of the currents evolves in a series of equal-area rectangles which is an observation made in experiments on the lock-release saline gravity currents. Furthermore, the Box model utilizes the relationship of the front propagation with the concentration and height of the flow established by Benjamin (1968). Using these two assumptions, Huppert & Simpson derived the length and time scale of the flows in inertia-buoyancy and viscous-buoyancy regimes which agree well with the experimental predictions on the rate of propagation of the front of the flows. Later, Dade & Huppert (1995) extended the Box models to suspension-driven gravity currents. They modified the models so that flow loses its concentration through deposition during its propagation. The model achieves good comparison with the experimental data on the rate of propagation of the front of the flows and the deposit thickness profile.

The attractive feature of the Box model is its simplicity. It shows that the physics of a lock release flow is governed either by the balance of inertia force and the flow buoyancy or the balance of the viscous force and the flow buoyancy at late stage of the flow. It also provides quick estimates on key characteristics of a flow such as the run-out distance and the deposit thickness and grain size characteristics. The limitation of the Box model is its rigidity. How well the theory of the model can be extended to other kind of boundary condition, such as the flow propagating downslope and particle resuspension, is not clear. Furthermore, the model still relies on empiricism to achieve good comparison with the experimental data which question its general validity.

2.6.2 Shallow Water Model

The Shallow Water Model (SWM) is based on the shallow water equations first derived by Saint-Venant (1871). The shallow water equations are derived from depth-integrating the Navier-Stokes equations assuming that the horizontal length scale of the flow is much greater than the vertical length scale. This assumption implies that the vertical pressure gradients in the flow are nearly hydrostatic which means that the horizontal velocity field and concentration is constant throughout the depth of the flow. In addition, the model only allows very small vertical velocities. Rottman & Simpson (1983) were the first to use the shallow water equations to investigate some aspects of the compositional/saline gravity currents generated by

means of lock-release configuration. Bonnecaze et al. (1993) later extended the models to particle-driven gravity currents by solving the models along with an equation describing the conservation of particle mass. They discovered that, for the case of a deep ambient, the motion of the overlying fluid can be neglected and the so-called single-layer shallow water equations hold. For shallow ambient, it is necessary to extend this approach by formulating a two-layer system that accounts for the dynamics of the overlying fluid layer. While the shallow water equations are typically integrated numerically, Harris et al. (2001) generalized the similarity solution for homogeneous currents to particle-driven currents and this permits the derivation of analytical solutions to the governing equations. Their solutions show that both the box model and shallow-water model produce propagation equations that are mathematically very similar, and this explains why the box model produces surprisingly good results when compared with experimental data. Harris et al. (2002) extended their analysis to polydisperse-driven gravity currents. The shallow water equations have also been employed to study many variants of gravity currents, such as axisymmetric particle driven currents and rotating particle-driven gravity currents (e.g. Hogg et al., 2001), and dam-break flows (Hogg, 2005). More examples of the use of the shallow-water equations in the context of gravity currents can be found in the textbook by Ungarish (2009).

Comparing SWM with the Box Model, they both assume a uniform velocity and concentration in the flows and rely on the equation (2.1) to dictate the propagation of the flows. The key difference between SWM and the Box Model is that SWM does not assume a constant in the flow thickness and horizontal gradient of the velocity and concentration field. Therefore, SWM has an advantage over the Box Model because it does not refined to geometric assumption on the shape of the flow and it is more theoretically sound than the Box Model since it is based on the Navier-Stokes equations. Therefore, SWM is more flexible than the Box model and can be used to investigate more diverse kind of flows in different boundary conditions. The limitation of the model is that it is restricted by its assumption that the length of the flow must significantly greater than the thickness of the flow. This ultimately restricts the model to describing a fully developed quasi-steady turbidity currents with a quasi-uniform vertical concentration. For a rapid-evolving turbidity currents and sediment-entraining flow propagating down a steep flow, concentration and velocity vertical gradient become important and the accuracy of the model may

suffer. Nonetheless, SWM remains a popular tool among researchers because the form of the governing equations are more amenable to analytical solution that are useful for providing estimation on the behaviour of the turbidity currents such run-out distance and deposit characteristics.

2.6.3 Depth-Resolved Model

Depth-resolved models remove the restriction imposed by the Box Model and Shallow Water Models on the velocity and concentration gradient within the flows and fully resolves the dynamics of the particle and fluid interaction within the flows including the structure of the turbulence within the flows. Generally depth-resolved model can be further classified according to the approach taken to resolve the flow turbulence which profoundly influences the form of the governing equation, the technique required to solve the equations and the form of the solution. The choice is either to model or resolve the structure of the turbulence. The first choice is known as RANS turbulence model (or RANS in general) and the second choice is known as Direct Numerical Simulation (DNS). An example of RANS has been given in Section 2.4. In section 2.4, we see the need to apply averaging procedure to separate the averaged quantities and the additional quantities induced by turbulence. The additional turbulence term is then modelled using turbulence closure scheme. In DNS, such procedures are not required. Instead, the original governing equations are numerically discretised and then resolved using high degree of spatial and time resolution in order to capture the entire length scale and time scale of the turbulence, which means DNS is computationally expensive and restricted to low Reynolds number flow since the computational costs increases with greater Reynolds number. The attractive feature of DNS is that its solution (after being averaged) can be used to validate RANS and understanding the physics of the problem which is valuable for improving simpler model such as RANS. It is worth mentioning that, between RANS and DNS, there exists an approach which utilizes both RANS and DNS to solve the turbulence. This approach is known as Large Eddy Simulation (LES). The principal operation in LES is low-pass filtering and this operation is applied to the Navier-Stokes equations to eliminate the need to resolve the small eddies in the flow. Therefore, in LES, the large eddies are resolved directly while the small eddies are modelled. LES is becoming increasingly popular among the modellers who are interested to understand the physics and detail of a problem without being limited by

flows Reynolds number. However, LES is still considerably more expensive than RANS and, similar to DNS, considered to be more of a research tool for studying the physics of a particular phenomenon in order to improve the existing theoretical model.

Early works done by Eidsvik and Brors (1989) and Brors and Eidsvik (1992) showed the prediction of the vertical turbulent structure of turbidity currents using $k-\varepsilon$ and Reynolds stress turbulence models compared well with experimental data. Interestingly, some features predicted by these models, such as low turbulent kinetic energy at the level of the velocity maximum, were deemed to be unrealistic by the authors but have since been observed in laboratory experiments (Kneller et al., 1999). More recently, validations have been performed on the multiphase model and RANS in predicting turbidity currents. For instance, Choi and Garcia (2002) studied the validity of RANS in predicting the water entrainment in a density currents on a slope. Huang et al. (2005) compared RANS model prediction on the turbidity currents vertical concentration profile with experimental data and attempted to improve the comparison by adjusting one of the model constants. Imran et al. (2004) modelled a turbidity current propagating in a three-dimensional channel using RANS model. Huang et al. (2008) further validate their RANS model in predicting the deposition of a lock release turbidity currents. Felix (2001) had adapted the Mellor-Yamada level 2.5 closure models (Mellor and Yamada, 1982) and used his model to predict the deposition of a historical flow (Grand Banks).

It should be noted that there exists a depth-resolved RANS model that is different from the Mixture Model. This model utilises the Boussinesq approximation in order to simplify the mathematical form of the governing equations. Assuming the density difference between the flow density and the ambient fluid density is sufficiently small, the effect of the particle on the flows can be taken into account by modifying only the gravitational term in the time-averaged momentum equation. An additional equation is prescribed in order to model the transport of the particle within the flow. This additional equation generally takes the following form:

$$\frac{\partial C}{\partial t}+\frac{\partial[(u_j-u_s\delta_j)C]}{\partial x_j}=\frac{\partial}{\partial x_j}\left[\left(\tau_{ij}+\frac{v_{tf}}{Sc_t}\right)\frac{\partial C}{\partial x_j}\right] \tag{2.62}$$

The second term in the bracketed term at the right hand side describes a turbulent dispersion on particles, and Sc_t is a constant value for the turbulent dispersion. The

appealing feature of the Boussinesq-approximation model is that it is mathematically simpler than the Mixture Model because it has one less equation to be solved (the additional equation in the Mixture Model is the Algebraic Slip Equation). The drawback of this approach is that it is limited only to dilute flows whereas the Mixture Model does not suffer such limitation. The use of the Boussinesq-approximation model in predicting turbidity currents can be found in the works of Huang et al. (2005; 2008).

2.7 Conclusion

In this chapter, a short review is given on the current understanding on the dynamics of a turbidity current. The physics within turbidity currents are described using the turbulence-averaged mathematical models. The pros and cons of various kind of numerical models that have been employed in studying turbidity currents are discussed.

Chapter 3

Modelling 2D Particle-Laden Lock-Release Flows

3.1 Introduction

In Chapter 2, a review was given on the current understanding of the fluid dynamics within turbidity currents, which shows that turbidity currents can exhibit ~~a~~ very complex velocity, concentration and turbulence fields that can strongly influence the deposit characteristics. In order to predict the complex flow structure of turbidity currents, the physics that govern the motion of the flows must be properly prescribed. For instance, the settling motion of the particle, fluid turbulence, and the interaction between the flows and the bottom boundary must be accurately described. The details of this physics are described in Section 2.4. The class of numerical models that can incorporate such physics are known as depth-resolved models. As outlined in Section 2.5, there exists simpler models, such as the the Box Model, and Shallow Water Model which do not resolve the internal flow variations. Such models rely on empiricism to incorporate the effect of the flow variation on the macroscopic behaviour of the flow, such as the depth-averaged velocity and concentration. For instance, shape functions are commonly used to estimate velocity and concentration profiles of a turbidity current without needing to resolve the physics that is responsible for them. Therefore these models produce accurate predictions if they are applied in well-validated situations but are dubious when they are employed to study unfamiliar problems. Therefore, in order to have a generalized model that is unrestricted by the boundary conditions of the problem, the model must be depth-resolved and based on sound physics.

As discussed in Section 2.6, a depth resolved model can be further categorized into RANS-based and DNS-based models. The latter yields a prediction that resembles more closely the actual turbulence since they resolve all scales of turbulence eddies in the flow whereas the former yield a time-averaged solution and rely on a closure

scheme to predict the effect of the turbulence on the averaged quantity. Therefore naturally a DNS-based model is more accurate than a RANS-based model but also it requires a considerably larger amount of computational power which leaves it impractical for simulating many flows of natural scale. For this reason, RANS-based models remain both the most practical approach (they are unrestricted by the flow Reynolds number) and generalized approach (they can be applied to arbitrary boundary condition with confidence) for the foreseeable future. Within the RANS-based model, there exist two types of Eulerian multiphase solvers that differ in simplicity and generality, namely a Boussinesq-based model and an Eulerian-Eulerian model. The former employs the Boussinesq approximation which states that the density different $\Delta\rho$ in a buoyancy-driven flows is sufficiently small to be neglected, except where it appears in terms which multiply the gravitational acceleration. The consequence of this assumption is that the original form of the momentum equation for the fluid phase can be retained, except for the gravitational acceleration term which is replaced by the reduced gravity g', and the volume of the particles is neglected (the particle is assumed to co-exist with the fluid phase). Particle transport is modelled using a modified species transport equation (see equation 2.50), an equation commonly used for solving the transport of the chemical species, except that it is modified to take into account the effect of the particle settling. The Boussinesq approximation breaks down when the ratio of the density difference between the flow density and the fluid density to the fluid density is close to unity, which is usually the case when the concentration of the flow is very high. The Eulerian-Eulerian model removes the limitation faced in the Boussinesq based model by taking into account the volume of the particle, but this is at a cost in the increased complexity in the model equations because an additional pair of transport equations (continuity and momentum equations) is needed for the particle phase. The Mixture Model simplifies the Eulerian-Eulerian model by replacing the momentum equation for the particle phase with an algebraic equation, known as the Algebraic Slip Model, based on the assumption that the particle phase is strongly coupled with the fluid phase.

Most of the previous numerical investigations on the turbidity currents have been based on the Boussinesq-based model since it is simpler to resolve numerically than the Eulerian-Eulerian model (e.g. Choi et al., 2002, Huang et al., 2005 and Huang et al., 2007). Only a few numerical studies have been based on the Eulerian-Eulerian

model, e.g. Felix (2002) who investigated the flow behaviour and the deposit of natural-scale turbidity currents using this approach. A more detail review on the past numerical investigations is given in Section 2.6.4. We postulate that it is best to work with an Eulerian-Eulerian approach since it is not limited by the concentration of the flows, as is the Boussinesq model. It is known that turbidity currents are closely related to highly-concentrated flows, such as debris and pyroclastic flows. For instance, a debris flow in deep sea has an ability to transform into a turbidity current when it is being diluted by seawater. In this thesis, the focus is placed on the Mixture Model, which is a simplified version of an Eulerian-Eulerian model. Since the major dispersed components of the majority of marine underflows of interest are fine materials, such as mud, silts and sand, the limitation of the Mixture Model, in which the flows must be strongly-coupled, is valid within these flows.

In this chapter, a validation is performed on the Mixture Model in predicting flow development and deposition from surge-type turbidity currents with a wide range of concentrations and sediment size. The Mixture Model prediction on the propagation of the front of the flows and the deposit characteristics is compared with experimental data. A discussion is given on the model prediction on the internal structure of the flows.

3.2 Mixture Model

The Mixture Model assumes that all the flow phases exist as interpenetrating continua that interact on their boundaries. Each phase has its own mass and momentum conservation equations and an interfacial term is used to compute the interactions. The interfacial forces that commonly exist in a multiphase flow are the drag force, lift force, virtual added mass force etc. As outlined in Section 2.5.1, the drag force is the primary force for solid particles and it always exists whenever there is a relative density difference between the fluid and the particle. Other forces such as the lift force and the virtual mass force may be important in certain situations, but here are neglected in the first validation runs. Summation of the governing equations for each phase results in equations which describe the bulk flow properties, known as the Mixture equations (see equation (2.13 – 2.14) in Section 2.5). By assuming that the particle phase instantaneously reaches the equilibrium state with the mixture phase, an algebraic slip equation for calculating the particle velocity can be derived (see equation (2.44)) hence negating the need to resolve the momentum transport

equation for the particle phase. The turbulence in the flow is modelled using a modified RANS turbulence model. The chosen turbulence model is $k-\epsilon$ RNG which is an improved version of the standard $k-\epsilon$ model (see FLUENT, 2009; Orszag et al., 1993). Near the wall, the enhanced wall functions (see FLUENT, 2009) are employed in order to resolve the entire flow boundary layer profiles at the wall boundary. The interaction between particles and the fluid turbulence is described through incorporation of turbulence buoyancy and turbulence modulation into the turbulence model and turbulent dispersion into the algebraic slip equation (see section 2.5). However, whereas turbulence buoyancy and turbulent dispersion are almost always important in any multiphase flow and should be included in the model in principle, turbulence modulation is important only in certain situations and can often be neglected. For this reason, turbulence modulation is not considered in the first run of simulations. In this chapter, a key focus is the role of turbulent dispersion in turbidity currents. The significance of turbulent dispersion is evaluated by comparing the solutions from the models which include, or exclude, the appropriate term in the algebraic slip equation.

3.3 Validation Data

Experimental data are required in order to validate the Mixture Model's performance in predicting turbidity currents. The choice of the validation data depends on the initial conditions in the problem, the type of the measurements taken and the quality of the measurement data. The initial conditions, or experimental setup, varies significantly depending on the type of flow that it is intended to produce. As explained in Section 2.2, there are two types of turbidity currents that are frequently studied, i.e. sustained turbidity or surge-type currents. The former possesses a quasi-steady body and have been frequently modelled in order to understand the internal structure of the flow, i.e., the velocity, concentration and turbulence profiles of the flows. On the other hand, the latter is unsteady (changes with time) and has been used more for the understanding of the relation between the initial or boundary conditions on the flows and the characteristics of the resultant deposits. In this thesis, fixed-volume surge-typed turbidity currents are investigated since such flows have relatively simple initial conditions. A list of the previous experimental investigations performed on lock-release flows was given in Table 2.2 and the details of the initial conditions for these experiments is given in Table 3.1.

Table 3.1 Experiments on the lock-release generated turbidity currents.

Authors	Suspension Vol. m^3	Concentration %	Mass g	Size (Density) µm (kg/m3)
Middleton & Neal (1989)	0.0078, 0.0117	20, 40	4000	180 (2450)
Bonnecaze et al. (1993)	0.0117	0.2, 1, 2	100-800	9, 23, 37, 53 (3217)
Gladstone et al. (1998)	0.016	0.35	180	25, 69 (3217)
Rooij & Dalziel (2001)	0.0067	0.275	60	37 (3217)
Gladstone & Prichard (2009)	0.0015	2	96	13, 37 (3217)
Hodson & Alexander (2010)	0.018	0.8, 1	450-580	70

Among these experiments, Middleton & Neal (1989) employed an initial condition that is distinctively different from those used in the rest of the experimental investigations. The relative concentration plus the grain size used in their experiments is greater than those used in the other experiments. As a result, their flows deposit quicker than in the other flows. The rest of the flows employed lower densities and have particle smaller than 100µm. Furthermore, it should be noted that the concentration of the suspension depends on both the initial mass of the particles and the initial volume of the suspension. The greater the volume then the greater mass needed to maintain a concentration. For instance, the flows of Gladstone & Pritchard (2010) have a greater concentration than do the flows of Gladstone et al. (1998) despite having lower initial mass. This shows that the initial volume suspension plays an equally important role as the initial concentration in the dynamics of the flow. Clearly it is unrealistic to simulate all the flows in Table 3.1. Therefore in this thesis, focus is given to flows that carry a low initial mass in order to avoid the complex physics that arises in concentrated flows. The details of each individual flow from these experiments used to validate the Mixture Model are given in Table 3.2. The formulae used to predict some parameters in Table 3.2 are given in Table 3.3 Another reason that some of these data (i.e. G69, G25 and D37) is chosen is because refined two-fluid model has been performed on these flows (see the references in Table 3.2) and these results can be used to validate the solution obtained using the Mixture Model. These flows cover a reasonable range of particle sizes (12.8 to 69µm), suspension volumes (0.0015 to 0.016) and initial masses (60 –

180g) and hence cover an appropriate range of types of dilute turbidity currents, from slow moving, highly depositional flows (G69, D37) to fast moving, slowly depositing flows (G13). Simulating these flows should not only validate the general accuracy of the Mixture Model in predicting the turbidity currents but allows us to study how the flow structure varies with the initial conditions of the flows.

Table 3.2 Experimental flows used in this thesis for validating the Mixture Model.

	Unit	G69[a]	G25[a]	B1[b]	G37[b]	G13[c]	D37[c]
Concentration, C	%	0.35			2		0.275
Total Particle Mass	gram	180			96.51		60
Suspension Vol.	m^3	0.016			0.0015		0.006731
Reduced gravity g'	-	0.076			0.44		0.06
Initial mixture density ρ_m	kgm^{-3}	1007.8			1044.4		1006.1
$\Delta\rho/\rho_f$	-	0.00775			0.04434		0.0061
Particle density, ρ_p	kgm^{-3}	3217					
Grain size, d_p	µm	69	25	69,25	36.5	12.8	37
Stokes Settling Velocity, u_s	ms^{-1}	0.0057	0.00075	-	0.0016	0.0002	0.0016
Buoyancy velocity, u_b	ms^{-1}	0.123			0.209		0.089
Reynolds number, Re_f	-	24,500			20,640		11,750
Initial Mixture Viscosity, μ_m	$Ns\ m^{-2}$	0.001012			0.001055		0.001003
Refined-two fluids model result	-	Hoyes (2008)			-		Necker et al. (2002)

[a]Gladstone et al. (1998), [b]Gladstone & Pritchard (2009), [c]Rooij & Dalziel (2001)

Table 3.3 Formulae for parameters used in this thesis

Term	Formulae
Mixture density ρ_m	$\rho_m = (1-\alpha_p)\rho_f + \alpha_p\rho_p$
Excess density $\Delta\rho$	$\Delta\rho = (\rho_m - \rho_f)/\rho_f$
Reduced gravity g'	$g' = g\Delta\rho$
Buoyancy velocity u_b	$u_b = \sqrt{g'h/2}$
Reynolds number Re_f	$Re_f = \rho_m u_b h/\mu_f$
Stokes settling velocity u_s	$u_s = g(\rho_p - \rho_f)d_p^2/(18\mu_f)$

3.4 Numerical Approach

The governing equations for the Mixture Model are highly nonlinear and coupled which makes them difficult to resolve analytically. Hence, in order to obtain a solution for the equations, they have to be treated numerically. In the past, the finite volume method (FVM) has been proved to be a robust and reliable numerical technique for obtaining accurate solutions of the governing equations of fluid-flow. The FVM numerically integrates the governing partial differential equations over a control volume into a discrete set of algebraic equations that expresses the conservation laws on a control volume basis. Values of all unknown variables are calculated at discrete points on a meshed geometry. Finite volume refers to the small volume surrounding each point on a mesh. In this thesis, a commercial FVM code, called FLUENT, is employed to resolve the governing equations in the Mixture Model. The following algorithm is chosen in FLUENT:

1. Segregated pressure-based solver, employing the extended SIMPLE algorithm (Patankar 1980) whereby the velocity and pressure are updated sequentially to enforce the conservation equations, and this is followed by sequential updates of the other scalar conserved quantities.
2. Second-order accurate discretisation schemes are chosen in order to achieve accurate solutions. The second-order implicit scheme was selected to discretise the transient terms and the linear second-order upwind scheme was selected to discretise the spatial advection terms (see Table A2.1 in the appendix section).

In the iterative scheme, all the equations are solved iteratively for a given time-step Δt until the convergence criteria are met before the solution advances to the next time step.

While the algorithm of the FVM is robust, the accuracy of the solution from the FVM is subject to the prescription of the time step Δt and the mesh size Δx. However, there are no predetermined guidelines on how to choose the ‘correct’ values for the time-step and the mesh size since they largely depend on the nature of the problems under investigation. In general, it is accepted that the smaller is the time step and the mesh size then the more accurate is the numerical solution. However, there exists a threshold to the values of the time step and the mesh size

beyond which further reduction in its length should yield only a very small improvement or change in the results obtained. Such a threshold can be regarded as the correct value of the time step and mesh size for the particular problem and can be determined by performing a series of simulations with decreasing values of the time step and mesh size until the perceived quality of the result no longer improves. The mesh size and time step for the current problem is addressed in Section 3.7.

3.5 Boundary Conditions

The numerical treatment of the boundary conditions for the lock-release problem is described in this section. First and foremost, the flow is treated as a two-dimensional flow which evolves only along the downstream direction (flow across the width of the channel is neglected). The reason for such a simplification is to reduce unnecessary computational costs. Although the flow in the experiment develops in a three-dimensional manner, the lateral variation of the flows is much smaller than those in the horizontal and vertical directions and therefore to neglect of the lateral variation can be a valid approximation. In addition, the effect of the side wall of the flume on the flow is neglected in the numerical simulations. This assumption is made based on the fact that the flow is turbulent and possesses only a thin boundary layer on the vertical wall of the channel. Therefore, away from the wall of the flume, large portions of the flow are not influenced by the presence of the wall. The following list details the numerical treatment on the boundary conditions on the flow and their potential errors:

(i) Sediment size and shape. In the numerical model, the sediment is assumed to possess a discrete particle size. In fact all sediments possess a continuous size distribution. However, it is postulated here that the dynamics of the sediment can be represented by the average size of the particles. Therefore, the effect due to the variation of the particle size is not taken into account in the current modelling. In addition, all particles are assumed to be spherical in shape. In fact, the particles employed in these experiments (silica carbide) are irregular in shape and highly angular. Halleimeier (1981) reported that only large non-spherical particles (size of the order of 1mm) experience a reduction in the settling velocity due to shape anisotropy. Based on this conclusion, we rule out the importance of this variable.

(ii) The initial velocity and the turbulence of the suspension. Before the release of the lock-gate in the experiment, a very high swirl is generally introduced to the mixture in order to keep the sediment in suspension. Clearly, the velocity field is non-zero during the release of the flow. However, it is postulated that such a velocity field will quickly dissipate and thus its effect on the initial motion of the flow is negligible. Indeed, Hoyes (2008) observed that introducing a random perturbation to the initial velocity field of the suspension does not yield significant changes to refined-two fluids model simulations of the behaviour of the flow. Therefore, in the current numerical model, the actual swirling motion in the lock gate is not modelled and the initial flow before its release is assumed to be stationary.

(iii) Removal of the lockgate**.** In the experiment, the lock gate has finite thickness, takes a finite time (1-2s) to be completely removed from the flume, and has a frictional effect on the surrounding fluid when it is being removed. However, all these mechanisms are considered to have a negligible effect on the motion of the flows and thus they are not considered in the model (c.f., Giorgio-Serchi et al., 2012).

(iv) The free surface of the ambient flow. The free surface of the ambient fluid does not allow any flow exchange across the boundary. Therefore, it is a valid assumption to model any flow parameter to have zero gradients across it. This is the assumption that is employed in the current numerical model. In addition, for simplicity, the free-surface is assumed to be horizontal and stationary at all times. However, it should be noted that once the lock-gate is removed from the flume, the free surface is perturbed by the motion of the lockgate and this generates surface waves. The magnitude of the surface waves depends on the speed of the release of the lock gate. A fast release leads to large waves which have undesirable effects on the flow (Giorgio-Serchi et al., 2012). It is assumed here that the removal of the lockgate in these experiments has created only insignificant surface waves that have a negligible effect on the behaviour of the flow. For this reason, the surface waves are not modelled in the current investigation.

(v) Deposition from the flows. Particles that fall out from the flow accumulate on the bottom of the flume and form a sediment bed. The thickness of the bed depends on the rate of sediment deposition from the flows as well as the concentration of the

flows. A high concentration and a quickly depositing flow results in a locally thick bed and vice versa. However, in the model, the bed thickness is neglected by extracting particles from the computational domain once they have reached the bottom of the flume. This is a valid assumption provided that the flows investigated are all dilute and only leave a thin bed behind. In addition, the particle re-suspension is not allowed. It is assumed here that the flow has insufficient turbulence strength to re-suspend particle that have fallen out from the flows.

(v) The wall of the flume. The condition on the wall of the flume influences the flow very near to the boundary. In this case, the surface of the flume is smooth enough to be approximated as a wall with zero roughness. However, it should be noted that while the front of the flows along a smooth wall, the body of the flow travels on the sediment bed deposited by the front of the flows. Thus the former propagates on a surface whose roughness is a function of the size of the particles being carried by the flows. A good estimate on the significant of the roughness of the surface of the deposit is the ratio of the particle size to the flow is the ratio of the particle size to the flow height. Taking the coarsest particle size and the flow height, this ratio is 7e-4, which is very small. Thus the surface of the deposit may be considered hydraulically smooth.

3.6 Simulation Setup

The computational domain (or mesh) is created using a meshing software called GAMBIT. A quadrilateral mesh of uniform size is created in the main computational domain and a dense mesh of small size is employed near the boundary in order to resolve the boundary layers in the flows. The flows are modelled using FLUENT, which is a commercial FVM code for solving the Mixture Model. Within FLUENT, additional programs (i.e., user-defined functions, UDFs) are provided in order to incorporate some additional desired features that are unavailable in the original code. These features are the turbulence buoyancy production of the turbulence model and the mass sink that is added to the particle volume fraction transport equation at the bottom cell in order to simulate the extraction of the deposited particle. Furthermore, if turbulence modulation is to be included in the model, a UDF also has to be used. On the other hand, the turbulent dispersion function of Simonin (1991) is available in the original code and can, at choice, be incorporated into the Mixture Model.

3.7 Numerical Accuracy

An investigation was carried to determine a suitable value of the mesh size and time step for the current problem, based upon simulations of flows G69 and G37. The mesh size and the time step are investigated independently. Thus if the mesh size is varied, the time step is kept constant and vice versa. The assumption made here is that the effect of changing one variable (the mesh size or time step) does not significantly vary when another variable is changed. Similar numerical schemes and convergence criteria for the calculations were chosen for all simulations. It is assumed here that no significant change will be observed if more accurate numerical schemes and tighter convergence criteria are employed.

Table 3.4 Details of the mesh used to simulate the flows of (a) Gladstone et al. (1998) (Domain length = 8m, domain height = 0.4m), and (b) Gladstone & Pritchard (2009) (Domain length = 6m, domain height = 0.2)

(a)

Name	Main Domain Cell Size (m)	Total No. Cell in the domain
400 x 20	0.02 x 0.02	17,200
800 x 40	0.01 x 0.01	48,000
1200 x 60	0.00666 x 0.00666	93,600
1600 x 80	0.005 x 0.005	153,600

(b)

Name	Main Domain Cell Size (m)	Total No. Cell in the domain
600 x 20	0.01 x 0.01	24,000
900 x 30	0.005 x 0.005	43,200
1200 x 40	0.004 x 0.004	67,200
1500 x 50	0.00333 x 0.00333	97,500

Figure 3.1(a) shows the prediction of the Mixture Model on the deposit mass profile of flow G69 based on four different meshes given in Table 3.4(a). It can be observed that increasing the number of cells from 400 x 20 to 800 x 40 increases the height of the peak located approximately at downstream distance x = 0.6m. Further increasing the number of cells in the domain to either 1200 x 60 or 1600 x 80 does not result in any significant change to the solution. Thus, it can be concluded that mesh 800 x 40 is fine enough to produce an accurate numerical solution. Mesh 800 x 40 is then used to perform further four simulations with time steps of 0.005s, 0.01s, 0.02 and

0.05. All simulations predict almost identical results as shown in Fig. 3.2(a), which suggests that even the longest time step considered here is short enough to predict the evolution of the flows.

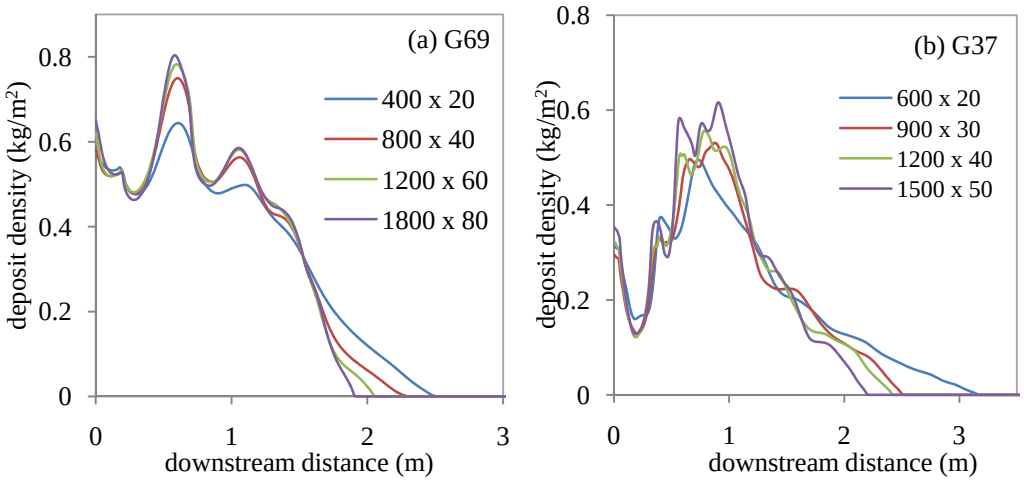

Figure 3.1 Mixture Model prediction on the final deposit mass density as a function of the downstream distance of flows (a) G69, and (b) G37 based on different mesh sizes. See Table 3.1 & 3.2 for the detail of the mesh. The employed time step is 0.01s.

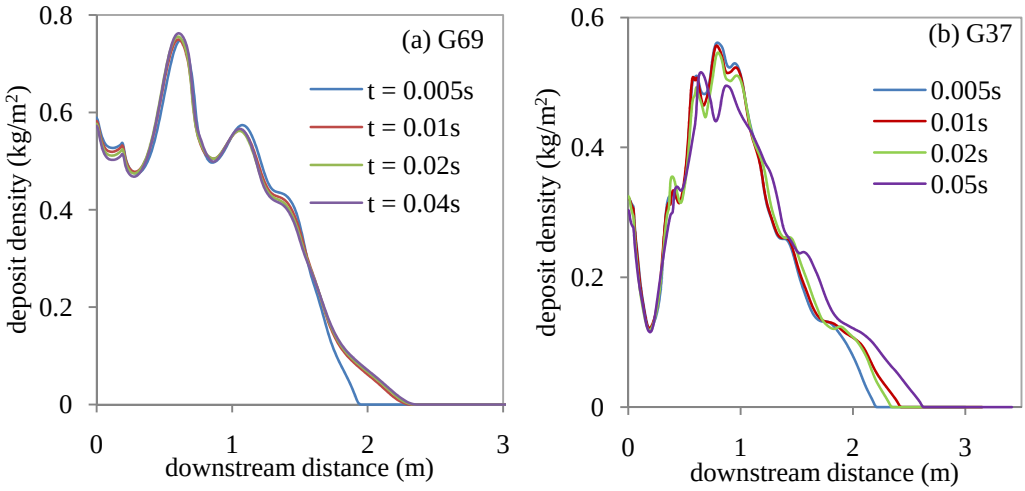

Figure 3.2 Mixture Model prediction on the final deposit mass density as a function of the downstream distance of flows (a) G69, and (b) G37 based on different time steps (0.05s, 0.02s, 0.01s, 0.005s).

Figure 3.1(b) shows the prediction of the Mixture Model on the deposit mass profile of flows G37 based on four different meshes given in Table 3.3(b). Increasing the number of cells in the domain from 600 x 20 to 900 x 30 increases the deposit mass at the approximate downstream distance x = 1m. Further increasing the number of cells in the domain to 1200 x 40 yields only slight changes to the solution. Refining

the mesh to 1500 x 50 results in some small oscillations at the peak located at downstream distance x = 1m. Despite the appearance of the small oscillations, the overall changes in the solution when the mesh is refined from 1200 x 40 to 1500 x 50 are small compared to those when the mesh is increased from 600 x 20 to 900 x 30. Therefore, we conclude that mesh 1200 x 40 should be fine enough to models flows such as G37. The prediction of the Mixture Model on the mass density profile of flows G37 using different value of time step (0.05s, 0.02s, 0.01s, 0.005s) is shown in Fig. 3.2(b). Decreasing the value of time step from 0.05s to 0.02s results in an increase in the deposit mass density at the peak located at x = 1m. Further decreasing the time step to 0.02s, 0.01s, and 0.005s does not result in any significant change to the solution. Therefore it is concluded that the time step 0.02s or smaller can be employed to produce a temporally accurate solution.

Validation on the effect of mesh size and time step on flows G69 and G25 is not performed. It is assumed that the validation performed for G69 and G25 holds for flows G25 and G13, respectively.

3.8 Simulation Results and Discussion

Simulations are performed on flows G69, G25, G37, G13 and D37 using the Mixture Model both with and without the turbulent dispersion (denoted as TD hereafter). In this section, the numerical results are discussed, with a focus given on the comparison between the numerical solution with and without turbulent dispersion, and a comparison between both the numerical solutions and the experimental data. A discussion is given on the comparison between the numerical results and the refined-two fluids model solution where the comparison is available. The evolution of the concentration fields of the flows is discussed.

3.8.1 Temporal Flow Evolution

Similarly to lock-release - generated saline gravity currents, turbidity currents undergo three distinct phases before they terminate. The first phase (slumping phase) is characterized by a rapid collapse of the suspension in which the current propagates at a constant velocity. A backward propagating current is thereby generated due to the displacement of the ambient fluid by the collapsing suspension. The current continues to remain in this phase until the depth ratio of the current to

the ambient fluid is reduced to less than 0.075 (for saline turbidity currents, see Huppert and Simpson, 1980), followed by the inertia-buoyancy phase wherein the buoyancy force of the current is balanced by the inertial force. The inertia-buoyancy regime continues until the viscous effects dominate (Simpson 1997).

Figure 3.3(a & b) shows the prediction from the Mixture Model, with and without TD, on the temporal evolution of the volume fraction contours for mono-disperse flows bearing coarse particles (G69) at t = 0, 5, 10, 15 and 20s. It can be observed that including the effect of TD results in a distinctive change in the concentration fields. Without TD, the currents have an almost uniform particle concentration with thin layers of abrupt decrease of volume fraction surrounding the current core. Including TD, the currents exhibit strong vertical concentration stratification along their entire length and have a greater flow thickness. Such behaviours characterise the entire duration of the flow. For instance, at t = 15s, where the length of the flows G69 is elongated and the thickness is decreased, the model without TD still predicts a relatively uniform concentration within the flow whereas the model with TD predicts a flow that has developed a strong horizontal stratification in the concentration. Clearly the effect of TD is significant but whether the effect is an accurate representation of the actual flows can only be determined by comparing it with the experimental data, or refined-two fluids model, where available. Unfortunately the experimental observation on the concentration distribution is unavailable and hence a conclusion on the accuracy of the numerical predictions can only be inferred from the comparison of the model's prediction and the experimental data on the flows deposit thickness.

The concentration distributions of flows G25, G37, G13 and D37 exhibit characteristics similar to those of flow G69. The model with TD predicts larger flows, initially with a strong vertical stratification in the concentration but later develops a strong horizontal concentration stratification. On the other hand, the Mixture Model without TD predicts a uniform distribution of concentration within the flows which later develop into flows with a large head but small body and tail. Furthermore, flows predicted by the Model with TD appear to dissipate slower than the flows predicted by the model without TD (see Figs. 3.3 – 3.7 for the flows at the later stages). While the TD flows exhibit similar characteristics in the concentration distributions, they are different in terms of their size and duration. Flows with a

large initial suspension volume, and carrying fine particles become larger and propagate further than those with a small initial volume and carrying coarser particles.

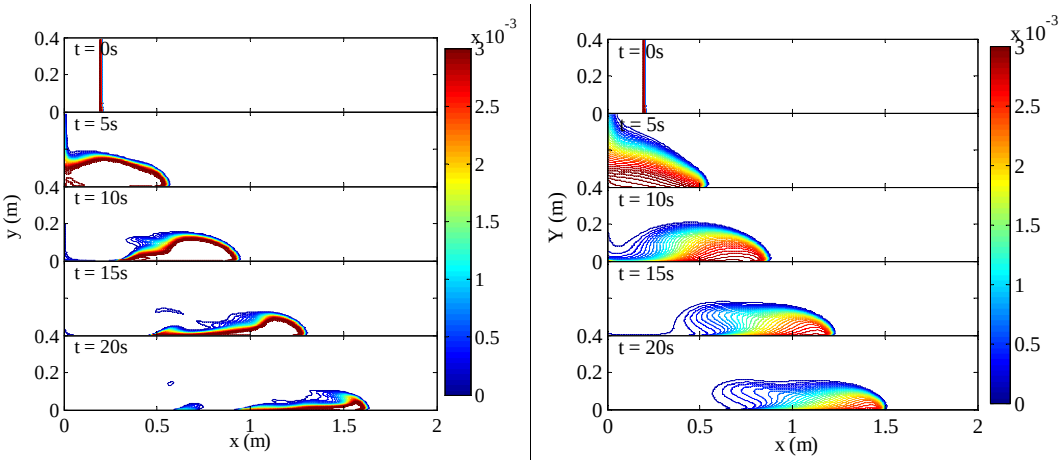

Figure 3.3 Prediction from the Mixture Model without TD (left), and the Mixture Model with TD (right), on the concentration field of flows G69 at *t* = 0, 5, 10, 15, and 20s.

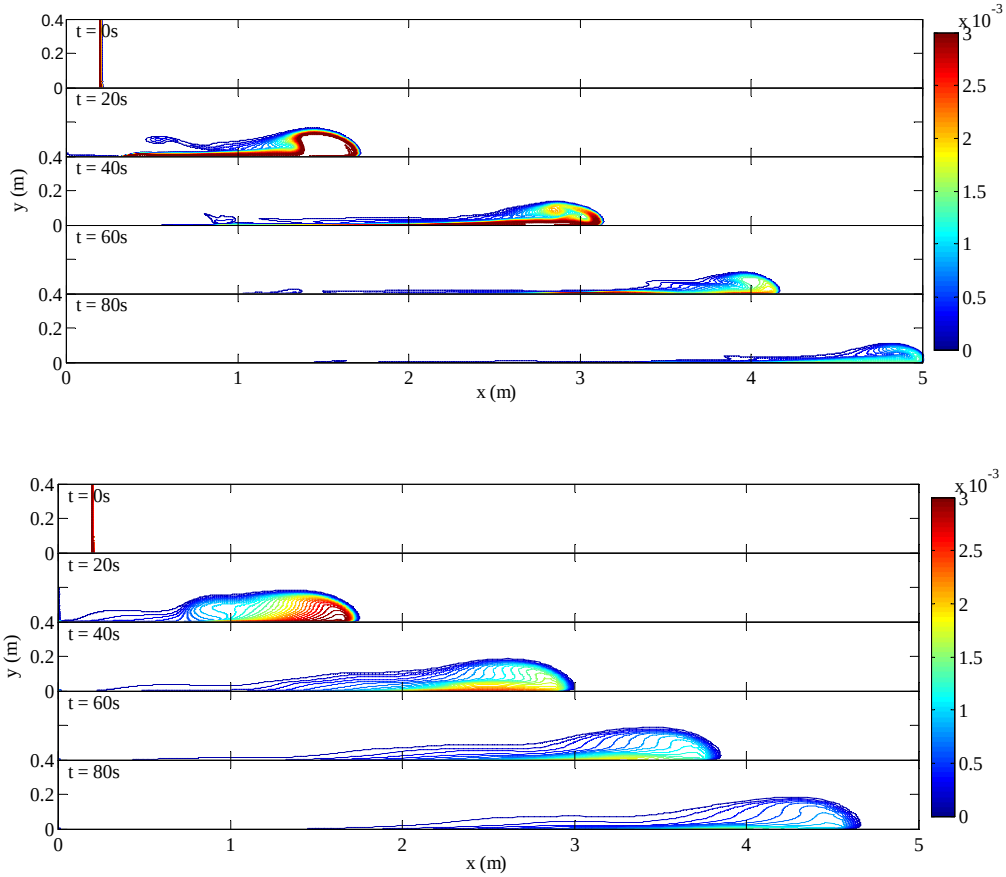

Figure 3.4 Prediction from the Mixture Model without TD (top), and (b) the Mixture Model with TD (bottom), on the concentration field of flows G25 at *t* = 0, 20, 40, 60, and 80s.

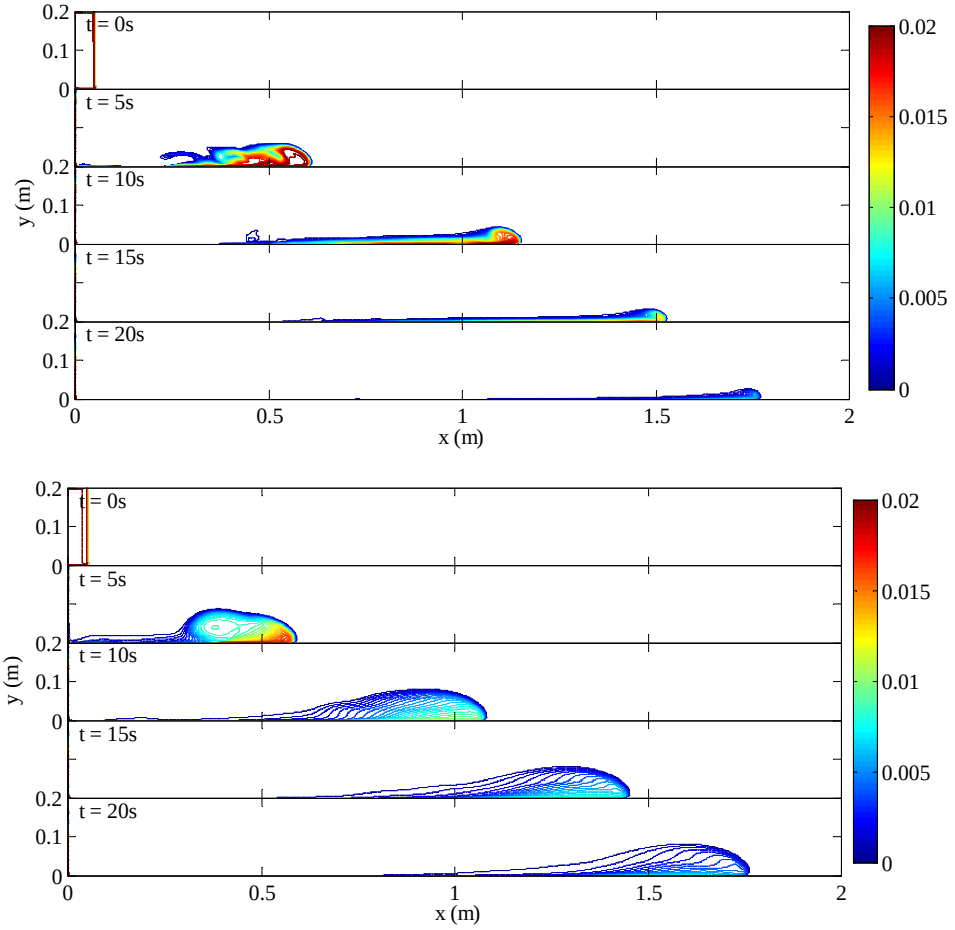

Figure 3.5 Prediction from the (a) the Mixture Model without TD, and (b) the Mixture Model with TD, on the concentration field of flows G37 at *t* = 0, 5, 10, 15, and 20s.

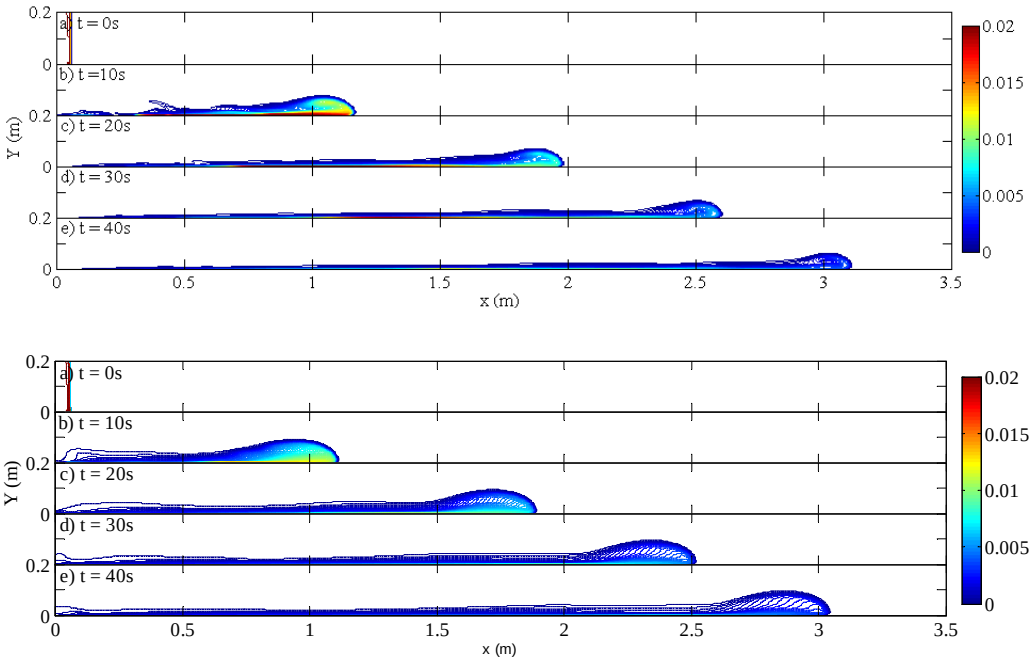

Figure 3.6 Prediction from the (a) the Mixture Model without TD, and (b) the Mixture Model with TD, on the concentration field of flows G13at *t* = 0, 10, 20, 30, and 40s.

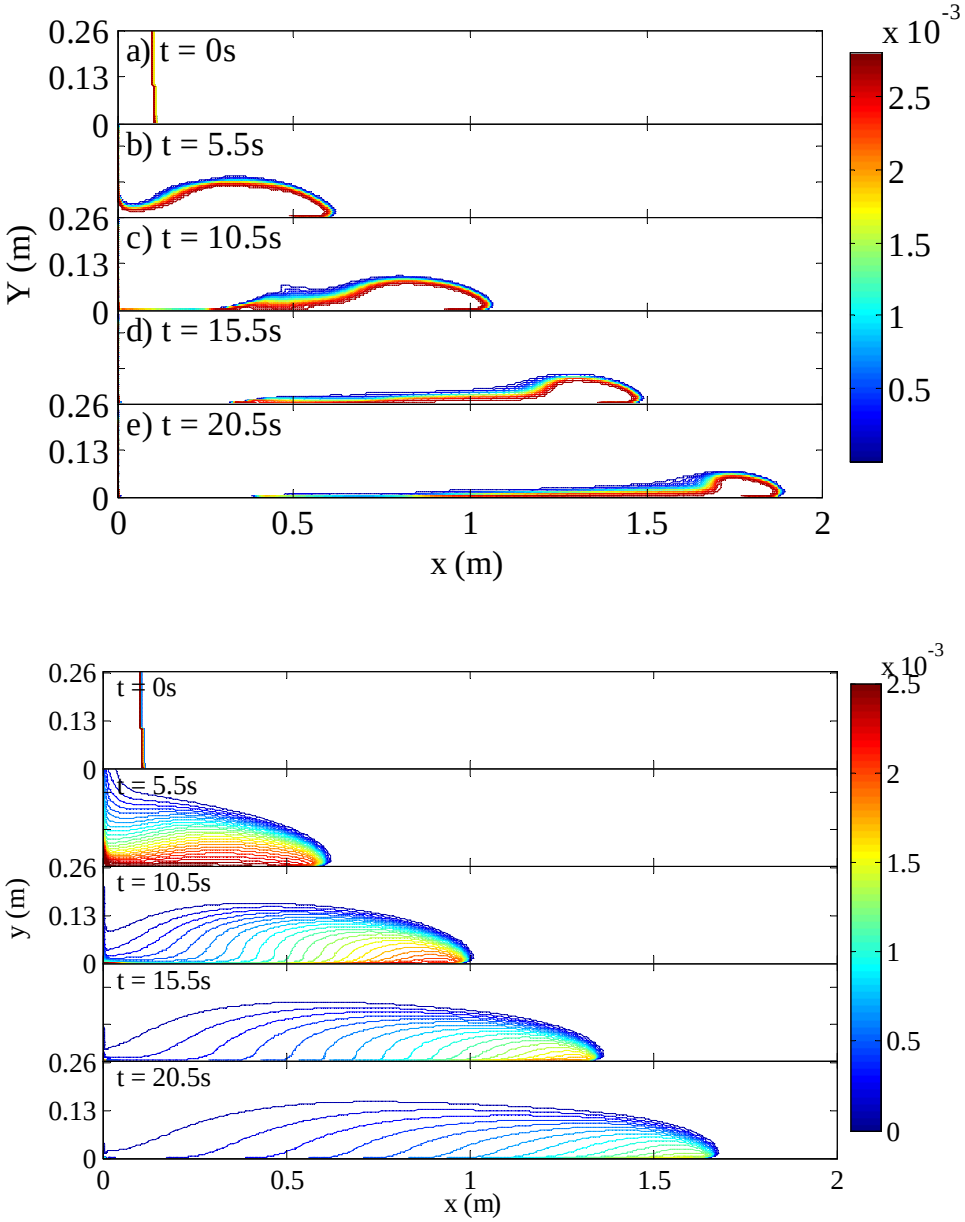

Figure 3.7 Prediction from the Mixture Model without TD (top), and (b) the Mixture Model with TD (bottom), on the concentration field of flows D37 at t = 0, 5.5, 10.5, 15.5, and 20.5s.

3.8.2 Rate of Propagation and Total Mass in Suspension

Figure 3.8(a – e) shows a comparison between the prediction of the Mixture Model without and with TD on the rate of propagation of the front and the percentage mass in the suspension as a function of time for the flows G69, G25, G37, G13, and D37. The current front in the simulation is defined as the furthest downstream point where the particle volumetric concentration in the current exceeds 1%. In any of these cases, both models match well the propagation of the front of the flows, thus

indicating that the effect of TD on the propagation of the flow is insignificant. On the other hand, a comparison between the models on the percentage mass in suspension is less good. The model with TD predicts a slower decrease in the suspended mass over time, thus indicating that the TD has decreased the rate of the deposition from the flow, which is consistent with the observations on the concentration fields shown in the previous section which shows TD dispersing the sediment upwards and causing the sediment to migrate away from the bottom boundary. As a result, the model with TD predicts the flow to have a longer duration of propagation and a further run-out distance. The results can be further synthesized to show how the effect of TD on the rate of the deposition of the flows varies with the initial condition. Figure 3.9 shows that the difference between the percentage mass in the suspension predicted by the model without and with TD as a function of time for the flows G69, G25, G37, G13 and D37. It appears that the finer the grain carried by the flows, the greater is the effect of TD on reducing the rate of deposition from the flow. For instance, G13, G25 have significantly greater differences (a maximum difference of 35% and 25%, respectively) than does G69 (a maximum difference of 10%). In addition, flow speed has an effect on the effectiveness of TD. Slow-moving flows experience a greater effect of TD than the fast-moving flows do. For instance, flows D37 experience a maximum difference close to 50% whereas G37 only experience a maximum difference close to 30% despite both having a similar particle size. In all flows, the magnitude of the difference first increases greatly in short period of time but gradually decreases over time, which implies the effect of TD decreasing over time, possibly due to the dissipation in the strength of the turbulence in the flows.

Due to lack of experimental data on the flows G37, G13 and D37, validation on the accuracy of the numerical prediction regarding the propagation of the front of the flows can only be performed for flows G69, and G25 (see Fig. 3.8a & b). In these cases, both the numerical results compare well with the experimental data. Furthermore, it is interesting to observe how the front propagation of the flows may vary with the initial condition. Fig. 3.10 shows the prediction from the Mixture Model without TD on the front propagation of flows G69, G25, G37, G13 and D37. It can be observed that the effect of the particle size on the run-out distance and the duration of the flow is significantly more pronounced than those due to concentration and suspension volume. For instance, the suspension volume of G69

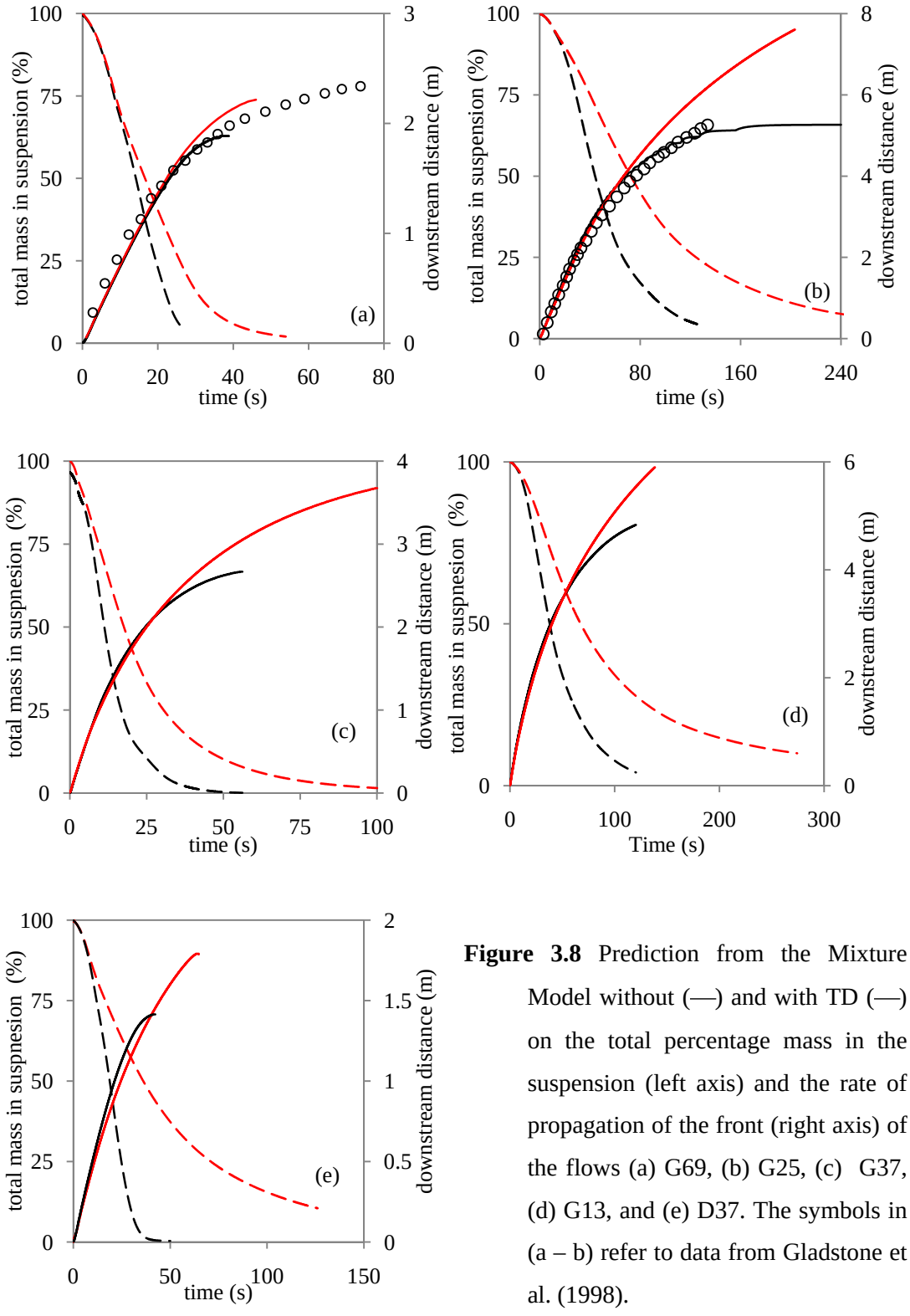

Figure 3.8 Prediction from the Mixture Model without (—) and with TD (—) on the total percentage mass in the suspension (left axis) and the rate of propagation of the front (right axis) of the flows (a) G69, (b) G25, (c) G37, (d) G13, and (e) D37. The symbols in (a – b) refer to data from Gladstone et al. (1998).

is ten times of that of G37 and G13 but has much shorter run-out distance due to its coarse size. Furthermore, G69 and G25 have equal initial concentration and volume but the latter has run-out distance twice longer than the former has because of its fine particle. The effect of the concentration on the duration of the flow is not significant. For instance, G37 and D37 have almost similar duration of propagation

but the run-out distance of the former is twice longer because its concentration is greater (about seven times greater than the latter).

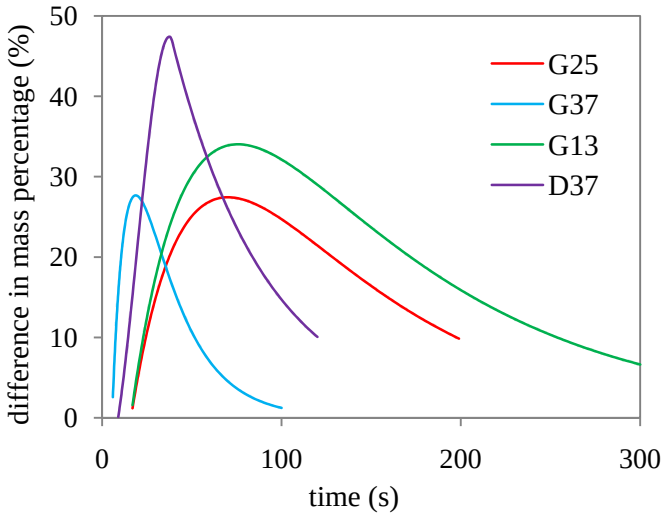

Figure 3.9 The difference between the prediction of the Mixture Model without and that with TD on the total for flows G69 (black), G25 (red), G37 (blue), G13 (green) and D37 (purple).

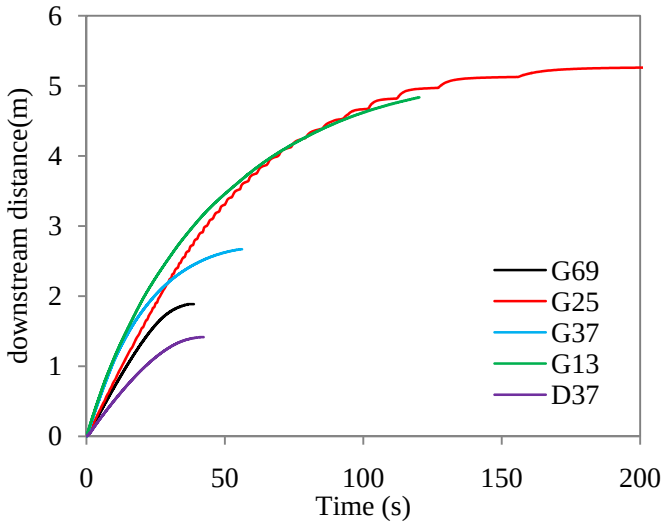

Figure 3.10 Combined plot of the prediction of the Mixture Model without TD on the front of propagation of flows G69 (black), G25 (red), G37 (blue), G13 (green) and D37 (purple).

3.8.3 Depositional patterns

In this section, the effect of TD on the deposit thickness profile of turbidity currents is discussed, and a comparison between the numerical predictions and the experimental data on the deposit thickness profile of turbidity currents given. Figure

3.11(a – e) shows the prediction from the Mixture Model without and with TD on the final deposit mass areal density (which corresponds to the deposit thickness) of the flows G69, G25, G37, G13 and D37. We observe that the model with TD predicts a distinctively lower deposit mass upstream than does the model without TD. This indicates that TD reduces the rate of deposition from the flow, and hence allows the flow to propagate to a further distance and deposit at a distance further away from the lockbox. It should be noted that this observation is consistent with the prediction of both models on the total mass in suspension as a function of time, see the previous section. Also, the finer the particle the greater the amount of sediment transported and deposited downstream. For instance, when TD is included into the model, G69 experiences about a 30% decrease in the deposit mass at the upstream location $x = 0$ to 1m whereas G25 experiences close to a 50% decrease in the deposit mass in the upstream location $x = 0$ to 3m. Another interesting difference in the predictions from both these models lies in the characteristics of the deposit profile. The Mixture Model with TD almost always predicts either a decreasing profile (G69, D37) or a smooth bell shaped-like profile (G25, G37 and G13). The latter actually has less sediment upstream. It appears that the finer the particle carried by the flows, the more likely it is that the flows develop a bell-shaped-like deposit. On the other hand, the deposit profile predicted by the Mixture Model without TD is rather irregular in shape. For instance, the deposit profile of G69 upstream has a sharp peak that is not seen in other flows; the deposit profile of all three G25, G13 and D37 has a sharp increase at the lockgate, and deposit of G37 dips at the lockgate. In addition, the deposit of G25 and G37 has multiple small, sharp perturbations all along the profile. The irregularities in the results obtained for the model without TD suggest that the result is unstable. The results with TD do not appear to be so irregular, and it may be that this approach incorporates some essential mechanics required for the model to produce a stable solution.

Also plotted in Fig. 3.11 are the experimental data for the purpose of validating the numerical predictions. Although the inclusion of TD results in a stable solution, its prediction compares poorly with the experimental data. Without TD, the comparison of the prediction of the Mixture Model with the experimental data improves significantly for the cases G69, G25, G37 and G13. It is not immediately clear as to why the result change substantially when TD is included in the model. Possible reasons are (i) the inaccurate prediction on the particle dispersion behaviour in a

gravity current when using the Simonin TD model, (ii) the inaccurate prediction on the turbulence characteristics when using the k-ϵ turbulence model (since the particle dispersion also relies on the eddy viscosity fed from the turbulence model to predict the dispersion of the particles, over-predicting of the strength on the turbulence may result in the particle dispersion being exaggerated), (iii) the angular shape of the silica carbide may induce a faster rate of particle settling (speculation), (iv) the cross-stream flows (which are not considered in the current model) may have a significant influence on the downstream characteristics of the flow, and (v) the assumptions in the mixture models may not be appropriate for these types of flows. Also plotted in Fig. 3.11(a & b) are the refined-two fluids model results of Hoyes (2008) for the cases G69 and G25, respectively which serve to provide a validation on the accuracy of the experimental data. It can be observed that the refined-two fluids model results agree well with the experimental data, which affirms their accuracy. A more detailed comparison between the refined-two fluids model solution and the prediction from both Mixture Models on the flows G69 and G25 can be performed by comparing all three solutions at different times, as shown in Fig. 3.12(a & b), respectively. Here the spatial and temporal variables have been non-dimensionalized using the following equation

$$\tilde{x} \rightarrow x/(h_0/2),\ \tilde{y} \rightarrow /(h_0/2),\ \tilde{t} \rightarrow t[g_0^{'}/(h_0/2)]^{1/2},\ \text{and}\ \tilde{m}_{dep} \rightarrow m_{dep}/(\alpha_p \rho_0 h_0/2) \qquad (3.1)$$

so that the Mixture Model solutions can be compared with the refined-two fluids model solution. It can be observed that the prediction from the Mixture Model without TD on the build-up of the deposit of G69 at a dimensionless time $\tilde{t}$ = 4, 8, 12, 16 and 32 (which looks like a series of advancing trapezoids) all agree well with the refined-two fluids model solutions. The Mixture Model with TD, which predicts a lesser amount of deposit, achieves a less satisfying comparison with the refined-two fluids model solution. On the other hand, for the flows G25, neither model fully agrees with the refined-two fluids model solution. In the vicinity of the lock box, although the prediction from the Mixture Model without TD on the final deposit mass agrees well with the refined-two fluids model solution, its prediction on the build-up of the deposit does not agree well. The Mixture Model predicts that the final deposit at the lock-gate is achieved at early dimensionless time ($\tilde{t}$ = 24) whereas the refined-two fluids model predicts a more gradual accumulation of the deposit mass and the final deposit mass is only achieved at dimensionless time $\tilde{t}$ =

80. This indicates that refined-two fluids model predicts a lower rate of deposit from the flow and greater sediment dispersion in the flows than the Mixture Model without TD does. Therefore, the good match in the final upstream deposit mass is coincidental. It is important that a model also is able to accurately predict the build-up of the deposits for the model. Naturally, we would expect that adding TD to the Mixture Model could bring the result closer to the refined-two fluids model solution. However, at any time, the Mixture Model with TD under-predicts the deposit mass and predict a much slower accumulation of the deposit which clearly implies the dispersion is over-predicted. These results bring the accuracy or generality of the Mixture Model without TD into question, despite having a good comparison with the refined-two fluids model solution for the case G69. In addition, it should be noted that there are discrepancies in the comparisons between the results of Mixture Model without TD and the experimental data. For instance, the predictions for G98 have a marked perturbation at the experimental data. The prediction for G25 has a lack of mass between x = 2 to 4m and predictions on both G37 and G13 have a lack of mass between x = 0 and 1m, and x = 0 and 2m, respectively.

Clearly these differences suggest that the model itself is still incomplete or perhaps missing some essential physics. We can postulate that TD remains an essential mechanism but there must exist an extra mechanism to counter the extra dispersive effect given by TD. Turbulence modulation is a strong candidate. The detail of this mechanism is given in Section 2.5.2. It essentially describes the increase, or decrease, in the flow turbulence due to the presence of the particles in the flow. In this case, it is the fine particles that decrease the turbulence in the flows. The model of Chen & Wood (1985) is employed in order to simulate the effects of the turbulence modulation (denoted as TM). It is incorporated into the Mixture Model via a user-defined function (UDF). Flows G69 and G25 are both re-simulated with the Mixture Model with TD and TM. The results obtained are presented on Figs. 3.11(a & b), respectively. However, it can be observed the inclusion of TM into the model yields only as small change in the solution which suggests that TM is probably insignificant in dilute turbidity currents presumably due to the low concentration of particles in the flow.

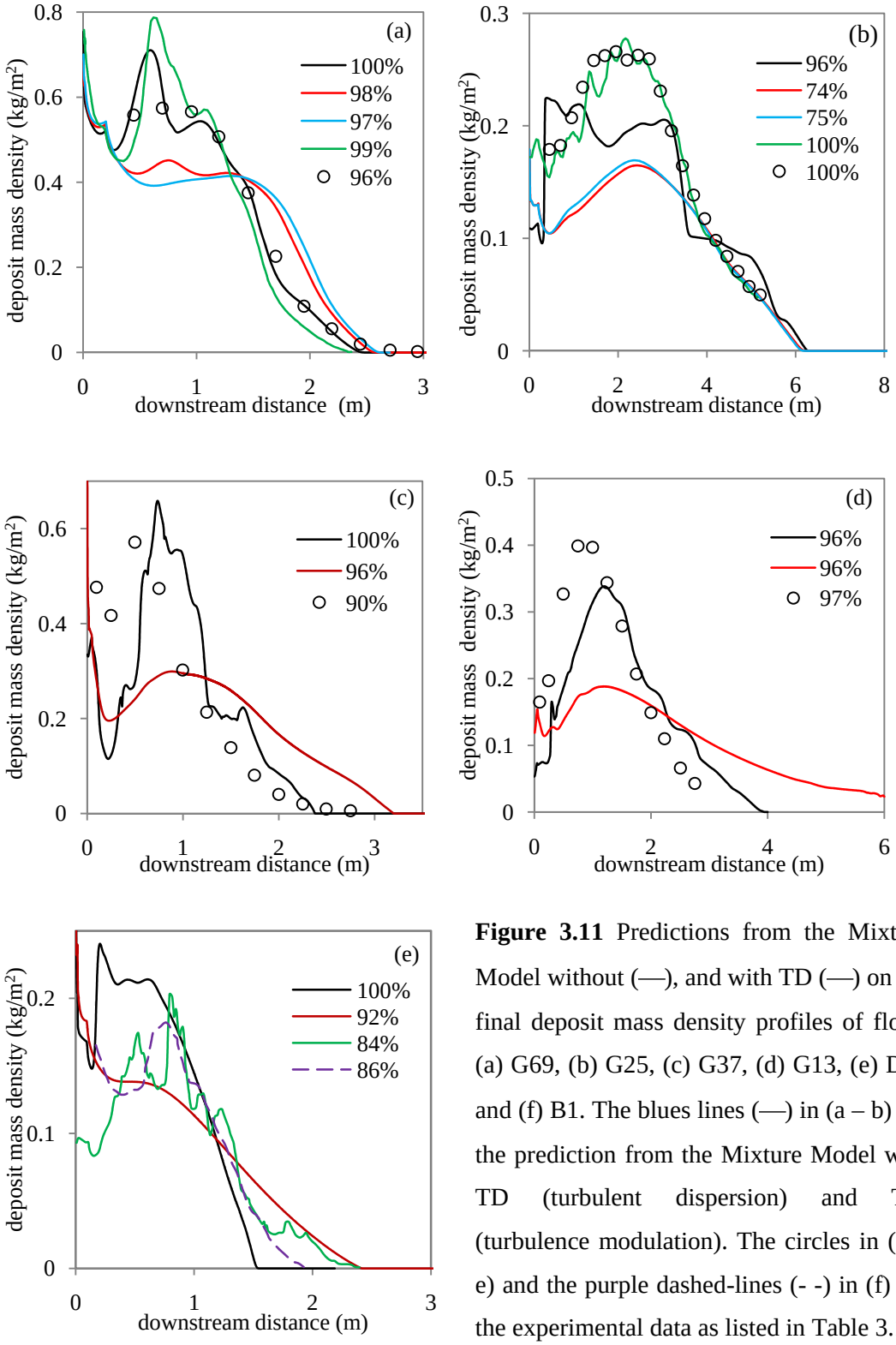

Figure 3.11 Predictions from the Mixture Model without (—), and with TD (—) on the final deposit mass density profiles of flows (a) G69, (b) G25, (c) G37, (d) G13, (e) D37 and (f) B1. The blues lines (—) in (a – b) are the prediction from the Mixture Model with TD (turbulent dispersion) and TM (turbulence modulation). The circles in (a – e) and the purple dashed-lines (- -) in (f) are the experimental data as listed in Table 3.1. The green lines in (a – c) and (f) are the refined two-fluids model predictions from Hoyes (2008), and Necker et al. (2003), respectively. The figures in the legends of each figure represent the percentage of the total mass under each curve relative to the initial mass.

For case D37 (see Fig. 3.11(e)), the deviation of the predictions from the Mixture Model with TD from the experimental data appears to be less substantial than that in other flows. In fact, its comparison with the experimental data agrees better with the experimental data than that for the model without TD. This is because the latter predicts an excessive amount of deposit mass near the lockbox. However, it is uncertain as to whether the deposited mass at the vicinity of the lockgate is under-predicted because a mass conservation check on the experimental data shows that the total mass in the deposit is slightly less than the mass initially employed in the lockbox. The 'missing' mass in the experimental data could correspond to the excess deposited mass predicted by the model without TD. In addition to the final deposit, the authors of the experimental data D37 also measured the build up of the deposit and these data can be used for a more complete comparison between the numerical predictions and the experimental data. Fig. 3.13 shows the prediction as obtained using the Mixture Model without and with TD, compared with the experimental data on the deposited mass at t = 6, 12, 18, 24, 30, 36, 42, and 48s. It can be observed that the Mixture Model with TD agrees well with the experimental data at x = 0 to 0.5m but the comparison becomes poor beyond x = 0.5m (the decrease in the deposit

(a)

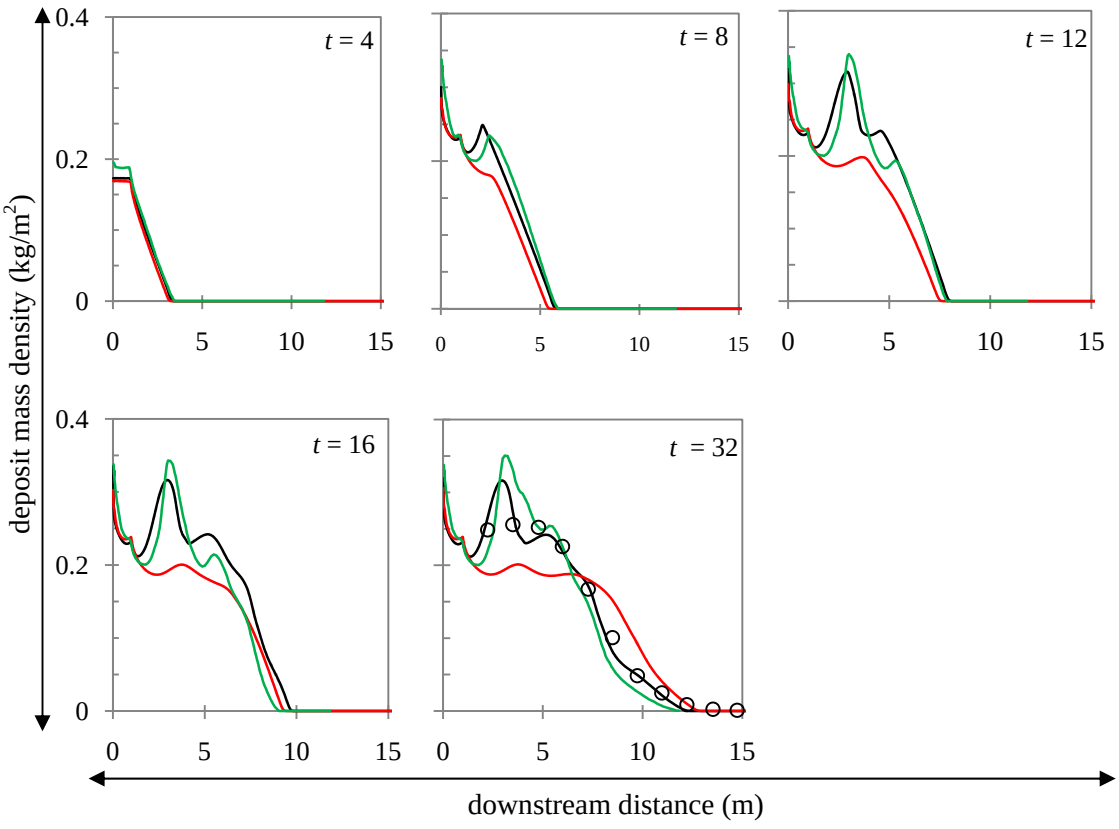

(b)

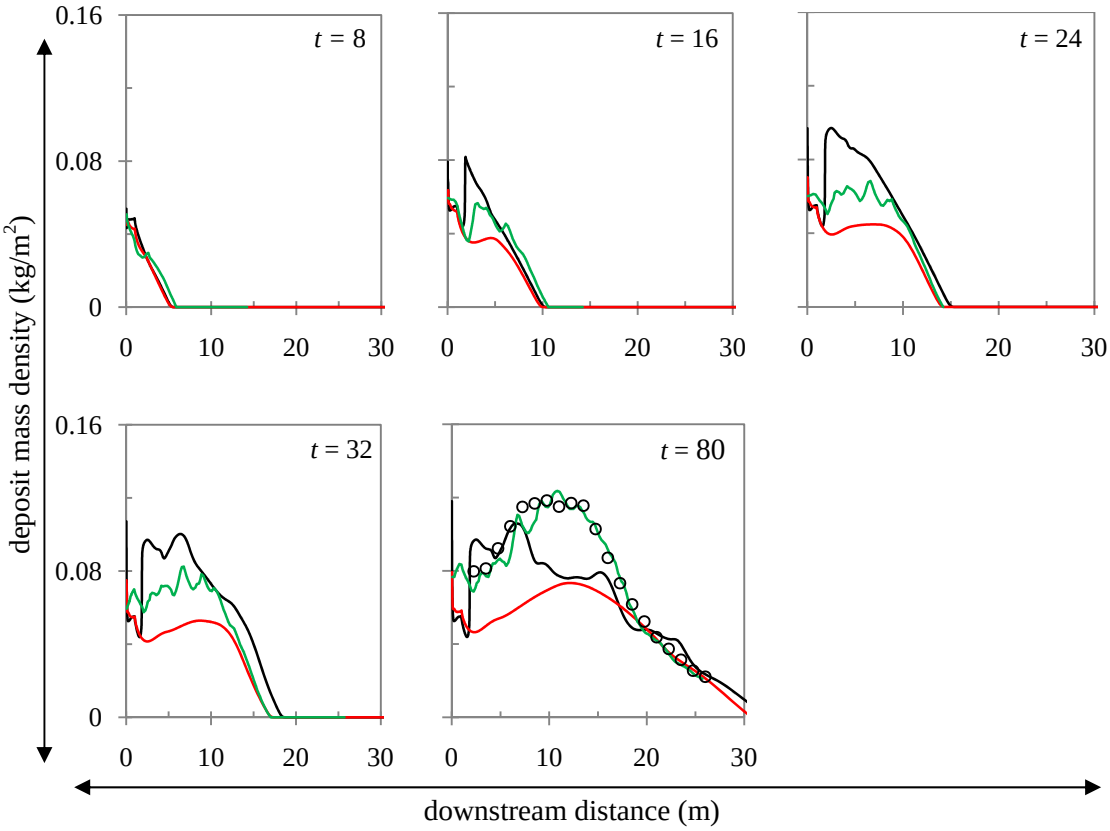

Figure 3.12 Predictions from the Mixture Model without TD (—), and with TD (—) on the temporal deposit mass density of flows (a) G69 at $\tilde{t}$ = 4, 8, 12, 16, and 32, and (b) G25 at $\tilde{t}$ = 8, 16, 24, 32, and 80. The green lines represent the refined two-fluids model solution of Hoyes (2008). Both the downstream distance and the deposit mass density are made dimensionless using equation (3.1).

predicted by the experiment is much steeper than that predicted by the model with TD). Also, the model with TD fails to predict the peak at x = 1m which is predicted in the experimental data. On the other hand, although the model without TD predicts an excess deposit mass before x = 0.5m, the model prediction on the deposit profile beyond x = 0.5m agrees well with the experimental observations. For this reason, we conclude that the model without TD is more accurate than the model with TD in this case.

The prediction obtained using the Mixture Model with and without TD on the deposit mass density of the coarse fraction and the fine fractions of the bi-disperse suspension currents (B1) at dimensionless time $\tilde{t}$ = 8, 16, 24, and 80 are shown in Fig. 3.14(a & b), respectively and are compared with the experimental data of Gladstone et al. (1998) (denoted by hollow circle) and the refined two-fluids model

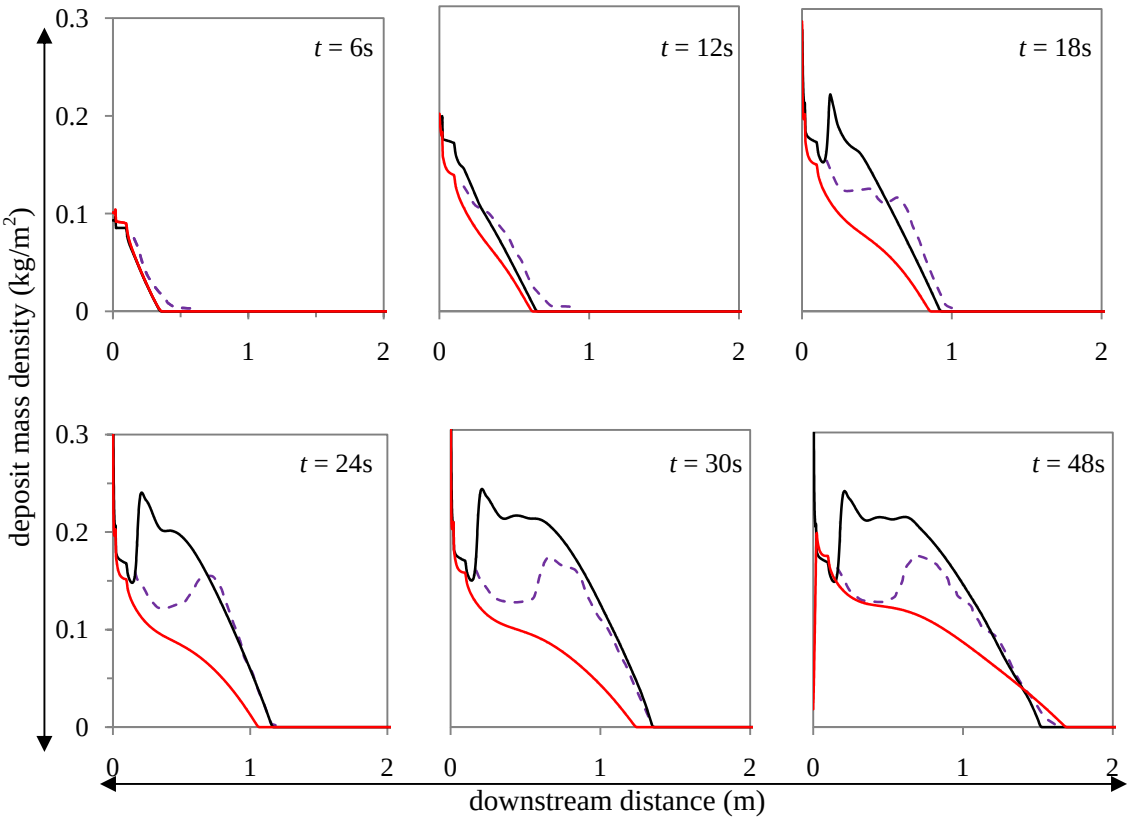

Figure 3.13 Predictions from the Mixture Model without TD (—), and with TD (—) on the temporal deposit mass density of flows D37 at $\tilde{t}$ = 6, 12, 18, 24, 30, and 48s. The purple dashed-lines represent the experimental data of Rooij & Dalziel (2001).

solution of Hoyes (2008). Here the data are made dimensionless using equation (3.1). On Fig. 3.14(a), it can be observed that both the Mixture Model and the refined two-fluids model simulations under-predict the final coarse fraction deposition but over-predict the fine fraction deposition. However, an inconsistency was noted by Hoyes (2008) and Huang *et al*. (2008) in the test data of Gladstone *et al*. (1998). If the numerical integration is performed on the latter to check for mass conservation, the mass of the coarse-grained deposit exceeds that in the initial sediment mix (Hoyes, 2008). The mass conservation of G69 and G25 also were checked and it was found that both are within 5% (see the legends of Fig. 3.11(a & b), respectively). Furthermore, the apparent excess mass in the coarse particle fraction compensates for the deficiency in the fine fraction deposition, so that the combined mass of both particle classes is therefore conserved. These data inconsistencies could arise from a systematic error in the sampling equipment. Alternatively, fine particles may have become agglomerated when the samples were dried for mass analysis, and thus have distorted the size analysis if they were not broken up during re-hydration prior to sizing. Nonetheless, we found that the errors

in the data were consistent so that a constant can be multiplied to the fine grain data to achieve mass conservation. Therefore, the experimental data can be used to compare against the numerical result after they are adjusted accordingly to match the initial mass. The adjusted experimental data are plotted as filled black circles on both Fig. 3.14(a & b). All models predict similar depositional profiles as the mono-disperse coarse (G69) particle currents, indicating that the coarse particle fraction deposition profile is almost independent of the fine particles in the bi-disperse flows. Both the Mixture Model without TD and refined two-fluids model match reasonably with the adjusted test data while the Mixture Model with TD under-predicts the proximal deposit. Such good comparison also re-affirms the validity of the adjustment applied to the experimental data. For the fine grain fraction deposition (see Fig. 3.14(b)), the predicted deposition profiles from the refined two-fluids model and the Mixture Models are distinctively different from those on the mono-disperse flows (G25). Both refined two-fluids model and the Mixture Model without TD predict oscillating profiles proximally reflecting dependency on the coarse fraction buoyancy (the deposition profile of the coarse particle in the B1 is similar to that of G25 but the deposition of the fine particle in the B1 is distinctly different from that of G25). However, the simulation results do not compare well with the adjusted test data which predict a bell-shaped profile. refined two-fluids model solution and the Mixture Model without TD over-predict the proximal deposit whereas the Mixture Model with TD under-predicts the peak located at the middle of the deposit (x = 14). It is unclear whether the discrepancy is due to either the adjustment that is applied on the experiment being wrong or that the numerical models are missing key physics that occur in these flows. The former is likely to be the reason because it is unlikely that refined two-fluids model is able to predict both G69 and G25 accurately but unable to accurately predict a flow of similar concentration but different proportion of coarse to fine particles. Similar to the mono-disperse case G25, we observe that although the Mixture Model without TD and refined two-fluids model agrees on the final deposit mass profile of the fine-fraction, they disagree on the build-up of the deposit profile.

All simulations discussed above are based on turbulence model $k-\epsilon$. It has been argued before that the standard $k-\epsilon$ d model may perform poorly in predicting low Reynolds number flows such as those near the wall (Wilcox, 1993). On the other hands, turbulence model $k-\omega$ is found to perform better in low-Reynolds number

flows. In order to circumvent the weakness in turbulence model $k-\epsilon$, Menter (1994) introduced an approach called $k-\omega$ SST (shear stress transport) that blends $k-\omega$ and $k-\epsilon$ into a single model (see the model equations in FLUENT, 2009). Flow near the wall region is solved using $k-\omega$ whereas flows away from wall is solved using $k-\epsilon$. Given that the advantage of $k-\omega$ SST over the $k-\epsilon$ model, it is desirable to determine whether any improvement in the solutions can be achieved if $k-\omega$ SST model is employed. Unfortunately, turbulent dispersion is not implemented in FLUENT version 12 when the $k-\omega$ SST model is employed. For this reason, it cannot be used to verify whether the excessive dispersion effect in the solution when the Simonin (1991) model is employed is due to an incorrect prediction of the value of the eddy viscosity by the $k-\epsilon$ turbulence model near the wall. Nevertheless, the $k-\omega$ SST model can be employed to verify the solution of $k-\epsilon$ model for the case without the turbulent dispersion. Simulations on flows

(a)

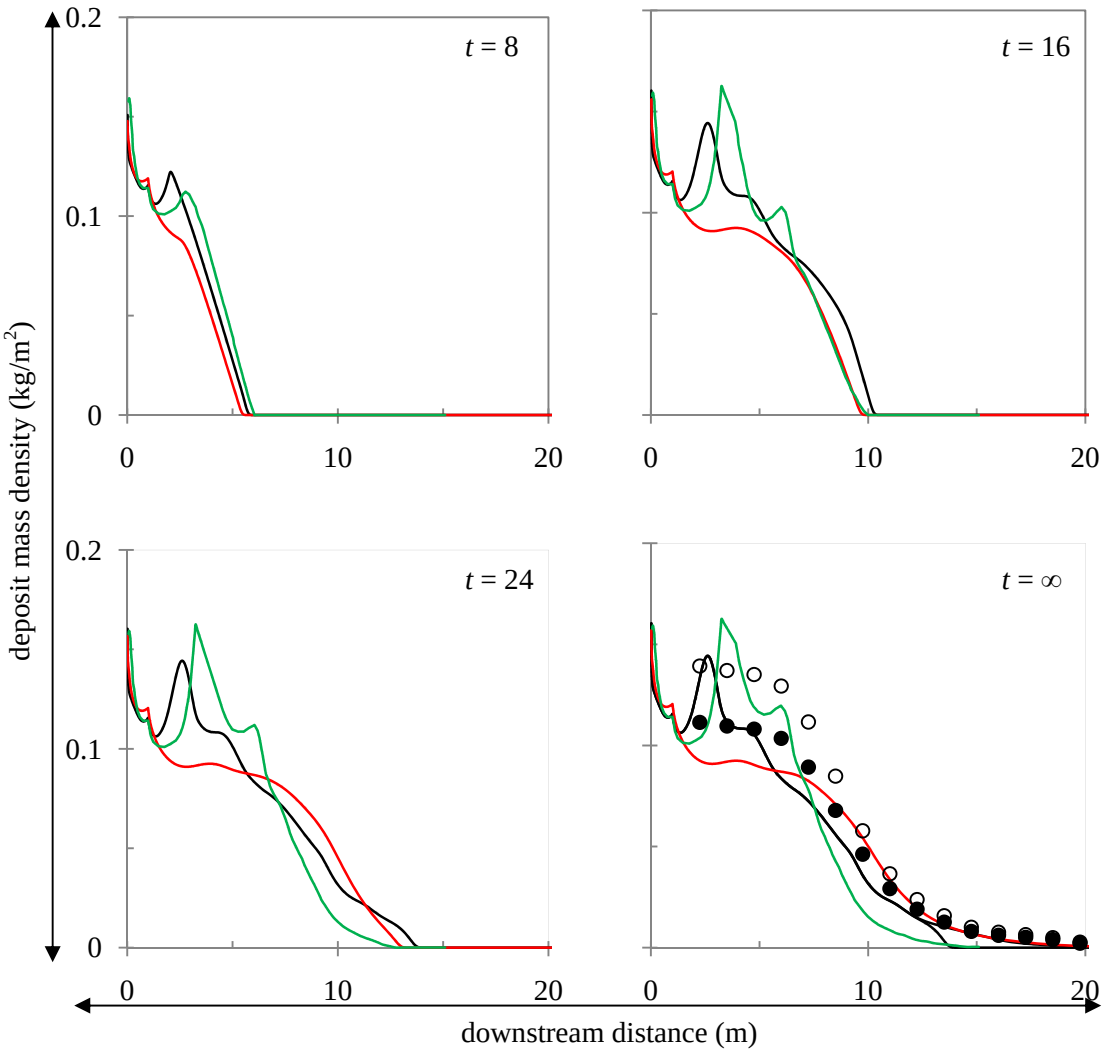

(b)

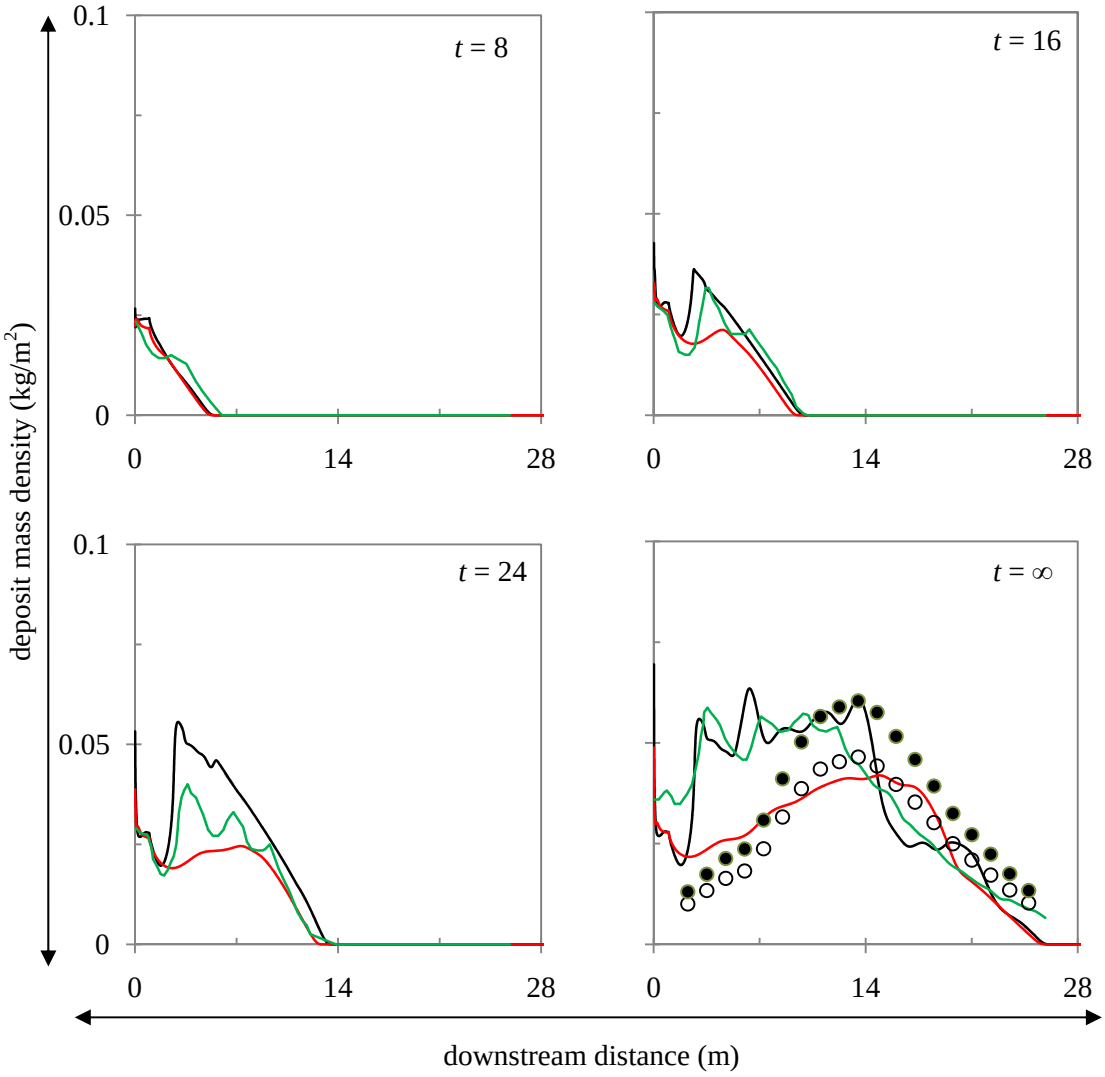

Figure 3.14 Prediction on the development of the dimensionless deposit mass density profile of the (a) coarse fraction and (b) fine fraction, of flows B1. The circles are the experimental data from Gladstone et al. (1998). Symbols (○) represent the original data and (●)the adjusted data.

G69, G37, G13 and D37 were repeated with the Mixture Model and the $k-\omega$ SST turbulence model. Other settings in the simulations are kept constant. It should be noted that the form of turbulence buoyancy in the ω transport equation is slightly different from that in the ϵ equation (see equation A(2.9) in the Appendix). Figure 3.15(a – d) shows the prediction of the deposit mass density profile of flows G69, G37, G13 and D37 from the Mixture Models with $k-\omega$ SST. It can be observed that the solution from $k-\omega$ SST model compares well with that from the $k-\epsilon$ model. For flows G37 and G13, the former predicts a slightly lower deposit mass at

the peak of the deposit (around x = 1m for flows G37 and before x = 2m for flows G13). Despite this slight difference, when compared with the experimental data, the $k-\omega$ SST model similarly under-predicts the upstream deposit mass (before downstream distance x = 1m in both flows). For flows D37, the $k-\omega$ SST model similarly predicts a large peak at x = 0.5m. However, $k-\omega$ predicts a sharp decrease after the peak which makes the solution compare better with the experimental data between x = 0.5m and 1m than the solution from $k-\epsilon$. Overall (considering all flows), the solutions from the two turbulence models are not significantly different from each other. Therefore, we conclude that the $k-\epsilon$ turbulence model is sufficiently accurate (or at least, it works as it is intended to). If the excessive dispersion in the solution is caused by an over-prediction of the eddy viscosity by the turbulence model, the error could be due to an inherent assumption employed in all two-equations models, namely, that the time and length-scale turbulence is isotropic in all directions. Whether this is the case can only be known by repeating simulations which employ models that resolve anisotropic turbulence, such as Reynolds Stresses Models and the Large Eddy Simulations (LES). It follows that the cross-stream components of the flows may also have a significant effect on the flows even though their magnitude is relatively small compared to the vertical and (especially) the downstream components of the flows. This speculation could be tested by carrying out three-dimensional simulations and comparing them with the two-dimensional case.

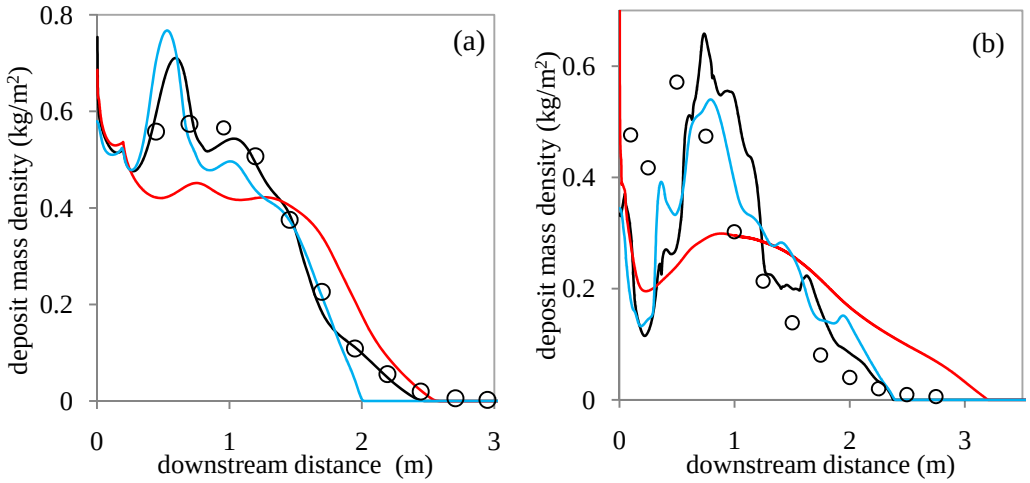

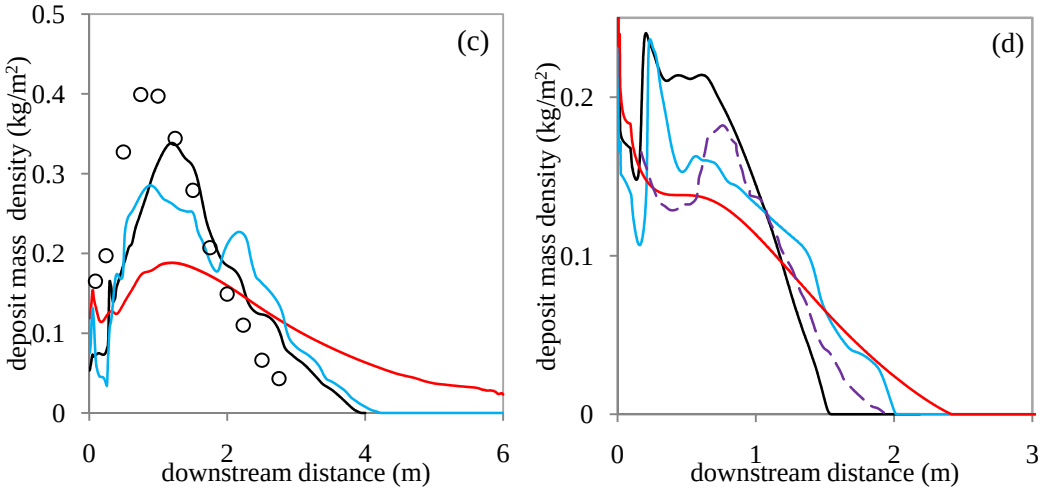

Figure 3.15 Prediction on the deposit mass density profile of flows (a) G69, (b) G37, (c) G13, and (d) D37 from the Mixture Model. The black, red and blue lines represent the solutions from the turbulence model $k-\epsilon$, $k-\epsilon$ with turbulent dispersion, and $k-\omega$ SST, respectively. The circles and the purple dashed line represent experimental data.

A conclusion can be drawn from the above discussion is that the Mixture Model without TD generally achieves a better comparison with both the experimental data and the refined two-fluids model solution than the Mixture Model with TD in predicting the final deposit of turbidity currents. However, in flows carrying fine particles, TD becomes important. The current employed TD model of Simonin (1991) over-predicts the dispersive force in turbidity currents, with the consequence that the Mixture Model under-predicts the deposit mass of turbidity currents proximally. The reason why the TD model is inaccurate is unclear. It can be speculated that two-equation turbulence model may have over-predicted the strength of the turbulence. Also cross-stream components of the flows could be significant.

3.8.4 Vertical structure

In this section, a comparison is given between the predictions from the Mixture Model without TD and with TD on the vertical structure of flows G69 and G25. Although the deposit profile predicted by the latter does not compare well with the experimental data, it is important to understand the effect of TD on the internal velocity and turbulence profile of the flows in order to understand the drawbacks of the model. Since no experimental data are available, no attempt is made to validate the accuracy of the models in predicting the internal structure of the flows. Figures

3.16 and 3.17 show the vertical structure of the flows bearing coarse and fine particle, respectively, in terms of the downstream velocity, particle concentration and turbulence intensity during the slumping ($\tilde{t}$ = 4, 8), inertia-buoyancy ($\tilde{t}$ = 12) and viscous-buoyancy ($\tilde{t}$ = 40) stages. The downstream velocity and the concentration (volume fraction) are scaled using the maximum velocity and the maximum concentration respectively. The height and time is made dimensionless using equation (3.1).

Overall, the vertical downstream velocity of both currents can be divided into two regions: an inner region characterized by a steep gradient of increasing velocity from the bottom to the velocity maximum occurring relatively close to the lower boundary, and an outer region above the velocity maximum characterized by a negative velocity gradient and a negative velocity value at the flow-ambient interface. Negative velocities at the upper boundary are due to the shearing action and mixing between the density currents and the ambient fluid arising from the counter flow of the ambient into the lock box. Negative velocities are at a maximum above the current heads as they travel at greater speed. Also, negative velocities reduce over time because current speed eventually diminishes. Notable differences between the velocity profile of the head and the body are their velocity maximum height from the bottom, in which is greater in the current body than the current head (compare G69 and G25 head and body velocity profiles at $\tilde{t}$ = 12). In addition, the height of the velocity maximum decreases as the currents progress from the inertia-buoyancy to viscous-buoyancy regimes (compare the G69 body and head velocity profiles at $\tilde{t}$ = 12 and 40). Experimental observations indicate that the height of the velocity maximum of a gravity currents body is about one third of the total current depth (e.g. Garcia 1994, Kneller and Buckee 2000 or Peakall *et al*. 1999). Note that the velocity profiles of both the coarse and fine particle currents at $\tilde{t}$ = 12 compare well with observations, and between the Mixture Model without and with TD. Overall, they produce similar velocity profiles except in the later flow stages, in which the model with TD predicts a higher velocity maximum due to the dispersion effect. Vertical concentration profiles differ between the head and the body of the currents, and also evolve in time (Fig. 3.16(b) and Fig 3.17(b)). Thus current bodies exhibit a progressive downward concentration increase from the top boundary profile while the currents head at early time $\tilde{t}$ = 4 or 8 exhibit a stepped profile. The body profile is comparable to low-concentration, weakly depositional flows

observed in the tests of Altinakar *et al*. (1996). The comparison indicates that the model with TD predicts a thicker and more stratified concentration profile due to the dispersion effect. The thickness of flow in the prediction of the model with TD increases slightly with time while that in the solution of the Mixture Model without TD decreases with time. It is anticipated that fixed-volume turbidity currents should spread to become thinner after they collapse into the light ambient fluid, indicating that the sediment dispersion by turbulence is excessive in the Mixture Model with TD.

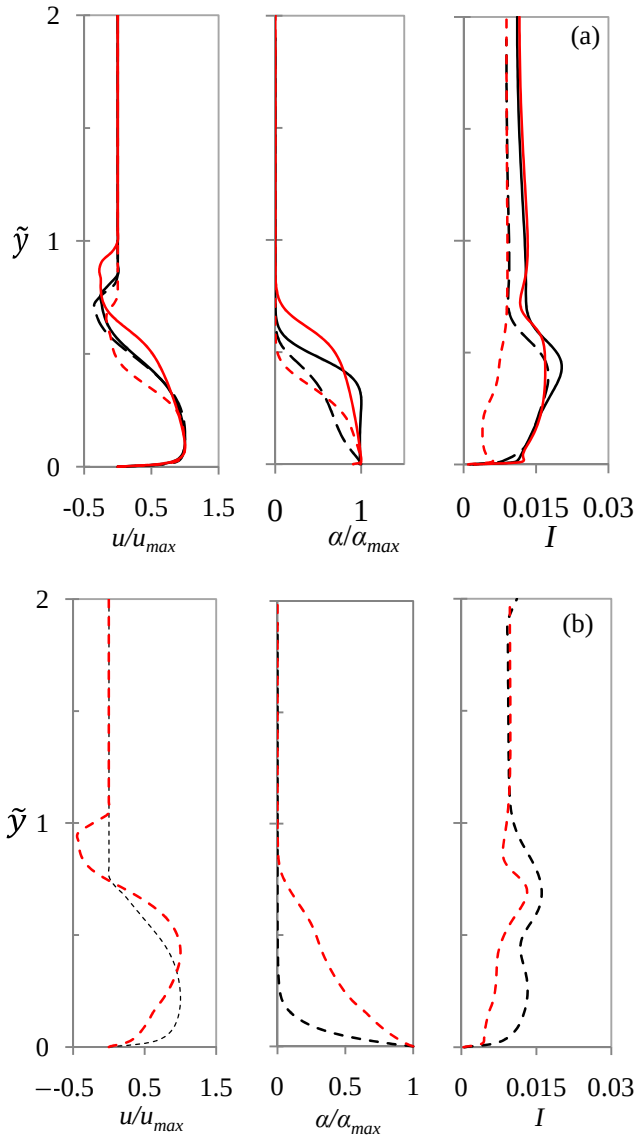

Figure 3.16 Dimensionless Downstream velocity, sediment concentration and turbulence intensity of flow G69, (a) head, and (b) body, from (black lines) Mixture Model without TD and (red lines) Mixture Model with TD, respectively, at (solid lines) t = 4 and (dashed lines) t = 12. The height y is made dimensionless using equation (3.1).

At times $\tilde{t}$ = 4 to 12, the turbulence intensity profiles of currents of both particle sizes are characterised by a steep increase from the bottom, followed by a gradual increase until reaching a peak and eventually a decease abruptly to the ambient condition. The peak occurs at $\tilde{y} \approx 0.4$ for G69 (head only) and $\tilde{y} \approx 0.5$ for G25 (both

head and body), corresponding to the upper interface of the density currents with the ambient fluid. The peaks result from the shearing action between the forward moving currents and the ambient counter-flow. The steep turbulence increase from the bottom at the lower part of the currents is also due to the shearing action between the currents and the no-slip wall. Both modelled features (high turbulence near the upper boundary and the lower portion of the currents) qualitatively resemble test data of Best *et al.* (2001). However, the modelled curves do not exhibit a turbulence minimum at the velocity maximum which is also another common feature observed, although the G69 body turbulence profile at $\tilde{t}$ = 12 exhibits two peaks with a noticeable dip in between. It is unclear why this feature is not captured well in the modelling. The cause may be due to the empirical assumptions and lack of

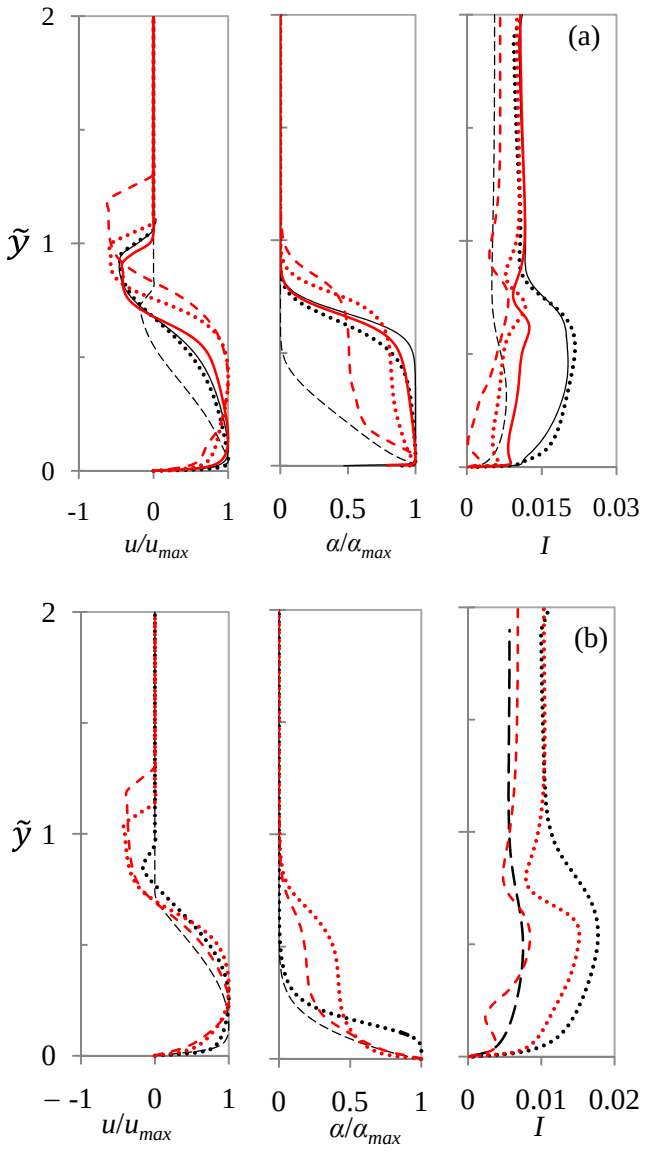

Figure 3.17 Downstream velocity, sediment concentration and turbulence intensity of flow G25, (a) head, and (b) body, from (black lines)Mixture Model without TD and (red lines)Mixture Model with TD, respectively, at t = 8 (solid lines), 12 (dotted lines), (dashed lines) 40. The height y is made dimensionless using equation (3.1).

turbulence contribution arising from the multiphase interaction in the turbulence model. Gore and Crowe (1989) demonstrated that the turbulent intensity is modulated by the particles, even at a low volume concentration. Thus this effect might be significant in density currents. The result shows that Mixture Model with TD predicts much lower turbulence intensity, because the fluid turbulence is being expended to disperse the sediment to the surrounding ambient fluid.

3.9 Conclusions

In this chapter, five mono-disperse flows and one bi-modal flow with different initial conditions are simulated using the Mixture Model both with and without the turbulent dispersion. The numerical results have yielded some intriguing findings:

(a) The Mixture Model without turbulent dispersion predicted well the deposit mass profile for the flows carrying coarse particles (G69), but over-predicted these for the flows carrying fine particles (G25, G37 and G13). It also over-predicted the initial deposit mass for the flows D37.
(b) The Mixture Model with turbulent dispersion increased the transportability of each flow and hence causes a poorer comparison with the experimental data.

These results suggest that changes in the Mixture Model are necessary in order to improve its comparison with the experimental data. High resolution results from the previous studies (Hoyes, 2008; Necker et al., 2003) are employed here to assist in the determination of the problem in the Mixture Model. All three high resolution results (G69, G25 and D37) show good comparisons with the experimental data, which suggests that the treatment on the turbulence of the flows in the Mixture Model maybe inaccurate. The following two adjustments have been incorporated into the models in an attempt to modify the prediction of the flow turbulence:

(a) It was speculated that turbulent modulation could play an important role in reducing the strength of the turbulence in the flow and hence reduce the particle dispersion. The turbulent modulation model of Chen & Wood (1985) was incorporated into the Mixture Model via the use of an UDF and flows G69 and G25 were re-simulated. However, no significant improvement in the results obtained was observed.

(b) It was further speculated that the $k-\epsilon$ model may have exaggerated the eddy viscosity of the flow and hence an alternative two-equation turbulence model, namely the k-ω, which effectively blends the $k-\omega$ and $k-\epsilon$ together, was employed and each mono-disperse flow was re-simulated. However, again, no significant improvements were observed in the obtained result.

With the above two adjustments failing to provide any satisfying explanation, a decisive conclusion on the accuracy of the Mixture Model cannot be drawn at this point. However, following speculations on the possible reasons responsible for the poor comparison of the Mixture Model with the experimental data are drawn:

(a) The cross-stream flow, albeit that it has a magnitude much smaller than that of the downstream and vertical flow, could have a significant effect on the downstream flow. A way to validate this is by comparing the current 2D solution with the 3D solution with a similar model setup.
(b) The two-equation turbulence model maybe inaccurate in this case. The prediction of *k* should be validated using experimental data.
(c) The shape of the particle (silica carbide is highly angular) may influence the motion of the particles in the flow. Therefore the assumption of spherical particles in the model may not be reasonable.
(d) The physics of the turbidity currents have not been fully described by the Mixture Model. In particular, we suspect that the shear within the turbidity currents may induce a significant lift force on the particles suspended within the flows. This is investigated in the next chapter.

Chapter 4

The influence of the lift force on the settling velocities of rotating particles in two-dimensional shear flow

4.1 Introduction

In Chapter 3, a numerical investigation was performed to determine the effect of turbulent dispersion (TD) in laboratory turbidity currents. In that investigation, the Simonin (1991) model was employed to simulate the effect of the turbulent dispersion. The results show that turbulent dispersion causes a significant reduction in the rate of deposition from the flows, which results in greater sediment mass being transported downstream. However, the prediction of deposit mass profile by the model incorporating turbulent dispersion does not agree well with the experimental data. On the other hand, the model without TD produces a result that agrees quite well with the experimental data, albeit some discrepancies. In the cases where the particles carried by the flows are fine grained, the model still under-predicts the deposit at the upstream. It was speculated that anisotropic turbulence or the secondary motions in the flows might cause the excessive dispersion in the solution of model with TD. It is also possible that $k-\epsilon$ over predicts turbulence levels and hence exaggerates the effect of TD. In addition to these factors, it is also possible that drag is not the only important force in the particle-fluid interactions. In this chapter, an investigation is carried out the effect of the lift force on the particle transport within turbidity currents and its importance relative to the drag force.

In many multiphase modelling applications, especially those in the field of hydraulics, such as open channel flow and gravity currents, the motion of particles in the fluid flow is assumed to be adequately described by a balance of the drag, gravity and turbulence dispersion forces. The lift force is generally neglected, unless the shear of the flow is strong, or the rotation of the immersed particle is significant.

On the other hand, recent work in other areas of multiphase flows, notably bubbly flows, has highlighted the importance of considering the influence of other interfacial forces. In particular, the balance between the lift force, near wall forces, and turbulence dispersion has been shown to have a decisive influence on the void fraction distribution in vertical bubbly pipe flow (Lahey et al. (1993), Burns et al. (2004)), and vertical fluid-solid pipe flow (Alajbegovic et al. (1994)). Moreover, an important phenomenon has been identified, whereby the shear-induced lift force changes sign as bubbles increase in size, and consequently change shape from spheres through ellipsoids to spherical caps (Tomiyama et al. (1995, 1998)). An important consequence of this is that small bubbles tend to drift towards the wall in vertical bubbly pipe flow, whilst larger bubbles drift towards the centre. This has been shown to have an important influence in predicting transition from bubbly flow to slug flow (Frank et al. (2004, 2008)).

The influence of non-drag interfacial forces on bubbly flows comes as no great surprise, in view of the fact that bubbles have almost negligible inertia relative to the carrier fluid. The influence of non-drag forces in liquid-solid flows is not expected to be as great, since in this case the dispersed-to-continuous phase density ratio is of order one. Nevertheless, the recent work on lift forces in bubbly flows naturally raises the question of whether or not similar interesting and unexpected phenomena may occur in liquid-solid flows. In particular, it is intriguing to ask whether or not the influence of differences in particle size and shape on the lift force has important consequences on particle fractionation phenomena. As a first step towards attempting to answer this question, it is be useful to estimate the significance of the lift force on an isolated particle in a flow with a given magnitude of shear. Accordingly, in this chapter, we derive simple expressions for the effect of the lift force on the equilibrium settling velocities of particles of different sizes immersed in a shear flow, based on the force balance equation,. The resulting analysis is used to estimate the effect of the lift force on sediment transport in turbidity currents and the entrainment of small particles embedded in the viscous sublayer of a shear flow.

4.2 Literature Review

A particle experiences lateral migration in the streamwise direction when it is immersed in a shear flow. This was first noted by Segre & Silberberg (1962) when they investigated the motion of a rigid sphere being transported in a Poiseuille flow

(a laminar flow with a pressure drop in a long cylindrical pipe). They observed that a sphere is transported to a certain equilibrium position at about 0.6 tube radii from the axis of the tube, irrespective of the radial position at which the sphere first entered the tube. Their observation has inspired theoreticians to better understand this phenomenon. The analytical expression for the lift on a sphere in a slow shear flow was first derived by Saffman (1965, 1968) using linearized theory. Saffman showed that a spherical particle of diameter d_p moving with velocity $\vec{u}_p$ through a fluid of velocity $\vec{u}_f$ and uniform shear experiences a lift force of magnitude:

$$F_L = 6.46\ \rho_f \frac{d_p^2}{4}\ |\vec{u}_r|\ \sqrt{\nu_f \omega_f} - \frac{11}{64}\rho_f |\vec{u}_r| \omega_f d_p^3 + \frac{\pi}{8}\rho_f |\vec{u}_r| \omega_p d_p^3 \qquad (4.2.1)$$

where ρ_f, ν_f are the fluid density and kinematic viscosity, $\vec{u}_r = \vec{u}_p - \vec{u}_f$ is the relative velocity of the particle with respect to the fluid (the slip velocity), ω_f is the magnitude of the fluid vorticity, and ω_p is the magnitude of the particle angular velocity. Equation (4.2.1) was derived under the assumptions:

$$Re_s \ll 1, \quad Re_\omega \ll 1 \quad \text{and} \quad Re_s \ll \sqrt{Re_\omega} \quad i.e. \quad \epsilon_s = \sqrt{Re_\omega}/Re_s \gg 1 \qquad (4.2.2a)$$

where $Re_s = |\vec{u}_r| d_p/\nu_f$ is the particle Reynolds number, and $Re_\omega = \omega_f d_p^2/\nu_f$ is the vorticity Reynolds number. The direction of the lift force depends on the sign of the flow shear. In a linear shear flow, it always acts towards the side of the sphere with the higher velocity. The first and second terms on the right side of equation (4.2.1) are the lift force due to the fluid shear and the third term takes into account the rotation of the sphere. For a freely rotating particle $\omega_p \approx \omega_f/2$, the second and third terms are smaller than the first term by an order of magnitude under the assumptions stated above, and thus are neglected (Saffman 1965). It is worth mentioning that the third term of equation (4.2.1) has a similar form to the lift force on a particle that has a small Reynolds number, rotating with an imposed angular velocity ω_p in a uniform flow (Rubinow & Keller 1961).

Saffman's analysis was generalised by many researchers, for instance to include the effect of a wall (Leighton & Acrivos, 1985), to relax the restrictions (4.2.2a) so that $Re_s \approx \sqrt{Re_\omega}$ (McLaughlin, 1991), and to predict the lift on bubbles (Legendre & Magnaudet 1997, 1998). The Saffman theory generally only describes the lift on a particle due to the shear. However, for particles immersed in a high shear flow, the

lift due to particle rotation becomes important and should to be taken into account. This effect can be observed in recent experimental and numerical investigations on the lift of a cylinder immersed in shear flows (Bluemink et al. 2008 and Bagchi & Balachandar 2002).

The leading order term in Saffman's equation (4.2.1) may be expressed in terms of the aerodynamic lift coefficient $C_{LA} = F_L/\frac{1}{2}\rho_f \pi r_p^2 |\vec{u}_r|^2$ as follows:

$$C_{LA} = \frac{2C_L'}{\pi}\epsilon_s \tag{4.2.3}$$

where $C_L' = 6.46$, and ϵ_s is the parameter defined in (4.2.2). The restriction to $\epsilon_s \gg 1$ in (4.2.2) was removed by McLaughlin (1991), who obtained a more general formula for the lift coefficient that multiplies Saffman's lift by a function of ϵ_s that tends rapidly to zero as $\epsilon_s \to 0$. Dandy and Dwyer (1990) performed numerical computations of the shear-induced lift force for finite particle Reynold's numbers $0.1 \leq Re_s \leq 100$ and finite dimensionless shear rate:

$$\alpha_s = \frac{r_p \omega_f}{|\vec{u}_r|} = \frac{1}{2} Re_s \epsilon_s^2 = \frac{1}{2}\frac{Re_\omega}{Re_s} \tag{4.2.4}$$

in the range $0.005 \leq \alpha \leq 0.4$. At Re_s = 0.1, Saffman's prediction for the shear lift force was verified for ϵ_s as small as 0.447 (or $\alpha_s = 0.01$). At $\alpha = 0.005$ ($\epsilon_s = 0.224$), Saffman's result is slightly larger than the numerical result. At higher Re_s, Dandy and Dwyer found that the lift coefficient decreases, levelling off around $Re_s = 40$, after which it increases linearly with $\alpha_s$instead of $\sqrt{\alpha_s}$.

Based on the numerical results of Dandy and Dwyer, Mei (1992) proposed an approximate correlation for the shear-induced lift force on a solid sphere that is valid for $0 \leq Re_s \leq 100$. Mei's formula may be expressed as follows:

$$\frac{C_{LA}}{C_{LA,Saffman}} = \begin{cases} f(Re_s, Re_\omega), & (0 \leq Re_s \leq 40) \\ 0.0524(\alpha_s Re_s)^{1/2}, & (40 \leq Re_s \leq 100) \end{cases} \tag{4.2.5a}$$

where $C_{LA,Saffman}$ is the aerodynamic lift coefficient according to Saffman, equation (4.2.3) and the function $f(Re_s, Re_\omega)$ is given by:

$$f(Re_s, Re_\omega) = \left(1 - 0.3315\alpha_s^{1/2}\right)e^{-0.1Re_p} + 0.3315\alpha_s^{1/2} \tag{4.2.5b}$$

Substituting (4.2.3) into (4.2.5a), gives the aerodynamic lift coefficient in the range $40 \leq Re_s \leq 100$:

$$C_{LA} = 0.074 \frac{C_L'}{\pi} \frac{Re_\omega}{Re_s} \qquad (40 \leq Re_s \leq 100) \tag{4.2.6}$$

It is convenient to express the first and third terms in equation (4.2.1) in the following vectorial form (Auton 1987, Drew and Lahey 1987, 1990):

$$\vec{F}_{LS} = C_L \rho_f V_p \vec{\omega}_f \times \vec{u}_r \tag{4.2.7}$$

$$\vec{F}_{LR} = C_R \rho_f V_p \vec{\omega}_p \times \vec{u}_r \tag{4.2.8}$$

where C_L and C_R denote non-dimensional lift coefficients for the shear-induced and the Magnus lift forces respectively, and V_p is the particle volume. Note that C_L is not the same quantity as the aerodynamic lift coefficient C_{LA}. Hence, we call it the shear-induced lift coefficient, and note that it is related to C_{LA} as follows:

$$C_L = \frac{3}{4} C_{LA} \frac{Re_s}{Re_\omega} \tag{4.2.9}$$

In this thesis, we work with the shear-induced lift coefficient. Substituting (4.2.3) into (4.2.9), we find that, within this framework, Saffman's formula correlates the shear-induced lift coefficient in terms of the vorticity Reynolds number as follows:

$$C_{L,Saffman} = \frac{C_{LS}}{\sqrt{Re_\omega}}, \quad => \quad C_{LS} = \frac{3}{2\pi} C_L' = 3.08 \tag{4.2.10}$$

Similarly, substituting (4.2.6) into (4.2.9) gives the shear-induced lift coefficient corresponding to Mei's correlation as follows:

$$C_{L,Mei} = 0.0555 C_{LA} \frac{C_L'}{\pi} \qquad (40 \leq Re_s \leq 100) \tag{4.2.11}$$

Thus, the large Reynolds number range of Mei's correlation is equivalent to a constant shear-induced lift coefficient $C_{LM} = 0.037 C_{LS} = 0.118$. The full range of Mei's correlation (4.2.5) may be expressed as:

$$C_{L,Mei} = \begin{cases} f(Re_s, Re_\omega) C_{LA,Saffman}, & (0 \leq Re_s \leq 40) \\ C_{LM}, & (40 \leq Re_s \leq 100) \end{cases} \tag{4.2.12}$$

Most work on the lift force at higher Reynolds numbers has used the formulation (4.2.7) and (4.2.8) for the shear-induced and Magnus lift forces. For inviscid flow

around a sphere, Auton (1987) and Drew and Lahey (1987, 1990) computed the value $C_L = 0.5$. Naturally, these calculations did not take wake effects into account. For fully developed bubbly flow in a vertical pipe, experimental data yield a much lower value $0.01 < C_L < 0.15$, with $C_L = 0.1$ fitting most of the data (Wang et al. 1986, Lahey et al. 1993). Similar results were observed by Alajbegovic et al. (1994) for solid-fluid up flow in a pipe. On the other hand, Bel Fdhila (1991) showed that in order to fit his experimental data of bubbly flow in a vertical pipe with a sudden expansion C_L would have to be negative. Note that the experimental and numerical comparisons referred to above are for turbulent bubbly flows, with turbulence modelled by RANS turbulence models. Hence, the values of C_L successfully fitted to experimental data are the result of ensemble-averaging. Moraga et al. (1999) proposed an explanation of the reduction and possible reversal of sign of the lift force in terms of the effects of asymmetric vortex shedding above the critical particle Reynolds number (around 300) for transition from a steady to an unsteady wake behind the sphere. When vortex shedding occurs in a background flow with a mean velocity gradient, the vortices are shed asymmetrically. Numerical calculations of Jordan and Fromm (1972) and Alajbegovic et al. (1998) indicate that the time averaged influence of the asymmetric vortex shedding produces an additional contribution to the shear-induced lift force which acts in the opposite direction to the lift force induced at low Reynolds numbers. This observation was further supported by the theoretical and experimental analysis of Moraga et al. (1999). Hence, it provides a convincing explanation of the observed reduction of C_L from its inviscid value of 0.5, possibly to negative values. Other researchers have observed negative values of the lift coefficient for large values of Re_s (e.g. Kurose & Kumori (1999), Bagchi and Balachandar (2002) but other researchers did not observe the phenomenon (e.g. Bluemink et al. (2008)). Hence there is no general agreement on whether the lift coefficient of spherical particles is negative or not at high values of Re_s.

On the other hand, the existence of negative lift coefficients for non-spherical particles is well established. Hölzer and Sommerfeld (2009) performed numerical computations of drag, lift and torque for flow around a variety of differently shaped solid particles, for particle Reynolds numbers between 0.3 and 240, under a variety of flow conditions. Drag, lift and torque coefficients were determined as functions of

Re_s and the angle of incidence ϕ. For spheroidal particles, the shear induced lift coefficient is observed to change sign both with increasing Re_s, and variation of ϕ.

For bubbly flow, it is well established that the shear-induced lift force changes sign with increasing bubble size, due to associated distortion of the bubble shape from spherical to distorted ellipsoidal shapes (Tomiyama et al. (1995, 1998)). Tomiyama et al. proposed an expression for the shear-induced lift force that changes sign with increasing mean bubble diameter. For bubbly upflow in a vertical pipe, this causes small bubbles with $C_L > 0$ to migrate towards the pipe wall, and larger bubbles with $C_L < 0$ to migrate towards the pipe axis. This phenomenon is found to play an important part in the transition from bubbly flow to slug flow with increasing gas flow rates in the pipe. Small bubbles migrate towards the wall, where, at sufficiently high concentrations they coalesce to form larger bubbles above the critical size for reversal of the lift coefficient. These larger bubbles then migrate towards the pipe centre, where they coalesce further to form large slug bubbles. The correlation of Tomiyama et al. was employed in numerical computations by Burns et al. (2004) and Frank et al. (2004), in combination with a suitable RANS turbulence model, and correlations for drag, turbulence dispersion and near wall forces. Good agreement was obtained with experiment for predictions of void fraction distribution for mono-dispersed bubbly upflow in a vertical pipe. This model was later employed to compare predictions with experiment for poly-dispersed bubbly upflow in a vertical pipe (Frank et al. 2008). Good agreement was obtained when the relative volume fractions of different bubble size groups were prescribed from the experimental results. Less good agreement was obtained when the bubble size distribution was predicted from empirically based coalescence and breakup models.

When the particle Reynolds number is greater than unity, i.e. $Re_s \geq 1$, the lift force due to the particle rotation for a freely-rotating sphere in a shear flow is no longer negligible. Bagchi & Balachandar (2002) and later Bluemink et al. (2008) showed that the lift force arising due to the rotation of the particle in a shear flow is about half of that derived by Rubinow & Keller (1961). Thus they concluded that the lift force on a rotating particle in a shear flow is the combination of equations (4.2.7) and (4.2.8), i.e.

$$\vec{F}_L\left(Re_s, G, \vec{\omega}_p\right) = \vec{F}_L\left(Re_s, G, \vec{\omega}_p = 0\right) + \vec{F}_L(Re_s, G = 0, \vec{\omega}_p) \qquad (4.2.13)$$

Table 4.1 Previous investigations on the lift force on a particle immersed in a linear shear or parabolic flow

Authors	Particle-Type	Flow Type	Type	Scope of Study/Limitation*
Segre & Silberberg (1961; 1962)	Rigid sphere	Parabolic flow	Experiment	
Saffman (1965; 1968)	Rigid sphere	Linear Shear	Theoretical (Analytic)	$Re_s \ll 1$, $Re_\omega \ll 1$ and $Re_s \ll \sqrt{Re_\omega}$
Bagnold (1974)	Rigid sphere	Linear Shear	Experiment	
Vasseur & Cox (1976)	Rigid sphere	Parabolic flow	Theoretical (Analytic)	
Auton (1987)	Rigid sphere	Shear flow	Theoretical (Analytic)	Inviscid flow
Schonberg & Hinch (1989)	Rigid sphere	Parabolic flow	Theoretical (Analytic)	Re_s <1500
Dandy & Dwyer (1990)	Rigid sphere	Linear shear	Theoretical (Numeric)	$0.1 \leq Re_s \leq 100$, $0.005 \leq Re_s \leq 100$
Ye & Roco (1991)	Rigid sphere	Linear shear	Experiment	Re_s = 4,6, 6.8, 9.2 x 10^4
McLaughlin (1991)	Rigid sphere	Linear shear	Theoretical	$Re_s \ll 1$
Legendre & Magnaudet (1998)	Spherical bubble	Linear shear	Theoretical (Numeric)	$0.1 \leq Re_s \leq 500$,
Cherukat et al. (1999)	Rigid sphere	Linear shear	Theoretical (Numeric)	$0 \leq Re_s \leq 2$
Kurose & Kumari (1999)	Rigid sphere	Linear shear	Theoretical (Numeric)	$1 \leq Re_s \leq 100$
Bagchi & Balachandar (2002)	Rigid sphere	Linear shear	Theoretical (Numeric)	$0.5 \leq Re_s \leq 200$
Tomiyama et al. (2002)	Bubbles	Linear shear	Experiment	
Asmolov (2002)	Rigid sphere	Parabolic Flow	Theoretical (Analytical)	$Re_s \ll 1$
Joseph & Ocando (2002)	Rigid sphere	Parabolic flow	Theoretical (Numeric)	
Adoua et al. (2009)	Oblate spheroid	Linear shear	Theoretical (Numeric)	
Bluemink et al. (2008; 2010)	Rigid sphere	Linear shear	Exp./Theoretical (Numeric)	$5 \leq Re_s \leq 200$

*some are left blank as they are not explicitly given by the authors

where the first term on the right hand side of equation (4.2.13) describes the lift on a stationary particle in a shear flow with a velocity gradient G and the second term describes the lift on a spinning particle in a uniform flow.

The lift coefficient for the lift force on a spinning sphere in a uniform flow was derived by Rubinow & Keller (1961) who found that $C_R = 3/8$. For the lift on a spinning sphere, Bagchi & Balachandar (2002) showed that the lift due to the rotation of the particle in a linear shear flow is about 50% of that derived by Rubinow & Keller (1961), that is $C_R = 3/16$.

Table 4.1 lists some experimental and numerical investigations performed in the past to study the lift force on particle immersed in shear flows.

4.3 Balance of the drag and lift forces with gravity

4.3.1 Drag Force Analysis

We briefly review the classical analysis that determines the settling velocity of a particle that is subject to gravitational and drag forces only. This is done in order to establish notation and preliminary concepts prior to our generalisation of this analysis to include lift forces. We assume that the drag force $\vec{F}_D$ is correlated in terms of a non-dimensional drag coefficient C_D, namely

$$\vec{F}_D = -C_D \frac{1}{2}\rho_f A_p |\vec{u}_r|\vec{u}_r \tag{4.3.1}$$

where A_p is the projected area of the particle in the direction of relative flow velocity. For incompressible flow, C_D may be correlated in terms of the particle Reynolds number $Re_p = |u_p| d_p/\nu_f$, and the drag curve $C_D(Re_p)$ is a function of particle shape. The motion of the particle is governed by a balance between drag and gravitational forces.

$$\rho_p V_p \frac{d\vec{u}_p}{dt} = \Delta\rho V_p \vec{g} - C_D \frac{1}{2}\rho_f A_p |\vec{u}_r|\vec{u}_r, \qquad \Delta\rho = \rho_p - \rho_f \tag{4.3.2}$$

For a spherical particle, $V_p = \pi d_p^3/6$, $A_p = \pi d_p^2/4$, and (4.3.2) may be rewritten as:

$$\frac{\rho_p}{\rho_f}\frac{d\vec{u}_p}{dt} = \overrightarrow{g_R} - \frac{3}{4}\frac{C_D}{d_p}|\vec{u}_r|\vec{u}_r, \qquad \overrightarrow{g_R} = \frac{\Delta\rho}{\rho_f}\vec{g} = \text{reduced gravity} \tag{4.3.3}$$

Note that (4.3.3) is also valid for non-spherical particles, provided that the drag coefficient is defined with respect to an assumed orientation, and with respect to the projected area of a volume-equivalent sphere. For a positively buoyant particle settling under gravity in a stationary fluid ($\vec{u}_f = 0$), we may assume that $\vec{g} = (0, -g, 0)$ and $\vec{u}_r = \left(0, -\left|\vec{u}_p\right|, 0\right)$, so (4.3.3) reduces to a one-dimensional equation:

$$\frac{\rho_p}{\rho_f}\frac{d|\vec{u}_p|}{dt} = g_R - \frac{3}{4}\frac{C_D}{d_p}\left|\vec{u}_p\right|^2 \tag{4.3.4}$$

Finally, as C_D is defined as a function of the particle Reynolds number, it is convenient to express (4.3.4) in non-dimensional form in terms of the particle Reynolds number $\mathrm{Re_p}$ and a non-dimensional time scale relative to the viscous time scale, $t' = t/t_{vis}$, where $t_{vis} = d_p^2/\nu_f$. This gives:

$$\frac{\rho_p}{\rho_f}\frac{dRe_p}{dt'} = Ga - \frac{3}{4}C_D Re_p^2 \tag{4.3.5}$$

where $Ga = g_R d_p^3/\nu_f^2$ is the Galileo Number. The settling velocity $\left|\vec{u}_p\right| = U_\infty$ is achieved when the right hand side of equation (4.3.5) is zero. This gives the classical formula for the particle settling Reynolds number $Re_\infty = U_\infty d_p/\nu_f$:

$$F_D^*(Re_\infty) = Ga \tag{4.3.6}$$

where $F_D^*\left(Re_p\right) = \frac{3}{4}C_D Re_p^2$ is the non-dimensional drag force. For a general drag curve, and a given value of Galileo number, the settling Reynolds number may be determined by numerically inverting (4.3.6), and the result is unique provided that F_D^* is a monotonically increasing function of particle Reynolds number.

For certain special forms of the drag curve, (4.3.6) can be inverted analytically to give an explicit formula for the settling Reynolds number. For example, in the limit of low particle Reynolds numbers, the drag curve for both spherical and non-spherical particles obeys the Stokes' law, $C_D = C_{DS}/Re_p$, where C_{DS} is the Stokes coefficient, equal to 24 for spherical particles. In this case, (4.3.6) is a linear equation, with solution:

$$Re_\infty = \frac{4}{3}\frac{Ga}{C_{DS}} \qquad \Rightarrow \qquad U_\infty = \frac{4}{3}\frac{\overrightarrow{g_R}}{C_{DS}}\frac{d_p^2}{\nu_f} \tag{4.3.7}$$

In the limit of high particle Reynolds number, the drag coefficient is independent of particle Reynolds number, so $C_D = C_N$, where C_N is the Newton coefficient, equal to 0.44 for spherical particles. In this case, (4.3.6) is a quadratic equation, with solution:

$$Re_\infty = \sqrt{\frac{4}{3}\frac{Ga}{C_{DN}}} \qquad \Rightarrow \qquad U_\infty = \sqrt{\frac{4}{3}\frac{\overrightarrow{g_R} d_p}{C_{DN}}} \tag{4.3.8}$$

Equations (4.3.7) and (4.3.8) state the classical result that 'small' particles settle at velocities proportional to the square of their diameters, whilst 'large' particles settle at velocities proportional to the square root of their diameters. Here, particles are regarded as 'small' if they settle at particle Reynolds numbers which are sufficiently small that the Stokes law approximation to the drag curve is valid. Particles are regarded as 'large' if they settle at particle Reynolds numbers for which the Newton approximation to the drag curve is valid. In order to quantify this definition, it is useful to have a formula for the settling velocity which is valid for the full range of particle Reynolds numbers between these two limits.

The simplest drag curve which has the correct asymptotic behaviour for low and high Reynolds numbers is the two-parameter Stokes-Newton drag curve:

$$C_D = \frac{C_{DS}}{Re_p} + C_{DN} \tag{4.3.9}$$

Note that this functional form of the drag curve may also be used to extend the Stokes regime of the drag curve to slightly higher Reynolds numbers, for which the Oseen correction is applicable:

$$C_D = \frac{C_{DS}}{Re_s}(1 + C_{DO} Re_s) = \frac{C_{DS}}{Re_s} + C_{DS} C_{DO} \tag{4.3.10}$$

where $C_{DO} = 3/16$ for spheres (Clift et al., 1978). In this case, C_{DN} in equation (4.3.9) should be replaced by the product of the Stokes and Oseen coefficients $C_{DS} C_{DO} = 9/2$ for spheres.

For the Stokes-Newton form of the drag curve, (4.3.6) is a quadratic equation in Re_∞, with unique positive solution:

$$Re_\infty = \frac{\sqrt{C_S^2 + \frac{16}{3} Ga C_N} - C_S}{2C_N} \tag{4.3.11}$$

In practise, a better fit to the drag curve between the Stokes and Newton limits may be obtained with the three-parameter Power-Law Stokes-Newton drag curve (Cheng, 1997):

$$C_D = \left[\left(\frac{C_S}{Re_p}\right)^p + {C_N}^p\right]^{1/p} \tag{4.3.12}$$

For this case, (4.3.6) can be expressed as a quadratic equation in Re_∞^p, with unique positive solution:

$$Re_\infty^p = \frac{\sqrt{C_S^{2p} + 4\left(\frac{4}{3}GaC_N\right)^p} - C_S^p}{2C_N^p} \tag{4.3.13}$$

The spherical particle drag curve may be approximated with $p = 1/2$ (Dallavalle 1948). Moreover, Camenen (2007) showed that the drag curves over a wide range of non-spherical particle shapes could be correlated in the form (4.3.12). Thus, (4.3.13) is potentially a very useful tool in analysing fractionation of sedimentary particles taking into account both particle size distribution and particle shape anisotropies.

4.3.2 Combined Drag and Lift Force Analysis

In this section, we aim to investigate to what extent the analysis reviewed in section 4.2 can be generalised to take account of the effect of shear induced and Magnus lift forces on particles settling under gravity. In particular, we establish simple explicit formulae analogous to equations (4.3.7) and (4.3.8) in the low and high Reynolds number limits, and we establish simple analytical procedures to examine the behaviour of the settling velocity over wider ranges of particles Reynolds numbers for which explicit formulae cannot be established. When shear –induced and Magnus lift forces of the form of equations (4.2.7) and (4.2.8) are included, the motion of the particle is governed by the equation:

$$\rho_p V_p \frac{d\vec{u}_p}{dt} = \Delta\rho V_p \vec{g} - C_D \frac{1}{2}\rho_f A_p |\vec{u}_r|\vec{u}_r + C_L \rho_f V_p \vec{\omega}_f \times \vec{u}_r + \rho_f V_p \vec{\omega}_p \times \vec{u}_r \tag{4.4.1}$$

Following the same manipulations as those for equation (4.1.3), this simplifies to:

$$\frac{\rho_p}{\rho_f}\frac{d\vec{u}_p}{dt} = \overrightarrow{g_R} - \frac{3}{4}\frac{C_D}{d_p}|\vec{u}_r|\vec{u}_r + \left(C_L\vec{\omega}_f + C_R\vec{\omega}_p\right) \times \vec{u}_r \tag{4.4.2}$$

In this case, the equation does not reduce to a one-dimensional equation, so it is convenient to non-dimensionalise with respect to the following vector Reynolds numbers:

$$\overrightarrow{Re_p} = \vec{u}_p d_p/\nu_f, \quad \overrightarrow{Re_s} = \vec{u}_r d_p/\nu_f, \quad \overrightarrow{Re_\omega} = \vec{\omega}_f d_p^2/\nu_f, \quad \overrightarrow{Re_R} = \vec{\omega}_p d_p^2/\nu_f \quad (4.4.3)$$

We obtain:

$$\frac{\rho_p}{\rho_f}\frac{d\overrightarrow{Re_p}}{dt'} = \overrightarrow{Ga} - \frac{3}{4}C_D\left|\overrightarrow{Re_s}\right|\overrightarrow{Re_s} + \left(C_L\overrightarrow{Re_\omega} + C_R\overrightarrow{Re_R}\right) \times \overrightarrow{Re_s} \quad (4.4.4)$$

where $\overrightarrow{Ga} = \overrightarrow{g_R} d_p^3/\nu_f =$ the vector Galileo Number. Hence, the condition for the equilibrium state is given by:

$$\overrightarrow{Ga} - \frac{3}{4}C_D\left|\overrightarrow{Re_s}\right|\overrightarrow{Re_s} + \left(C_L\overrightarrow{Re_\omega} + C_R\overrightarrow{Re_R}\right) \times \overrightarrow{Re_s} = 0 \quad (4.4.5)$$

For two dimensional shear flows, $\vec{u}_r = u_r\vec{\imath} + v_r\vec{\jmath}$, and $\vec{\omega}_f = \omega_f\vec{k}$, where$\omega_f = \left(\frac{\partial v_r}{\partial x} - \frac{\partial u_r}{\partial y}\right)$, so:

$$\overrightarrow{Re_s} \times \overrightarrow{Re_\omega} = Re_\omega\left(-Re_x\tilde{\jmath} + Re_y\tilde{\imath}\right) \quad (4.4.6a)$$

$$\overrightarrow{Re_s} \times \overrightarrow{Re_R} = Re_R\left(-Re_x\tilde{\jmath} + Re_y\tilde{\imath}\right) \quad (4.4.6b)$$

where $Re_x = u_r d_p/\nu_f$, $Re_y = v_r d_p/\nu_f$, $Re_\omega = \omega_f d_p^2/\nu_f$, and $Re_R = \omega_p d_p^2/\nu_f$ Therefore, equation (4.4.5) can be expressed as

$$\frac{3}{4}\,C_D\,Re_s\left(Re_x, Re_y\right) + (C_L\,Re_\omega + C_R Re_R)(Re_y, -Re_x) = (0, -Ga) \quad (4.4.7)$$

Note that Re_x , Re_y, Re_ω and Re_R may all take positive or negative signs, according to the signs of u_r, v_r , ω_f and ω_p respectively.

Let $Re_x = Re_s \sin\theta$, and $Re_y = Re_s \cos\theta$ where θ is the angle between the particle trajectory and that derived from the balance of drag and gravity as shown in Figure 4.2. The x and y-component of equation (4.4.7) becomes

$$\frac{3}{4}C_D Re_s^2 \sin\theta + (C_L\,Re_\omega + C_R Re_R)Re_s \cos\theta = 0 \quad (4.4.8a)$$

$$\frac{3}{4}C_D Re_s^2 \cos\theta - (C_L\,Re_\omega + C_R Re_R)Re_s \sin\theta = -Ga \quad (4.4.8b)$$

Using Trigonometric identities $cos^2\theta + sin^2\theta = 1$, the lift term can be eliminated to yield the following expression for the drag force:

$$F_D^* = Ga\,cos\,\theta \qquad (4.4.9a)$$

where $F_D^* = \frac{3}{4}C_D Re_s^2$ is the non-dimensional drag force, as defined in equation (4.3.6). Similarly, the drag term can be eliminated to give the following expression for the lift force:

$$F_L^* = Ga\,sin\,\theta \qquad (4.4.9b)$$

where $F_L^* = (C_L\,Re_\omega + C_R\,Re_R)Re_s$ is a non-dimensional lift force. Clearly, equations (4.4.9a,b) are the appropriate generalisations of equation (4.3.6) when lift force is included in the analysis. For fixed values of Ga, Re_ω, and Re_R, they may be used to determine Re_s and θ, and hence the magnitude and the direction of the equilibrium slip velocity. This process is facilitated by summing the squares of equations (4.4.9a,b), and dividing (4.4.9a) by equation (4.4.9b), to obtain two equivalent simultaneous equations:

$$F_D^{*2} + F_L^{*2} = Ga^2 \qquad (4.4.10a)$$

$$\frac{F_L^*}{F_D^*} = tan\,\theta \qquad (4.4.10b)$$

The advantage of the form of the equation (4.4.10a) is that the angle θ has been eliminated. For fixed values of Re_R, Re_ω and Ga, equation (4.4.10a) is a nonlinear equation for Re_s only, which can be inverted numerically. The result obtained for Re_s may then be substituted into equation (4.4.7b) to obtain the angle θ. In the absence of lift force ($F_L^* = 0$), $\theta = 0$ and $F_D^* = Ga$. It is informative to express the solutions of (4.4.10a,b) in terms of modifications to the solution Re_∞ of equation (4.3.6) where only drag force is considered. This obeys the equation $F_{D\infty} = \frac{3}{4}\,C_D\,Re_\infty^2 = Ga$, so (4.4.10a) may be expressed as:

$$F_D^{*2} + F_L^{*2} = F_{D\infty}^{*2} \qquad (4.4.11a)$$

On dividing by $F_{D\infty}^2$:

$$R_D^{*2} + R_L^{*2} = 1 \qquad (4.4.11b)$$

where $R_D^* = F_D^*/F_{D\infty}^*$ is the ratio of the modified non-dimensional drag force to the unmodified non-dimensional drag force, and $R_L^* = F_L^*/F_{D\infty}^*$ is the ratio of the total lift force to the unmodified drag force. Provided that $R_L^* < 1$, equation (4.4.11b) has a solution

$$R_D^* = \sqrt{1 - R_L^{*2}} \leq 1 \tag{4.4.12}$$

which indicates that $F_D^* \leq F_{D\infty}^*$. So, if F_D^* is a monotonically increasing function of Re_s (as it is in all examples considered in section 4.1), we can conclude that $Re_s \leq Re_\infty$ i.e. the magnitude of the settling velocity is always reduced by the lift force. For values of lift force that are sufficiently large that $R_L^* > 1$, no stable solution exists.

Equation (4.4.10b) indicates that the sign of the deflection angle depends on the sign of the non-dimensional lift force defined in equation (4.4.9b). In the absence of particle spin, the angle of defection has the same sign as the fluid vorticity for positive values of the shear-induced lift coefficient, and the opposite sign to that of the fluid vorticity for negative values of the shear-induced lift coefficient, as illustrated in Fig. 4.1.

Given correlations for drag, shear induced and rotation induced lift forces, the solution procedure above may be employed to determine the equilibrium particle settling velocity and angular deflection for fixed values of the three free parameters, Ga, Re_ω, and Re_R, or interchangeably, Re_∞, Re_ω, and Re_R. However, if the rotational motion of the sphere reaches steady state more quickly than the translational motion, then the angular velocity of the sphere can be taken to be equal to the torque-free angular velocity, thus reducing the number of independent variables to two. Bagchi & Balachandar (2002) performed detailed direct numerical simulations to study the effects of free rotation and translation on a solid sphere in an unbounded shear flow. They concluded that, for small values of particle Reynolds number, the time scale to achieve rotational equilibrium was much less than that for translational equilibrium. At higher particle Reynolds numbers, the rotational time scale increases significantly, until the two time scales become of the same order of magnitude. They also found that the equilibrium angular velocity was less than the

ambient fluid vorticity, with their ratio correlated with particle Reynolds number according to the formula:

$$\omega_p/\omega_f = 1 - 0.0364\, Re_s^{0.95} \qquad \text{for } 0.5 < Re_s \leq 5 \qquad (4.4.13a)$$

$$\omega_p/\omega_f = 1 - 0.0755\, Re_s^{0.4555} \qquad \text{for } 5 < Re_s \leq 200 \qquad (4.4.13b)$$

On the other hand, Bluemink et al. (2008) performed experiments and numerical simulations that indicated that the equilibrium angular velocity of a sphere in a uniformly rotating or shearing flow was greater than the ambient fluid vorticity, and was related to particle Reynolds number as follows:

$$Re_R/Re_\omega = 1 + 0.0045 Re_s \qquad (4.4.14)$$

Bluemink et al. (2008) observed that their result was at variance with that of Bagchi and Balachandar (2002), and stated that, at the time of writing, the discrepancy was unexplained. In view of this uncertainty, we present our results based on the assumption that Re_ω and Re_R are independent free parameters. We then use these to present results for the zero spin case. A brief discussion is given in section 4.3.6 of the relative effects of the results of Bagchi and Balachandar (2002) and Bluemink et al (2008) in the case of intermediate particle Reynolds numbers.

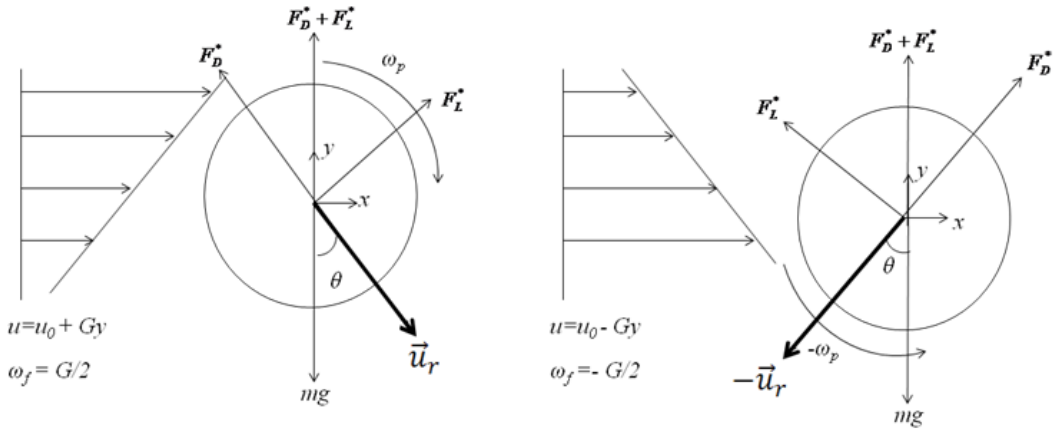

Figure 4.1 Schematic diagram illustrating the direction of the lift (F_L^*), drag (F_D^*) and gravitational force (mg) on a sphere rotating with an angular velocity ω_p in a positive (left) or negative (right) shear flow. The bold line is the settling direction of the sphere and θ represents the angle between the settling direction of the sphere and the gravitational force. The particle pushed forward ($\theta, \vec{u}_s$) in a positive shear G flow and pushed backward ($-\theta, -\vec{u}_s$) in a negative shear – G shear flow.

4.3.3 Small Particle Reynolds Number Limit

As for the case of small particle Reynolds numbers, it is straightforward to derive explicit formulae which generalise equation (4.3.7) for the settling velocity of particles in the Stokes drag limit. We assume Stokes' law for the drag force: $C_{D,Stokes} = C_{DS}/Re_s$ and we assume a generalisation of Saffman's correlation for the shear-induced lift force defined in equation (4.2.10), $C_{L,Saffman} = C_{LS}/\sqrt{Re_\omega}$. However, we work in terms of general Stokes and Saffman coefficients in order to facilitate application to non-spherical particles. We also assume a constant coefficient C_R for the Magnus lift force.

Based on these assumptions for the drag and lift coefficients, both the non-dimensional drag and lift forces are linear in Re_s, hence their ratio is independent of Re_s. In view of its subsequent importance, we will refer to this non-dimensional quantity Λ_S as the **Stokes Regime Lift Number**.

$$\frac{F_L^*}{F_D^*} = \Lambda_S = \frac{4}{3}\frac{1}{C_{DS}}\left(C_{LS}\sigma_\omega\sqrt{|Re_\omega|} + C_R Re_R\right) \tag{4.5.1}$$

where $\sigma_\omega = sign(\omega)$.

(4.4.11a) relates the ratio of the modified to unmodified settling Reynolds numbers to Λ_S as follows:

$$\frac{Re_S}{Re_\infty} = \frac{1}{\sqrt{1+\Lambda_S^2}} \tag{4.5.2a}$$

and equation (4.4.8b) relates the deflection angle θ to Λ_S as follows:

$$tan\,\theta = \Lambda_S \qquad \Rightarrow \qquad cos\,\theta = \frac{1}{\sqrt{1+\Lambda_S^2}}, \quad sin\,\theta = \frac{\Lambda_S}{\sqrt{1+\Lambda_S^2}} \tag{4.5.2b}$$

Note that (4.5.2a) represents the reduction of the magnitude of the settling velocity Reynolds number due to the lift force. Its decompositions into vertical and horizontal components are given by:

$$\frac{Re_y}{Re_\infty} = -\frac{Re_S}{Re_\infty}cos\,\theta = \frac{-1}{1+\Lambda_S^2}, \tag{4.5.3a}$$

$$\frac{Re_x}{Re_\infty} = \frac{Re_S}{Re_\infty}sin\,\theta = \frac{\Lambda_S}{1+\Lambda_S^2} \tag{4.5.3b}$$

Thus, there is a further reduction in the magnitude of the vertical settling velocity, and there is an induced horizontal drift that is not present in the absence of the lift force. It is of interest to see how these results scale in terms of particle diameter. In the absence of particle spin, we have:

$$\Lambda_S = \frac{4}{3}\frac{C_{LS}}{C_{DS}}\sigma_\omega\sqrt{|Re_\omega|} = \frac{4}{3}\frac{C_{LS}}{C_{DS}}\sigma_\omega\sqrt{\frac{|\omega|}{\nu_f}}d_p \tag{4.5.4}$$

Thus, the Stokes Lift Number Λ_S is proportional to the particle diameter. Performing a Taylor Series expansion of (4.5.2a,b) to lowest order in Λ_S gives:

$$\frac{Re_s}{Re_\infty} = 1 - \frac{\Lambda_S^2}{2} + O(\Lambda_S^4), \qquad \theta = \Lambda_S + O(\Lambda_S^3) \tag{4.5.5}$$

Hence, for small particle diameters, the deflection angle depends linearly on the particle diameter, and the magnitude of the settling velocity is reduced by a factor that differs from unity by a quantity that is proportional to the square of the particle diameter. As the unmodified slip velocity is proportional to the square of the particle diameter, this gives a lift-induced correction to the slip velocity which is proportional to d_p^4.

Similarly, (4.5.3a,b) gives the modifications to vertical and horizontal settling velocities to lowest order in Λ_S:

$$\frac{Re_y}{Re_\infty} = -1 + \Lambda_S^2 + O(\Lambda_S^4), \qquad \frac{Re_x}{Re_\infty} = \Lambda_S + O(\Lambda_S^3) \tag{4.5.6}$$

So, the vertical component of settling velocity is also reduced by a factor that differs from unity by a quantity that is proportional to the square of the particle diameter, and the reduction is double that of the settling velocity magnitude. On the other hand, the induced horizontal drift velocity is related to the unmodified settling velocity by a factor that directly proportional to the particle diameter, hence it is proportional to d_p^3.

4.3.4 High Particle Reynolds Number Limit

Another simple analysis can be made in the limit of large particle Reynolds number $Re_s \to \infty$. In this case, we assume that the drag coefficient is constant, $C_D = C_{DN}$, where $C_{DN} = 0.44$ for a spherical particle. We also assume that the shear-induced lift coefficient is constant, $C_L = C_{LN}$. As in the low particle Reynolds number

analysis, we work with general values of C_{DN} and C_{LN} in order to facilitate generalisation to non-spherical particles. Due to a lack of investigations of the lift coefficient over the full range of particle Reynolds numbers, the assumption of constant C_L requires careful interpretation. As discussed in section 4.20, the correlation of Mei (1992) gives a constant value $C_{LM} = 0.114$ equation (4.2.11) for the shear-induced lift coefficient for solid spherical particles in the range $40 < Re_s < 100$, which is well below the threshold for vortex shedding past the sphere. This range of Reynolds numbers is also below the Newton regime of the spherical particle drag curve, and hence is not applicable to this section. It is discussed in detail in the following sections 4.3.5 and 4.3.6. For particle Reynolds numbers above the threshold for vortex shedding, and within the Newton regime of the drag curve, good comparisons with experimental results can only be achieved using a much smaller constant lift coefficient $C_L = C_{LN} = 0.1 - 0.5$ (Wang et al 1986, Lahey et al. 1993, Alajbegovic et al 1994, Moraga et al. 1999). Because these results are obtained for high Reynolds number flows, it is necessary to interpret them in a time-averaged sense (Moraga et al. 1999).

As in the Stokes flow limit, the governing equations (4.4.10a,b) can be expressed in terms of a single non-dimensional parameter Λ_N, defined in terms of known quantities, which we will refer to as the **Newton Regime Lift Number Λ_N**:

$$\frac{Re_s^4}{Re_\infty^4} + \Lambda_N^2 \frac{Re_s^2}{Re_\infty^2} - 1 = 0 \tag{4.6.1a}$$

$$\frac{F_L^*}{F_D^*} = \Lambda_N \frac{Re_\infty}{Re_s} = tan\,\theta \tag{4.6.1b}$$

where:

$$\Lambda_N = \frac{C_{LN} Re_\omega + C_R Re_R}{\frac{3}{4} C_{DN} Re_\infty} \tag{4.6.1c}$$

Note that this is similar to, though not identical to, the Stokes Regime Lift Number defined in equation (4.5.1). Unlike the Stokes Regime Lift Number, it depends on Re_∞, and it is not identical to F_L^*/F_D^*. Equation (4.6.1a) is quadratic in Re_s^2/Re_∞^2, and has the unique positive solution:

$$\frac{Re_s^2}{Re_\infty^2} = \sqrt{1 + \frac{\Lambda_N^4}{4}} - \frac{\Lambda_N^2}{2} \approx 1 - \frac{\Lambda_N^2}{2} + O(\Lambda_N^4) \tag{4.6.2}$$

Equations (4.4.10a,b) and (4.6.1b) give trigonometric formulae for the angle of deflection:

$$cos\,\theta = \frac{Re_s^2}{Re_\infty^2} = \sqrt{1 + \frac{\Lambda_N^4}{4}} - \frac{\Lambda_N^2}{2} \tag{4.6.3a}$$

$$sin\,\theta = \Lambda_N \frac{Re_s}{Re_\infty} = \Lambda_N \sqrt{\sqrt{1 + \frac{\Lambda_N^4}{4}} - \frac{\Lambda_N^2}{2}} \tag{4.6.3b}$$

$$tan\,\theta = \Lambda_N \frac{Re_\infty}{Re_s} = \Lambda_N \sqrt{\sqrt{1 + \frac{\Lambda_N^4}{4}} + \frac{\Lambda_N^2}{2}} \tag{4.6.3c}$$

We can now deduce the settling Reynolds numbers in the vertical and horizontal directions:

$$\frac{Re_y}{Re_\infty} = -\frac{Re_s}{Re_\infty} cos\,\theta = -\left(\sqrt{1 + \frac{\Lambda_N^4}{4}} - \frac{\Lambda_N^2}{2}\right)^{3/2} \tag{4.6.4a}$$

$$\frac{Re_x}{Re_\infty} = \frac{Re_s}{Re_\infty} sin\,\theta = \Lambda_N \left(\sqrt{1 + \frac{\Lambda_N^4}{4}} - \frac{\Lambda_N^2}{2}\right) \tag{4.6.4b}$$

Finally, let us deduce the dependence of these results on the particle diameter. In the absence of particle spin, we have:

$$\Lambda_N = \frac{C_{LN} Re_\omega}{\frac{3}{4} C_{DN} Re_\infty} \tag{4.6.4c}$$

In dimensional form, Λ_N is proportional to the square root of the particle diameter, as follows:

$$\Lambda_N = \sqrt{\frac{4}{3} \frac{C_{LN}^2}{C_{DN}} \frac{\omega^2 d_p}{g'}} \tag{4.6.4d}$$

Expanding equations (4.6.3b) to lowest order in Λ_N gives:

$$\theta = \Lambda_N + O(\Lambda_N^3) \tag{4.6.5}$$

Thus, the deflection angle is proportional to the square root of the particle diameter. Similarly, expanding (4.6.2) and (4.6.4a,b) to lowest order in Λ_N gives:

$$\frac{Re_s}{Re_\infty} = 1 - \frac{\Lambda_N^2}{4} + O(\Lambda_N^4) \tag{4.6.6a}$$

$$\frac{Re_y}{Re_\infty} = -1 + \frac{3\Lambda_N^2}{4} + O(\Lambda_N^4) \tag{4.6.6b}$$

$$\frac{Re_x}{Re_\infty} = \Lambda_N + O(\Lambda_N^3) \tag{4.6.6c}$$

Hence, both the settling velocity magnitude and vertical component are reduced by a factor that differs from unity by a quantity that is directly proportional to the particle diameter. The induced horizontal drift velocity is related to the unmodified settling velocity by a factor that is proportional to the square root of particle diameter, so it is directly proportional to the particle diameter, as follows:

$$u_r = \frac{4}{3}\frac{C_{LN}}{C_{DN}}\omega d_p\left(1 + O(\Lambda_N^2)\right) \tag{4.6.7}$$

4.3.5 Intermediate Particle Reynolds Numbers (Semi-Analytical)

The previous two sections provide simple analytical formulae for the modification of settling velocity by lift forces in the Stokes Regime and Newton Regime limits of the drag force. In this section, we examine to what extent these results can be generalised to cover the full range of the drag curve between the Stokes and Newton limits. In particular, we wish to see to what extent the formula (4.3.13) can be generalised for the settling velocities of particles for which the Cheng (1997) Power-Law Stokes-Newton drag curve (4.3.12) is a reasonable approximation. This gives the following equation for the ratio of modified to unmodified particle Reynolds numbers, $r_{Re} = Re_s/Re_\infty$:

$$R_D^* = \frac{F_D^*}{F_{D\infty}^*} = \frac{r_{Re}}{C_{D\infty}}\left(\frac{C_{DS}^p}{Re_\infty^p} + C_{DN}^p r_{Re}^p\right)^{1/p} \tag{4.7.1}$$

Substituting (4.7.1) into (4.4.11b) gives a non-linear equation for r_{Re}:

$$\frac{r_{Re}^2}{C_{D\infty}^2}\left(\frac{C_{DS}^p}{Re_\infty^p} + C_{DN}^p r_{Re}^p\right)^{2/p} + (\Lambda\, r_{Re})^2 = 1 \tag{4.7.2}$$

where the **lift number** Λ is given by:

$$\Lambda = \frac{C_L Re_\omega + C_R Re_R}{\frac{3}{4}C_{D\infty}Re_\infty} \tag{4.7.3}$$

Note that Λ is equal to the Stokes lift number Λ_S (equation 4.5.1) and the Newton lift number Λ_N (equation 4.6.1), in the appropriate limits as $Re_\infty \longrightarrow 0$ and $Re_\infty \longrightarrow \infty$ respectively. Thus, it unifies both of these quantities into a single non-dimensional quantity.

In the special case of Stokes-Newton drag ($p = 1$), (4.7.2) is a quartic equation for r_{Re}, provided that C_L (and hence Λ) is independent of Re_s. For spherical particles, this is the case at low particles Reynolds numbers where Saffman's correlation applies, and for particle Reynolds numbers between 40 and 100, for which the Mei correlation gives a constant $C_L = 0.114$. Hence, within these Reynolds number limits, exact expressions may be obtained by solving the quartic equation (4.7.2) for r_{Re}. However, our experience indicates that the resulting expressions are too complex to be instructive. For full information on r_{Re}, it is better to solve (4.7.2) numerically, as outlined in section 4.3.2.

On the other hand, (4.7.2) may be used to provide a useful exact expression for r to first-order in Λ for any form of the Power-Law Stokes-Newton Drag Law. (4.7.2) has a unique solution for r_{Re} between the values of zero and unity, given by the intersection of a monotonically increasing function of r_{Re} and a monotonically decreasing function of r:

$$R_D^*(r_{Re})^2 = \frac{r_{Re}^2}{C_{D\infty}^2}\left(\frac{C_{DS}^p}{Re_\infty^p} + C_{DN}^p r_{Re}^p\right)^{2/p} = 1 - (\Lambda\, r_{Re})^2 \qquad (4.7.4)$$

The solution to first-order in Λ can be found by approximating $R_D^*(r_{Re})^2$ by its tangent at $r_{Re} = 1$, and finding the point of intersection with the curve $1 - (\Lambda\, r_{Re})^2$.

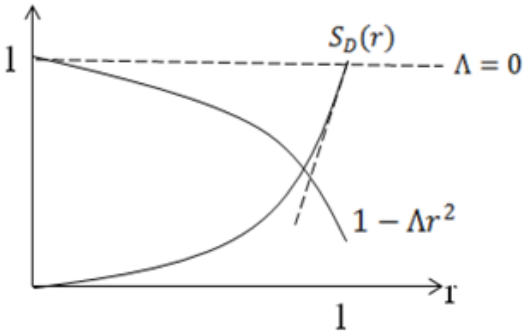

Figure 4.2 A sketch illustrates the intersection of curves $S_D(r)$ and $1 - \Lambda r^2$.

Let $S_D(r) = R_D^*(r)^2$, we have

$$S_D^p(r) = \frac{r^{2p}}{C_{D\infty}^{2p}}\left(\frac{C_{DS}^p}{Re_\infty^p} + C_{DN}^p r^p\right)^2, \text{ and } R_D^{*\,p}(r) = \frac{r^p}{C_{D\infty}^p}\left(\frac{C_{DS}^p}{Re_\infty^p} + C_{DN}^p r^p\right) \qquad (4.7.5)$$

(to keep the symbols neat, r is used instead of r_{RE} in equations (4.7.5 to 4.7.13))

The derivative of $S_D(r)$ is

$$S_D'(r) = 2R_D^*(r)\, R_D^{*\prime}(r) \tag{4.7.6}$$

The right hand side of the equation can be expanded to

$$pR_D^{p-1}(r)R_D'(r) = \frac{pr^{p-1}}{C_{D\infty}^p}\left(\frac{C_s^p}{Re_\infty^p} + C_{DN}^p r^p\right) + \frac{r^p}{C_{D\infty}^p} C_{DN}^p p r^{p-1} = \frac{pr^{p-1}}{C_{D\infty}^p}\left(\frac{C_s^p}{Re_\infty^p} + 2C_{DN}^p\right) \tag{4.7.7}$$

The $S_D(r)$ at $r = 1$ becomes

$$S_D'(1) = \frac{2}{C_{D\infty}^p}\left(\frac{C_s^p}{Re_\infty^p} + 2C_{DN}^p\right) = 2\left(1 + \frac{C_{DN}^p}{C_{D\infty}^p}\right) \tag{4.7.8}$$

Equation of the tangent for $S_D(r)$ at $r = 1$ is

$$S_D(r) = S_D(1) + S_D'(1)(r-1) \tag{4.7.9}$$

Equating (4.7.9) to the right hand side of (4.7.4) gives the following quadratic equation

$$S_D'(r-1) = \Lambda^2 r^2 \tag{4.7.10}$$

The solution of (4.7.10) is

$$r = \frac{-S_D' \pm \sqrt{{S_D'}^2 + 4S_D'\Lambda^2}}{2\Lambda^2} \quad => r = \frac{S_D'}{2\Lambda^2}\left[\sqrt{1 + \frac{4\Lambda^2}{S_D'}} - 1\right] \tag{4.7.11}$$

Expressing the first term in the bracketed term on the right hand side of (4.7.11) using the Taylor series expansion gives

$$r = \frac{S_D'}{2\Lambda^2}\left[1 + \frac{2\Lambda^2}{S_D'} - \frac{1}{8}\left(\frac{4\Lambda^2}{S_D'}\right)^2 + \cdots - 1\right] = \frac{S_D'}{2\Lambda^2}\left[\frac{2\Lambda^2}{S_D'} - \frac{2\Lambda^4}{{S_D'}^2} + \cdots\right] \tag{4.7.12}$$

Therefore,

$$r = 1 - \frac{\Lambda^2}{2\left(1 + \frac{C_{DN}^p}{C_{D\infty}^p}\right)} + O(\Lambda^4) \tag{4.7.13}$$

This result generalises the results (4.5.5) and (4.6.6) which apply in the Stokes and Newton limits respectively. We see that the leading coefficient of Λ^2 decreases continuously from $1/2$ in the Stokes Regime to 1/4 in the Newton Regime.

Equation (4.7.13) is useful for spherical particles in the range $40 \leq Re_s \leq 100$ where the Mei correlation yields a constant lift coefficient $C_L = 0.114$. This range of Reynolds numbers is in the transitional region of the drag curve, and can be approximated by the Power-Law Stokes-Newton Drag Curve with $C_{DS} = 24$, $C_{DN} = 0.44$, and $p = 1/2$ (Dallavalle 1948). In addition (4.7.5) may be used to extend the Stokes Regime result to slightly higher particle Reynolds numbers where the Oseen drag law (4.3.10) applies. In this case, p should be taken to be unity, and the Newton coefficient should be replaced by the product of the Stokes coefficient C_{DS} and the Oseen coefficient C_{DO}.

4.3.6 Intermediate Particle Reynolds Numbers (Numerical)

For spherical particles, the semi-analytical analysis of the previous section was applicable for small particle Reynolds numbers within the range of validity of the Stokes-Oseen approximation (4.3.10) to the drag curve, and for higher particle Reynolds numbers in the range 40 to 100. For intermediate particle Reynolds numbers, the Mei correlation for the lift coefficient is too complex to yield to an analytical solution. Hence, we employ the numerical methodology outlined in section 4.3.2. For this purpose, we use the Mei (1992) correlation for lift in conjunction with the well-known Schiller-Naumann correlation for the spherical particle drag coefficient:

$$C_D = \frac{24}{Re_s}(1 + 0.15Re_s^{0.687}) \tag{4.8.1}$$

Equations (4.8.1) are solved using Matlab for fixed values of the vorticity Reynolds number Re_ω and the unmodified particle Reynolds number Re_∞ (the latter may be used interchangeably with the Galileo number). In order to investigate the effect of the shear-induced lift force on a stationary particle and Magnus lift-force separately, we present the solutions of the shear-induced lift force both without and with the Magnus lift force. Since there is no general agreement on the correlation for the freely rotating particle spin in a torque-free state, we present both solutions that are based on a particle spin correlation of either Bagchi & Balachandar (2002) or Bluemink et al. (2008) (denoted as BB and BL, respectively). In the following, we

present and discuss the result showing the effect of the lift force on r and the trajectories of the particle over a wide range of values of Re_∞ and Re_ω.

Figure 4.3(a) shows the percentage change in the ratio of the particle Reynolds number to the unmodified particle Reynolds number by the lift r_{Re} (which also represents the ratio of the settling velocity of the particle influenced by the lift force to that without lift force) as a function of Re_∞, when Re_ω is fixed at values of 2, 5 and 10. This figure shows that r_{Re} decreases for any values of Re_ω and Re_∞ and decreases the most when Re_∞ is small ($Re_\infty \leq 1$). As Re_∞ increases, the decrease in r_{Re} becomes increasingly smaller and the rate of decrease become steeper with larger value of Re_ω. The addition of the Magnus lift force further reduces the value of r_{Re}, and this effect appear to be more significant for higher value of Re_ω. It can be noted that results based on the particle spin correlation of BB do not vary significantly from those of BL. When $Re_\infty > 10$, the effect of the lift force on r is virtually negligible (less than 2%) and this applies to both solutions with and without the Magnus-like lift force. The effect of Re_ω on r_{Re} in this range of Re_∞ appears to be insignificant since only little change is observed when the value of Re_ω is increased from 2 to 10.

The angle of deflection θ that corresponds to the case in Figure 4.3(a) is presented in Figure 4.3(b). This figure shows that θ is at its maximum value when Re_∞ is the smallest, i.e. $Re_\infty \to 0$ and decreases as Re_∞ increases. It appears that θ starts to decrease drastically at values of $Re_\infty \sim 1$ irrespective of the value of Re_ω. At large values of Re_∞, θ decreases to a very small value. Increases in Re_ω increase θ but at a much lower rate compared to that at small values of Re_∞. Including the Magnus-like lift force slightly increases the values of θ. The change in the profile of θ around $Re_\infty = 40$ is due to the change in the shear lift coefficient from a decreasing value to a constant value The results based on BB or BL agree at low values of Re_∞ but less well at large value of Re_∞ where the latter predicts a slightly larger value of θ than the former does.

It is interesting to see how r_{Re} and θ change with Re_ω when Re_∞ is at a fixed value. Figure 4.4(a) shows the percentage change in r as a function of Re_ω when Re_∞ is fixed at values of 0.1, 1 and 10. It can be observed that r_{Re} decreases as Re_∞ increases. The trend in the decrease of r varies for different values of Re_∞. Small

Re_∞ experiences a more gradual decrease and starts at smaller values of Re_ω whereas larger values of Re_∞ experiences a steeper decrease that starts at larger values of Re_ω. Also plotted on the figure are the solutions in the Stokes regime for comparison with the numerical solution at low values of Re_∞, and both solutions match well. Including the Magnus-like lift force does not result in much change to the solution at low values of Re_ω but the effect becomes increasingly more pronounced with the increase of Re_ω. For instance, for Re_∞ = 1 and Re_ω = 100, the Magnus-like lift force further reduces r_{Re} by 15%. The corresponding values of θ is shown in Figure 4.4(b). It can be seen that the effect of the lift force on θ is similar to its effect on r_{Re}. Thus θ increases exponentially with an increase in Re_ω and the rate of such an increase increases with larger values of Re_∞.

It is worth summarising the above discussion on how r_{Re} and θ vary with the parameters Re_ω and Re_∞ by plotting them in contour form, as shown in Figure 4.5(a) and (b). These figures clearly show how r_{Re} and θ increase as Re_ω increases but decreases as Re_ω increases.

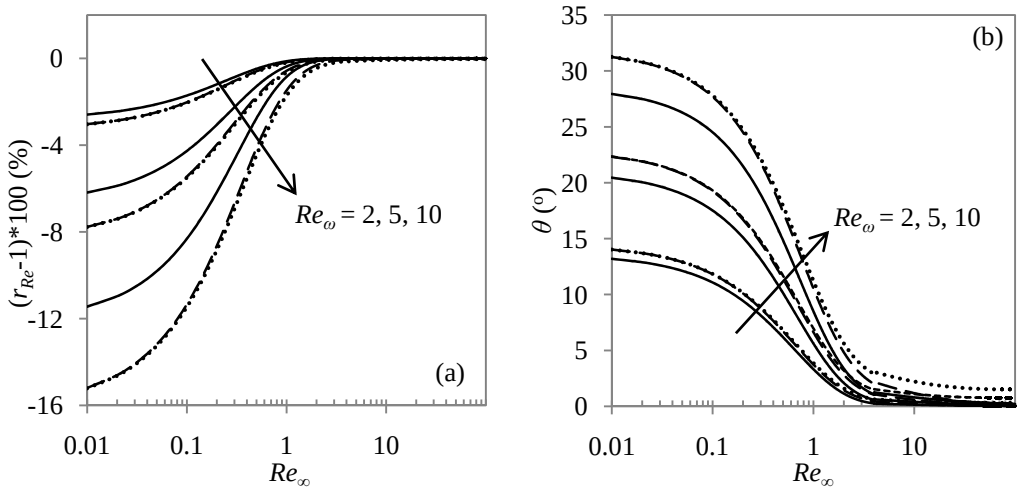

Figure 4.3 (a) Percentage change in r_{Re}, and (b) angle of deflection θ, as a function of Re_∞ when Re_ω= 2, 5 and 10. The solid lines represent solutions with only shear-induced lift force. The dashed lines (– –) represent solutions with both shear-induced and rotation-induced lift force based on Bagchi & Balanchandar (BB) correlation whereas the dot-lines (···) are those based on Bluemink et al. correlation (BL)).

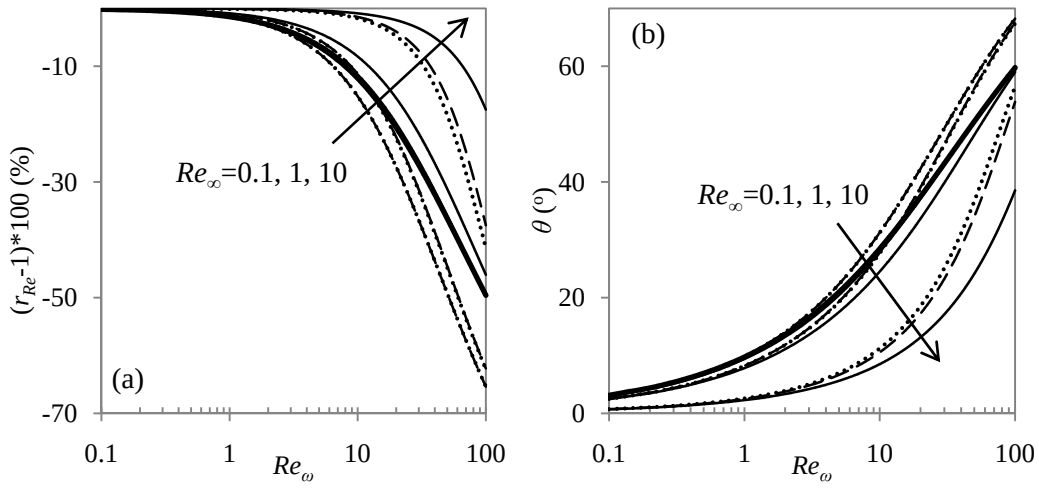

Figure 4.4 (a) Percentage change in r_{Re}, and (b) angle of deflection θ, as a function of Re_ω when Re_∞ = 0.1, 1, 10. The bold solid lines represent the Stokes solution (Re_∞ = 0.1). The other notation is as in Figure 4.3.

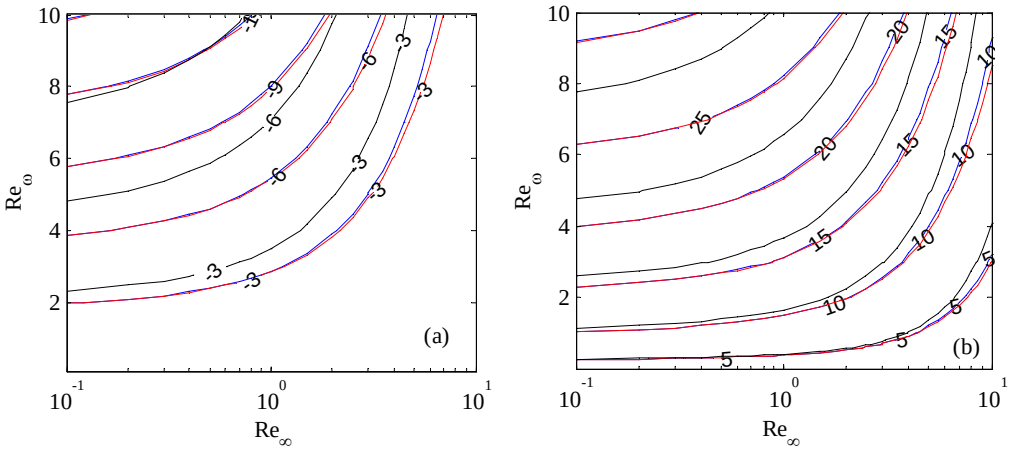

Figure 4.5 (a) Percentage change in r_{Re}, and (b) angle of deflection θ, as a function of Re_ω and Re_∞. The blacks lines represent solutions with only shear-induced lift force. The blue lines represent solutions with both shear-induced and rotation-induced lift force based on BB correlation whereas the red lines are those based on BL.

4.4 Implications

The analysis above may be used to estimate the effect of lift on a particle immersed in a fluid where the shear is significant. In this section, we apply our analysis to determine under what situations the lift force may have a significant effect on the particle settling velocity and trajectory. In subsequent sections, we apply this analysis to turbidity currents and particle entrainment as examples of the usefulness of the theory.

4.4.1 General Considerations

In section 4.3, simple expressions were obtained for determining the particle slip Reynolds number Re_s and the angle of deflection θ of a freely-rotating sphere in a 2D shear flow. Exact expressions have been obtained in the Stokes and Newton Regime limits, and approximate expressions have been obtained for intermediate particle Reynolds numbers. It was found that the particle slip Reynolds number was always reduced by the lift force. The reduction in magnitude of the slip velocity, $r_{Re} = Re_s/Re_\infty$ and the angular deflection θ both depend on a single non-dimensional quantity Λ, the lift number, which is defined by:

$$\Lambda = \frac{C_L Re_\omega + C_R Re_R}{\frac{3}{4} C_{D\infty} Re_\infty} \tag{4.9.1}$$

Thus, the effects of the lift force are large when the lift number is large. In the Stokes flow limit, Λ is independent of Re_∞. Outside this range, Λ is a decreasing function of Re_∞. Thus, the effects of the lift force are large when Re_ω and/or Re_R are large, and decrease gradually with increasing Re_∞. The magnitude of the angular deflection θ is directly proportional to the value of Λ. The sign of θ depends on the direction of the shear. A positive shear pushes the particle forward and hence results in a positive θ and vice versa (see Figure 4.1). For example, for sediment-laden open channel flow, the vorticity is negative below the free surface. Hence, the settling velocities of particles with positive lift coefficient will be deflected backwards, and those with negative lift coefficient will be deflected forwards. This velocity lag phenomenon has been observed in a limited number of experiments which are reviewed in Cheng (2004). Cheng also observed that the lag velocity is a function of the shear Reynolds number. Cheng presented a theoretical analysis of this phenomenon based purely on the balance between gravity and hindered settling drag laws for high concentrations of particles. However, the fact that the velocity lag increases with the shear Reynolds number strongly suggests that it is a direct consequence of the lift force. Comparisons with experimental results based on this assumption should be performed in future work.

4.4.2 Turbidity Currents

Turbidity currents are dilute subaqueous particulate gravity currents. They are known to have a shear-layered velocity profile. Indeed laboratory (e.g. Kneller et al.,

1999) and field (Xu, 2010) observations have concluded that the maximum velocity occurs at approximately one third of the depth of the flows. The velocity profile below this point approximately follows a logarithmic relation whereas the velocity profile above follows a Gaussian relation (Kneller et al., 1999, Xu, 2010). The lift force is generally neglected in the modelling of turbidity currents but the strong velocity gradient within the bulk flows suggests it could be significant. Using existing understanding of the mechanics and properties of turbidity currents, the shear within the bulk flow can be estimated and typical particle characteristic can be inferred from field studies on turbidity currents. On this basis, the effect of the lift (change in slip velocity and angle of deflection θ) can be evaluated using the analysis outlined in the previous section.

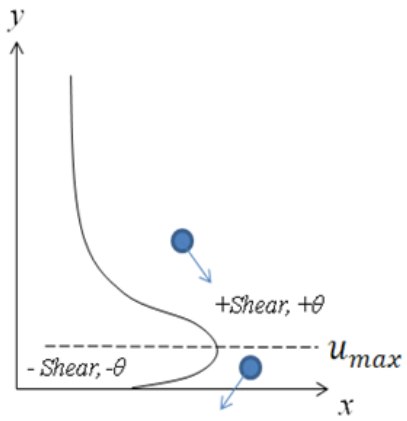

Figure 4.6 A typical velocity profile of a turbidity currents. The upper part of the flow has positive vorticity and the lower part has negative vorticity.

The shear above and below the maximum velocity are different in magnitude and sign. The former has positive sign and acts to push the sediment forward whereas the latter is negative in sign and acts to push the sediment backward (see Figure. 4.6). Since the maximum velocity is closer to the bottom boundary, the shear below the maximum velocity is greater than that above the maximum velocity and can be estimated as follows:

$$\frac{\partial u}{\partial y} = \frac{\omega_f}{2} \sim \frac{u_N}{h_{max}} \tag{4.9.2}$$

where u_N is the velocity of the front of the flows and h_{max} is the height where the maximum velocity occurs, i.e. $h_{max} \sim h/3$. The front velocity of the gravity current can be deduced from the following simple formula (Benjamin, 1968) :

$$u_N = Fr(g'h)^{1/2} \tag{4.9.3}$$

where g' is the reduced gravity which is defined as $g' = g(\rho_m - \rho_f)/\rho_f$, ρ_m is the mixture density, Fr is the Froude number, and h is the flow height. Huppert & Simpson (1980) showed that Fr = 1.19 for flows propagating in very deep water, i.e., for $h/H < 0.075$, where H is the height of the ambient fluid. The range of natural flow heights is not well constrained, but it has been reported that natural flows have a maximum flow height of about 300-400m (Meiburg & Kneller, 2009). Equations (4.9.2) & (4.9.3) yield the relationship between the shear and the front velocity as follows:

$$\omega_f \propto \frac{Fr^2 g'}{u_N} \tag{4.9.4}$$

This equation indicates that the flow shear decreases with an increase in the flow velocity. Substituting equation (4.9.3) into equation (4.9.4) for u_N shows that the shear decreases with increasing flow height, $\omega_f \propto h^{-0.5}$.

Xu et al. (2002) reported that the settling velocity of the particle in a natural system is in the range of 0.001 to 1cm/s and the density of the particle is approximately 2500 kg/m^3. The concentration of the flows vary with the flow height but takes a value of 5% on the average (Xu et al. 2002), which results in the reduced gravity acceleration g′ being about 0.74.

Using the information described above, Re_∞ and Re_ω are evaluated and equation (4.7.1) is solved numerically to yield r and θ for a range of flow front velocities and particle settling velocities. Figures 4.7(a) and (b) show the percentage change in the values of r_{Re} and θ as a function of the flow front velocity u_N for four different particle settling velocity (u_s = 0.001, 0.01, 0.1 and 1cm/s). The figures show that the larger particle settling velocity experiences a greater decrease in the values of r and θ. However, as the scale of the flow increases, r_{Re} and θ decrease because the shear decreases with an increase in velocity u_N. The maximum effect of the lift force on r for the range of particle settling velocity considered in this study is within 2%, implying that the effect of the lift force on the magnitude of the settling velocity of the particle is practically negligible in any scale of the flow. On the other hand, the value of θ reaches values as high as 12^o when u_N is the lowest, which implies that particle still experience a significant deflection in small-scale turbidity current. In addition, because the different particle settling velocity experiences different values

of θ, flows carrying polydisperse material will experience a horizontal fractionation with the heaviest particle being deflected the most.

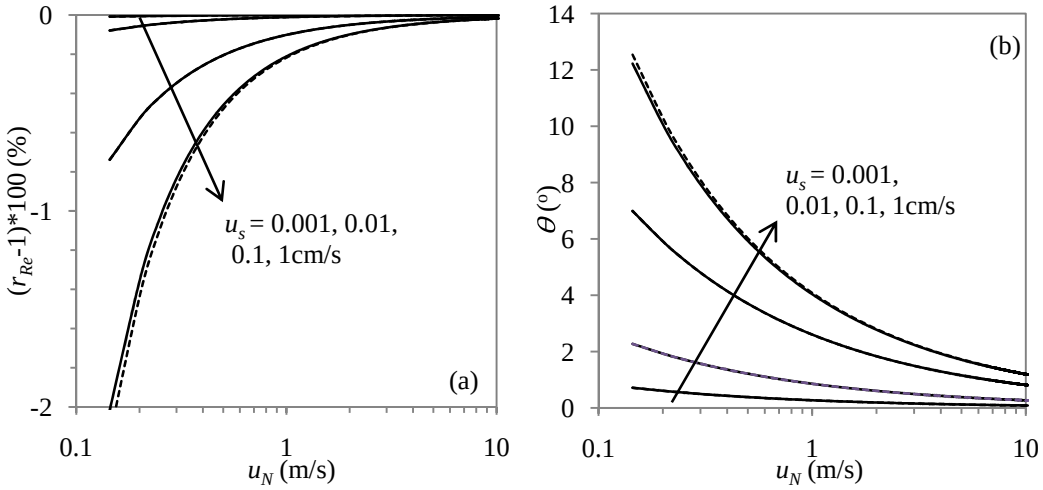

Figure 4.7 (a) Percentage change in r_{Re}, and (b) angle of deflection θ, as a function of the front velocityu_N of a gravity current travelling in deep water carrying particle with settling velocity of 0.001, 0.01, 0.1 and 1cm/s, assuming the reduced gravity acceleration g'= 0.74, Fr = 1.19 and particle-fluid density ratio $\rho_p/\rho_f = 2.5$. The corresponding particle diameter d_p for each aforementioned settling velocity are 11, 49, 160, and 520μm, respectively. The solid lines and the dashed lines represent the solution using BB and BL correlations, respectively.

4.4.3 Particle Entrainment

Stationary small particles that are embedded within the viscous sublayer of a turbulent boundary layer are subject to a shear-induced lift force that may cause the particle to re-suspend into the flow. For a particle to be lifted into the flow, the lift force needs to be greater than the net weight of the particle. Such a lift force is often parameterized as the critical shear stress. Experiments have been performed in the past to establish a criterion for particle entrainment by determining the flow critical shear stress required to entrain particles of different size.

The analysis presented here can be applied to provide another perspective on how particles are entrained from the bed, i.e. the amount of deflection experienced by particles when they are entrained into the fluid flow. To achieve this, we have used the experimental observations of Niño et al. (2003) on entrainment of particle in an open channel flow. The method we have used to estimate the deflection of the particle is described as follows. The shear within the viscous sublayer can be readily

deduced using the law of the wall function and the shear velocity u_τ of the flow given by the experiments. The shear can be estimated as follows:

$$\left(\frac{du}{dy}\right)_t = \frac{\omega}{2} \sim \frac{u_t}{h_t} \tag{4.9.5}$$

where h_t is the thickness of the viscous sublayer which is about 5, $y^+ \sim 5$, where $y^+ = h_t u_\tau / \nu_f$, and u_t is the velocity at the edge of the viscous sublayer, which is given by $u_t = 5u_\tau$ since $u^+ \sim y^+$, where $u^+ = u/u_\tau$. Having deduced the shear of the flow, the particle Reynolds number Re_∞ can be easily determined based on the particle size given by the experiment. Equation (4.7.1) is then solved to yield the deflection θ based on the values of Re_ω and Re_∞ determined from experiment. Since the particles lying on the bed are stationary, the particle has zero rotation and equation (4.7.1) is solved with $C_R = 0$. The result is plotted as a contour plot of θ that varies with Re_ω and Re_∞ as shown in Figure 4.8. The observations of Niño et al. (2003) comprise four different values of Re_∞. Each value of Re_∞ is applied with increasingly larger values of Re_ω until resuspension occurs (denoted by the circular symbol in the figure). It can be observed that increasingly higher values of θ are needed for particle of higher values of Re_∞ to be entrained, e.g. a particle with Re_∞ = 8 entrains at θ = 20°, whereas a particle with Re_∞ = 0.04 entrains at only θ = 5°. This suggests that the larger particles will entrain upwards into the flows whereas the entrained smaller particles are likely to hover near the bottom boundary. It should be noted that this conclusion is only valid for small particles immersed in a viscous flow and where the flow turbulence is negligible. The effect of the turbulence needs to be taken into account for the entrainment of particles larger than the size of the viscous sublayer.

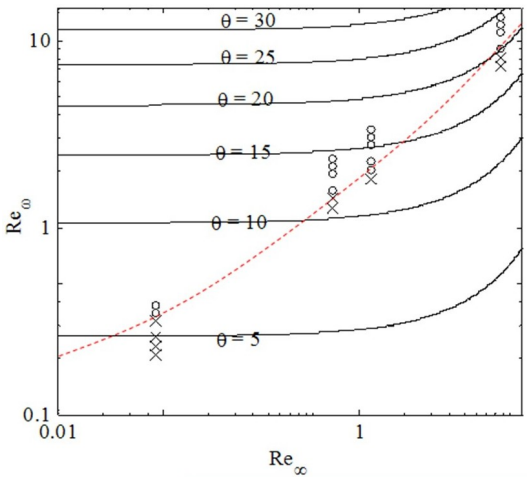

Figure 4.8 Contour plot of the prediction on the angle of deflection θ as a function of Re_∞ and Re_ω for particle entrainment. The experimental data of Niño et al. (2003) is included where the cross × represents where no entrainment occurs and the circle O represents where entrainment occurs. The red dashed-line shows the lowest value of Re_ω and θ for an entrainment to occur.

4.5 Conclusions

Simple expressions have been obtained for determining the particle slip Reynolds number Re_s and the angle of deflection θ of a freely-rotating sphere in a 2D shear flow. The expressions are valid over a wide range of values of Re_s. The expressions depend on a single non-dimensional quantity Λ, the lift number, which is defined by:

$$\Lambda = \frac{C_L Re_\omega + C_R Re_R}{\frac{3}{4} C_{D\infty} Re_\infty}$$

We have found that, for fixed values of Re_ω and Re_R, the slip velocity is always reduced by the lift force and this effect increases with an increase in the particle Reynolds number Re_∞. The angle of deflection θ is the highest when Re_∞ is small and decreases with an increase in Re_∞. The particle maybe pushed backward or forward, depending on the sign of the vorticity of the flows and the lift coefficient.

The results of the analyses are applied to turbidity currents and particle entrainment to study the effect of the lift force on the sediment transport in each case. In gravity currents, it is predicted that the larger particle sizes experience the greater angles of deflection than do small particles. This potentially could affect how the particles of different size fractionate within the turbidity currents. For particle entrainment, it is predicted that as the particle size increases then the particle is re-entrained at a larger angles to the main flow direction. It would be of interest to investigation this prediction experimentally.

Chapter 5

Physical and Numerical Modelling of Lock-Release Turbidity Currents

5.1 Introduction

In Chapter 3, the experiments of Gladstone et al. (1998), Gladstone & Pritchard (2009), and Rooij & Dalziel (2000) were modelled using the Mixture model with the inclusion of the turbulent dispersion term (TD) to the algebraic slip equation. However, the numerical results do not agree well with the experimental data. The model predicts an excessive dispersion that substantially decreases a flow's sedimentation rate and hence results in a greater amount of sediment being predicted in the distal deposit than observed in the experiment. This is consistently predicted for flows carrying different concentrations, grain size and flume geometry but the discrepancy is significantly greater for flows carrying finer grains. On the other hand, on excluding TD from the model, then the agreement of the CFD predictions with the experimental data improves significantly. This observation leads us to the following speculations, (i) turbulent dispersion (TD) is not important in this scenario so the term actually can be excluded from the model, or, (ii) essential physics are still missing in the model that acts to counter the dispersive effect manifested by TD, or (iii) the TD model is not appropriate in this scenario. It was though that point (ii) was the cause of the discrepancy and therefore, in Chapter 3, the discrepancy was further investigated by incorporating additional physics, i.e. the effect of turbulence modulation (TM) into the model. TM describes the suppression/enhancement of flow turbulence due to the presence of the particles in the flow. Small particles lead to a suppression of turbulence whereas large particles lead to an enhancement of turbulence. TM yields insignificant changes to the result and this prompts the conclusion that TM is not the important missing physics. It was then postulated that the particle lift force could be a major factor in influencing the particle settling characteristics, since gravity currents have a non-uniform vertical velocity profile. In Chapter 4, an analysis based on the force balance equation is carried out to

determine the relative significance of the lift force to the drag force in turbidity currents and it was found that the lift force only slightly reduces the magnitude of the particle settling velocity, but it also changes the particle settling trajectories. Very large particles in turbidity currents are likely to experience a maximum 2% reduction in its settling velocity and a maximum 10 degree change to the particle settling trajectories. For this reason, it is concluded that the lift force is not significant in turbidity currents.

The investigations carried out so far have been based on low volumetric concentration (0 – 2%) flows carrying fine sediment (12 – 70μm). While it is possible to continue to increase the level of sophistication in the model in order to determine the cause of the discrepancy, it may also be interesting to investigate the performance of the model at predicting the behaviour of the flows of higher volumetric concentrations (2 – 5%), carrying coarser material (>70μm). A literature search shows that there is a lack of documented experiments that investigate lock release configured turbidity currents in this regime. In addition to those referred to in Chapter 2, which mostly are low-concentration flows carrying fine grains, there are studies by Bonnecaze et al. (1993) and Hodson & Alexander (2010). The former reported two deposit profiles of flows of concentration (0.26%, 1%) and particle size (23, 53μm). The latter investigated the effect of flows carrying particles with different density (the flows they studied has 1% concentration and particle average diameter of 70 μm). For this reason, experimental investigations have been performed to study the effects of flows carrying mono-disperse suspension over a wide range of concentrations (0.25 – 5%) and grain size range (58 - 115μm) in order to validate the Mixture model over a wider range of initial conditions.

5.2 Objectives

The objective of this chapter is to perform a series of lock-release configured experiments to determine the front propagation and deposit characteristics of flows over a wide range of grain sizes and concentrations. The experimental data are then used to validate the Mixture model.

5.3 Experimental Technique

The experiments were carried out in the Sorby laboratory at the University of Leeds in a flume 5m long, 0.2m wide and 0.3m high (see Fig. 5.1(b)) and was made

entirely of plexiglass, as shown in Fig. 5.1(a), allowing direct observations of the flow from the sides and through the bottom. The top of the flume is open.

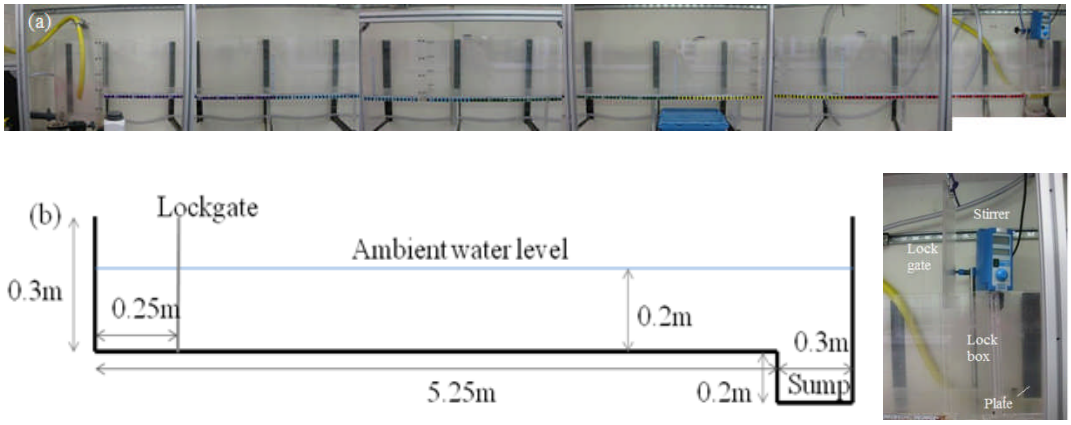

Figure 5.1 (a) Photograph showing the flume, the lock box (right end of the flume), a mechanical stirrer that is installed inside the lock box, and (b) a schematic diagram showing the dimensions of the flume and flume width is 0.2m.

The entire flume is supported by multiple stands made of steel that are attached to a vertical wall next to the flume. At one end of the flume (25cm from the end wall), the flume has vertical guides with a gap of 0.5cm for securing a lockgate. If the lockgate is inserted into the flume, a lock-box of volume $0.015m^3$ is formed. A weir is attached to the other end of the flume for collecting the over-flow during the experiment as well as draining out the water and sediment from the flume after the experiment is finished. A mechanical stirrer is placed inside the lock box to produce a uniform sediment suspension. The shaft of the stirrer has a diameter of 0.5cm and a propeller of diameter 3cm is attached at its end. The rotational speed of the stirrer is adjustable up to a maximum value of 2000 RPM (revolutions per minute). Using the mechanical stirrer results in a large circulation in the suspension mixture which is undesirable because it produces a large eddies that are characterised by the size of lock-box. In order to reduce this effect, a thin plate is attached to end walls of the lock box to break down the large circulation into a smaller irregular flow. Most of the experiments that have been conducted in the past (e.g. Gladstone et al. (1998)) employed a manual removal of the lockgate which gives rise to inconsistencies in the speed at which the lockgate is removed. The numerical investigation carried out by Giorgio-Serchi (2011) showed that the speed of the removal of the lock-gate and the size can profoundly affect the propagation of the flows. Waves are generated at the free surface when the lockgate is removed which causes alternating phases of

acceleration and deceleration in under-running turbidity currents. Slower moving lock-gate release causes waves of larger amplitude to form and hence larger perturbations of the velocity of the flows to develop. Thus, to avoid such complications, the lock gate is removed in a consistent and rapid manner for every run of the experiment to reduce variability and improve the repeatability of the experiments. For this purpose, a weight-driven pulley system is installed for removing the lock gate at a consistent speed.

5.3.1 Material Size

The material that is used in this experiment for creating a sediment suspension is glass beads (also known as Vaquasheen) acquired from the Wheelabrator Group Ltd. The glass beads have bulk density of 2650kg/ m^3 and can be described as reasonably spherical (Figure 5.2).

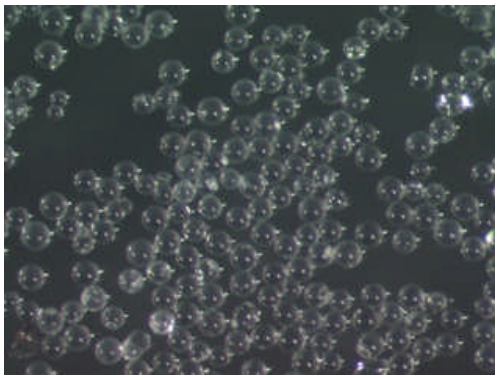

Figure 5.2 A microscopic image of a sample of the glass beads employed in the experimental investigation. Eighty % of the beads are spherical.

Three different size grades of glass beads (Grade 0-100, Grade 53-105, and Grade 75-150) were acquired from the supplier. The size distribution of each grade was determined using a Malvern Mastersizer 2000E grain sizer, which can measure materials within the size range of 0.1 to 1000 μm with a high degree of accuracy (±1% on the mean size). The Malvern Mastersizer is a laser diffraction system, which is a technique that has been widely accepted across a wide range of applications as a means of obtaining rapid, robust particle size data.

It should be pointed out that the Malvern still relies on its user to provide information on the nature of the sample (monodisperse or bidisperse) in order for it to accurately convert the light scattering data into the particle size distribution. The Malvern contains three mathematical models for calculating three different types of samples. The default model is called the General Purpose model, which is suitable

for calculating natural sediments which are generally coarser than those in laboratory flows (particle diameter greater than about 300μm). The second model is called the Single-Narrow model which is appropriate only for measuring a fine mono-disperse sample (particle diameter less than about 300μm). The last model is called the Multiple Narrow model which is intended for measuring samples that have more than a single peak in the size distribution (e.g. bi-modal materials). A study was carried out to determine the sensitivity of the results obtained in the different models. Figure 5.3(a) shows the measurements for the cumulative size distribution of Grade 0-100 and 53-100 using the General Purpose and the single-mode Narrow models. Indeed the latter model predicts a significantly narrower size range which is in better agreement with the information obtained from the supplier. Therefore our subsequent measurements are all performed using only the single-mode Narrow model. Also we found that only the Multi-Narrow model is able to determine bi-modal distributions. Thus, for cases where the nature of the distribution is not known, the Multiple Narrow model is preferred.

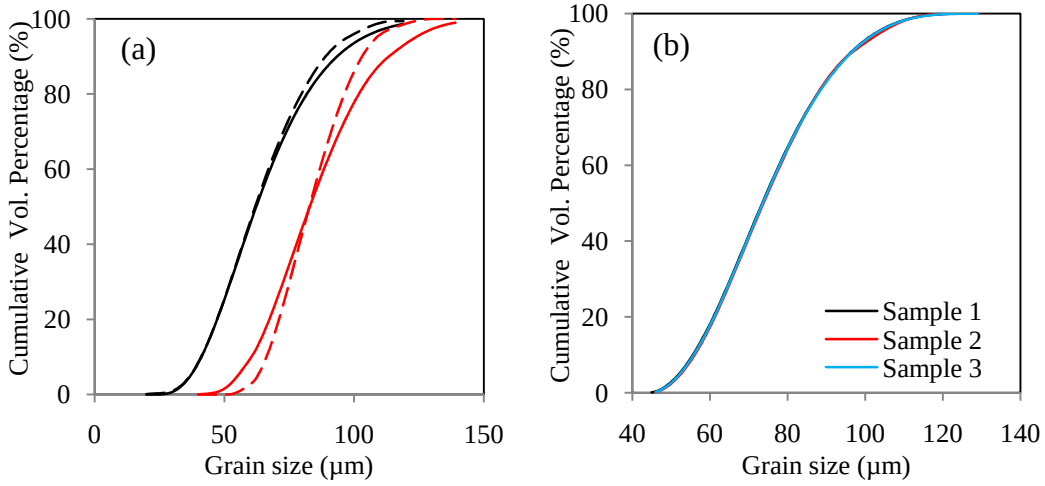

Figure 5.3 Cumulative volumetric percentage of (a) Grade 0-100 (black) and Grade 53-105 (red), that is calculated using the General Purpose model (solid line) or the Narrow model (dashed line), and (b) Grade 0-100 (2) taken from three different sub-samples, calculated based on the Narrow Model.

The size distribution of the three grades (0-100, 53-105, and 75-100) of glass beads were determined using the Malvern. Since two bags of Grade 0-100 were acquired, separate measurements were performed on each bag of glass beads. We have found that they have significantly different size distributions (their mean grain size differ by 10μm). Thus, the material from the second bag is named as Grade 0-100(2).

Figure 5.4(a) shows the cumulative size distributions of each grade. Although there are overlaps in the size range of different grade, all grades have a distinctive average size, standard deviation and mean settling velocity (see Table 5.1). The material from each bag is decanted into multiple smaller containers prior to use. As a result, there is a possibility that each container has a different size distribution due to size fractionation in the bag. To verify this possibility, separate measurements were performed on a grade of glass beads from different containers. Fig. 5.3(b) shows three measurements performed on Grade 0-100(2) from three separate containers; they all have similar size distributions. Thus this implies that the fractionation effects within the bag are unlikely to be significant.

Table 5.1 The size and hydraulic characteristics of each material investigated

Name	Mean diameter $\boldsymbol{d_p}$ (μm)	Standard deviation (μm)	Mean diameter's settling velocity, $\boldsymbol{u_s}$ (mm/s)	Mean settling velocity*, $\overline{\boldsymbol{u}}$ (mm/s)	$\boldsymbol{r_u}$= $\overline{\boldsymbol{u}}$/ u_s -
Grade 0-100	64.6	18.4	3.67	4.12	1.09
Grade 0-100 (2)	74.6	15.4	4.84	5.17	1.07
Grade 53-105	86.1	13.4	6.06	6.41	1.04
Grade 75-150	109	16.4	10.41	10.98	1.02
Sieved 45-63	57.9	7.9	2.92	3.07	1.02
Sieved 63-75	71.1	10.5	4.42	4.65	1.02
Sieved 75-100	86.7	9.6	6.6	6.86	1.01
Sieved 105-125	115.2	10.8	11.5	11.98	1.01

*$\overline{u} = \sum v u_s$ where v is particle volume.

It is worth commenting on the accuracy of the Malvern measurements. As mentioned above, the measurement obtained using the Malvern is accurate, given that the particles are all approximately spherical. Unfortunately, 20% of the material in this case is non-spherical and varies in shape (from slightly deformed to rod-like particle), which slightly alters the measured size distribution. While it difficult to determine the exact error incurred by the non-spherical particles (which requires knowing the size distribution of the non-round material), it is possible to assess the consistency of the error by repeating the measurement on any grade of glass beads. We have shown in Figure 5.3(b) that all the measurements from the three separate samples of Grade 0-100 (2) match well, and this implies that the error is consistent.

In addition, the results obtained from Malvern agree well with the information provided by the supplier, except for Grade 0-100(2), which are taken to indicate that the Malvern measurement is reliable.

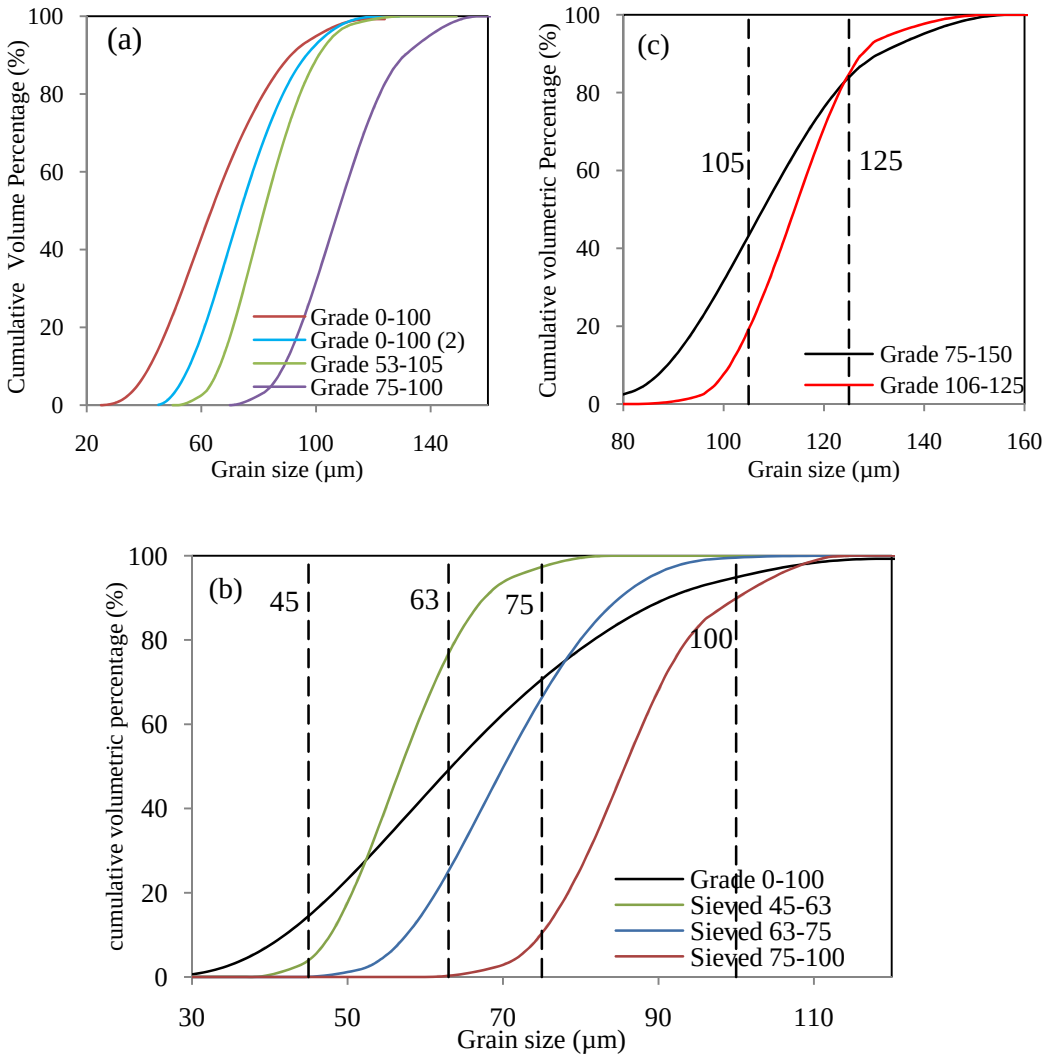

Figure 5.4 Cumulative volumetric percentage of the (a) original material (Grade 0-100, Grade 0-100(2) Grade 53-105, Grade 75-150), (b) the material sieved from the Grade 0-100 (sieved 45-63, 63-75 and 75-100), and (c) the material sieved from Grade 75-150 (sieved 106-125), as a function of the grain sizes, determined using the Malvern Mastersizer 2000E. The vertical dashed-lines represent the sieve sizes.

In order to obtain more material with different mean sizes, the original materials were sieved through different interval sizes. Grade 0-100 was sieved through grid sizes 75, 63 and 45 μm (first 75μm, followed by 63μm and finally 45μm) to create three sub-distributions of different sizes, collected on the 75μm, 63μm, and 45μm sieves respectively. For convenience, they are named according to their sieve sizes, namely Sieved 75-100, Sieved 63-75 and Sieved 45-63, respectively. Grade 75-150

was sieved through a 125μm sieve, and then a 106 μm sieve to create a relatively coarse material. The material collected on the sieve 106 is named as Sieved 106-125. All sieving was performed manually. It worth mentioning that in this case manual sieving is found to be significantly more effective than sieving via a shaker (which is a more convenient method) because the glass beads are prone to become trapped in the sieve mesh and thus block any smaller material that still remains in the sieve from passing through thus resulting in the sieving being ineffective unless the trapped sediment is cleared. An effective sieving can only be achieved by constantly clearing the trapped sediment from the sieve, and it is more convenient to do this by manual sieving than in the shaker which requires the unloading and reloading of the sieve back into the shaker.

All the sieved materials were analysed using the Malvern Mastersizer to determine their size distribution. Figure 5.4 (b & c) shows the cumulative size distribution of the Sieved 45-63, 63-75, 75-100 and 106-125. It can be seen that the Sieved 45-63, 75-100 and 106-125 have 10-20% of sediment that falls outside of the upper and lower sieve size domain. This indicates that some of the materials that are finer or coarser than the size of the sieve are still present in the sieved material. This is likely to be due to the combination of the incomplete sieving and the slightly inaccurate representation of the actual size distribution of the particles due to the fact that the material has non-spherical particles. In addition, it is surprising to find that the sieved 63-75 has more than 30% of sediments that falls outside of its upper and lower sieve size and this means that there is only about 40% of the material that has a size within the sieve size range. Nonetheless, sieving results in a smaller size standard deviation and the ratio of the settling velocity of the material to that of its average diameter (see Table 5.1).

5.3.2 Experimental Procedure

Designing the experimental procedure largely depends on the kind of measurements that need to be taken during the experiment. In this work, three types of measurements are taken, namely the propagation of the front of the flows, the deposit thickness profile of the flows and the deposit grain size characteristics.

The measurement of the propagation of the front of the flow is relatively simple. The only equipment needed is a video camera, which is placed on an arm that is

movable alongside the flume. During the experiment, the arm is manually moved according to the speed of the flows. A length scale which is placed on the surface of the flume is recorded as well. From the video, the propagation of the flows can be easily determined by identifying the position of the front of the flow through the length scale and the time elapsed since the release of the flows. Fig. 5.5 shows an example of the flow recording taken from a video camera. To aid the visualisation of the flows, the back of the flume is covered with black paper (the suspension of glass beads is white in colour).

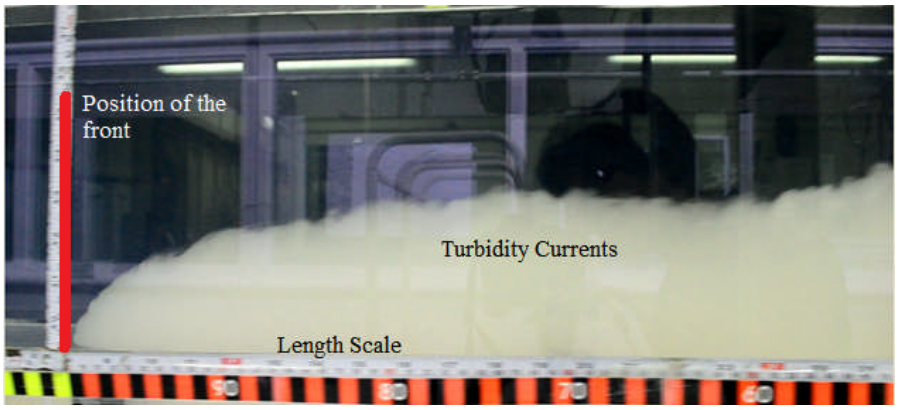

Figure 5.5 An image of the front and body of a turbidity current as captured using a camera.

The deposit characteristics of the flows can be measured after the flow has terminated and all its sediments have settled. There are three essential elements of a deposit of a turbidity current, i.e. the thickness, size distribution and the vertical structure of the particle size. In this case only the first two elements are important since the deposit is too thin to yield any meaningful information regarding vertical stratification. It is worth discussing the existing methods for measuring the deposit's thickness. The most convenient method is by using advanced equipment such as a sonar scanner which detects upper surface of the bed measuring via the time difference between sending and the receiving a sonar wave. Human error is small in this method and the profile of the entire bed can be determined. However, at the distal end, the bed is very thin and the sonar scanner can be inaccurate. Thus we resort to the conventional approach that has been adopted in previous experiments on lock-release flows, which is to determine the mass of the deposit from a fixed sampling area (Gladstone et al., 1998) which corresponds to the thickness of the bed. This technique is performed by inserting a hollow cylinder into the bed deposit and then extracting the sediment enclosed within the cylinder via a pipette. This

procedure is performed at multiple downstream distances and the extracted mass is stored in separate pots. Then the pots, which contains the wet sediment, are left to dry in the oven before their weight is determined. The advantage of this approach is that it is accurate since only small amount of the sediment is lost during the extraction. The disadvantage of this technique is that it is somewhat laborious if there are many locations to be measured. More recently, Rooij & Dalziel (2001) have devised a more sophiscated method based on electrical resistance that not only measures the deposit thickness but also the rate of the deposition during the development of the flows. While this method is clearly more superior to the extraction method, its setup is complicated and expensive and it has not been employed in this work.

To determine the grain size of the deposit, we resort to analysing the size distribution of the extracted deposit using the Malvern Mastersizer. The procedure in using the Malvern has been discussed in the previous section. The important step that needs to be taken note of is that the dried sediment needs to be rehydrated before it can be analysed using the Malvern Mastersizer. The purpose of doing this is to break up any particle agglomeration that occurs when the particles are dried and thus returning the sample to its original state of condition. An alternative approach for determining the size distribution was employed by Barker (2005) where he extracted a solidified deposit and then analyse its structure through a scanning electron microscope. However, this approach is considerably more complex and time consuming and therefore it has not considered in this thesis.

It is important to outline the details of the exact sequential steps taken during the experiment and these are described as follows:

i. Flume Cleaning and Water Filling. First, the flume is flushed with water to remove any dirt from the flume. After that, the flume is filled with tap water to a depth of 0.2m.
ii. Video camera, material and lock-gate. The video camera is switched on. The amount of material needed for the experiment is determined using a scale. The lock gate is inserted into the flume and the weight connected to the lock-gate is locked and suspended to prevent it from pulling the lock-gate up.
iii. Stirrer, mixture suspension, lock-gate release, video-recording. The stirrer is switched on and the speed is adjusted to 1500 RPM. The sediment is then poured

into the lock box and is allowed to be stirred for a duration of 20 to 30 seconds. After that, the stirrer is switched off and without any delay, the weight is release to pull the lock gate out from the flume. Then the camera is manually moved to record the advancement of the head of the flow. The recording is performed until the flows have terminated.

iv. Bed thickness sampling. After the recording has been completed, the flume is left untouched for 5-10 minutes to allow all fine materials that are still suspended in the ambient water to completely settle. After that, the pipe at the weir is opened to partially drain the water out from the flume. Then the bed is ready to be sampled. The sediment is extracted from the bed for every 10cm downstream locations along the central plane of the bed, from the inside of the lock box to the termination point of the flow. The extracted sediment is transferred to a separate pot. The pots with wet sediments are placed in the oven for drying. After the sediments are dry, they are weighed to determine the mass of the sediment.

v. Bed grain size measurements. The dried sediment is rehydrated with tap water and stirred vigorously for a few minutes. The mixture is then analysed using the Malvern Mastersizer 2000E to determine the size distribution.

5.3.3 Measurement Technique Verification

It is important that verification is carried out to ensure that the initial conditions for the experiment are well-constrained and the adopted measurement techniques are reliable and accurate. One important aspect of the initial conditions that needs to be verified is the concentration of the mixture in the lockbox. It is assumed that the mixture is in a uniform suspension before it is released. Hence, the stirring operation confirm to produce a uniform suspension in the lock box. We carry out this verification by employing the highest mass concentration (5%) and the coarsest particle (168μm) and a mixing speed of 1500RPM. If a uniform concentration can be attained with the coarse material, then it is reasonable to assume that a similar uniform mixture can be achieved with lighter particles and flows with smaller concentrations. After the mixture is prepared, some mixture in the lock box is extracted at intervals of 2cm from the bottom to the top of the lock box using a syringe. The extracted mixture is then transferred into separate pots and weighed. The clear water in each pot is drained out and the wet sediment left in the pot is left

in the oven for drying. After that, the weight of the dried sediment is determined and the mass concentration can then be determined by dividing the weight of the dried sediment over the weight of the mixture. A typical mass concentration of the suspension at the eight vertical positions is shown in Fig. 5.6. It can be observed that the concentration suspension is quite uniform across its height and this leads us to conclude that the stirrer has sufficient power to produce a uniform suspension.

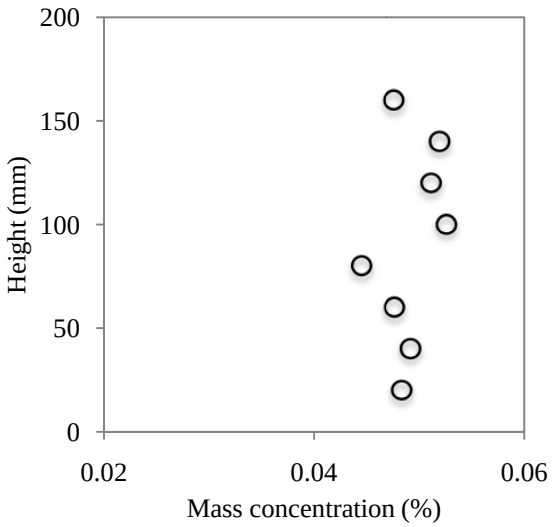

Figure 5.6 A typical mass concentration as a function of the height in the lock box of glass particles; samples taken from a suspension carrying particles with mean diameter 168μm that are stirred in the lock box with a rotational speed = 1500RPM. Samples taken 5cm from the side walls.

The accuracy and reliability of each measurement technique described in the previous section needs to be tested. The simplest way to determine the reliability of the measurement technique is by repeating similar measurements on two or more separate experiments with similar initial conditions and then to compare the measurements taken from each run. Three experiments with an initial mass of 750g of Grade 0-100 were carried out and their front propagation, deposit mass density and deposit grain size characteristics determined. Fig. 5.7(a – c) shows the rate of propagation of the front of the flows, the deposit mass density profile, and the deposit grain size profile (d20, d50, and d80) that are measured from the three runs. It is observed that, in general, very good agreement is obtained between the measurements taken from the three separate runs. A further two runs were performed on flows with an initial mass 1000g and material Grade 0-100 (2) and flows with initial mass 750g and material Grade 53-105 to determine their front propagation. Fig. 5.8(a & b) shows the measurement from two runs on the front propagation of the two aforementioned flows. Again, the two sets of results are found to be in good agreement. This shows that all the employed techniques are robust and the experimental results are repeatable using the same initial conditions.

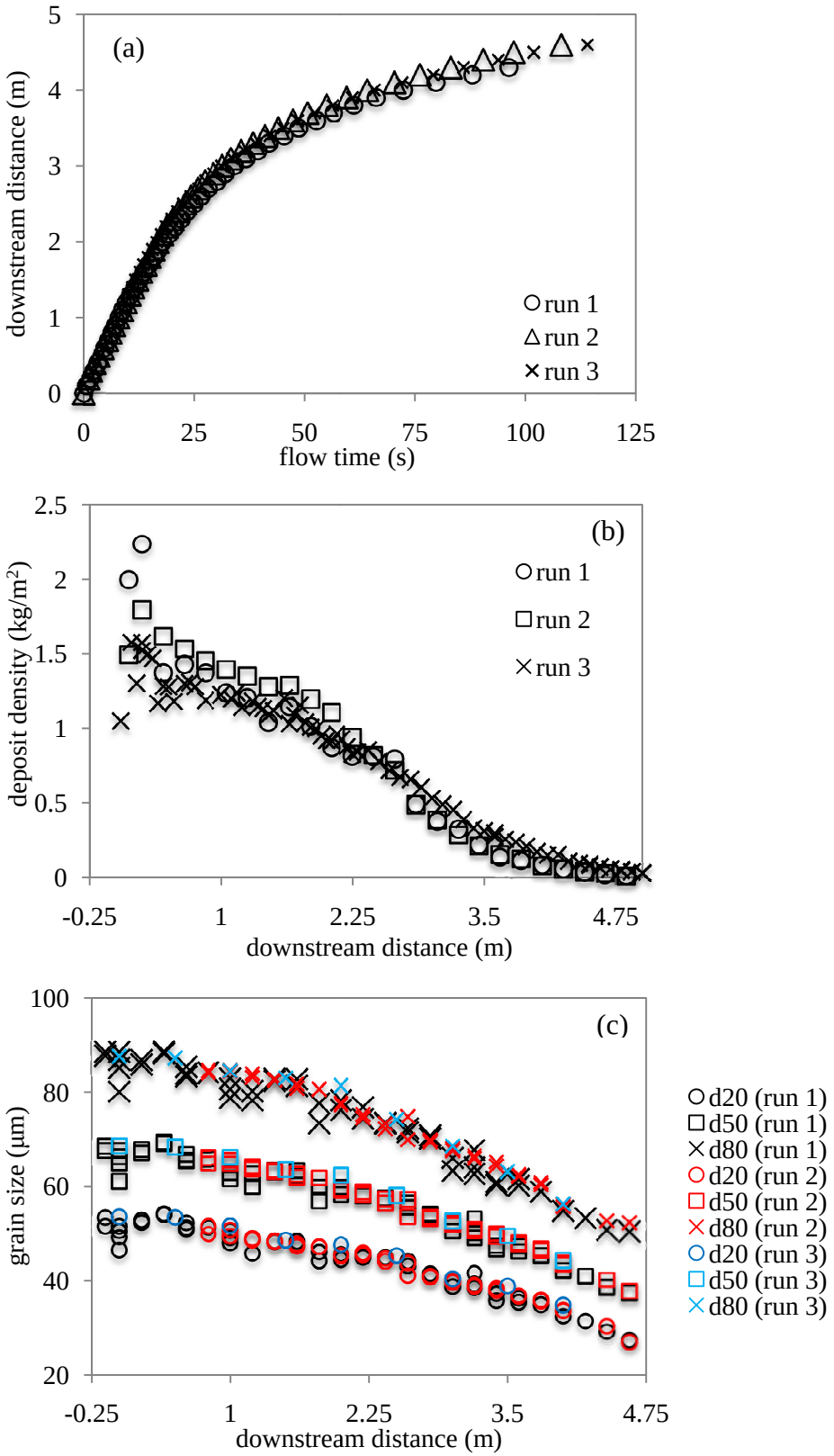

Figure 5.7 (a) The rate of propagation of the front of the flows, (b) the deposit density profile, and (c) and the deposit grain size (d20, d50, d80) profile, of three gravity currents (runs 1, 2, & 3) carrying 750g of material Grade 0-100. d20; d50 and d80 represent the 20th, 50th and 80th percentile in the particle's volumetric concentration distribution. The location of the lockgate is considered as the starting point (x = 0).

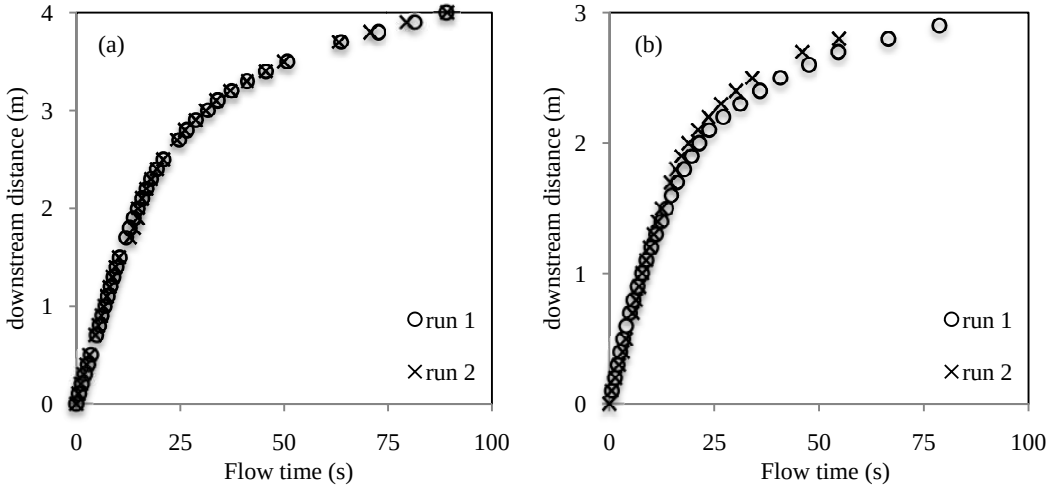

Figure 5.8 The rate of propagation of the front of the flows from two runs each of (a) 3.8% (1000g) Grade 0-100(2), and (b) 2.8% (750g) Grade 53-105.

5.4 Experimental Programme

Fifteen flows with different initial conditions were investigated. Eight of them have similar initial concentrations 2.8% (initial mass of the material is 750g) but has different size range and average size (each material as listed in Table 5.1). For convenience, they are named after the size range (original or unsieved material is named as UNS, which implies that the flows have a large size range, whereas the sieved material is named as S which implies that the flows have a small size range), followed by the average size of the material. These eight flows are grouped under Series A. Table 5.2 summarises the material used, the type of measurements taken and the run-out distance in each flow for Series A. The other seven flows have similar material (Grade 0-100(2)) but differ in concentration (ranging from 0.27% - 5%). Each flow is given a name according to its concentration. Table 5.3 details the concentration used in each flow, the measurement that has been performed and the run-out distance of the flow for Series B. It should be noted that flow C28 is equivalent to UNS74 (it has been renamed to avoid confusion). It is interesting to compare the initial conditions for the flows studied in the previous experiments to those in the current investigations. The details of the five flows that are used to validate the Mixture model in Chapter 2 are given in Table 5.4. Since they may be referred to in the discussion of the subsequent sections, it is convenient to group these flows as Series C. Figure 5.9 shows a comparison of the Stokes settling velocity of the particle used in the Series A and C. All the particles in the Series C have a settling velocity smaller than the particles used in Series A and B do, except

for flow G69. In addition, the concentration of the flows in Series C is considerably low, which is equivalent to the two lowest concentrations considered in Series B.

Table 5.2 Series A Experiments

Flow	Material	Measurement*	Run-out distance (m)
UNS64	Grade 0-100	P, DM, DS	3.85
UNS74	Grade 0-100 (2)	P, DM	3.05
UNS83	Grade 53-105	P, DM	2.35
UNS109	Grade 75-150	P, DM	1.95
S58	Sieved 45-63	P, DM, DS	4.05
S71	Sieved 63-75	P, DM, DS	3.25
S87	Sieved 75-100	P, DM, DS	2.55
S115	Sieved 106-125	P, DM, DS	1.85

*P = front propagation, DM = deposit mass areal density, DS = deposit grain size

Table 5.3 Series B Experiments. Each flow used Grade 0-100(2)), but in differing initial concentrations.

Flow	Volume, % (mass,g)	Measurement*	Run-out distance (m)
C025	0.25 (70g)	P, DM	1.25
C050	0.5 (130g)	P, DM, DS	1.55
C100	1 (260g)	P, DM, DS	1.95
C150	1.5 (390g)	P, DM	2.2
C200	2 (540)	P, DM	2.55
C280	2 (750)	P, DM	3.05
C380	3.8 (1000g)	P, DM	3.2
C500	5 (1300g)	P, DM	3.55

Table 5.4 Series C Experiments.

Flow	Concentration, % (mass, g)	Particle mean size, μm	Reference
G69	0.35 (180)	69	Gladstone et al. (1998)
G25	0.35 (180)	25	Gladstone et al. (1998)
G37	2 (96.5)	37	Gladstone & Pritchard (2009)
G13	2 (96.5)	13	Gladstone & Pritchard (2009)
D37	0.275 (60)	37	DeRooij & Dalziel (2000)

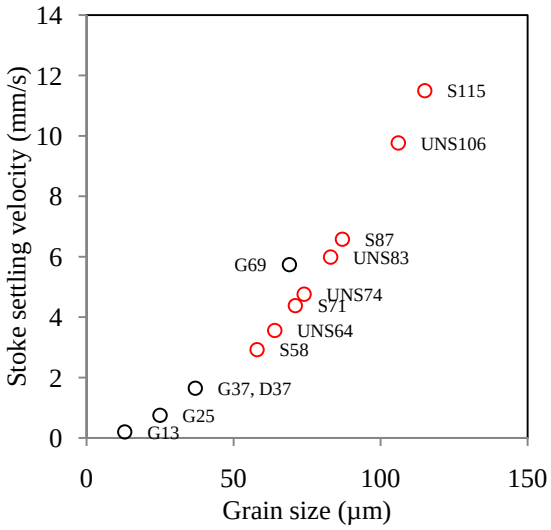

Figure 5.8b The Stoke settling velocity of the particles used in Series A (red circle) and Series C (black circle) as a function of the particle sizes.

5.5 Experimental Result and Discussion

5.5.1 Flow Images

The difference in the appearance of the flows at different concentrations and carrying different grain sizes is discussed in this section. Figure 5.9 shows a photograph of the head and the body of the Series A flow S58 at t = 10, 20, 30 and 40s. At t = 10s, the head of the flow is characterized as having a sharp tip that is located very close to the lower boundary, and behind the tip, the thickness of the flows gradually increases. Further, the surface of the flow consists of multiple billows that appear due to the turbulent shear between the rapidly advancing flow and the quiescent ambient fluid. These billows are known as the Kelvin-Helmholtz instabilities. It can be seen that the colour of the flow is uniformly white, which suggests that the flow everywhere exceeds the necessary concentration threshold. This also suggests that the sediment is well-mixed within the flow and this is presumably due to the strong turbulence and swirl within the flow. At t = 20s, the size of the billows on the surface of the flows has increased, and the number of billows is reduced. This indicates that the intensity of the Kelvin-Helmholtz instabilities has reduced, and this is possibly due to the decrease in the turbulence within the flow and also the decrease in the speed of the flow. In addition, the intensity of the colour at the back of the flows has reduced and this indicates that concentration stratification maybe significant. At t = 30s, the number of the billows on the top of the flows has decreased, and this may indicate a further dissipation in the turbulence. Also, the intensity of the colour is further reduced, indicating that the

flows have lost a significant amount of sediment through deposition. The reduction in the colour intensity with the increase in the flow height strongly suggests that sediment stratification has developed at this stage. This is possibly because the turbulence intensity in the upper part of the flows has became lower than that in the lower part of the flow, and consequently the upper part of the flows has lesser capacity to keep the sediment in suspension than that in lower part of the flow. Further, the sediment stratification could possibly be due to turbulent diffusion, which is a mechanism that acts to disperse the sediment away towards a lower concentration region, analogous to the turbulent diffusion observed in substrate flows. At t = 40s, the tip of the flows have became blunt and a thin layer of low concentration flow has appeared at the top of the flows. As a result, the flow concentration stratification in the body of the flow is also thought to have increased.

The flow carrying coarser material (S115) evolves in a similar manner as that described above but its transformation from the turbulent-mixing stage to the diffusion stage appears faster than that of the flow S58 which is assumed to be due to its higher rate of deposition. As depicted on Figure 5.10, the flows are turbulent at t = 5s and 10s but appear to have experienced significant diffusion at t = 15s. This shows that the decay in the turbulence in this flow is significantly faster than that in flows S58. By the time t = 20s, the flow has already lost most of its sediment and it is close to its termination. Other flows from Series A, which have particle sizes between that of S58 and S115, exhibit characteristics that lie between the extreme shown by the results of S58 and S115.

The flow of low-concentration C050 of Series B, contrary to the above description, apparently already exhibits strong turbulent diffusion at early times as shown in Figure 5.11 (t = 10s). This is thought to be because this flow is relatively slow and hence results in the turbulence mixing being ineffective. Without mixing, the slow expansion of the size of the flows may be enhanced by the molecular diffusion. As the time elapses, the turbulence decays and the size of the flows also reduces (see t = 20, 30 and 40s in Figure 5.11).

In summary, any surged-typed fixed volume turbidity currents may go through the following three phases:

i. A rapid elongation of the flow accompanied with vigorous turbulent mixing or swirl within the flows, which results in a uniform concentration within the flow. Highly irregular surface features (Kelvin Helmholtz instabilities) appear on the upper boundary of the flow and is caused by the intense shearing between the rapidly advancing flows and the quiescent ambient flows.
ii. A decrease in the number of billows at the top of the flows which implies a decrease in Kelvin Helmholtz instabilities, and the onset of the sediment stratification, is possibly due to the decrease in the flow turbulence intensity.
iii. The overall flow concentration decreases due to the sediment deposit. Stronger concentration stratification develops, possibly because the turbulence in the upper part of the flows has significantly decreased, and also turbulence diffusion may be responsible for increasing the migration of the sediment towards lower concentration region.

The grain size and concentration may affect the duration of each phase. Turbulent mixing is less effective in low-concentration flow due to the low velocity or flows carrying coarse grain due to the large particle settling velocity.

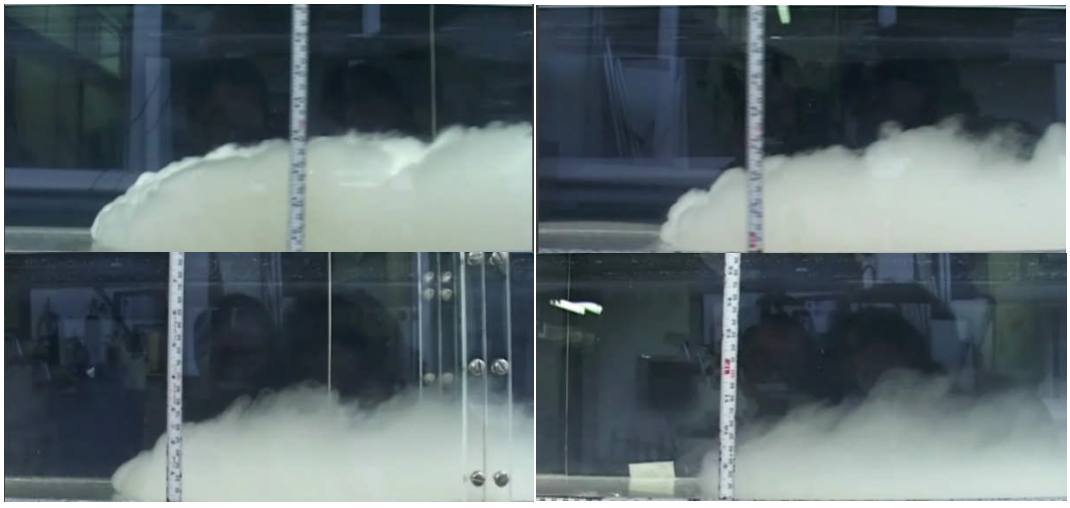

Figure 5.9 Photographs showing the flow of S58 from Series A at t = 10, 20, 30 and 40s (top left, top right, bottom left, bottom right, respectively).

Figure 5.10 Photographs showing the flow of S115 from Series A at t = 5, 10, 15 and 20s (top left, top right, bottom left, bottom right, respectively).

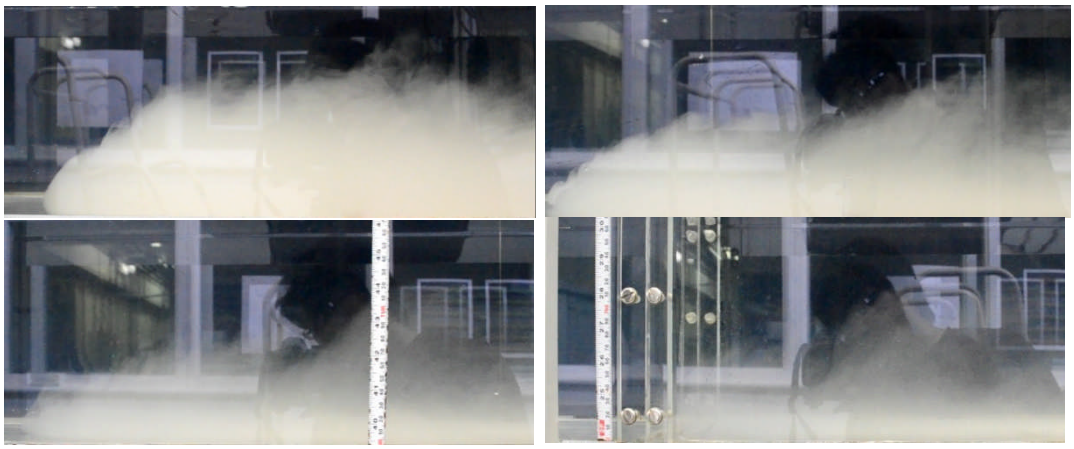

Figure 5.11 Photographs showing the flow of C050 from Series B at t = 10, 20, 30 and 40s (top left, top right, bottom left, bottom right, respectively).

Figure 5.12 Photographs showing the flow of C500 from Series B at t = 5, 12, 23, 58 (top left, top right, bottom left, bottom right, respectively).

5.5.2 Front Propagation

Figure 5.13(a) shows the rate of the propagation of the front of the flows of Series A. All flows initially have a similar propagation speed, which is not surprising since

all flows have similar concentration and the initial velocity of the flows is determined by the initial buoyancy force of the flows. It has been established that the initial velocity of the front of a gravity current u_f is described by the relation (e.g. Benjamin, 1968): $u_N = Fr\ (g'h)^{0.5}$ where Fr is the Froude number, h is the flow height and g' is the reduced gravitational acceleration (see equation 2.1). As the flows propagate forward, the front of the flows lose the buoyancy force through sedimentation but more material is continuously being fed from the body of the flows to replenish the loss. At one point, when the flow has lost most of its sediment, such that the loss of the sediment at the front of the flow exceeds the feeding rate from the body of the flows, the speed of the flows starts to decrease. This is the moment that the effect of grain size on the speed of the flows is manifested. Clearly, the coarser material the flow carries, the earlier a flow experiences a decrease in speed. As shown in Fig 5.13(a), flows S115 and UNS109 are the first to experience a divergence from (i.e., their speed becomes slower than) the rest of the flows at t = 15s. This is followed by UNS83, S87, UNS74, S71, UNS64 and S58, which carries the finest material and has the largest propagation distance in Experiment A. In addition, the decrease in the speed of the flows becomes more gradual for flows carrying finer material. As shown in Fig 5.13(a), flow S115 comes to an abrupt end, whereas flows UNS64 decrease slowly. This reflects the important role of the turbulent diffusion has on flows carrying fine material. Turbulent diffusion disperses the fine materials upwards, reduces the flow sedimentation rate and extends the propagation of the flows.

An interesting characteristic was noted in the propagation profile of S58. It gains speed at t = 20s which makes it propagate significantly further than UNS64 despite its average size being only slightly smaller than that of UNS64, although S58 has a smaller size range. The reason for this phenomenon is unclear and can only be speculated about. It is possible that some of the deposited material has been re-entrained into the flows which give the flow an additional buoyancy force to propagate further. In addition, it is possible that the turbulent diffusion has dispersed some sediment upwards and thus reduces the rate of deposition from the flow once turbulent mixing ceases to be effective.

The effect of the concentration on the rate of the front propagation profile of the flows is shown in Figure 5.13(b). As expected, the discrepancy between the flows in

this case is more pronounced since the concentration controls the initial velocity of the flows. Higher concentration flows have a greater initial velocity than do the lower concentration flows. In addition, increasing the concentration extends the run-out distance of the flows although the effect appears to diminish at higher concentrations. For instance, increasing the concentration from 0.25 to 1%, increases the run-out distance x_r by 1m whereas increasing the concentration from 3.8 to 5% only extends the run-out distance by no more than 0.5m. On the other hand, varying the concentration does not change the length of the duration of the flow as significantly as varying the grain size does. Increasing the concentration of the flows only slightly increases the length of the duration of the flows and this is thought to be because the influence of the turbulent diffusion increases with a decrease in the concentration of the flow. As shown in the previous section, flow C050 appears to exhibit very strong dispersion of particles at early times and this is not observed in higher concentration flows. Another observation that is worth mentioning is that flows with different concentrations exhibits rather similar speeds after their initial speed has reduced.

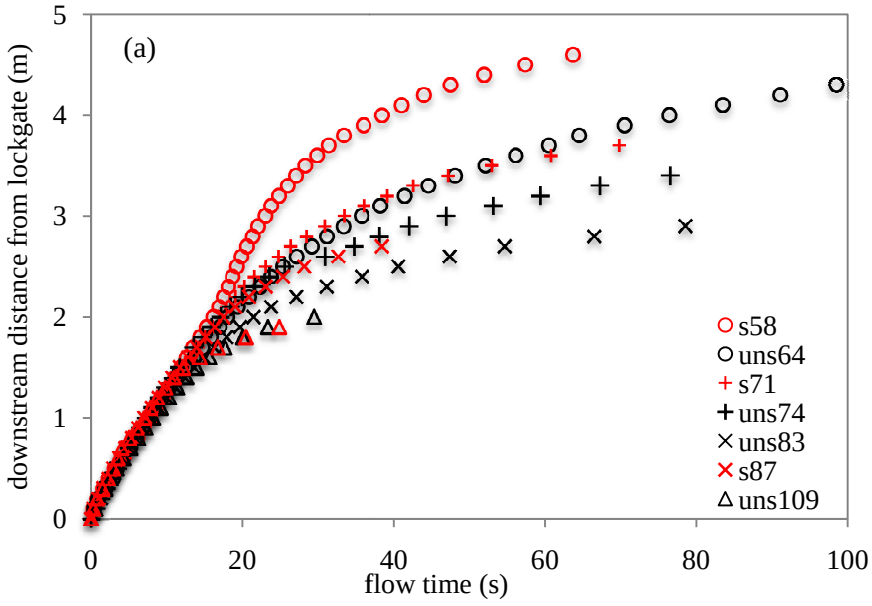

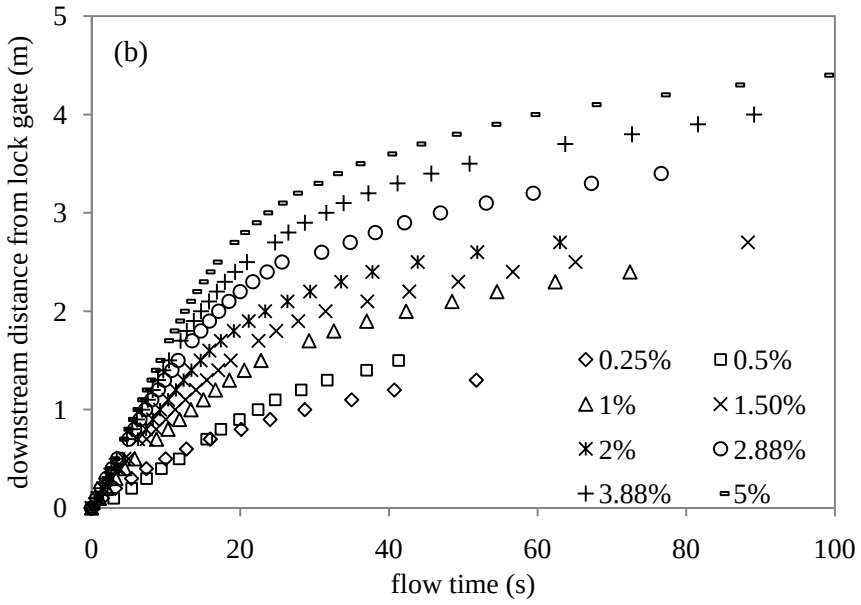

Figure 5.13 The rate of propagation of the front of the flows from (a) Series A, and (b) Series B.

5.5.3 Deposit Mass Density

Fig. 5.14 (a & b) show the deposit mass density profile of the flows from Series A. All flows exhibit a longitudinal profile of decreasing mass, except for the deposit inside the lock box where an initial increase in mass is shown by some flows. As a flow propagates downstream, it loses its mass and its rate of deposition also decreases. Thus it is not surprising that the mass density decreases downstream. Also, since gravity currents evolution approximates to a series in of rectangular shapes in a horizontal channel of greater length and lower height, the duration of the flows upstream is longer than that at the downstream. Therefore naturally the flow deposits more mass at the upstream than it does at the downstream. On the other hand, the reason why the deposited mass inside the lock box initially increases is less obvious, because the flow inside the lock box is influenced by the removal of the lock gate and the initial conditions and these effects may vary with flows carrying different grain sizes. The reason may well be because some deposited materials are entrained back into the flows. The difference between the flows in Series A is clear. Flows carrying coarse material have a large deposit mass upstream but low deposit mass downstream whereas the flows carrying fine material exhibit the opposite effect. The reason for this is because the coarse particles have a large settling velocity. A difference can be noted between the deposit profile of the flows carrying coarse material and that of fine material. The profile of the former is almost

a single straight line (S87, S115, UNS109) whereas for the latter (i.e. S58, UNS64), it consists of two straight lines with different slopes.

The deposit mass density of the flows of different concentrations (Experiment B) is shown in Fig. 5.14(c). Similar to the flows in Experiment A, all the flows exhibit an almost linearly decreasing profile from the location of the lock-gate to the termination point of the flow. The effect of the concentration is such that increasing the concentration of the flows increases the deposit mass everywhere. Thus, there is no overlap between two profiles of flows with different concentration. This is consistent with the theory that the higher concentration resulst in a greater deposition rate and therefore a greater deposit mass. The interesting effect of the concentration is again the change in the shape of the deposit mass profile for high concentration flows. The deposit mass profile of low concentration flows (0.25 – 2%) exhibits an almost straight line decrease whereas that of flows with concentrations greater than 2% has two decreasing straights lines (the second line is steeper than the first line). The greater the concentration the clearer the deposit profiles divides into two parts (see the result for concentration 5%). A red dashed line is placed on Fig. 5.14(c), which is at about x ~ 2m (about the first half of the deposit), to mark where the line changes its slope. Also, two separate straight lines

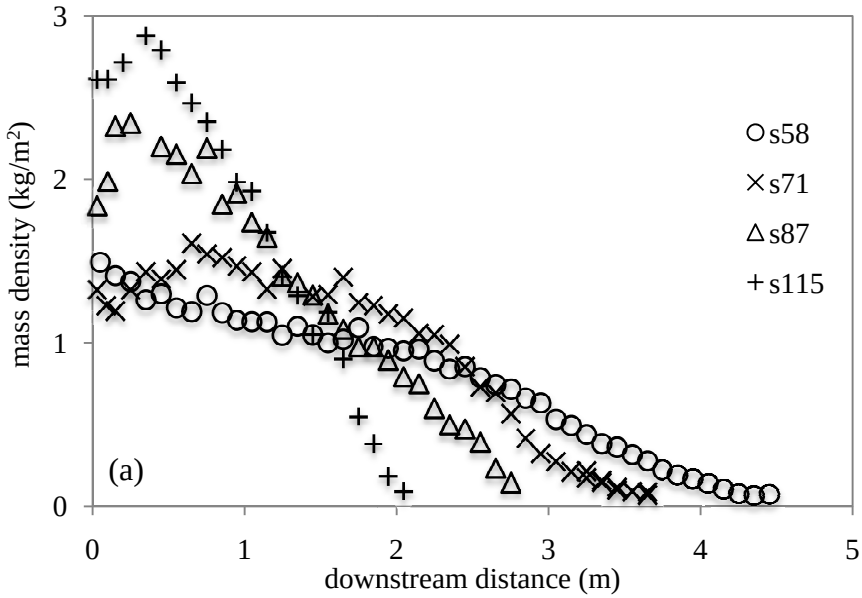

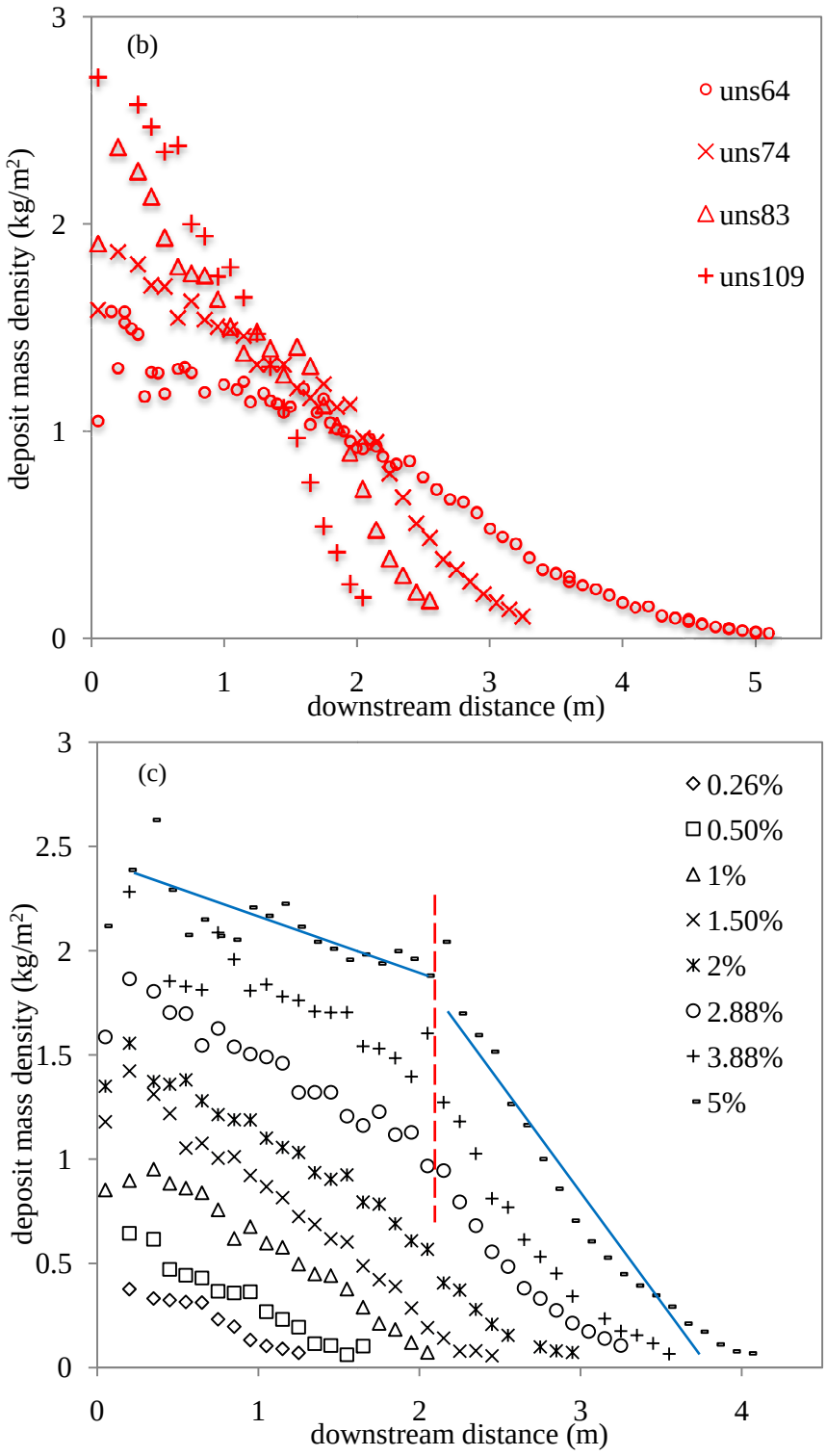

Figure 5.14 The deposit mass density as a function of the downstream distance from the end wall from (a & b) Series A, and (c) Series B. The blue lines are the approximations to the deposit of flows 5% and the red line marks the location where the flows experience an abrupt decrease in the deposit mass.

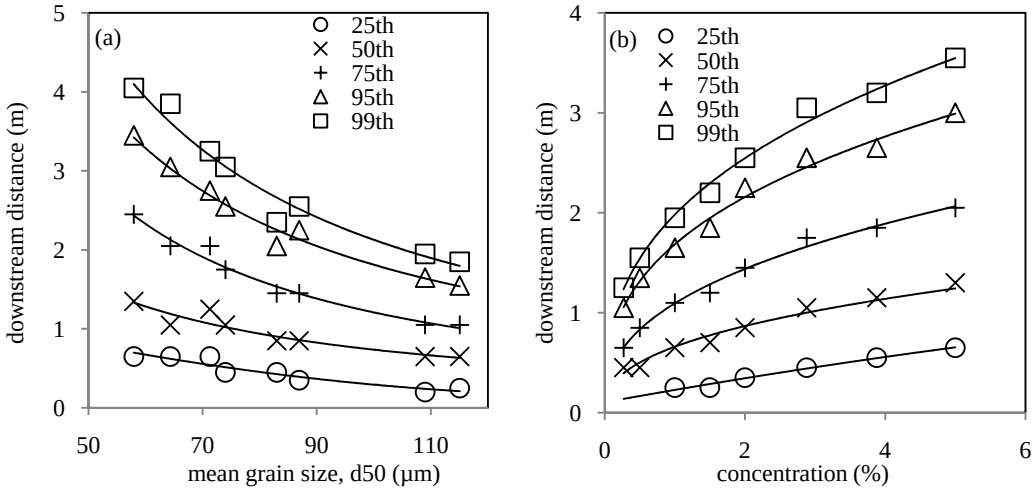

Figure 5.15 The distance from the lock gate for the 25th, 50th, 75th, 95th and 99th percentile of the deposit mass distribution as a function of (a) the mean size of the material carried by the flows from Series A, and (b) the initial volumetric concentration of the flows from Series B.

are drawn on the profile for the flows of 5% concentration and the trend in the results suggests that the effect could be yet more pronounced in flows with concentration greater than 5%. The implication that can be drawn from this observation is that as the concentration of the flows increases, a greater proportion of material will be deposited upstream.

It is possible to synthesise the results of Experiments A and B into a more meaningful result. To better illustrate the influence of the particle size and concentration on the deposition, the positions of the 25th, 50th, 75th, and 99th percentile of the deposit mass density of the flows (denoted as P25, P50, P75 and P99 hereafter) from Experiments A and B are plotted as a function of the particle average size and the particle concentration, as shown in Fig. 5.15 (a & b), respectively. It can be observed that the P25, P50, P75 and P99 decrease with an increase in particle size, linearly for P25 and P50, but exponentially for P75 and P99. This result implies that the run-out distance increases exponentially as the grain size decreases. On the other hand, increasing the concentration of the flow increases P25, P50, P75 and P99, linearly for P25 and P50 and convexly for P75 and P99. The results suggest that there is a threshold where increasing the concentration no longer increases run-out distance of the flows.

5.5.4 Deposit Grain Size Distribution

In this section, we describe the deposit grain size distribution of several flows from Series A. The left hand side of Fig. 5.16(a – e) shows the actual grain size distribution in the deposit of the flows UNS64, S58, S71, S87 and S115, respectively, at multiple selected downstream distances. It can be observed that only flows UNS64 exhibit a grain size distribution that change significantly downstream (the grain size becomes increasingly coarser and the size range also increases). On the other hand, flows S58, S71, S87 and S115 all only exhibit slight changes in the grain size distribution. Only approaching the distal deposit, these flows show noticeable changes in the grain size distribution. For instance, a drastic decrease in the volume of the mean grain size in the deposit of flows S71 from downstream distance x = 2.8 to 3.1m. Note that the deposit mass at this distance has already diminished significantly, which makes the change in the grain size relatively unimportant.

The change in the grain size distribution with downstream distance in the deposit of these flows can be better studied from the plots of the D20, D50 and D80 distribution in the deposit, where D20, D50 and D80 represents the value of the grain size at the 20, 50 and 80 percent of the actual grain size distribution as shown in the right hand side of Fig. 5.16 (f – j). All flows exhibit only a slight decrease in D20, D50 and D80 from upstream to the downstream, except for flows UNS64 which show a significant decrease in its grain size. Numerically, the maximum decrease in D20, D50 and D80 for flows S58, S71, S87 and S115 is within 5μm, whereas that of flow UNS64 drops as much as 40μm. Clearly there is a stark contrast between the results obtained for UNS64 and the rest of the flows and this begs the question as to why. The reason can only be determined by seeking the difference in the initial conditions of the flows since this consequently changes the dynamics of the sediment transport. In this regard, aside from the value of the average grain size, which is not possibly the reason since the size of UNS64 does not differ significantly from the sizes of the rest of the flows, the grain size range is the only initial condition UNS64 does not have in common with the rest of the flows. Clearly UNS64 has a greater particle size range than the rest of the flows presented in this thesis. As shown in Table 5.1, UNS64 has a standard deviation of 18.4 whereas the rest of the sieved flows have a standard deviation less than 11.

Between 18 and 11, there apparently exists a threshold in the standard deviation of particle size where the grain size distribution changes much more slowly everywhere in the deposit. The lack of variance in the grain size distribution also implies that particle size fractionation within the flows is unlikely to be significant at any location and for any period of the flows. However, there are two more important questions that need answers, namely (i) what sort of physical mechanism is induced by the small size range of the material that leads to virtual absence of particle fractionation? (ii) how does the result scale up to other flow conditions? These questions cannot be answered at the present without conducting a more thorough investigation. In addition, it is important to determine how the grain size distribution changes for flows carrying particles with standard deviation between 11 and 18, and beyond 18. Therefore future investigations should be conducted on flows carrying such particles that are sieved from similar material (UNS64) and have similar flow concentration.

It is insightful to condense the information in Figure 5.16 into a single figure. Figure 5.17 shows the percentage change in the mean grain size (D50) relative to that of the initial condition of all the aforementioned flows. This figure shows that the D50 of the flow UNS64 increases slightly at the upstream in the vicinity of the lock box (increases within 10%) and then decreases until the difference is about 50% downstream whereas the changes in D50 over the rest of the flows are within 10%.

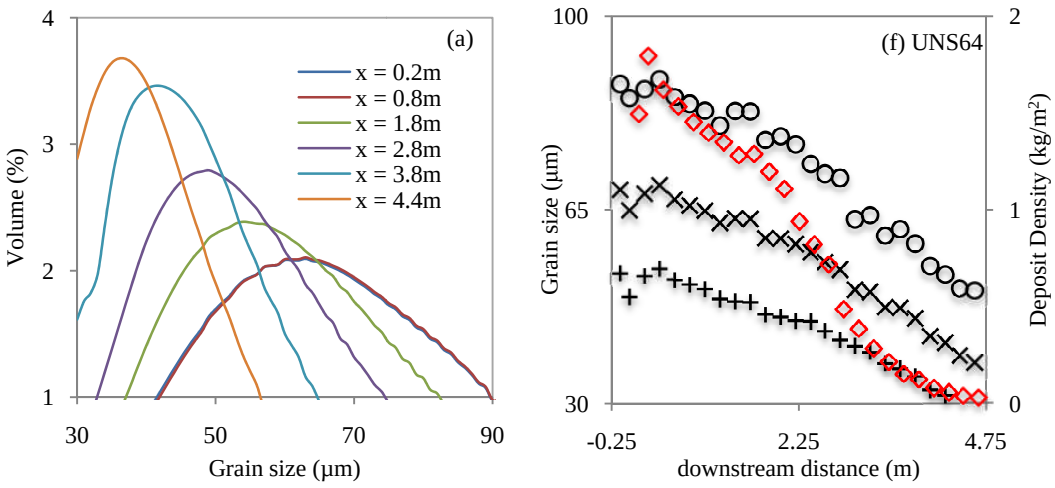

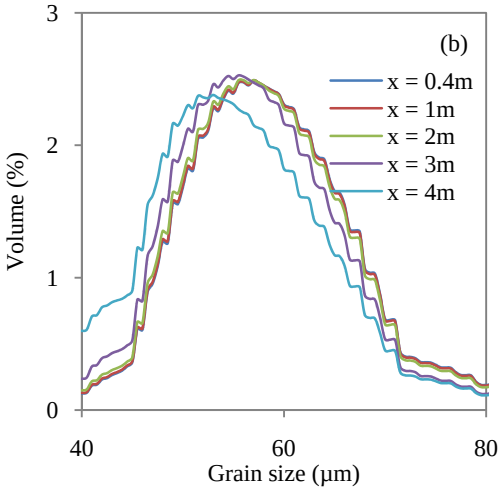
(b)
x = 0.4m
x = 1m
x = 2m
x = 3m
x = 4m
Volume (%)
Grain size (µm)

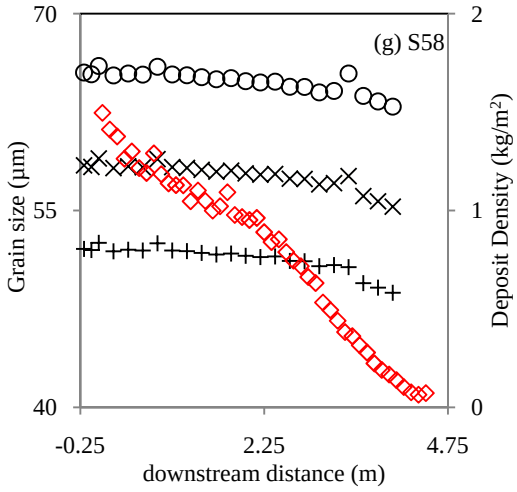
(g) S58
Grain size (µm)
Deposit Density (kg/m²)
downstream distance (m)

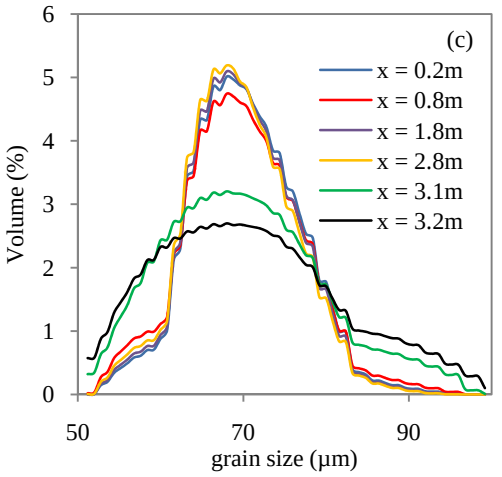
(c)
x = 0.2m
x = 0.8m
x = 1.8m
x = 2.8m
x = 3.1m
x = 3.2m
Volume (%)
grain size (µm)

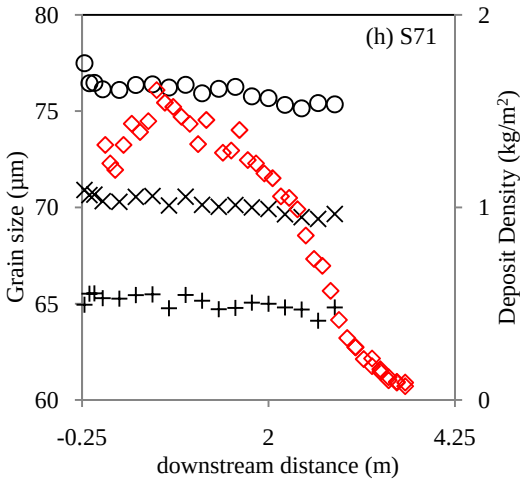
(h) S71
Grain size (µm)
Deposit Density (kg/m²)
downstream distance (m)

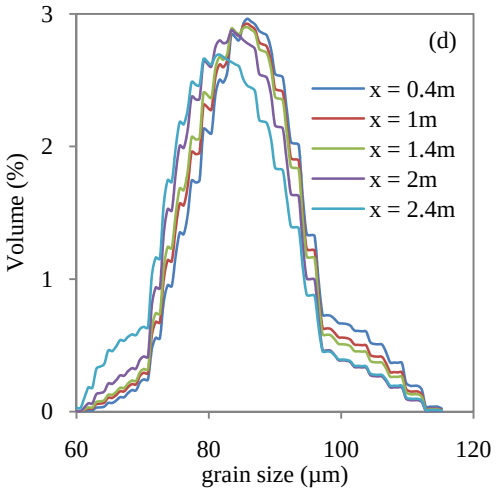
(d)
x = 0.4m
x = 1m
x = 1.4m
x = 2m
x = 2.4m
Volume (%)
grain size (µm)

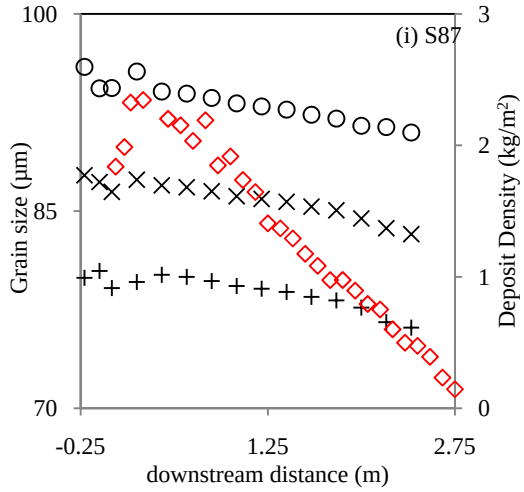
(i) S87
Grain size (µm)
Deposit Density (kg/m²)
downstream distance (m)

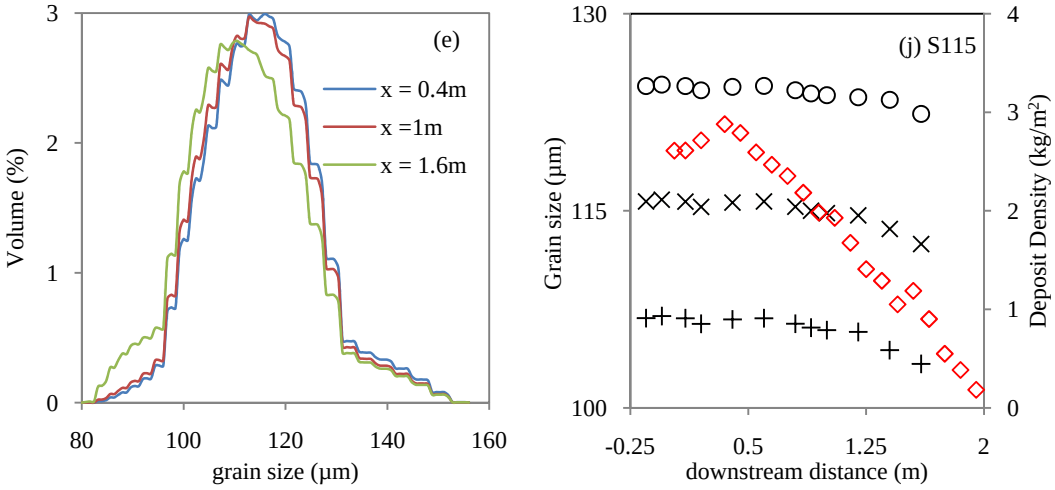

Figure 5.16 (Left figure; a-e) The deposit's grain size distribution at multiple selected downstream locations. (Right figure; f-j) The 20th (O), 50th (×) and 80th (+) in the deposit's grain size distribution as a function of the downstream distance from flows (a) UNS64, (b) S58, (c) S71, (d) S87, and (e) S115. In each figure, the deposit mass density distribution (red diamond) is plotted to correlate it with the deposit size distribution.

Another useful plot is to correlate the percentage change of D25, D50, D75 and D99 (relative to the initial size) to the standard deviation of the size of the material as shown in Fig. 5.18. If the standard deviation is smaller than about 11, the change of all the cases D25, D50, D75 and D99 is negligible. When the standard deviation is 18, a significant change is observed. However, the figure is somewhat incomplete without more data being available between the standard deviations of 11 and 18, which can only be accomplished in the future investigations due to the time constraint imposed on the current work.

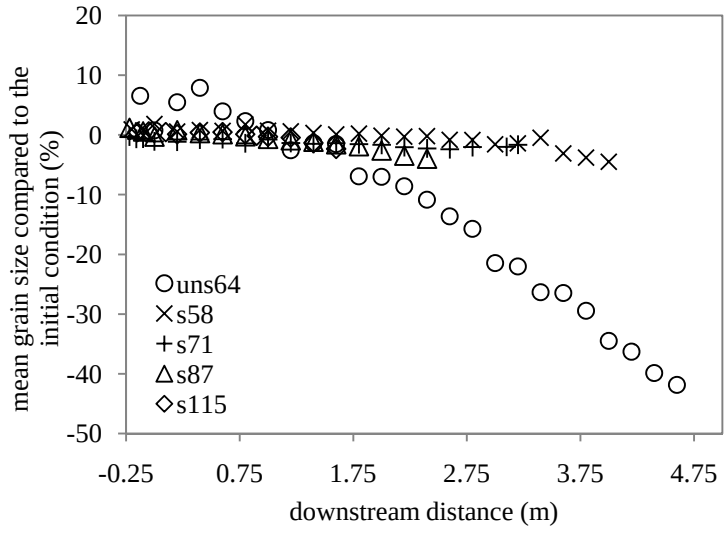

Figure 5.17 The percentage ratio of the mean grain size relative to the initial mean size as a function of downstream distance of flows.

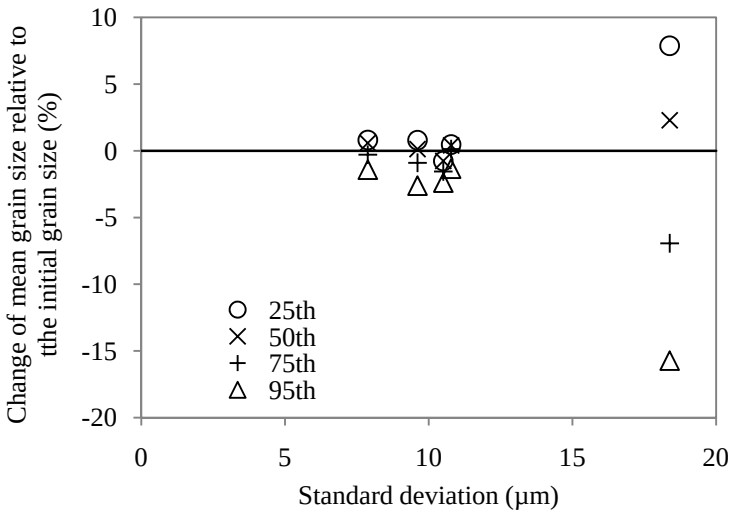

Figure 5.18 The percentage ratio of the mean grain size to the initial mean grain size as a function of the standard deviation of the initial size distribution of the glass beads carried by the flows S58, S71, S87, S115 and UNS64.

5.6 Numerical Modelling

Further investigations using the Mixture Model have been performed with the aim of resolving the following issues:

(i) We have not found why the Mixture Model predicts an excessive dispersive effect in all the flows (G69, G25, G37, G25 and D37) in Series C, as shown in Fig. 3.11(a – e) in Chapter 3. In terms of the initial conditions, the flows for Series C have finer particles and lower initial concentrations than the flows considered in Series A and B. The question is, how does the prediction of the Mixture Model, both without and with turbulent dispersion (TD), compare with the experimental data in this case? Answering this question should give us an assessment of the performance of the Mixture Model in predicting turbidity current behaviour over a wide range of initial conditions. In turn, this should then allow us to be able to effectively identify the source of any error within the model.

(ii) The grain size distributions in the deposits of the flows carrying the sieved materials S58, S71, S87 and S115 are intriguing. Granted that the Mixture Model is able to accurately predict the deposit mass density distribution of the flow, does it predict the same grain size distribution in the deposit of the aforementioned flows? If so, can the Mixture Model explain the subdued changes in the deposit grain size distribution in terms of the dynamics of the sediment transport?

5.7 Model Details and Assumptions

The details of the governing equations of the Mixture Model and the treatment of the boundary conditions are described in Chapter 3 and are not repeated here. However, the treatment on the particle size in the numerical modelling is slightly different. Instead of considering only the mean size of the particle, the particle size distribution is divided into five non-overlapping size ranges of equivalent volume (i.e., 20% for each size range) and the mean value of each size range is considered in the model. While this approach results in an increase in the computational costs, it is more accurate and also takes into account particle fractionation within the flows. Furthermore, a round of validation on the mesh size and time step needs to be performed for the flows in question before the numerical results can be further analysed. This is discussed further in the next section.

5.8 Simulation Validation

An investigation was performed to determine a suitable value of the mesh size and time step for the current problem. Simulations with different mesh sizes and time steps were performed. Since it is time consuming to investigate the sensitivity of the mesh size and time step to all the initial conditions of the flows, the test was only performed on flows C500. Because the behaviour of the flows does not vary significantly, the mesh size and time step that works for flows C5 is expected to work for other flows as well.

The mesh sizes considered here are 800 x 20, 1200 x 30, 1600 x 40, 2000 x 50, and 2400 x 60 (the number of cells along the horizontal axis of the domain times the number of cell along the vertical axis of the domain) (see Table 5.5). The aforementioned numbers represent the mesh size in the internal domain. Near to the wall, in order to resolve the boundary layer profile of the flows, very small mesh sizes are employed. Figure 5.19 shows an example of the mesh size distribution in the domain. All four meshes were used to simulate C500 using FLUENT. The time-step was kept constant at 0.01s. It is assumed here that the choice of the time-step would not affect the rate of convergence of the calculation in any mesh considered above. (How the results from each mesh size change with different prescriptions of the time-step is investigated below). Figure 5.20 shows the numerical prediction on the deposition of mass from flow C500 using different mesh sizes. It is observed that

decreasing the mesh size from 800 x 20 to 1600 x 40 slightly changes the prediction on the deposit mass between x = 1 and 2m, where the smaller mesh size predicts a slightly higher value of deposit mass. The changes in this region become negligible when the mesh size is further decreased to 2000 x 50 or 2400 x 60. On the other hand, between x = 0 and 1m, we can observe an increase in the oscillations in the deposit mass profile when the mesh size is decreased (one, two and three oscillations are predicted in the results of simulation using mesh 1600 x 40, 2000 x 50, 2400 x 60). It is uncertain whether further decrease in the mesh size would increase the number of oscillations beyond three. It is postulated here that the choice of the value of time step may influence the occurrence of the oscillations. Nonetheless, it is found that the overall change in the solution becomes relatively small when the mesh size is decreased further from 1600 x 40. Hence it can be concluded here that the 1600 x 40 is maybe the most efficient mesh size in this case.

Table 5.5 Detail of different mesh used in this study

Name	Main Domain Cell Size (m)	Total No. Cell in the domain
800 x 20	0.01 x 0.01	32,000
1200 x 30	0.006667 x 0.006667	56,400
1600 x 40	0.005 x 0.005	80,000
2000 x 50	0.004 x 0.004	130,000
2400 x 60	0.00333 x 0.00333	177,600

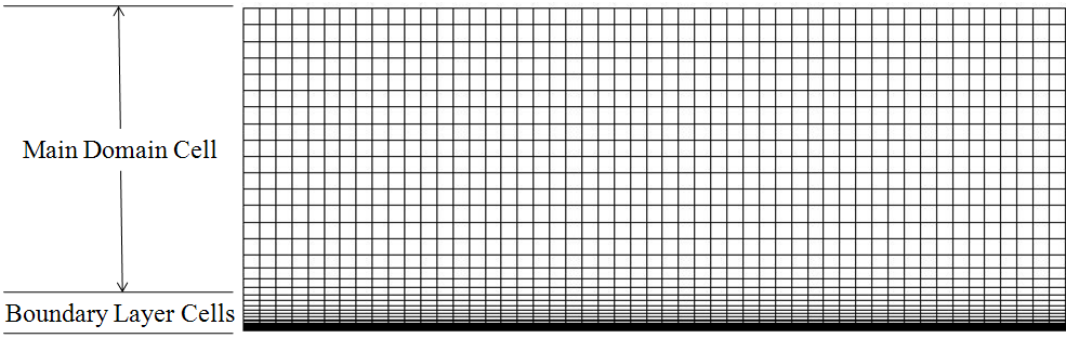

Figure 5.19 Schematic diagram showing the mesh distribution in the main domain and the boundary layers.

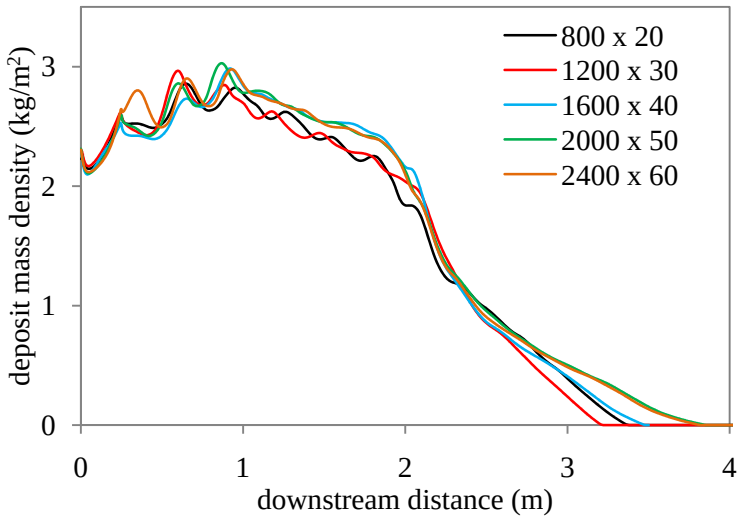

Figure 5.20 Prediction on the final mass density profile of flows C500 from simulations using mesh size 1200 x 20, 1600 x 40, 2000 x 60, and 2400 x 80 and experiments (circle). The time step value is 0.01s.

Using the mesh size 1600 x 40, further simulations are performed using different time steps in order to investigate whether the value of time step has an influence on the characteristics of the oscillations predicted in the proximal deposit mass when small mesh size is used. The value of the time step used in the simulation in the previous investigation (0.01s) was both decreased and increased. A value of the time step as large as 0.05s and as small as 0.0005s was considered. Generally it is expected that the solution should become increasingly inaccurate with an increase in the size of the time step, whereas it should converge into a final solution with a decrease in the time step. Figure 5.21 shows the prediction on the final deposit profile of flows C500 using Δt = 0.05, 0.04, 0.025, 0.015, 0.01, 0.002 and 0.0005s, compared with the experimental data. It is observed that increasing Δt from 0.01s to 0.04s does not result in significant changes to the solution. Some mild oscillations are predicted in the upstream region when a large time step is used (Δt = 0.025s and 0.04s) but they are still very close to each other, in general. Further increasing Δt to 0.05 causes a convergence difficulty in the calculation and this subsequently results in the solution deviating significantly from the experimental result. Thus we conclude that 0.04 is the limit of the largest value of the time step where accurate solutions can be obtained in this case. On the other hand, decreasing the value of Δt to 0.002s yields an unexpected observation. Instead of improving the solution, the model under-predicts the deposit mass density inside the lock-box. Away from the lock-box, the mild oscillations that appear in the solution with a large time step

becomes significantly large, which is not observed in the experiments. On further decreasing the time step to 0.0005s the magnitude of the oscillations increases and thus reduces the accuracy of the solution. These observations suggest that the model experiences a numerical instability if very small time steps are employed and the instability increases with a decrease in the time step. The exact cause for the numerical instability is not clear but it can be speculated that it is likely due to a correlation between the mesh size and the time step. In order for the solution to be accurate, the mesh size must be small enough to predict the spatial change in the solution that occurs at a small time step. If the change in the solution is smaller than the mesh size, the model may over-predicted or under-predict the solution. In short, there is a lower limit to the value of the time step for a specific mesh size in a specific problem in order to obtain realistic solutions. In this case, an estimation of the change in the flow to the mesh size can be made by comparing the mesh size x_m to the distance the flows propagates within the time step x_f (the velocity of the flows multiplied by the time step). The condition is that x_m must be smaller than x_f in order for the mesh to be able to accurately describe the change in the flow. The above speculation can be validated by performing another round of simulations with different values of the time step but on a coarse mesh size 1200 x 20. In this case, the model should predict a numerical instability at a time step greater than 0.002s. A series of simulations of the flows C500 have been carried out on the mesh 1200 x 20 using time steps ranging from 0.05 to 0.0005s and the results obtained are plotted in Fig. 5.23. It can be observed that a numerical instability is predicted when a time value as large as 0.01 is employed. Thus we conclude that a small mesh size must be used if a small time step is prescribed in order to obtain a stable solution. For a fixed mesh size, there exists a range of time steps where the solution is stable and accurate. Employing a time step that is too large results in convergence difficulties in the calculations, whereas employing too small a value for the time step induces numerical instabilities. This suggests a multi-variate approach in mesh size and time step is needed to optimise the modelling setup.

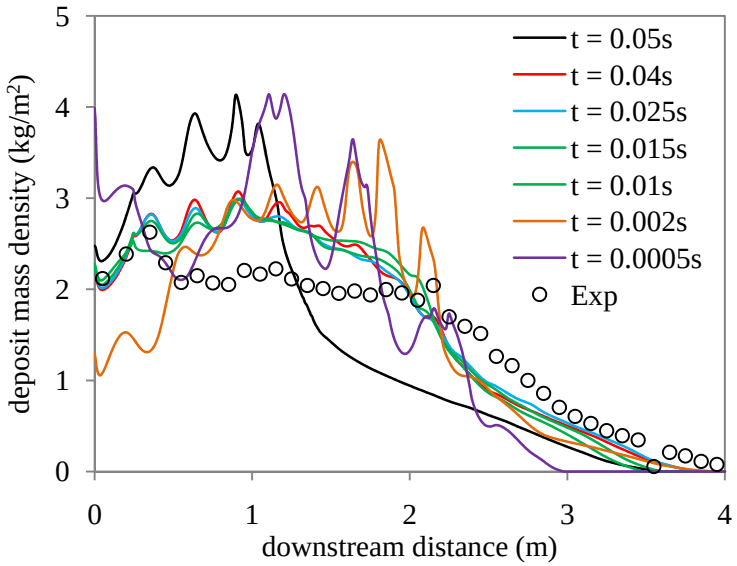

Figure 5.21 Prediction on the final deposit mass density of flows C5 from the Mixture Model using mesh size 1600 x 40 and time step = 0.0005, 0.002, 0.005, 0.01, 0.015, 0.025, 0.04 and 0.05s, and experiment (circle).

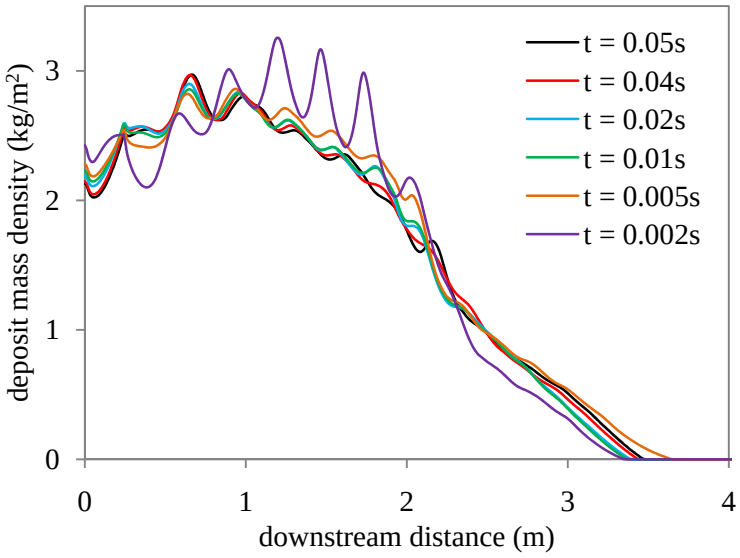

Figure 5.22 Prediction on the final deposit mass density of flows C5 from the Mixture model using the mesh size 800 x 20 and time step = 0.002s, 0.005s, 0.01s, 0.02s, 0.04 and 0.05s.

5.9 Simulation Result

Having established the appropriate mesh size and the time step for the model, simulations can be performed for the rest of the flows representing Experiment A and B using similar mesh sizes and time steps. As mentioned before in Section 5.6, the numerical investigations are carried out with two aims,

(i) To verify the accuracy of the Mixture Model incorporating turbulent dispersion in predicting the behaviour turbidity currents with relatively high concentration (2 to 5%) and carrying coarse particles, and then compare the results obtained with modelling the Series C flows.

(ii) To seek an explanation for the seemingly unfractionated grain size distribution in the deposit observed in some experiments.

To achieve aim (i), the numerical results from models both without and with TD, for flows from Series A and B are acquired in a similar manner as the results obtained for the flows from Series C. Both the numerical prediction on both the deposit mass density profile and the propagation of the front of the flows are then compared with the experimental data and discussed (see sections 5.9.1 & 5.9.3). A parameter λ is devised to quantitatively describe the goodness of the fit between the experimental data and the numerical data on the deposit mass density profile. Using all the results from Series A, B and C, we are able to plot λ from the numerical results in both models for a range of particle size and flow concentrations. This analysis allows us to assess the performance of the Mixture Model over a wide range of initial conditions. To further understand the effect of TD in the flows with different initial conditions, the internal structure of the flows (the distribution of the concentration, turbulence structure and TD inside the flow) is discussed (see sections 5.9.4 to 5.9.8).

To achieve aim (ii), the numerical prediction of the deposit mass profile for each size class is compared with the experimental data and the discrepancies in the comparison are discussed (see section 5.9.2).

5.9.1 Deposit Total Mass Density

Fig. 5.23 (a – h) shows the prediction of the Mixture Model (black and red lines) and the experiments (circle) on the deposit mass density profile of the flows from Series A, where the black lines represent the numerical solution without TD and the red lines represent the numerical solution with TD, respectively. Firstly, we discuss the numerical results obtained from the Mixture Model without TD (black lines). The model predicts oscillations in the profiles of all flows for Series A (mostly in the upstream or first half of the profile). The first oscillation has the greatest magnitude and the magnitude declines with distance downstream. The magnitude of the

oscillation increases with an increase in particle size. The oscillation is clearly a numerical artefact and is thought to occur due to an inappropriate prescription of the value of the time step (Δt = 0.002s), as discussed in the previous section. Time steps larger than 0.002s must be prescribed. This shows that the numerical instabilities vary with the flows of different initial conditions and in this case a larger time step size should be used for flows carrying coarse particle in order to eliminate the oscillation. Regarding the comparison between the numerical results and the experimental data, the simulations always over-predict the deposit mass upstream and under-predict deposition downstream with the discrepancy larger for flows carrying finer material.

The numerical results obtained using the model with TD (red lines) can now be discussed. Contrary to the model without TD, the model predicts little to no oscillations in the deposit mass profile. Thus no oscillations are predicted for flows carrying the fine particles whereas slight oscillations are predicted for flows carrying coarse particles. Regarding the comparison between the numerical results and the experimental data, a significant improvement is achieved. This shows that the TD has pushed the numerical results closer to the experimental data and may be an essential mechanism that should be incorporated in the model. TD increases the sediment diffusion in the flow, and this decreases the rate of sedimentation and thus causes more sediment to be deposited downstream. Clearly, this conclusion is inconsistent with the observations made on the flows of Series C, which had low initial mass and carried fine particles (see Figure 3.11 in Chapter 3). At this point, we can only conclude that the TD is essential for flows of higher initial mass and carrying coarse particles but it induces a numerical error if it is used for predicting flows with a low initial mass and carrying fine particles.

Although the numerical results are significantly improved by including the effect of TD in the model, there are slight discrepancies between the numerical results and the experimental data. The numerical model still always predicts more deposit mass in the upstream regions and less deposit in the downstream regions than do the experimental data. Experimental error may contribute slightly to this discrepancy. For instance, in flows S58 and UNS83, the measured deposit mass is 6-7% less than the original mass; this is thought to be due to human error. However, we are still inclined to postulate that there are physical mechanisms that are responsible for

these discrepancies. These could include particle re-suspension and bed-load transport.

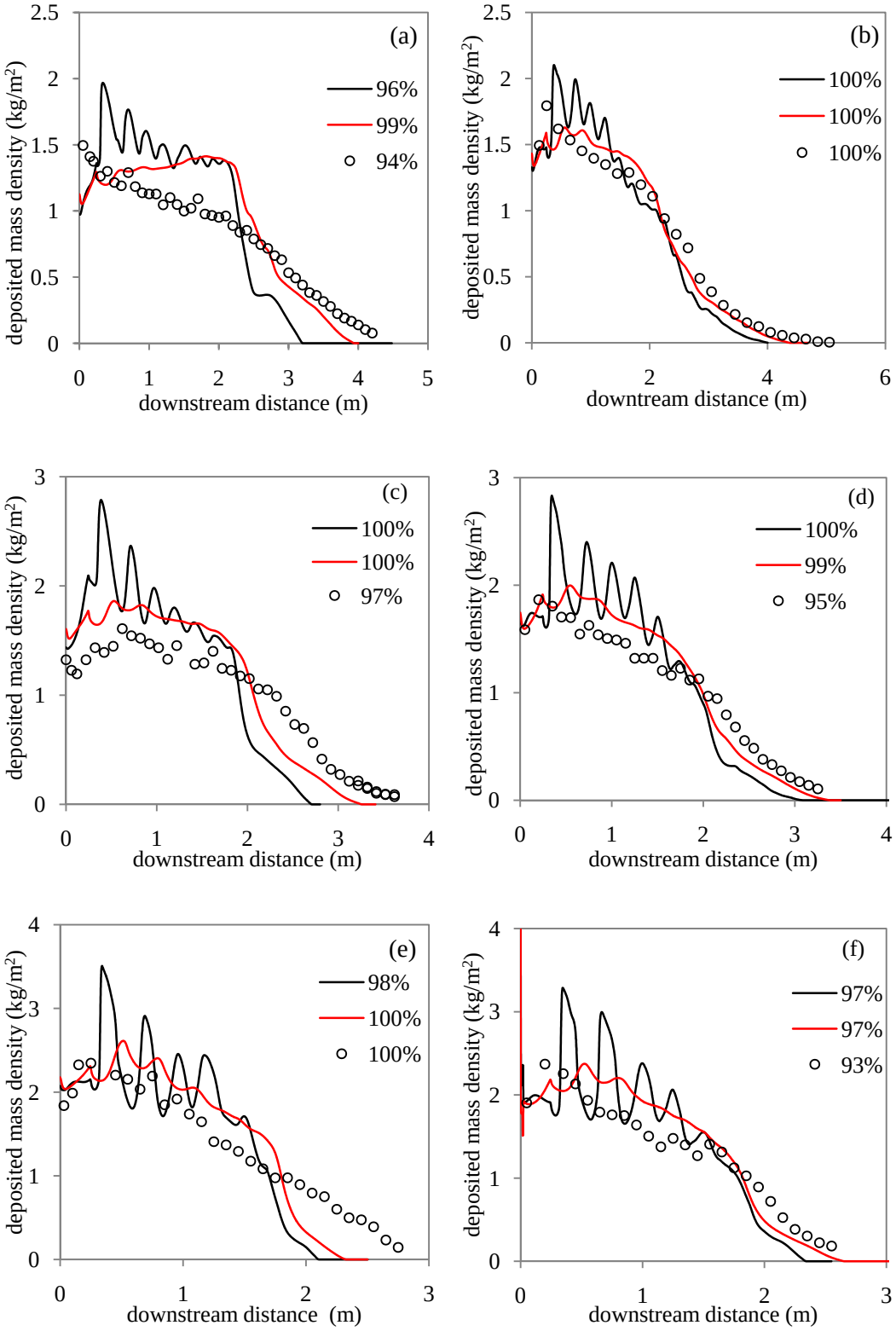

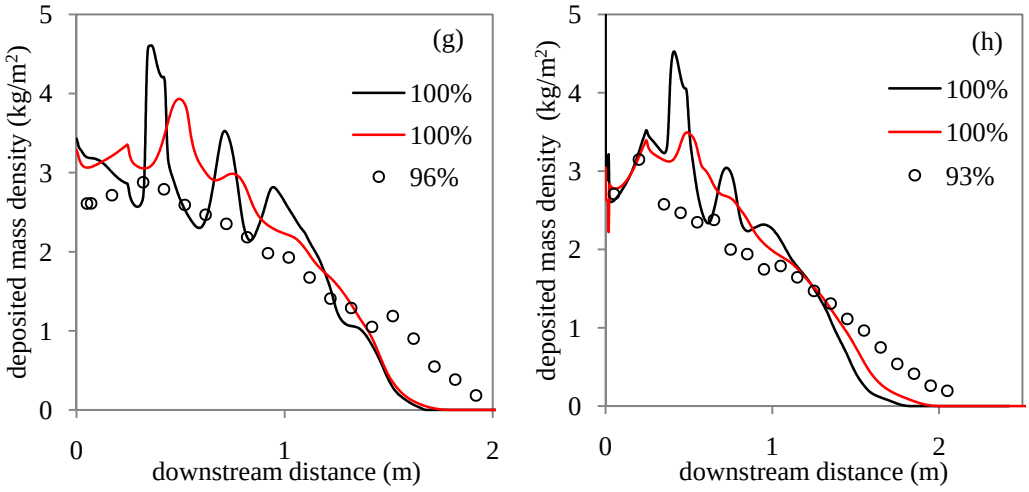

Figure 5.23 Comparisons between the numerical and experimental predictions on the deposit mass density as a function of the downstream distance of the flows for Series A, (a) S58, (b) UNS64, (c) S71, (d) UNS74, (e) S87, (f) UNS83 (g) S115 and (h) UNS109. The black lines represent the simulation using the k-ϵ turbulence model with the addition of the turbulence buoyancy force. The red lines represent the simulations with the further addition of turbulence dispersion. The legend in each figure represents the percentage of the total mass in the deposit relative to the initial mass.

The predictions of the Mixture Model (black and red lines) on the deposit mass density profile and the experimental data (circle) of Series B flows are shown in Fig. 5.24. In this figure, we study how the comparison between the numerical model both without TD and with TD and the experimental data varies with different flow concentrations. Both models yield rather similar predictions on the deposit mass profile for flows with low concentrations (C027, C050 and C100) see Fig. 5.24 (a – c), and compare very well with the experimental data. This shows that TD yields little effect on the deposit profile of the flows for flows with low concentration. Again this is in contrast with the observations made on flow with low concentration but carrying finer particles from the Experiment C. Therefore we rule out concentration as a factor that could results in TD predicting excessive dispersion. The remaining factor is the particle size (or the settling velocity). For flows with high concentrations (e.g., 1% - 5%), the results obtained from both models disagree with each other. The model without TD predicts multiple oscillations in the deposit profile in the upstream region whereas the model with TD predicts a smooth profile and the latter agrees better with the experimental data. This shows that TD has a

better modelling outcome and the effect is more pronounced for flows of high concentration.

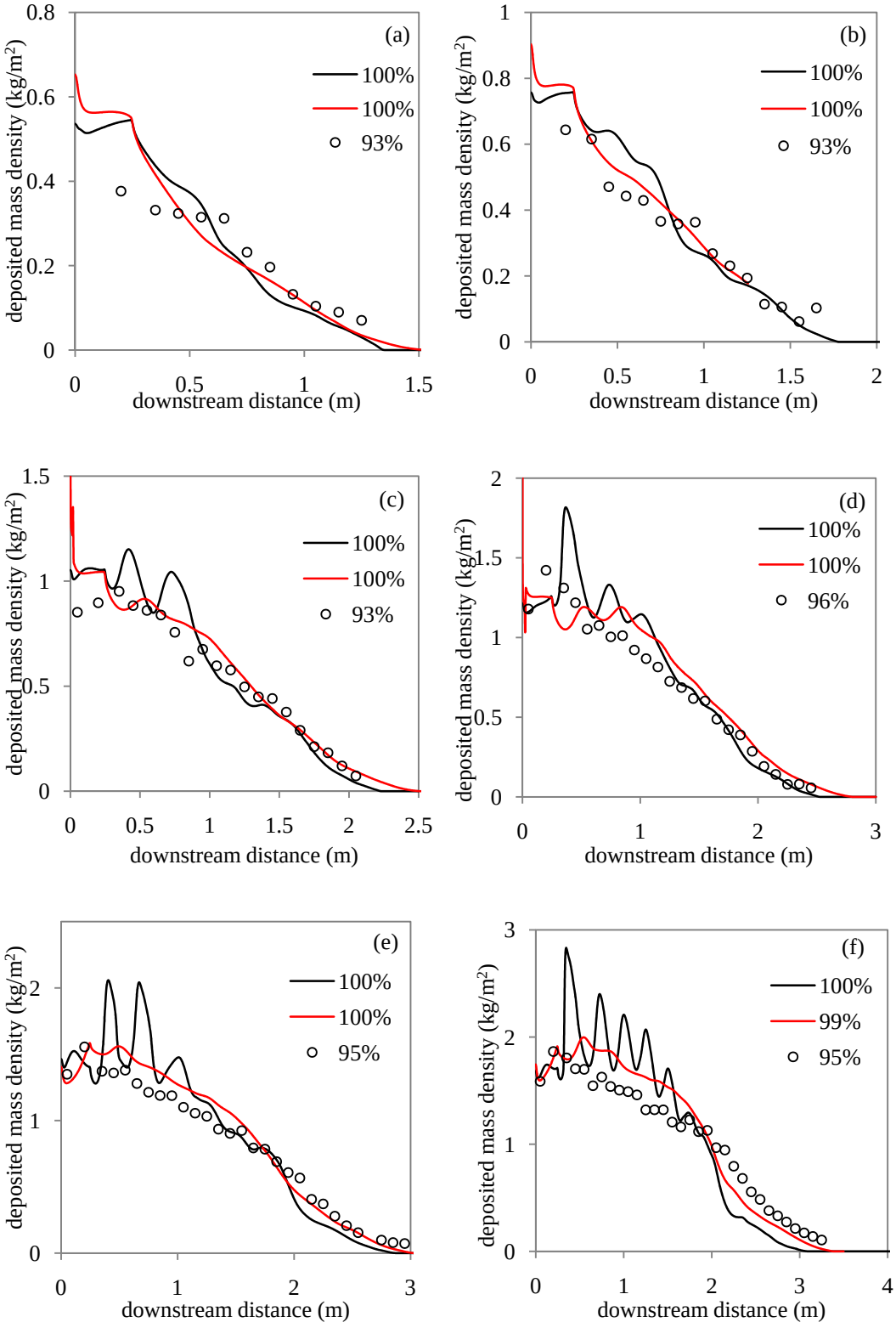

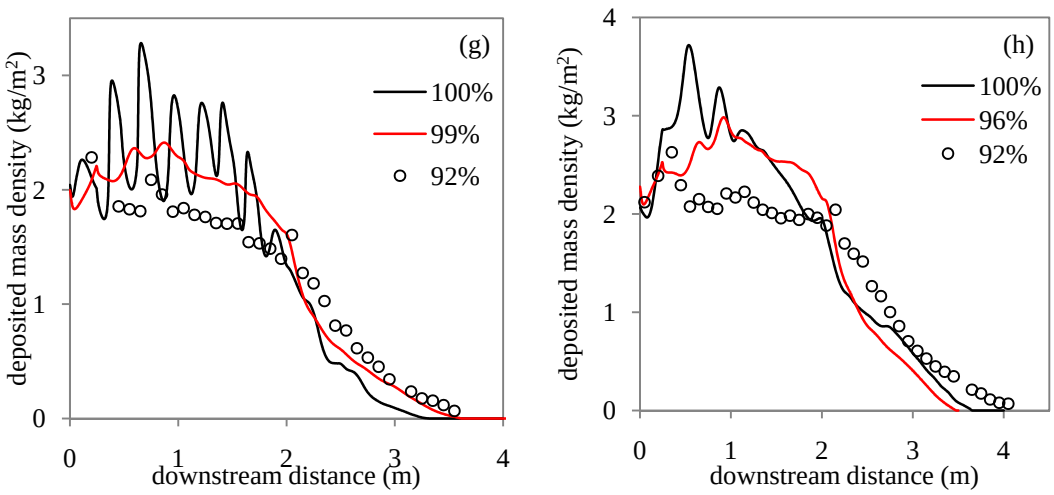

Figure 5.24 Comparisons between the numerical and experimental prediction on the deposit mass density as a function of the downstream distance of the flows for Series B, (a) C027, (b) C050, (c) C100, (d) C150 (e) C200, (f) C288 (g) C388 and (h) C500. The black lines represent the simulation using the k-e turbulence model with the addition of the turbulence buoyancy force. The red lines represent the simulations with the further addition of turbulence dispersion.

While graphical representative of the deposit mass distribution such as Figs. 5.23 & 5.24 allows us to qualitatively compare numerical and experimental results and assess the nature of any discrepancies in the comparison, it is difficult to evaluate from these figures relatively how well different simulations compare (which is essential for assessing the accuracy of model changes across a range of parameters such as concentration and particle size). Therefore a method was introduced which allows the discrepancy between the numerical and the exprimental result to be quantified in the form of a single value parameter (known as λ). To determine the value of λ, both numerical and experiment results are expressed in the form of cumulative mass percentage (which is made dimensionless by dividing it by the initial mass) as a function of the downstream distance and then the absolute difference between the numerical and experimental results at every 10^{th} of the run-out distance are calculated and summed up. The smaller the value of λ the closer is the numerical prediction to the experimental data and hence the more accurate a numerical result is, assuming there is no error in the experimental data.The weakness of λ is that it does not describe the nature of the discrepancy, for instance, whether the model over-predict or under-predict the mass of the deposit and the locations of the discrepancy. It simply quantifies the total discrepancy between the experiment and the numerical result on the deposit mass distribution.

Table 5.6 shows the values of λ for the Mixture Model with and without TD for flows of Series A, B and C. It can be observed that the Mixture Model with TD has two biggest value of λ, 3.03 (G13) and 2.1 (G25), indicating the comparison of the model prediction with the experimental data are the worst in these two cases. This is consistent with the graphical observation shown in Fig. 3.11 (Chapter 3) which shows that the Mixture Model with TD significantly underpredicts the deposit mass. The two lowest values of the λ are also belongs to the Mixture Model with TD, namely flows Series A UNS65 (0.19) and Series C flows G69 (0.27). The values of λ from both models lie in the range of 0.4 to 2. The two largest difference in the values of λ from both models are Series C flows G25 (1.29), and G13 (1.47), which shows that the effect of TD is less strong for Series A & B flows.

A more meaningful analysis was achieved by plotting the values of λ graphically as a function of grain size, concentration and initial mass as shown in Figure 5.25(a - c). It can be observed most of the values of λ of the Mixture Model with TD at large grain size (greater than 50μm), large concentration (greater than 2%) and large initial mass (greatert than 300g) are lower than those from the Mixture Model without TD, which means that the Mixture Model with TD is a better model in these ranges of parameters. Outside the aforementioned range of parameters, the Mixture Model without TD has lower values when the grain size is less than 50μm. On the other hand, there is no distinctive difference between the values from both models for low concentration (less than 2%) and low initial mass (less than 400g) flows. These observation quantitatively reinforce the earlier conclusion that the accuracy of TD most likely only depends on the particle size. In high concentration flows with coarse particle, TD actually becomes essential for achieving an accurate solution.

A further investigation has been performed to determine the possibility of particle re-suspension in the flows, which could explain the small discrepancy between the numerical results (red lines) and the experimental result. Since it is difficult to physically monitor particle re-suspension in the experimental investigation, an easy way to determine whether particle re-suspension could be important or not is by using the numerical solution and the re-suspension criterion suggested by, for example, Niño et al. (2003) who proposed the following criterion based on their experimental investigation:

Table 5.6 The value of λ of flows of Experiments A, B and C for the Mixture Model both with and without TD.

Series	Flow	Particle Size	Concentration	λ (KE + TB)	λ (KE + TB + TD)
C	G69	69	0.35	0.27	0.44
	G25	25	0.35	0.81	2.10
	G37	37	2	1.00	1.45
	G13	13	2	1.56	3.03
	D37	35	0.275		0.27
A	S58	58	2.88	0.70	0.71
	UNS64	64	2.88	0.24	0.19
	S71	71	2.88	0.76	0.42
	S87	87	2.88	0.42	0.42
	UNS83	84	2.88	0.68	0.58
	UNS109	109	2.88	1.19	1.02
	S115	115	2.88	1.52	0.67
B	C027	74	0.27	1.64	1.68
	C050	74	0.5	1.20	1.09
	C100	74	1	0.90	0.64
	C150	74	1.5	1.60	1.20
	C200	74	2	0.84	0.59
	C288	74	2.88	1.95	0.63
	C388	74	3.88	1.08	0.79
	C500	74	5	1.12	0.72

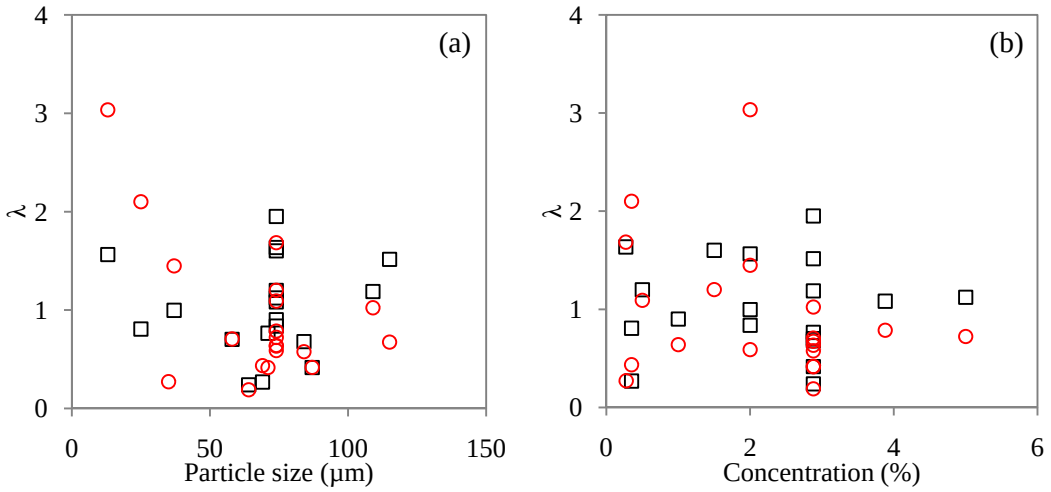

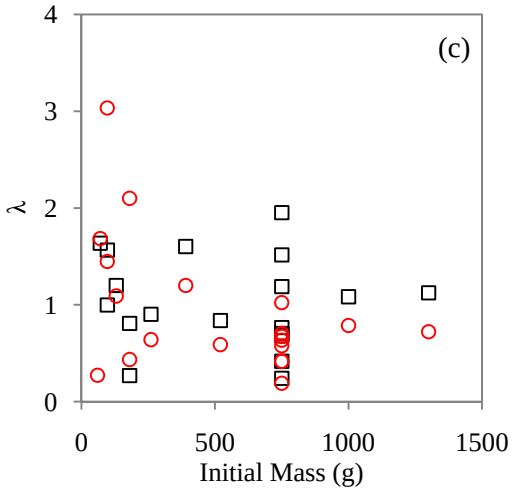

Figure 5.25 The value of λ of Series A,B and C as a function of (a) particle size carried by the flows (μm), (b) flow initial concentration, and (c) initial mass. The red circle represents the solution of the Mixture Model with TD whereas the black square represents the solution of the Mixture Model without TD.

$$\tau^* = \frac{u^*}{w_s} = \begin{cases} 21.2\, R_p^{-1.2} & 1 \le R_p \le 27.3 \\ 0.4 & R_p \ge 27.3 \end{cases} \qquad (5.1)$$

where the particle Reynolds number $R_P = \frac{(g'd^3)^{\frac{1}{2}}}{\nu_f}$, $g' = \frac{g(\rho_p - \rho_f)}{\rho_f}$, w_s is the particle settling velocity and u^* is the shear velocity. Thus, from equation (5.1), the parameters governing the particle re-suspension are the shear velocity u^* and the characteristics of the particle (density and size) which are expressed as the particle Reynolds number and settling velocity. The shear velocity describes the flow condition near the wall and its value is determined from the viscous sublayer of the boundary layer through the following formula:

$$u_* = \sqrt{\tau_w / \rho_f} \qquad (5.2)$$

where τ_w is the wall shear stress which is predicted numerically. The accuracy of the prediction on the wall shear stress depends on the density of the mesh near the wall. The mesh must be sufficiently dense so that the model is able to predict u^+ (dimensionless wall velocity) to have a value less than 1 inside the the viscous sublayer of the boundary layer.

Turbidity currents have a non uniform wall shear stress profile at the boundary which also evolves with time. In general, the front of the flows at early times have the greatest shear stress since this is when and where the velocity is at its greatest (the shear stress is directly proportional to the velocity gradient). For this reason, we choose the wall shear stress at *t* = 3s because this is the time when the flow has just becomes a turbidity currents. Fig. 5.26 (a – b) shows the numerical prediction

(model with turbulent dispersion) on the wall shear stress profile at time t = 3s for flows from Series A and B, respectively. It can be observed that the wall shear stress is the greatest within the body of the flows (x = 0.25m). Flows carrying coarser particles have slightly higher wall shear stress than those flows carrying finer particles. On the other hand, the wall shear stresses beneath flows with different concentrations vary significantly. Flows with higher concentrations have a greater wall shear stress. This is not surprising since the flows with higher concentrations propagate faster.

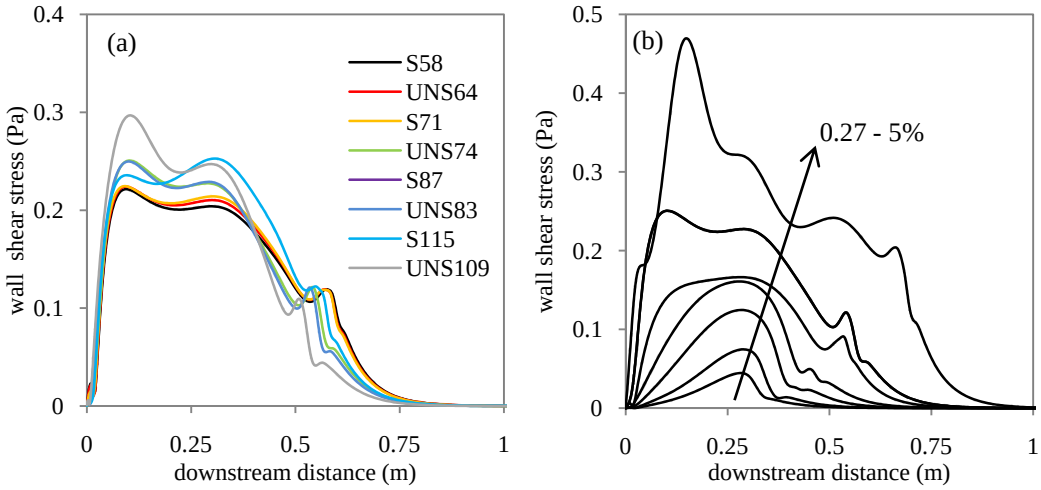

Figure 5.26 The numerical prediction on the wall shear stress profile at t = 3s for flows of (a) Series A, and (b) Series B.

The prediction of the maximum shear velocity to the particle settling velocity u^*_{max}/u_s of the flows for Series A and B, and the re-suspension threshold of Niño et al. (2003), is shown in figure 5.27 (a & b), respectively. It can be observed that value of the ratio is well below the threshold for the re-suspension suggested by Niño et al. (2003) for any type of flow. Therefore we can conclude that the particle re-suspension is unlikely to be important in the flows considered in this investigation. The discrepancy between the numerical and experimental data therefore remains an open question.

5.9.3 Individual Grain Size Deposit Mass Density

Another important characteristic of a turbidity current deposit is the individual mass density of each particle size which represents the internal structure of the deposit. In the numerical modelling, (and based on the grain size distribution of the material determined from the Malvern equipment), the particles are divided into 5 groups of

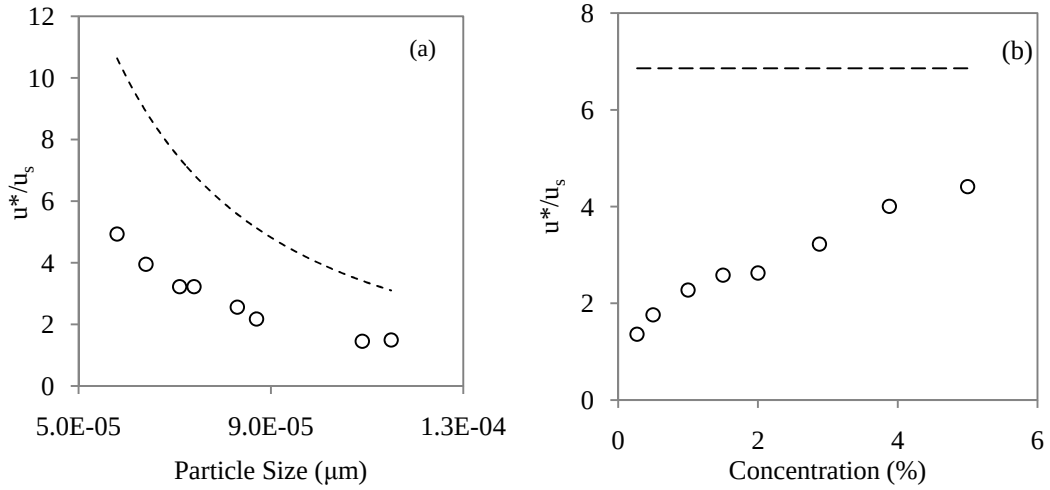

Figure 5.27 The numerical prediction of the ratio of the maximum shear velocity to the particle settling velocity at t = 3s for flows from (a) Series A, and (b) Series B, (circles) and the threshold for the particle re-suspension to occur based on Niño et al. (2003) (dashed lines). The particle size is assumed to be equal to the average size of the material.

different size ranges with equivalent mass or volume. Each group is modelled with its average size. In other words, the 10^{th}, 30^{th}, 50^{th}, 70^{th} and 90^{th} percentile sizes in the actual particle size distribution are used in the numerical model. In order to compare the experimental and the numerical results, the experimental data must be expressed in a similar format to that of the numerical result. This is achieved by adding all the volume of the particle within the size range considered initially. Five flows from Series A (S58, UNS64, S71, S87 and S115) are investigated in this way and the five grain size ranges employed for these flows are given in Table 5.7.

Figure 5.28 (a – e) shows the experimental results on the mass density of the five size ranges of the flows S58, UNS64, S71, S87 and S115, respectively at the left hand side of the figures and the corresponding comparison between the numerical predictions and the experimental results at the right hand side of the figures. The experiments show that all size ranges decrease essentially monotonically from upstream to downstream in all flows, except for the flow S71 which has a non-linear curve profile. The characteristics of the difference between the different size ranges vary for the different flows. For flows S58, S87, and S115, there are differences between the different size ranges at the source and these differences diminish with downstream distance. On the other hand, the flow UNS64 exhibits the opposite characteristics, namely, small differences between the different size ranges at the

source but the differences become larger downstream. In addition, flow S71 exhibits an entirely different behaviour, the difference between the size ranges is greater than those observed in the other flows, appearing to slightly increase, then decrease.

It is important to discuss the relative differences between the mass density profiles for fine coarse grains. Again we observe no consistent trend in all the flows. Ideally, the fine grains (black lines) should possess a lower mass density at the source but greater mass density further downstream than do the coarse grains (purple lines), based on the rationale that the fine grains settle slower than do the coarse grains and hence are able to remain in the suspension longer and ultimately prompt the flow to travel further. The flows UNS64 and S87 exhibit such behaviour. S58 and S115 exhibits similar behaviour upstream but, downstream, the mass of the fine grain converge with the mass of the coarse grain. Clearly such results are unlikely to be accurate as they suggest that that the total mass of the fine grains in the deposit is less than that of coarse grain (each size range has equal initial mass). This raises a concern on the accuracy of the results. For this reason, a further investigation is needed to re-run the experiments to verify the accuracy of the results. Among these five flows, only the result of flows UNS64 has been verified for its consistency (see Fig. 5.7(c)). The good match was obtained between the measurements from three separate runs which suggest that the adopted methodology is robust. The results on the individual grain size deposit mass profile also suggests the total mass is conserved (coarse particle has greater upstream mass and lower downstream mass.

In a comparison between the numerical and experimental results, we observe that the numerical results (Mixture Model with TD) do not agree well with the experimental data. At the proximal deposit, the numerical model consistently predicts that the fine grains have a lower mass density than that of coarse grains. Downstream, the deposits mass of all grain sizes are converging towards each other until they all have similar or approximately similar deposit mass density at about the mid point of the longitudinal deposit range (the “intersection point”). Beyond the intersection point, the deposit of all grain sizes diverges; the deposit mass of coarse particle decreases at a greater rate than the fine particles. In addition, the Mixture Model with TD predicts the difference between the deposit mass of each grain size of flows UNS64 is greater than those of flows S58, S71, S87 and S115, which is an observation consistent with the values of the particle size standard deviation in these

flows. However, these differences are still significant enough to indicate that the particle size does fractionate in the flows, in contrast to the experimental observations (see Section 5.5.4), especially for flows S58 and S71. Therefore, the Mixture Model with TD fails to provide an explanation on the why the experiments show a lack of particle size fractionation in flows carrying sieved particles. None of the numerical results agree completely with the experimental data. The best comparison is for UNS64 where a good agreement is seen between the numerical and experimental data at the distal part of the deposit. At the proximal part, the comparison is still poor. Based on the numerical results, further important observations can be made as follows:

i. There is a link between the particles size range and the existence of an intersection point. It appears that the larger the size range (UNS64, S71) the less well defined is the intersection point.
ii. The particle size has an effect on the characteristics of fractionation. Flows with predominantly fine particle may exhibit an increasing deposit mass downstream (S58, UNS64, S71) whereas the coarse particle exhibit a decreasing mass profile (S87, S115).

Although the numerical results are insightful, their accuracy needs to be better validated against experimental data. In this case, inconsistencies noted in the experimental data casts doubts on the accuracy of the data. Therefore the experiments for the flows carrying sieved particles may need to be repeated in order to verify the existing experimental data.

Table 5.7 Size ranges and the mean size of the particle in the flows for Experiment A. The mean size is listed in the brackets.

Flow name	Size range 1	Size range 2	Size range 3	Size range 4	Size range 5
S58	38 – 50 (47)	51 – 55 (53)	56 – 59 (57)	60 – 64 (62)	65 – 85 (68)
UNS64	25 – 49 (42)	50 – 59 (55)	60 – 69 (65)	70 – 81 (75)	82 – 122 (91)
S71	50 – 62 (58)	63 – 68 (65)	69 – 74 (72)	75 – 82 (78)	83 – 100 (88)
S87	59 – 78 (75)	79 – 83 (81)	84 – 88 (85)	89 – 94 (91)	95 – 115 (101)
S115	81 – 105 (101)	106 – 111 (108)	112 – 117 (114)	118 – 123 (120)	124 – 156 (128)

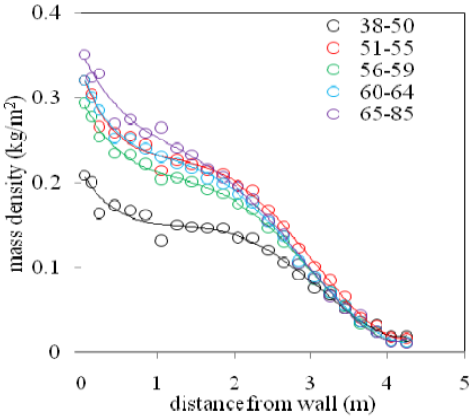
38-50
51-55
56-59
60-64
65-85
mass density (kg/m²)
distance from wall (m)

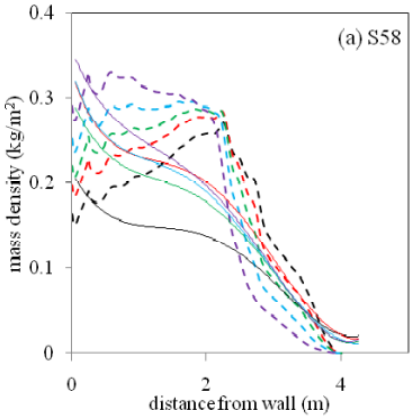
(a) S58
mass density (kg/m²)
distance from wall (m)

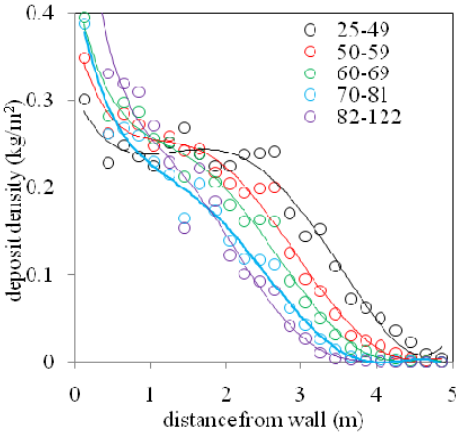
25-49
50-59
60-69
70-81
82-122
deposit density (kg/m²)
distance from wall (m)

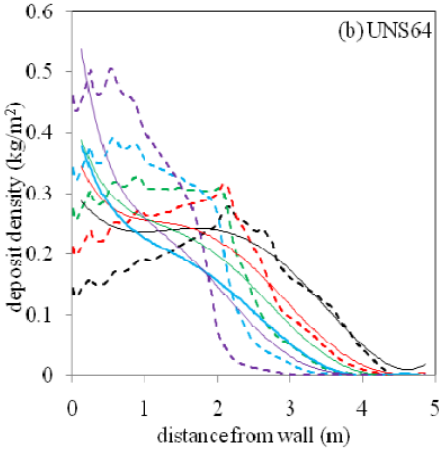
(b) UNS64
deposit density (kg/m²)
distance from wall (m)

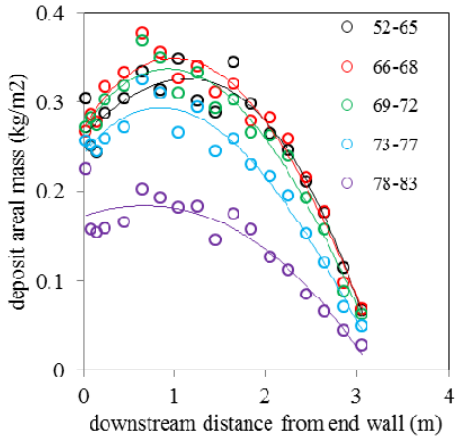
52-65
66-68
69-72
73-77
78-83
deposit areal mass (kg/m2)
downstream distance from end wall (m)

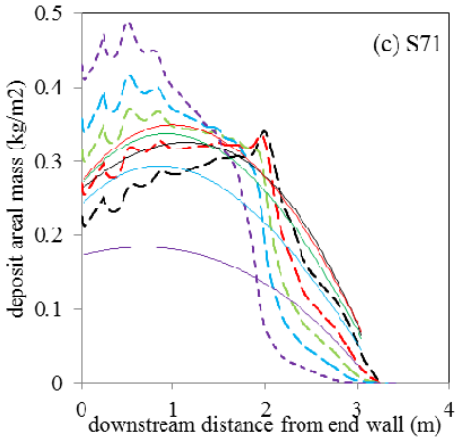
(c) S71
deposit areal mass (kg/m2)
downstream distance from end wall (m)

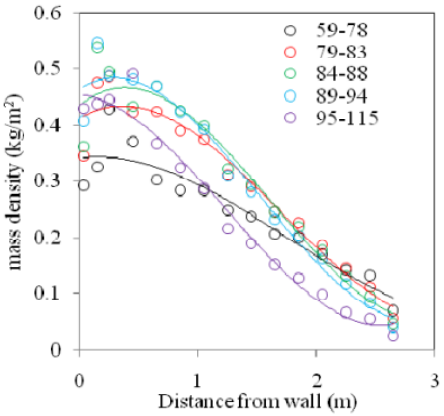
59-78
79-83
84-88
89-94
95-115
mass density (kg/m²)
Distance from wall (m)

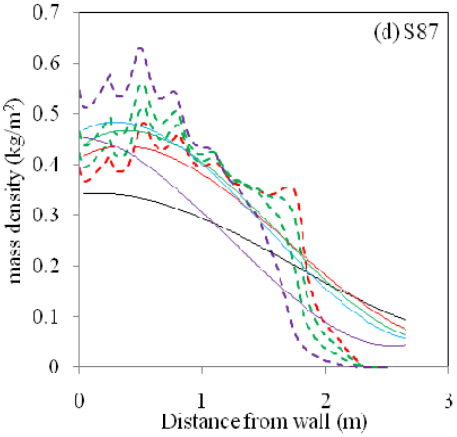
(d) S87
mass density (kg/m²)
Distance from wall (m)

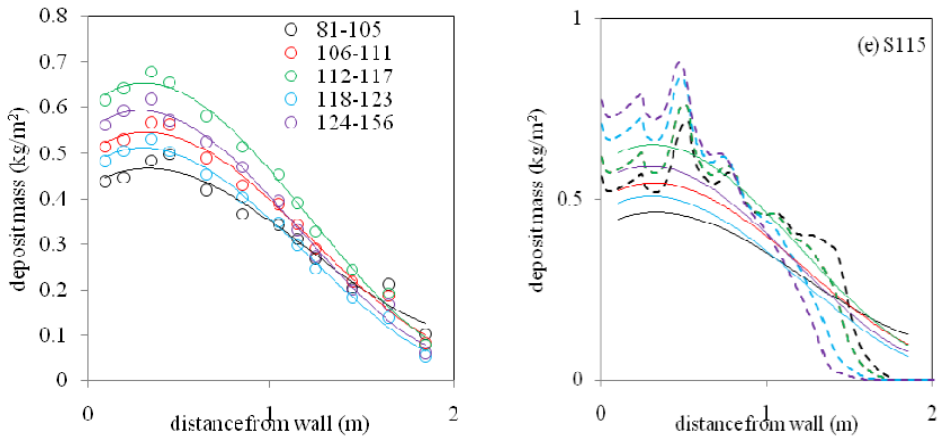

Figure 5.28 (Figures on the left hand side) Experimental measurement (circles) on the mass deposit profile of the five size ranges of flows (a) S58, (b) UNS64, (c) S71, (d) S87, and (e) S115, and trendlines (solid lines) drawn to approximate each profile. The lowest size class has black colour, followed by the red, green, blue, and purple colour. (Figures on the right hand side) Comparison between the corresponding numerical predictions (dashed lines) on the mass deposit profile for the five size ranges of the flows and the trendlines drawn based on the experimental data.

5.9.3 Front Propagation and Total Mass in Suspension

The propagation profile of the front of the flow is another important characteristic that is useful for validating the numerical predictions. Plotted on the right axis of Figs. 5.29(a – h) is the comparison between the Mixture Model results (black lines represents the result without TD and the red line represents results with turbulent dispersion) and the experimental data on the propagation of the front of the flows for Experiment A (flows S58,UNS64, S71, UNS74, S87, UNS83, S115 and UNS109). Plotted on the left axis of the figures is the corresponding numerical prediction on the percentage of the total mass in suspension as a function of time. While there are no experimental data to ascertain the accuracy of the numerical results on the change of the total mass in suspension, it is still useful to correlate it with the propagation of the flows.

Firstly, we comment on the differences between the numerical results from the Mixture Model with and without TD. Both models agree well on the propagation of the front of the flows except that the model with the TD predicts that the flows to have a longer run-out distance. On the other hand, both the model predictions on the

evolution of the total mass in suspensions agree less well for the flows carrying the fine grains (a – f), but they agree well for the flows carrying the coarse grains (g & h). For the former, it can be observed that the model with TD predicts a lower rate of deposition from the flows after the total mass has decreased to about 75%. In summary, the results obtained imply that TD is only significant in the flows which carry finer grains. The grain sizes used in the cases (g) & (h) represents the threshold of the grain size where TD has only a small effect on the propagation of the flows. For a comparison between the numerical model with the TD and the experimental data on the propagation, both agree well in all cases for most of the duration of the flows, except in the later stages of the flows where the numerical model under-predicts the speed of the flows. This is not surprising given that the discrepancy between the results only becomes significant at the later stages of the flows where most of the particles have already been deposited from the suspension (less than 10% of the initial total mass, as indicated by the evolution of the total mass). Since the flows contain a small amount of particles that are finer than those employed in the numerical model, these particles persist in the flows longer and thus cause the flow to propagate further. In addition, the lack of turbulence in the flows may also results in inaccurate predictions when employing the turbulence model. In some cases (b, d & f), surprisingly good agreement is achieved between the numerical results and the experimental data, and this is likely to be just coincidence.

It is worth commenting on how the change in the total mass with time varies for flows that carry particles of different sizes. Clearly the flow carrying the coarser particles has a larger sedimentation rate and hence the total mass decreases faster. The interesting feature is the bend in the curve just before it terminates and this substantially lengthens the duration taken to deposit all the particles from the flow. The bend is small and abrupt for flows carrying the coarse grains (g – h) and becomes increasingly smooth and gradual for flows carrying the finer grains.

Next we discuss the results obtained for Series B, which comprises eight flows with different initial concentrations. Plotted on the right axis of figures 5.30 (a – h) are the numerical prediction (black and red lines, which represents the models without and with TD, respectively) and experimental result (circle) on the propagation of the front of the flow of experiment B (0.27%, 0.5%, 1%, 1.5%, 2%, 2.8%, 3.8% and 5%). Plotted on the left hand side of the figures are the corresponding numerical

predictions on the percentage total mass in suspension as a function of time. Comparing the results from both models, we observe that both models predict almost similar results, except for low concentrated flow (0.27% & 0.5%) where the model with the TD (red lines) predicts a slower flow. This, again, reinforces the conclusion that the TD has little effect on the propagation of the flow for any size (58 – 120μm) and concentration within 1 – 5%. On the other hand, TD has a non-negligible effect on the evolution of the total mass in suspension. The model with TD predicts a lower rate of deposition in flows with any concentration. This reflects the important role played by TD in accurately predicting depositional structure.

For a comparison between the experimental data and the numerical results, both results agree well for flows of concentration 1% - 5% (b – h) but there is a slight disagreement for the flows of concentration 0.5% and the models agree poorly for flows at the lowest concentration 0.27%. This suggests that the TD does not work well for low concentrated flows.

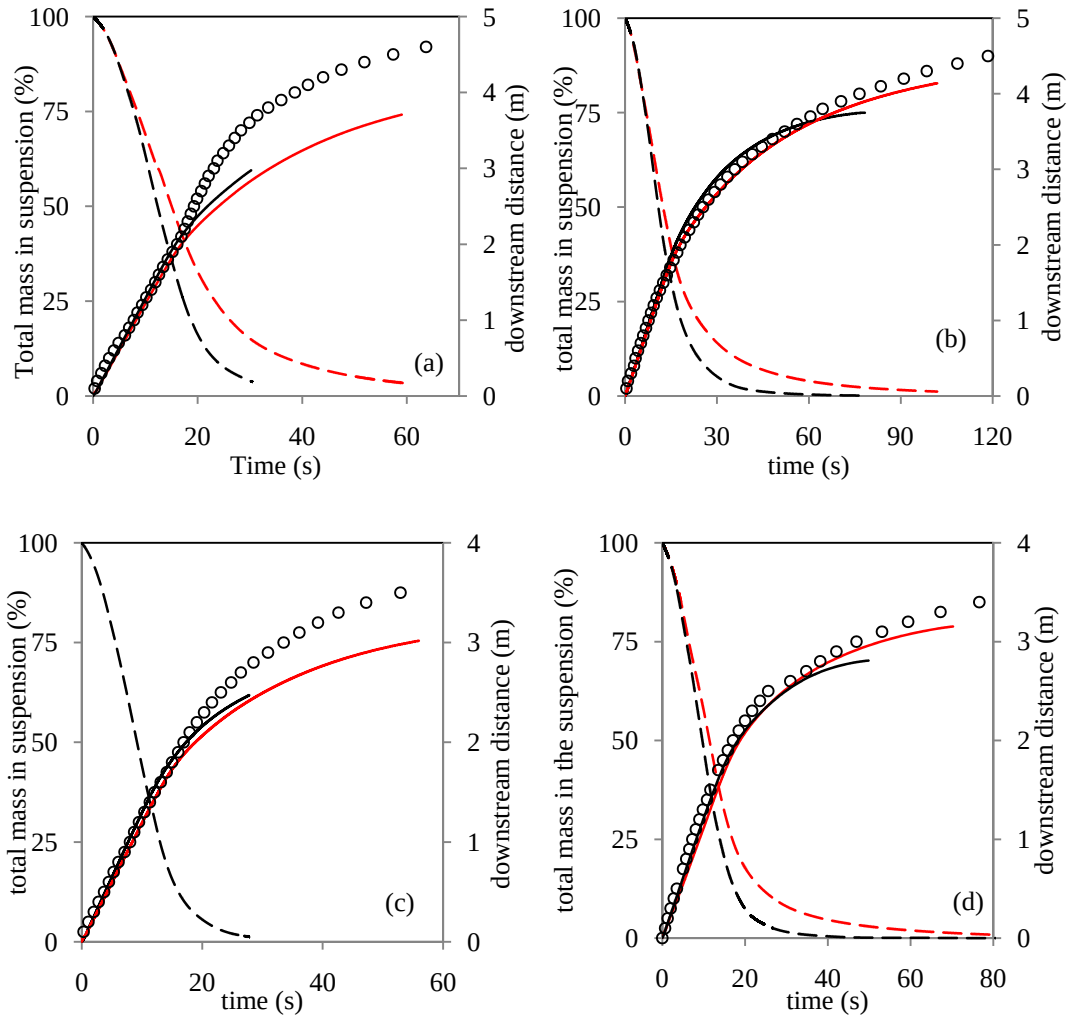

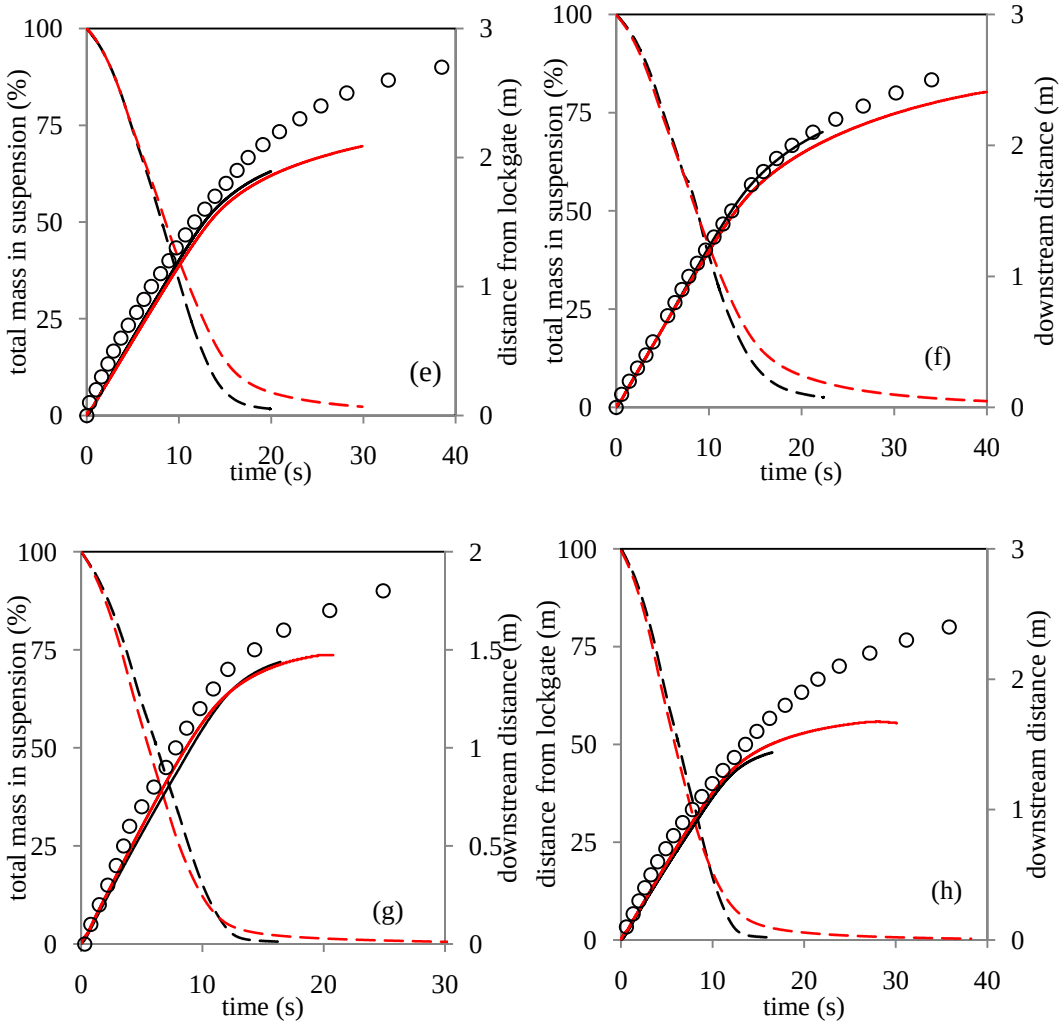

Figure 5.29 The prediction on the percentage total mass in suspension as a function of time (left axis, dashed-lines) and the propagation of the front (right axis, solid lines) of the flows for Series A, (a) S58, (b) UNS64, (c) S71, (d) UNS74, (e) S87, (f) UNS83 (g) S115 and (h) UNS109. The circles (O) represent the experimental data, the black lines represent the solution of the Mixture Model without TD and red lines represent the solution of the Mixture Model with TD.

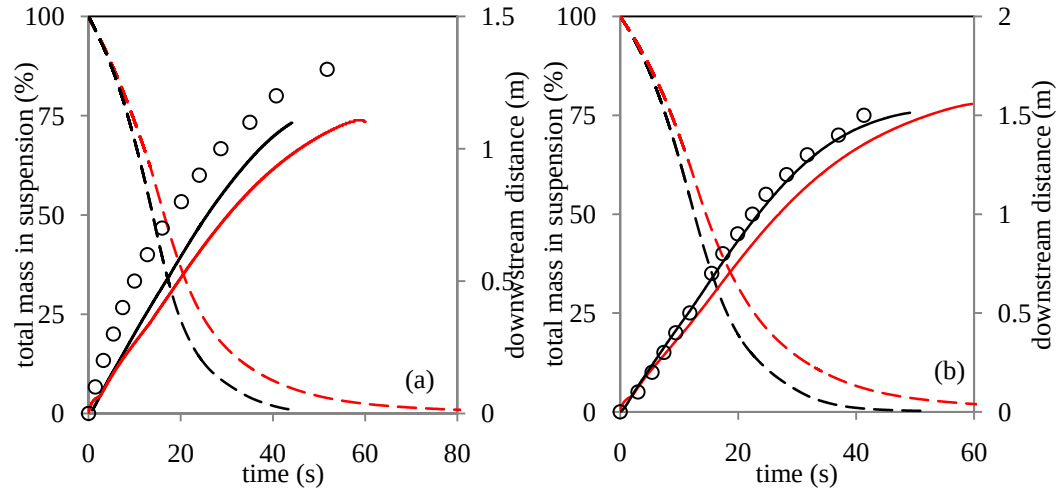

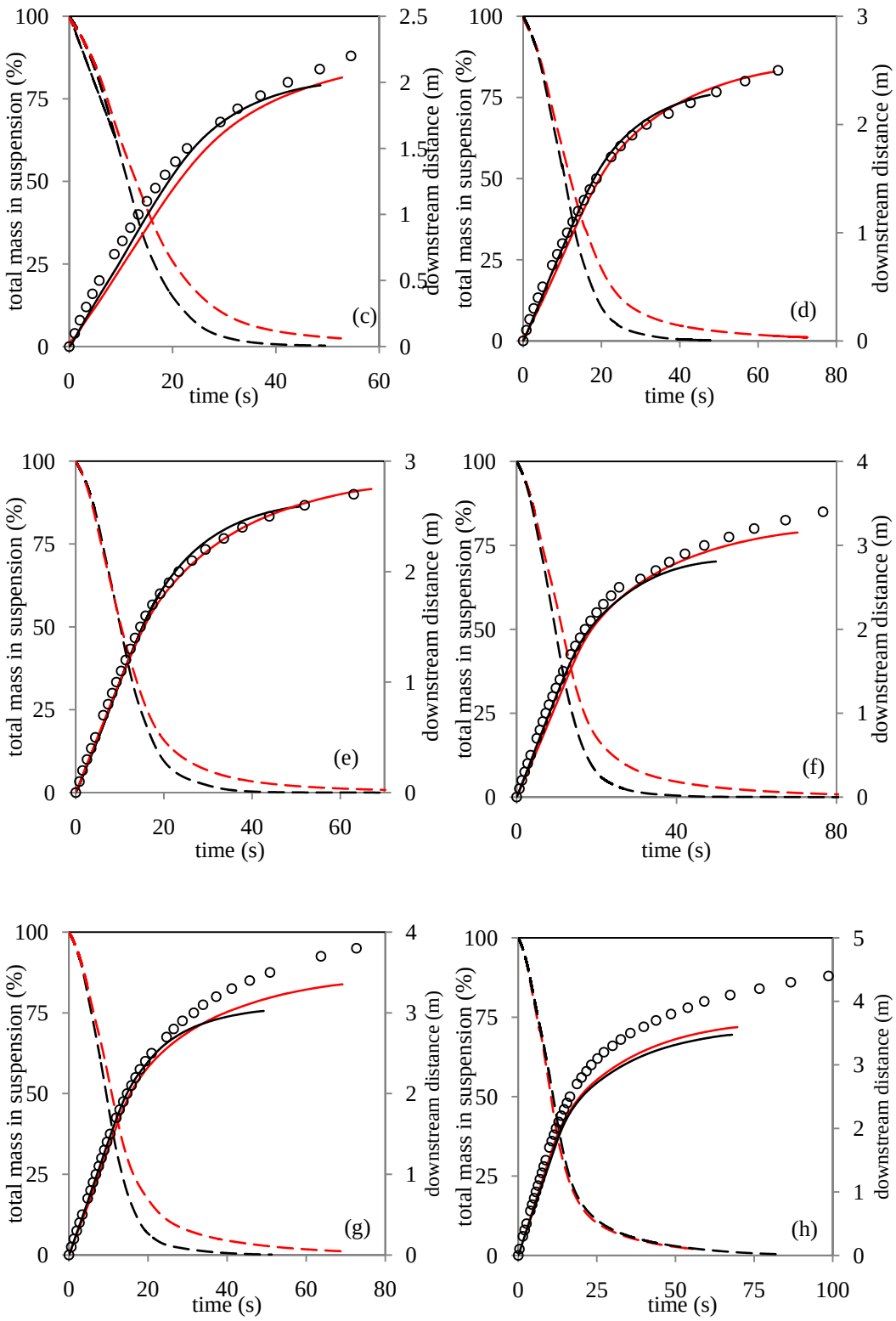

Figure 5.30 The prediction on the percentage total mass in suspension as a function of time (left axis, dashed lines) and the propagation of the front (right axis, solid lines) of the flows for Experiment B, (a) C027, (b) C050, (c) C100, (d) C150, (e) C200, (f) C288 (g) C388 and (h) C500. The circles (O) represent the experimental data, the black lines represent the numerical solution without turbulent dispersion and red lines represent the numerical solution with turbulent dispersion.

5.9.4 Concentration Field

In section 5.9.1, we have noticed two major trends in the results that contradict the observations that we made in Chapter 3, i.e.

i. the prediction of the Mixture Model with TD on the deposit mass compares better with the experimental data than the Mixture Model without TD, and
ii. the differences between the numerical results of the Mixture Model with and without TD are not as great as that observed for the cases studied in Chapter 3 (Series C).

These two observations lead to a question regarding the differences between the predictions of both models on the concentration fields, for the A and B Series of experiment, and also for the Series C data. In addition, we observe that the influence of TD on the deposition becomes increasingly less pronounced with increases in particle size, and when the flow concentration is low; these effect might be explained from the studying the concentration distribution of the flows. Despite having no experimental data on the concentration field for comparing with the numerical prediction, it is still worthwhile to present the numerical prediction on the concentration fields to evaluate the effect of turbulent dispersion.

The concentration fields of flows S58, S71 and S115 of Series A, and flows C050, C200, and C500 of Series B from the predictions of the Mixture Model without and with TD are presented here and compared. These flows represent the extremes in the range of particle size or concentration employed in the current investigations. The behaviour of the rest of the flows is thought to lie between the selected flows and hence they are not presented here.

Figures 5.31 – 5.36 shows the prediction from the Mixture Model both without (top) and with (bottom) TD on the evolution of the concentration fields of flows S58, S71, S115, C050, C200 and C500, respectively. From these figures, the following observations can be made:

(i) Similarly to the prediction of the flows of Series C (see Figures 3.3 – 3.7), solutions from model with TD shows a strong concentration stratification within the flows and the size of the flows is bigger than those predicted by model without TD as a result of sediment dispersal (see flows S58 and S71).

On the other hand, the flows without TD predict the concentration to be rather uniform within the flows and the flows dissipate much more quickly than those predicted by models with TD. These results convince us that TD acts consistently in the flows from Series A, B and C in a way that accords with the purpose of TD algorithm.

(ii) The effect of TD is significantly diminished in flows carrying coarse particles, e.g., S115, where we can observe only a small difference between the solutions from both models with and without TD at t =5s and 10s. This implies that the effect of TD decreases with an increase in the particle size and there is a threshold to the grain size for a specific flows speed where TD ceases to be effective. In this case, the grain size employed in flows S115 appears to be coarse enough to resist the effect of TD in the flow.

(iii) The effect of TD increases with decreasing flow concentration. It can be observed that very strong and thick concentration stratification is developed in the low concentration flow C050 and this effect decreases with an increase in the flow concentration. For instance, only a small difference between the concentrations of flows C500 from both models with and without TD is observed, which clearly suggests the effect of TD has been suppressed. What is surprising here is that the prediction of the model with and without TD on the final deposit mass profile of low concentration flows C050 matches well. This could be coincidental but may also show that different concentration distributions could result in a similar final deposit thickness profile.

We showed that the models with and without TD yield a consistent prediction in flows of all Series A, B and C. Also, we demonstrated the effect of particle size and concentration on the effect of TD in a flow. However, comparing the concentration fields does not reveal why TD model works better in flows of Series A and B but poorly in flows of Series C.

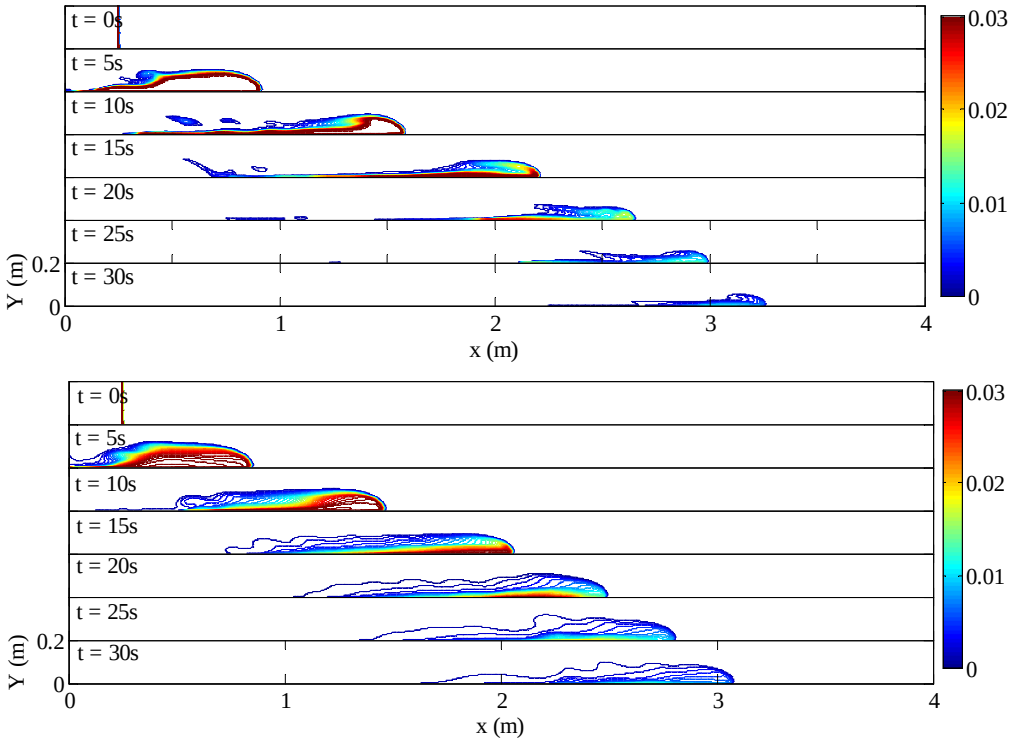

Figure 5.31 Prediction from the Mixture Model (above) without TD and (bottom) with TD on the concentration distribution of flows S58 at t = 5, 10, 15, 20, 25, and 30s.

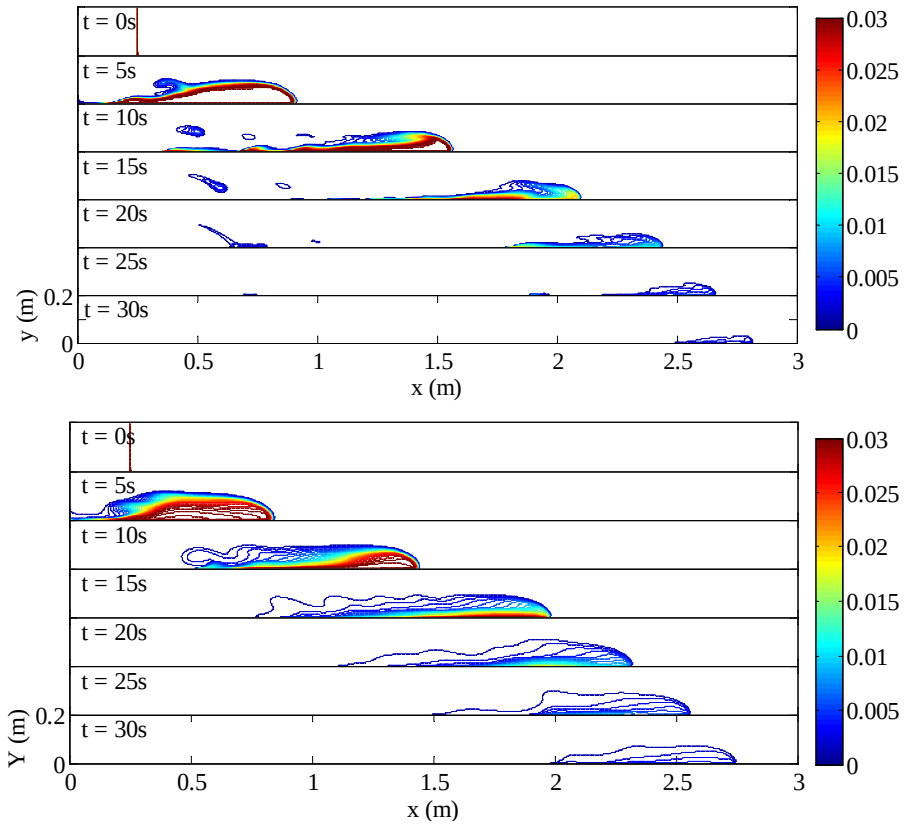

Figure 5.32 Prediction from the Mixture Model (above) without TD and (bottom) with TD on the concentration distribution of flows S71 at *t* = t = 5, 10, 15 and 20s.

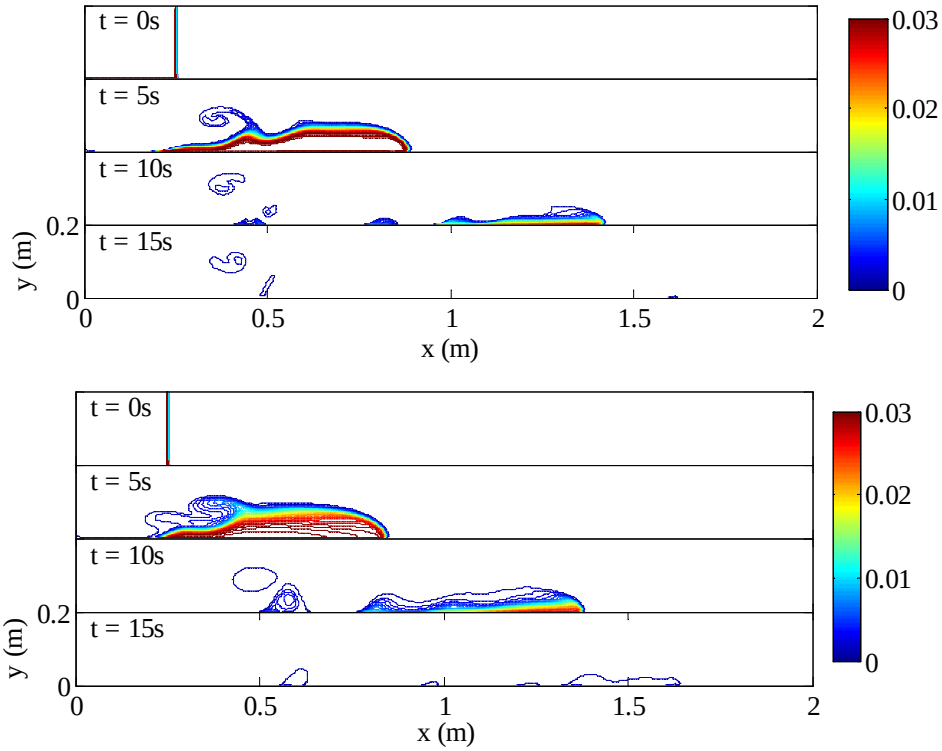

Figure 5.33 Prediction from the Mixture Model (above) without TD and (bottom) with TD on the concentration distribution of flows S115 at t = 5, 10, 15 and 20s.

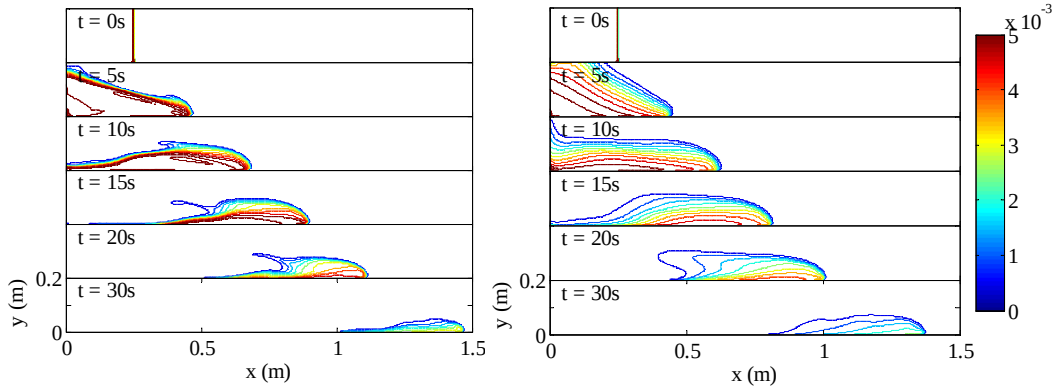

Figure 5.34 Prediction from the Mixture Model (left) without TD and (right) with TD on the concentration distribution of flows C050 at t = 5, 10, 15, 20 and 30s.

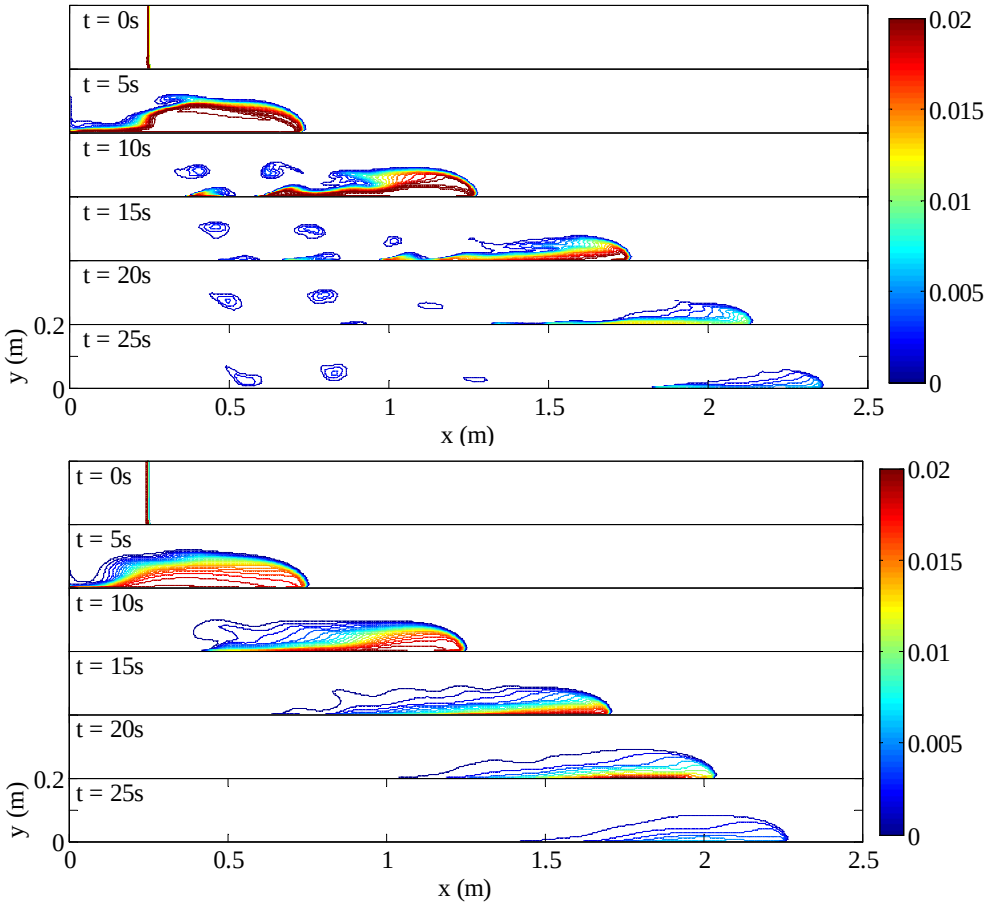

Figure 5.35 Prediction from the Mixture Model (above) without TD and (bottom) with TD on the concentration distribution of flows C002 at *t* = 5, 10, 15 and 20s.

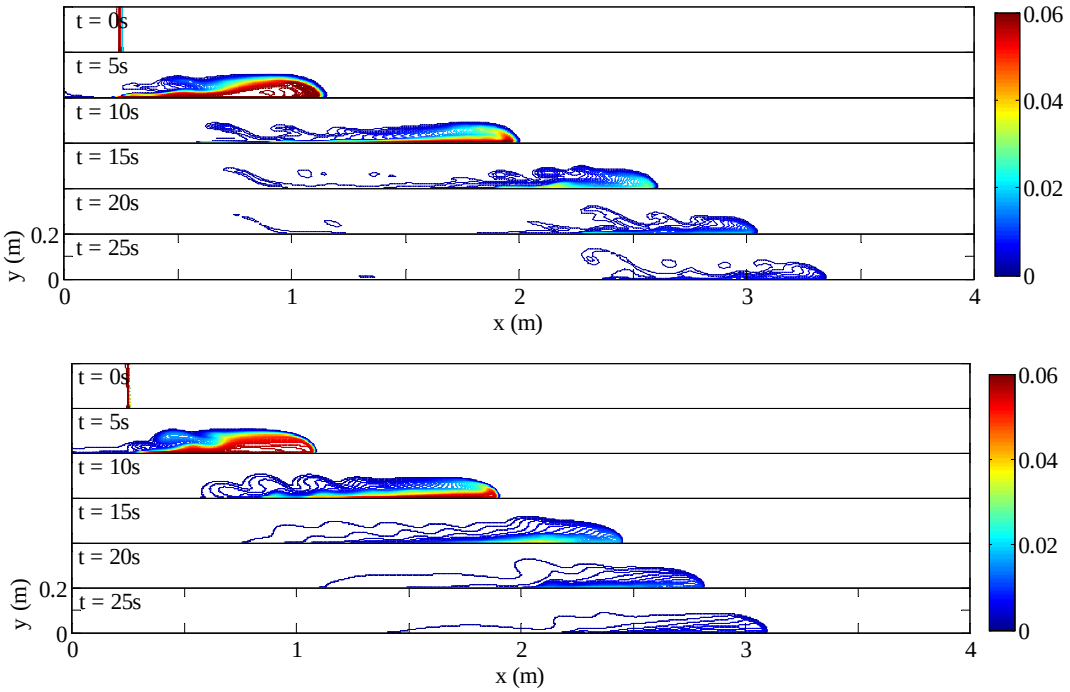

Figure 5.36 Prediction from the Mixture Model (above) without TD and (bottom) with TD on the concentration distribution of flows C005 at *t* = 5, 10, 15, 20 and 25s.

5.9.5 TD Distribution

Comparison of modelled concentrations fields only allows a qualitative evaluation of the effect of TD in the flows. A quantitative evaluation is needed in order to better assess how significance of TD varies in flows from Series A, B and C. This can be achieved by plotting the ratio of TD to the particle slip velocity, namely (see section 2.4.3)

$$r_{TD} = \frac{\left|-\frac{D_t}{\sigma_t}\left(\frac{\nabla\alpha_p}{\alpha_p}-\frac{\nabla\alpha_f}{f}\right)\right|}{|U_s|} \tag{5.3}$$

If the values of r_{TD} > 1, TD is greater than the particle downward velocity and particles are then pushed upward by TD if the concentration gradient is negative.

Figures 5.37 shows the distribution of r_{TD} within flows G69, G25, G37 and G13 (Series C) at *t* = 10s (top), flows S58, S71 and S115 (Series A) at *t* = 5s, and flows C050, C100, C200 and C500 (Series A) at *t* = 10, 8, 5, and 3s, respectively (Series B). It can be observed that, aside from the flows C050, the values of r_{TD}in flows from Series A and B are all, in overall, significantly smaller than those in flows G25, G37 and G13 from Series C. The former has values about 0.5 in the bulk flow whereas the latter has 2 or greater. This implies the effect of TD in flows from Series C is four or more times greater than those investigated here. Clearly from these figures, it can be seen that the strength of TD is increased by many-fold when the particle grain size is decreased to below 40 μm or concentration less than 0.5%. This raises a question on whether the accuracy of TD only breaks down in flows carrying fine particles and low concentration flows. However, it should be noted that G69 from Series C has valued of r_{TD} close to those from Series A and B. Therefore it is still surprising that TD yield accurate results for Series A and B but not for Series C.

A question that remains to be answered is whether it is the over-prediction of the turbulence (characterised by eddy viscosity μ_t) in the flow or a fault in Simonin model that causes the apparently contradictory results. We recall that the Simonin model adjusts the strength of TD by multiplying the eddy viscosity with C_{TD} (see equation (2.41), whose value ranges between 0 and 1. If C_{TD} has a value of 1, TD is at the maximum strength. Large particles decrease the value of C_{TD} and vice versa. Therefore, comparing the distribution of C_{TD} in flows from Series A, B and C can

partially indicate whether it is C_{TD} or the eddy viscosity μ_t that results in the large changes in the values of TD in different flows. Figure 5.38 shows the distribution of C_{TD} within the flows represented in Fig. 5.37. It can be observed that C_{TD} is about 1 in flows G25, G37 and G13 and varies from 0.7 to 1 in flows G69. On the other hands, C_{TD} in flows from Series C is about 0.4 to 0.8. The values of C_{TD} vary more significantly within the various flows of Series A, i.e. it varies between 0.5 and 1 in flows S58, is more or less 0.5 in flows S71, and only about 0.1 in flows S115. Clearly, C_{TD} is only significantly reduced when the particle size is very coarse (d_p = 115μm). The value of C_{TD} decreases from 1 to about 0.5 or more when the particle size is increased from range 13-37μm to range 58-74μm. This small change suggests that C_{TD} (hence the Simonin model) is unlikely to be the reason r_{TD} varies so significantly in these flows.

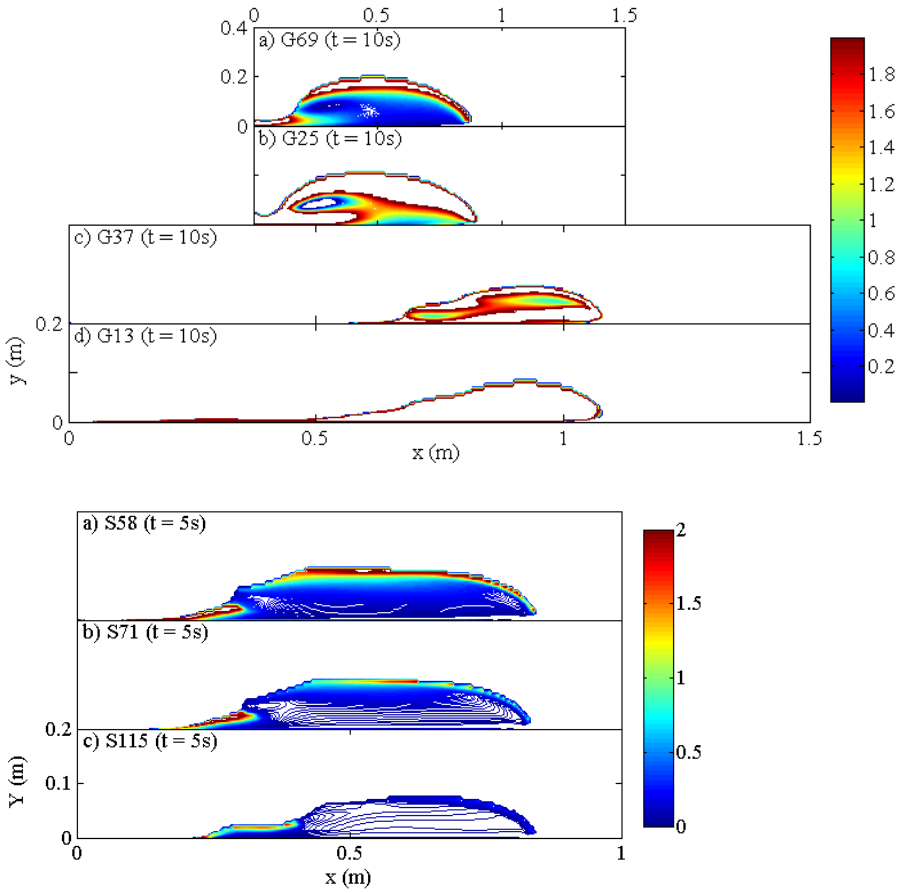

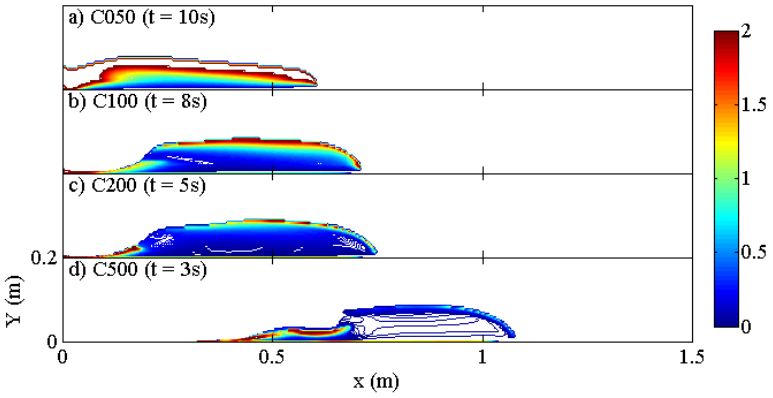

Figure 5.37 Contours plot of the ratio of the TD to the magnitude of the particle slip velocity from the prediction of the Mixture Model with TD on flows investigated in Chapter 3 (top), selected flows from Series A (middle) and B (bottom). See each figure for the name and the time of each flow. The values are clipped to range 0 to 2.

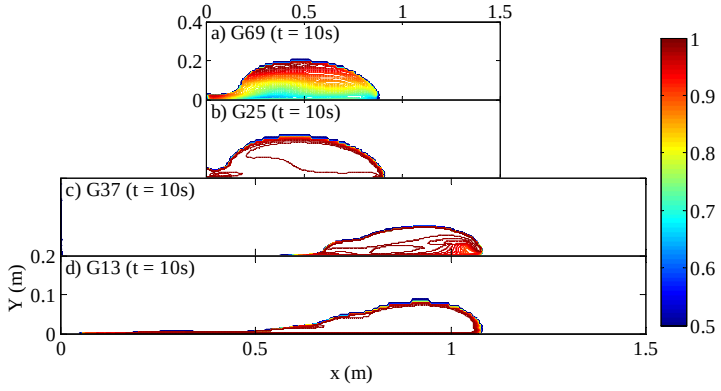

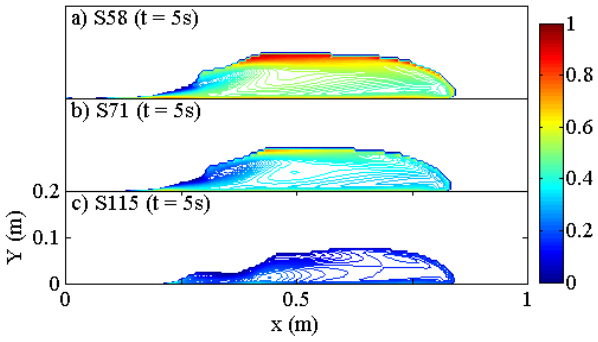

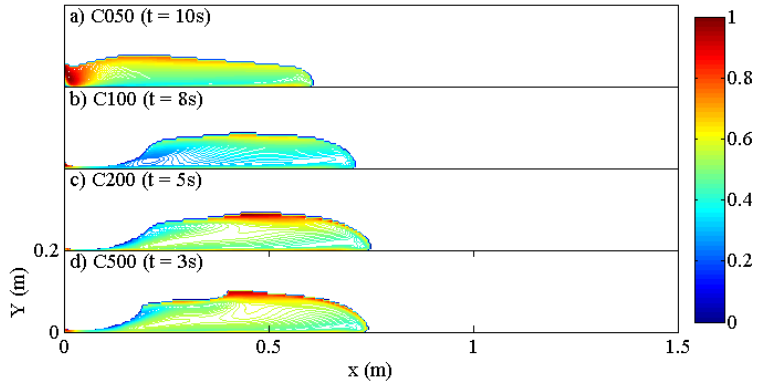

Figure 5.38 Contours plot of the parameter M_{TD} of Simonin model (see equation (3)) from the prediction of the Mixture Model with TD on flows investigated in Chapter 3 (top), selected flows from Series A (middle) and B (bottom). See each figure for the name and the time of each flow.

5.10 Conclusions

This work comprises two parts, namely:

i. an experimental investigation performed in order to extend the validation data (propagation and deposit characteristics of the flows) of surge-type lock-release flows to a greater range of concentration and grain size,
ii. numerical investigation of the experiment flows conducted herein in order to further assess the performance or accuracy of the Mixture Model in simulating turbidity currents of a wide range of concentration and grain size.

The experimental investigation was successfully conducted. The accuracy and robustness of the measuring technique employed in the experiment was successfully verified. The experimental data agree well with the previous investigations, namely flows carrying coarse particle leave greater mass in the proximal deposit and terminate earlier than those carrying fine particles. Despite conventional results being achieved for the rate of propagation and the deposit mass profile, a surprising result has been observed for the grain size characteristics of the deposit. It was found that the grain size in the deposit from the flows carrying sieved materials changes relatively little from upstream to down-stream, compared that from the flows carrying unsieved materials. The change in the mean grain size in the deposit with respect to that of the original material of flows S58, S71, S87 and S115 (flows carrying sieved material) is within 10% from proximal to distal, whereas that of

UNS64 (flows carrying unsieved material) drops from +10% at the lock box to -50% at the distal part of the deposit. Such observation suggests that there is a lack of grain size fractionation in the flows carrying sieved material and there is a threshold in the grain size range (characterized by grain size standard deviation) of the original material carried by the flows below which little to no grain size fractionation occurs in the flows. In this case, we observed threshold is in between the grain size standard deviation of 11 and 18 (see Fig 5.18).

All flows investigated in this study have been simulated using a modelling approach similar to that employed in Chapter 3 and the results are compared with experimental prediction. The following key observations and conclusions can be drawn from the comparison between the experimental data and the numerical result:

i. In contrast to its poor agreement with the experimental data and the refined two-fluids model prediction on the deposit mass profile in Chapter 3, the Mixture Model with TD agrees better with the experimental data than the Mixture Model without TD, for the flows investigated in this chapter. In particular, the Mixture Model without TD predicts predict multiple oscillations in the proximal deposit. These oscillations are smoothed out when TD is incorporated into the model.
ii. The prediction from the Mixture Model with TD on the grain size characteristics does not agree well with the experimental data. The Mixture Model always predicts the coarse particle to have a greater relative mass than the fine particle at the proximal deposit and to have lesser relative mass in the distal deposit. On the other hand, the experiment prediction does not produce a consistent trend of observation. In most cases, the differences between the deposit mass profiles of different size classes are relatively small compared to those predicted by the Mixture Model. In other words, the Mixture Model is unable to explain the apparently unfractionated grain size in the deposit. Nevertheless, an inconsistency was noted in the experimental data which suggests the particle mass may not be conserved. Therefore it would be advisable to obtain a new set of data to verify the accuracy of the present data in any follow-on work.

A comparison was carried out on the distribution of the ratio of the TD to the particle slip equation r_{TD} in the flows from Series A, B and C. It was found that that

r_{TD}in flows carrying fine particle (13-37μm) or of low concentration (0.5%) has values of r_{TD} 2-3 times greater than those in flows carrying (>58 μm).

A comparison on the distribution of C_{TD} in flow from from Series A, B and C was performed in order to determine whether a fault in Simonin model contributes to the large variation of r_{TD} in flows from Series A, B and C. It was found that the value of C_{TD} varies mostly between 0.5 to 1; this small change suggests that it is not the case.

Chapter 6

Concluding Remarks

6.1 Thesis Summary

This thesis comprises of a series of investigations performed in order to: (i) better understand the physics governing the transport of particles within turbidity currents, and (ii) build a simple mathematical model for predicting the behaviour of turbidity currents, in particular the propagation of the flow and the sedimentation patterns. The chosen mathematical model is a depth-resolved and time-averaged multiphase model called the Mixture Model, which is suitable for modelling a wide range of multi-phase flows. To improve the robustness of the model, the Mixture Model employs an algebraic slip equation derived by Manninen et al. (1995) in order to algebraically calculate particle velocities. The Mixture Model is solved via a commercial CFD code called FLUENT (FLUENT, 2009).

Chapter 2 outlines in detail the governing equations of the model, the assumptions made in its development, how the model treats flow near the walls, the physics governing the settling motion of particles and the methods used to resolve the turbulence of the flow. Furthermore, a brief review is conducted on the types of mathematical models that have been used to model turbidity currents in the past, including their advantages and limitations, linked to a discussion regarding why the Mixture Model was chosen over other possible approaches. A review is also given on the current understanding of turbidity current mechanics.

Chapter 3 details the validation of the Mixture Model in simulating lock-release flows of low concentration. A total six lock-release flows chosen from three separate authors (Gladstone et al. 1998; Gladstone & Pritchard 2010; Rooij & Dalziel, 2001) have been used to validate the accuracy of the Mixture Model. Refined two-fluids model solutions (Hoyes 2008; Necker et al. 2002) are also available for some of the chosen flows, and provide a further validation. A focus was the role that turbulent dispersion (TD) plays in turbidity currents. The chosen turbulent dispersion

formulation incorporated into the model is that derived by Simonin (1991). Evaluation of turbulent dispersion was performed by comparing the numerical solutions both with and without this phenomenon. In the modelled scenarios it was found that turbulent dispersion induces excessive dispersion, resulting in very low deposit mass being predicted upstream. Mixture Model predictions of deposit mass profile made without turbulent dispersion compare significantly better with both experimental data and the refined two-fluids model solution than those with turbulent dispersion. Turbulence modulation was incorporated into the Mixture Model with TD in order to dampen the excessive dispersion in the solution, but its effects were found to be insignificant, and this is probably due to the low mass loading within the flows. A firm conclusion cannot be drawn on whether the formulation of turbulent dispersion is faulty or there are unknown important physics that have yet to be taken into account that counteract the modelled dispersion effect. The accuracy of the turbulence model $k-\epsilon$ RNG was verified by comparing the results with those from turbulence model $k-\omega$ SST.

In Chapter 4, the significance of the lift force on a particle due to flow shear and particle rotation is investigated. Using the force balance equation, simple expressions are derived for evaluating the effects of the lift force on particles of small (Re_p < 0.1) and large (Re_p > 1000) particle Reynolds number. For fixed values of Re_ω and Re_R, the slip velocity is always reduced by the lift force and this effect increases with an increase in the particle Reynolds number. A non-dimensional quantity Λ expressing the ratio of the lift force to the drag force was derived and is defined by

$$\Lambda = \frac{C_L Re_\omega + C_R Re_R}{\frac{3}{4} C_{D\infty} Re_\infty}$$

The quantity Λ is known as the lift number. The value of the lift number can be evaluated for fixed values of Re_ω and Re_R. If Λ is greater than 1, it implies that the lift force is greater than the drag force and vice versa. The lift force may act to push the particle forward or backward depends on the sign of the shear. The derived analytical expressions are used to evaluate the effect of the lift force on particles immersed in turbidity currents. The lift force has little effect on the magnitude of the settling velocity of the sand sized particles commonly carried by turbidity currents, but may slightly deflect the settling direction of large particles in small-scale flows.

It was concluded that it is unlikely that the lift force could be important for surge-type turbidity currents that predominantly carry sand. The lift force may be significant if turbidity currents can achieve a velocity significantly higher than that governed by equation (4.9.3) (i.e. $u_N = Fr(g'h)^{1/2}$) which describes the front propagation of turbidity currents.

Chapter 5 describes new experimental investigations performed on lock-release flows of a wide range of concentration and grain size in order to provide data for a more comprehensive validation of the Mixture Model. Three different kinds of measurements were performed, to characterise flow front propagation, and the axial variation in deposit mass distribution and grain size characteristics. The experimental data agree well with previous investigations (e.g., Gladstone et al. 1998), confirming that flows carrying coarse particles have relatively greater mass in the proximal deposit and terminate earlier than those carrying fine particles. On the other hand, an unexpected result has been observed for the grain size characteristics of some deposits. It was found that the grain size in the deposits from flows carrying particles whose grain size range was reduced, following sieving, change relatively little from upstream to downstream compared with that from the flows carrying unsieved materials. This observation suggests that there is a lack of grain size fractionation in the flows carrying sieved material and there is a threshold in the grain size range (i.e., the standard deviation) of the original material carried by the flows, below which little or no grain size fractionation occurs in the flows. In this case, we observed that the threshold is between the grain size standard deviation values of 11 and 18.

All the flows investigated in this work were simulated using a modelling approach similar to that employed in Chapter 3 and the results are compared with the experimental data. Output from the Mixture Model with TD agrees better with the experimental data than the Mixture Model without TD, in contrast to its poor agreement with the experimental data and the refined two-fluids model prediction on the deposit mass profile in Chapter 3. A firm conclusion cannot be drawn on whether it is a fault within the turbulence model of Simonin (1991) or an extra unknown turbulent mechanism that is missing in the model that results in the inaccurate prediction of the Mixture Model on the deposit mass profile of flows

carrying low concentrations of silicon carbide (i.e., all the flows investigated in Chapter 3).

The prediction from the Mixture Model with TD on the grain size characteristics does not agree well with the experimental data. The Mixture Model always predicts the coarse particles to have a greater mass than the fine particles in the proximal deposit and the opposite in the distal deposit.

6.2 Key Conclusions

The aims of the thesis were to

(i) Build a robust and practical numerical model for predicting natural turbidity currents.
(ii) Investigate the key physics governing sediment transport within turbidity currents.

6.2.1 The Accuracy of the Mixture Model in Predicting the Turbidity Currents

The accuracy of the Mixture Model has been partially verified in these studies. The major problem lies with the excessive dispersion exhibited in the simulations of the flows carrying silicon carbides. Whether the cause is due to a fault within the turbulent dispersion model itself or in the inaccurate prediction on the eddy viscosity of the flow is not resolved in this study. On the other hand, incorporation of turbulent dispersion effects has been found to be essential to ensure accurate predictions of flows carrying glass beads, such as those investigated in Chapter 5. Nevertheless, it is difficult to argue that the experimental data on flows carrying silicon carbide particles are inaccurate since three sets of refined two-fluids model solutions from previous authors all agree well with these data. Clearly further investigation is needed in order to shed light on these contradictory points. If refined two-fluids model solutions and the experimental data on flows carrying silicon carbide particles are deemed to be accurate, the problem could lie within the capacity of the Mixture Model to solve the turbulence of the flows or the three dimensional affects that are neglected in the simulations in this studies. Other possible reasons are particle entrainment, particle shape and possibly the turbulent dispersion model. If the experimental data of flows carrying glass beads and the

Mixture Models are deemed accurate, further experimental investigation on flows carrying glass beads should be conducted in order to further validate the accuracy of the Mixture Models in predicting flows carrying particles of different density. It is also important to mention that it is rather counter-intuitive that the numerical instabilities in the solution of the simulations increase when an increasingly smaller time-step is employed and the precise reason for this is still not known, although a stable solution does exist for a range of value of time steps which gives us confidence on the accuracy of the solution.

6.2.2 Physical controls on the settling motion of particles suspended in turbidity currents

We have investigated the effects of several commonly known particle-flow interaction forces on the settling motion of particles in turbidity current. They are the drag force, the shear-induced lift force, turbulent dispersion and turbulent modulation. The effects of turbulent modulations are concluded to be generally insignificant, probably due to the low particle mass loading in the flows investigated in these studies. However, the extent of its significance in high concentration flows is not investigated here.

The shear-induced lift force is found to always reduce the magnitude of the settling velocity of particles and additionally changes the direction in which the particles settle. Particles maybe pushed forward or backward depending on the sign of the shear in the flow. However, in turbidity currents, it was estimated that the effect of lift force on sand particles is unlikely to be significant. The lift force is only likely to be significant if the flows have significantly high velocity (hence high shear) or when the ratio of particle to fluid density approaches unity.

Turbulent dispersion is greatest for small particles carried in low concentration flows. For instance, the ratio of the turbulent dispersion velocity to the magnitude of the particle slip velocity decreases from a value greater than 1 to less 0.5 when the concentration is increased from 0.5% to 5%. The significance of turbulent dispersion in flows is also influenced by the ratio of the particle size to the flow velocity. The smaller the ratio, the greater is the turbulent dispersion effect.

It can be concluded that the drag force and turbulent dispersion are the key physical mechanisms governing the settling motion of particles suspended in low

concentration turbidity currents. The significant of turbulent dispersion decreases with an increase in the particle size. Therefore, there is a threshold in particle size above which only the drag force is important.

6.3 Future work

The reason for the discrepancy between the experimental data and the Mixture Model prediction on the deposit thickness of flows carrying silica carbide particles has not been determined in this thesis. However, it may be due to the effect of particle shape. This can be ascertained by comparing the Mixture Model prediction with the experimental data for flows carrying silica carbide particles or glass beads with all the other initial conditions being fixed (same flow concentrations, flume geometry and particle settling velocities). Since the Mixture Model already achieves a good comparison with the flows carrying glass beads, we only need to conduct experiments on flows similar to those carrying fine silicon carbide particles, as studied in Chapter 3, but using glass bead particles, using similar flow concentrations and particle settling velocities. Then the consistency of the Mixture Model in predicting the flows carrying glass beads or silica carbide particles can be determined by comparing how well it predicts the mass deposit profile of these flows. In addition, it should be noted that particle concentration profiles of the flows play an important role in influencing the accumulated deposit thickness; adding turbulent dispersion to the model significantly changes the concentration distribution which subsequently changes the accumulated deposit thickness. Therefore, it would be beneficial to obtain experimental measurements on the flow concentration so that a comparison with the numerical prediction can be performed and the accuracy of the Mixture Model can be further ascertained. If the Mixture Model cannot accurately predict these flows (carrying silica carbide particles in new experimental conditions) well, it is almost certain that the effect of shape is important and therefore it is worth investigating the interaction of particle shape with the flow turbulence in turbidity currents, etc. If the Mixture Model predicts these flows well, then this indicates that the effect of particle shape is not the cause of the discrepancy, and it appears that the Mixture Model could be inconsistent in predicting flows of different flume geometry. On the other hand, it was shown that the Mixture Model does not agree well with the predictions of refined two fluids model. Given that the Mixture Model is a simplified model which employs

numerous assumptions, it is worthwhile assessing how these assumptions potentially could affect the prediction on the flows. The following is the list of the assumptions and the possible further work that could be performed on them:

(a) In addition to the treatment of the turbulence, one major difference between the refined two phase model and the Mixture Model is that the latter is a three-dimensional simulation whilst the former is a two-dimensional simulation. Therefore, it would be advantageous to conduct a three-dimensional simulation using the Mixture Model in order to assess the three-dimensionality effect (e.g. cross-stream flow) on the sediment dispersion within the flows.

(b) Again, a possible reason that the refined two phase model performs better than the Mixture Model is because the former resolves the structure of the turbulence. Therefore, it will be beneficial to compare the prediction on the turbulence characteristics from a model, such as the LES against those obtained from a two-equation model in order to ascertain their differences and the possible effects that these differences have on the deposition characteristics of turbidity currents.

(c) While the accuracy of the turbulent dispersion model of Simonin (1991) has been validated in gas-solid flows, its accuracy in solid-liquid flows has yet to be validated. It would be worth comparing the Simonin model against the turbulent dispersion model that is more conventionally employed in the modelling of sediment-laden water channel flows (e.g. Huang et al., 2005).

(d) In the derivation of the algebraic slip equation, a number of the simplifications have been made. The terms that have been dropped can be rewritten as follows:

$$\alpha_p\rho_p\left[\rho_p\ \frac{\partial U_{Mpk}}{\partial t}+\left(U_{Mpi}\cdot\nabla\right)U_{Mpk}\ \right]$$
$$+\alpha_p\rho_p\left[(U_{mi}\cdot\nabla)U_{Mpk}+\left(U_{Mpi}\cdot\nabla\right)U_{mk}\right]+$$
$$\alpha_p\nabla\cdot(\tau_{mik}+\tau_{Dik})+\nabla\cdot\left(\alpha_p\tau_{pik}\right)$$

Essentially these simplifications are only valid if (i) $U_{Mp}\rightarrow 0$, which means that the particle phase instantaneously reaches the equilibrium state with the mixture phase, and (ii) the flow is highly turbulent such that the turbulent stresses are much larger than the diffusion stresses ($\tau_{mik},\ \tau_{Dik}$, and τ_{pik}). In the future work, condition (i) should be checked by comparing the particle

relaxation time against the mixture characteristic time scale which can be estimated using the expression (Manninen et al., 1995):

$$t_m = \left| \frac{U_{mk}}{\frac{\partial U_{mk}}{\partial t} + (U_{mi} \cdot \nabla) U_{mk}} \right|$$

Further, condition (ii) should be checked by computing the ratio of the diffusion terms to the turbulent stresses. In addition, it would be insightful to compare the Mixture Model against the full Eulerian-Eulerian multiphase model which models the complete particle momentum equation.

(e) The turbulence modulation model of Chen and Wood (1985) has been well-validated in the application of gas-solid flows but it is untested in liquid-solid flows. It may be advantageous to compare the model prediction against experimental data on the turbulence modulation in the liquid-solid flows in order to ascertain its accuracy.

It is interesting to note that when the grain size standard deviation (SD) is decreased to 11μm or less, the reduction in the grain size from the upstream to the downstream deposit is significantly inhibited; the mean grain size only decreases by as much as 5% in the distal deposit (compared to the initial condition). This implies reducing the grain size range may impede the grain size fractionation within the flows. Given the strong implications of such a conclusion on the sedimentary studies, it would be worthwhile to further investigate these aspects. In the future, it would be interesting to investigate the grain size in the deposit of flows carrying grain sizes with SD greater than about 18μm and those between 11μm and 18μm in order to gain more complete understanding on the influence of SD on the particle fractionation. In addition, varying the flows concentration but fixing the particle grain size could be valuable for determining the influence of the flow concentration on the decrease in the deposit grain size. Also the influence of the grain size standard deviation on the run-out distance and the deposit thickness profile is not explicitly studied in this paper and therefore it would also be interesting to carry out further investigations in order to study those aspects.

References

Adoua, R., Legendre, D. and Magnaudet, J. (2009) Reversal of the lift force on an oblate bubble in a weakly viscous shear flow. *Journal of Fluid Mechanics*, 6289(1), 23–41.

Alajbegovic, A., Assad, A., Bonetto, F., and Lahey Jr., R.T. (1994) Phase distribution and turbulence structure for solid fluid up flow in a pipe. *International Journal of Multiphase Flow*, 20(3), 453-479.

Altinakar, M.S., Graf, W.H., Hopfinger, E.J. (1996). Flow structure in turbidity currents. *J. Hydraulic Res.* 34(5), 713-718.

Asmolov, E.S. (2002) The inertial lift on a small particle in a weak-shear parabolic flow. *Physics of fluid*, 14(1), 15-28.

Auton, T.R. (1987) The lift force on a spherical body in a rotational flow. *Journal of Fluid Mechanics*, 183, 199-218.

Bagchi, P. and Balanchandar, S. (2002) Effect of free rotation on the motion of a solid sphere in linear shear flow at moderate Re. *Physics of fluids*, 14(8), 2719-2737.

Bagnold, R.A. (1966) An Approach to the Sediment Transport Problem for General Physics. *Geological Survey Professional Paper 422-I*. Geological Survey, Washington, DC.

Bagnold, R.A. (1974) Fluid forces on a body in shear-flow; experimental use of ‘stationary flow. *Proc. R Soc. London. A*, 340(1621), 147-171.

Bahari, A. M. and Hejazi, K. (2009) Investigation of Buoyant Parameters of $k-\epsilon$ turbulence model in gravity stratified flows. *World Academy of Science, Engineering and Technology*, 31, 533-540.

Bel Fdhila, R'Bei, (1991) Analyse experimentale et modelisation d'un ecoulement vertical a bulles un elargissement brusque. PhD thesis, L'Institute National Polytechnique de Tolouse, Tolouse, France.

Benjamin, T.B. (1968) Gravity currents and related phenomena. *Journal of Fluid Mechanics*. 88, 223-240.

Bernard, D.C. and Harlow, F.H. (1988) Turbulence in multiphase flow. *International Journal of Multiphase Flow*, Vol. 14, p. 679.

Benjamin, T.B. (1968) Gravity currents and phenomena. *Journal of Fluid Mechanics*, 31, 209-248.

Bonnecaze RT, Huppert HE, Lister JR. (1993) Particle-driven gravity currents. *Journal of Fluid Mechanics*, 250, 339-369.

Bridge, J. S. and Bennett, S.J. (1992) A model for the entrainment and transport of sediment grain sizes, shapes, and densities. *Water Resources Research*, 28(2), 337-363.

Brors, B. and Eidsvik, K.J. (1992) Dynamic Reynolds stress modelling of turbidity currents. *Journal of Geophysical Research*, 97(C6), 9645-9652.

Bluemink, J.J., Lohse, D., Prosperetti, A. and Wijngaarden, L.V. (2008) A sphere in a uniformly rotating or shearing flow. *Journal of Fluid Mechanics*, 600, 201-233.

Bluemink, J.J., Lohse, D., Prosperetti, A. and Wijngaarden, L.V. (2010) Drag and lift forces on particles in a rotating flow. *Journal of Fluid Mechanics*, 643, 1-31.

Burns, A.D., Frank, T., Hamill, I., Shi, J.M. (2004). The Favre-averaged drag model for turbulent dispersion in *Eulerian Multi-Phase flows. 5th International Conference of Multiphase flow* Yokohama (316), 1-17.

Camenen, B. (2007) Simple and general formula for the settling velocity of particles. *Journal of Hydraulic Engineering*, 133(2), 229-233.

Chen, C.P., Wood, P.E. (1985). A turbulence closure model for dilute gas-particle flows. *Canadian J. Chemical Eng.* 63(3), 349-360.

Cheng, N. S. (1997) Simplified settling velocity formula for sediment particle. *Journal of Hydraulic* Engineering, 123(2), 149–152.

Cherukat, P., McLaughlin, J.B., and Dandy, D.S. (1999) A computational study of the inertial lift on a sphere in a linear shear flow field. *International Journal of Multiphase flow*, 25, 14-33.

Chhabra, R.P., McKay, A. and Wong, P. (1996) Drag on discs and square plates in pseudplastic polymner solutions, *Chemical Engineering Science*, 51(24), 5353-5356.

Choi, S.-U., and Garcia, M. H. (2002) k--epsilon Turbulence Modeling of Density Currents Developing Two Dimensionally on a Slope. *Journal of Hydraulic Engineering*, 128(1), 55-63.

Choux, C. M., and Druitt, T. H. (2002) Analogue study of particle segregation in pyroclastic density currents, with implications for the emplacement mechanisms of large ignimbrites, *Sedimentology*, 49, 907-928.

Clift, R., Grace, J.R. and Weber, M.E. (1978) Bubbles, drops and particles. *Academic Press,* pp. 380.

Csanady, G.T. (1963) Turbulent diffusion of heavy particles in the atmosphere. *Journal of the Atmospheric Sciences,* 20, 201-208.

Dallavalle, J. (1948) Micrometrics: The technology of fine particles. *Pitman,* London.

Dandy, S.D. and Dwyer, H.A. (1990) A sphere in shear flow at finite Reynolds number: effect of shear on particle lift, drag and heat transfer. *Journal of Fluid Mechanic,* 216, 381-410.

Dade, W.B., Huppert, H.E. (1995). A box model for non-entraining suspension-driven gravity surges on horizontal surfaces. *Sedimentology* 42(3), 453-471.

Davidson, L. (1990) Second-order correction for the k-ϵ model to account for non-isotropic effects due to buoyancy. *International Journal of Heat and Mass Transfer,* 33, 2599-2608.

Deutsch, E. and Simonin, O. (1991) Large eddy simulation applied to the modelling of particulate transport coefficients in turbulent two-phase flows. *Symposium on Turbulent Shear Flows, 8th, Munich, Federal Republic of Germany,* Vol. 1, p. 10-1-1 to 10-1-6.

Dietrich, W.E. (1982) Settling Velocity of Natural Particles. *Water Resources Research,* 18(6), 1615-1626.

Drew, D. A. (1983) Mathematical Modelling of Two-Phase Flow. Annual Review of Fluid Mechanics. Vol. 15, 261-291.

Drew, D.A. and Lahey Jr., R.T. (1987) The virtual mass and lift force on a sphere in rotating and straining inviscid flow. *International Journal of Multiphase Flow,* 13(1), 113-121.

Drew, D.A., Lahey Jr., R.T. (1990) Some supplemental analysis concerning the virtual mass and lift force on a sphere in a rotating and straining inviscid flow. *International Journal of Multiphase Flow,* 16(6), 1127-1130.

Eidsvik, K.J. and Brors, B (1989) Self-accelerated turbidity current prediction based upon ($k - \epsilon$) turbulence, *Continental Shelf Research*, 9(7), 617-627.

Ellison TH, Turner J.S. (1959)Turbidity entrainment in stratified flows. *Journal of Fluid Mechanics,* 6, 423-448.

Felix, M. (2001) A two-dimensional numerical model for a turbidity current. *Particulate gravity* currents, pages, W. McCaffrey, B. Kneller, J. Peakall, eds. Blackwell, Oxford UK.

Felix, M. (2002) Flow Structure of turbidity currents. *Sedimentology*, 49(3), 397-419.

Ferguson, R.I. and Church, M.J. (2004) A simple universal equation for grain settling velocity. *Journal of Sedimentary Research*, 74(6), 933-937.

Fonseca, F. and Hermann, H.J. (2004) Sedimentation of oblate ellipsoids at low and moderate Reynolds number. *Journal of Sedimentary Research*, 342(3-4), 447-461.

Fonseca, F. and Hermann, H.J. (2005) Simulation of the sedimentation of a falling oblate ellipsoid. *Physica A: Statistical Mechanics and its Applications*, 345(3-4), 341-355.

Frank, Th., Shi J.M., and Burns, A.D. (2004) Validation of Eulerian multiphase flow models for nuclear safety applications. *3rd International Symposium on Two-phase Flow Modelling and Experimentation*, Pisa, Italy.

Frank, Th., Zwart P.J., Krepper, E., Prasser H. M., and Lucas, D. (2008) Validation of CFD models for mono- and polydisperse air-water two-phase flows in pipes. *Nuclear Engineering and Design*, vol. 238(3), 647-649.

Gabitto, J. and Tsouris, C. (2007) Drag coefficient and settling velocity for particles of cylindrical shape. *Powder Technology*, 183, 314-322.

Ganser, G.H. (1993) A rational approach to drag prediction of spherical and nonspherical particles. *Powder Technology*, 77, 143-152.

Garcia, M.H. (1994) Depositional turbidity currents laden with poorly sorted sediment. *J. Hydraulic Eng.* 120(11), 1240-1263.

Garcia, M., Lopez F., and Niño, Y. (1996) Characterization of near-bed coherent structures in turbulent open channel flow using synchronized high-speed video and hot-film measurements. *Experiments in Fluids*, 19(1), 16-28.

Gibbs, R.J. (1985) Estuarine flocs: Their size, settling velocity and density. *Journal of Geophysical Research, 90(C2), 3249-3251*.

Giorgio-Serchi, F. (2010) CFD modelling of density currents in straight and sinuous channels. *PhD Thesis*, University of Leeds, Leeds, UK, pp. 284.

Giorgio-Serchi, F., Peakall, J. Ingham, D.B., and Burns, A.D. (2012) A numerical study of the triggering mechanism of a lock-release density currents. *European Journal of Mechanics, B/Fluids,* 33, 25-39.

Gladstone, C., Phillips, J.C., Sparks, R.S.J. (1998) Experiments on bi-disperse, constant-volume gravity currents: propagation and sediment deposition. *Sedimentology* 45(5), 833-843.

Gladstone, C. and Woods, A.W. (2000) On the application of box models to particle laden gravity currents. *Journal of Fluid Mechanics*, (416), 187-195.

Gladstone C. and Pritchard D. (2010) Patterns of deposition fron experimental turbidity currents with reversing buoyancy. *Sedimentology*, 57 (1), 53-84.

Gore, R.A., Crowe, C.T. (1989) Effect of particle size on modulating turbulent intensity. *Int. J. Multiphase Flow* 15(2), 279-285.

Field, S.B., Klaus, M., Moore, M. G. and Nori, F. (1997) Chaotic dynamics of falling disks. *Nature*, 388, 252-254.

FLUENT (2009). ANSYS FLUENT 12.0 Theory Guide. ANSYS, Inc.

Härtel, C., Meiburg, E., Necker, F. (2000) Analysis and direct numerical simulation of the flow at a gravity-current head 1: Flow topology and front speed for slip and no-slip boundaries. *J. Fluid Mech.* 418(1), 189-212

Hacker, J., Linden, P.F. and Dalziel, S.B. (1995) Mixing in lock-release gravity currents. *Dynamics of Atmosphere and Oceans*, 24(1-4), 183-195.

Haider, A. and Levenspiel, O. (1989) Drag coefficient and terminal velocity of spherical and nonspherical particles. *Powder Technology*, 58(1), 63-70.

Hallermeier, R.J. (1981) Terminal settling velocity of commonly occurring sand grains. *Sedimentology*, 28(1), 859-865.

Happel, J.R. and Brenner, H. (1965) Low Reynolds number hydrodynamics: with special applications to particulate media. *Springer*, pp. 553.

Harris, T.C., Hogg. A.J., and Huppert, H.E. (2001) A mathematical framework for the analysis of particle-driven gravity currents. *Proceeding of Royal Society London*, 457, 1241-1272.

Harris, T.C., Hogg, A.J., and Huppert, H.E. (2002) Polydisperse particle-driven gravity currents. *Journal of Fluid Mechanics*, 472, 333-371.

Haughton, P., Davis, C., McCaffrey, W., and Barker, S. (2009) Hybrid sediment gravity flow deposit. *Marine and Petroleum Geology,* 26(10), 1900-1918.

Heezen, B. C. and Ewing, M. (1952) Turbidity currents and submarine slumps, and the 1929 Grand Banks earthquake. *American Journal of Science*, 250(12), 849-873.

Henkes, R.A.W.M., Van Der Vlugt, F.F. and Hoogendoorn, C.J. (1991) Natural-convection flow in a square cavity calculated with low-Reynolds-number turbulence models. *International Journal of Heat Mass Transfer,* 34(2), 377-388.

Hodson, J.M. and Alexander, J. (2010) The effects of grain-density variation on turbidity currents and some implications for the deposition of carbonate turbidites. *Journal of Sedimentary Research*, 80, 515-528.

Hogg, A.J., Ungarish, M., and Huppert, H.E. (2001) Effects of particle sedimentation and rotation on axisymmetric gravity currents. *Physics of Fluids,* 13(12), 3687- 3698.

Hogg, A.J. (2006) Lock-release gravity currents and dam-break flows. *Journal of Fluid Mechanics,* 569, 61-87.

Holzer, A. and Sommerfeld, M. (2008) New simple correlation formula for the drag coefficient of non-spherical particles. *Powder Technology,* 184, 361-365.

Hölzer, A. and Sommerfeld, M. (2009) Lattice Boltzmann simulations to determine drag, lift and torque acting on non-spherical particles." *Computers & Fluids*, 38(3), 572–589.

Hosseini, S.A., Shamsai, A., and Ataie-Ashtiani, B. (2006) Synchronous measurements of the velocity and concentration in low density turbidity currents using an Acoustic Doppler Velocimeter. *Flow Measurement and Instrumentation*, 17(1) 59-68.

Hoyes, J. (2008) Homogeneous and particle-driven gravity currents. *PhD Thesis*. University of Leeds, Leeds UK, pp. 312.

Huang, H.Q., Imran, J., and Pirmez, C. (2005) Numerical model of turbidity currents with a deforming bottom boundary. *Journal of Hydraulic Engineering,* 131(4), 283-293.

Huang, H., Imran, J., Pirmez, C. (2007) Numerical modelling of poorly sorted depositional turbidity currents. *Journal of Geophysical Research,* 112(C0104), 1-15.

Huang, H., Imran, J., Pirmez, C. (2008) Numerical study of turbidity currents with sudden-release and sustained-inflow mechanisms. *Journal of Hydraulic Engineering,* 134(9), 1199-1209.

Huppert, H.E. and Simpson, J.E. (1980) The slumping of gravity currents. *Journal of Fluid Mechanics,* 99, 785-799.

Ishii, M. and Mashima, K. (1984) Two-fluid model and hydrodynamic constitutive relations. *Nuclear Engineering and design,* 82(2-3), 107-126.

Jha, S.K. and Bombardelli, F.A. (2009) Two-phase modelling of turbulence in dilute sediment-laden, open-channel flows. *Environmental Fluid Mechanics,* 9, 237-266.

Jones, W.P. and Launder, B.E. (1972) The prediction of laminarization with a two-equation model of turbulence. *International Journal of Heat and Mass Transfer,* 15(2), 301-314.

Joseph, D.D. and Ocando, D. (2002) Slip velocity and lift. *Journal of Fluid Mechanics,* 454, 263-286.

Kader, B. (1981) Temperature and concentration profiles in fully turbulent boundary layers. *International Journal of Heat and Mass Transfer,* 24(9), 1541-1544.

Keevil, G.M. (2005) Flow Dynamics of Sinuous Submarine Channel Systems. *PhD Thesis, University of Leeds,* pp. 222.

Kneller B.C., Bennett S.J. and McCaffrey W.D. (1997) Velocity and turbulence structure of density currents and internal solitary waves: Potential sediment transport and the formation of wave ripples in deep water. *Sedimentary Geology*, **112** (3-4), 235–250.

Kneller B.C., Bennett, S.J. and McCaffrey, W.D. (1999) Velocity structure, turbulence and fluid stresses in experimental gravity currents. *Journal of Geophysical Research*, 104(C3), 5381-5391.

Komar, P.D. and Reimers, C.E. (1978) Grain shape effects on settling rates. *The Journal of Geology*, 86(2), 193-209.

Kuenen, P.H. and Menard, H.W. (1952) Turbidity currents, graded and non-graded deposits. *Journal of Sedimentary*, 22(2), 83-96.

Kurose, R. and Komori, S. (1999) Drag and lift forces on a rotating sphere in a linear shear flow. *Journal of Fluid Mechanics,* 384, 183-206.

Lahey Jr., R.T., Lopez de Bertodano, M. and Jones Jr., O.C. (1993) Phase distribution phenomena in complex geometry conduits. *Nuclear Engineering and Design*, 141(1-2), 177-201.

Laval, A., Cremer, M., Beghin, P. and Ravenne (1988) Density surges: two-dimensional experiments. *Sedimentology*, 35(1), 73-84.

Launder, B. E., and Spalding, D.B. (1974) The numerical computation of turbulent flows. *Computer Methods in Applied Mechanics and Engineering,* 3(2), 269-289.

Leeder, M.R., Gray, T.E., and Alexander, J. (2005) Sediment suspension dynamics and a new criterion for the maintenance of turbulent suspensions. *Sedimentology*, 52(4), 683-691.

Legendre., D., and Magnaudet, J. (1997) A note on the lift force on a spherical bubble or drop in a low-Reynolds-number shear flow . *Physics of Fluids,* 9(11), 3572-3574.

Legendre., D., and Magnaudet, J. (1998) The lift force on a spherical bubble in a linear shear flow . *Journal of Fluid Mechanics,* 368, 81-126.

Le Roux, J. P. (2002) Shape entropy and settling velocity of natural grains. *Journal of Sedimentary Research*, 72(3), 363-366.

Leighton, D. and Acrivos, A. (1985) The lift on a small sphere touching a plane in the presence of a simple shear flow. *Journal of Applied Mathematics and Physics*, 36, 174-178.

Lightstone, M.F. and Hodgson, S. M. (2004) Turbulence modulation in Gas-Particle Flows: A comparison of selected models. *The Canadian Journal of Chemical Engineering,* 82, 209-219.

Loth, E. (2008) Drag of non-spherical solid particles of regular and irregular shape. *Powder Technology*, 182, 342-353.

Manninen, M., Taivassalo, V., Kallio, S. (1995). On the mixture models for multiphase flows. *Report* 288. Tech. Res. Centre of Finland, VVT Publications, Espoo.

McCaffrey, W.D., Choux, C.M., Baas, J.H. and Haughton, P.D.W. (2003) Spatio-temporal evolution of velocity structure, concentration and grain-size stratification within experimental gravity currents, marine and *Petroleum Geology*, 20, 851-860.

McLaughlin, J. B. (1991) Inertial migration of a small sphere in linear shear flows. *Journal of Fluid Mechanics*, 224, 261-274.

Meiburg, E., Kneller, B. (2010) Turbidity currents and their deposits. *Annual Review of Fluid Mechanics*, 42, 135-156.

Mellor, G.L. and Yamada, T. (1982), Development of a turbulence closure model for geophysical fluid problems. *Rev. Geophys. Space Phys*., 20, 851–875.

Mei, R. (1992) An approximate expression for the shear lift force on a spherical particle at finite Reynolds number. *International Journal of Multiphase flow*, 18(1), 145-147.

Menter, F.R. (1994) Two-equation eddy-viscosity turbulence models for engineering applications. *AIAA Journal*, 32(8), 1598-1605.

Middleton, G.V. and Neal, W.J. (1989) Experiments on the thickness of beds deposited by Turbidity currents. *Journal of Sedimentary Petrology*, 59(2), 297-307.

Morega F.J., Bonetto F.J, and Lahey Jr., R.T. (1999) Lateral forces on spheres in turbulent uniform shear flow. *International Journal of Multiphase Flow*, 20(6-7), 1321-1372.

Mostafa, A.A. and Mongia, H.C. (1988) On the interaction of particles and turbulent fluid flow. *International Journal of Heat and Mass Transfer*, 31(10), 2063-2075.

Necker F., Härtel, C., Kleiser, L., and Meiburg, E. (2002) High-resolution simulations of particle-driven gravity currents. *International Journal of Multiphase Flow*, 28, 279-300.

Nezu, I. and Nakagawa, H. (1993) Turbulence in Open channel flow. *A.A.Balkema*, Rotterdam, Netherlands, pp. 281.

Nikuradse, J. (1932) Gesetzmässigkeiten der turbulenten Strömung in glatten Rohren. Ver. Deut. Ing. Forschungsheft.

Niño, Y., Lopez, F., and Garcia, M. (2003) Threshold for particle entrainment into suspension. *Sedimentology*, 50(2), 247-263.

Normark, W.R. and Piper, D.J.W. (1991) Initiation process and flow evolution of turbidity currents: implications for the depositional record. *SEPM Special Publication*, **46**, pp. 207–230.

Oberbeck, A. (1876) Ueber discontinuirliche Flüssigkeitsbewegungen, *Annalen der Physik*, 238(9), 1-16.

Orszag, S.A., Yakhot, V., Flannery, W.S., Boysan, F., Choudhury, D., Maruzewski, and Patel, B.. (1993) Renormalization Group Modelling and Turbulence Simulations. In *International Conference on Near-Wall Turbulent Flows*, Tempe, Arizona.

Peakall, J., Ashworth, P., Best, J.L. (1996) Physical modelling in fluvial geomorphology: principles, applications and unresolved issues. *The Scientific Nature of Geomorphology*, Wiley & Sons, Chichester, 221-253.

Riddell, J.F. (1969) A laboratory study of suspension-effect density currents. *Canadian Journal of Earth Sciences*, 6, 231-246.

Robinson, S.K. (1991) Coherent motions in the turbulent boundary layer. *Annual Review of Fluid Mechanics,* 23, 601-639.

Rodi, W. (1980) Turbulence models and their application in hydraulics. *International Associations of Hydraulic Research,* Delft, pp. 104.

Rooij, F. de and Dalziel, S.B. (2001) Time-resolved measurements of the deposition under turbulent currents; *Spec. Publs. in. Ass. Sediment* **31**, 207-215.

Rosendahl, L. (2000) Using a multi-parameter particle shape description to predict the motion of non-spherical particle shapes in swirling flows. *Applied Mathematical Modelling,* 24, 11-25.

Rottman, J.W., Simpson J.E. (1983) Gravity currents produced by instantaneous releases of heavy fluids in a rectangular channel. *Journal of Fluid Mechanics,* 135, 95-110.

Rubinow, S.I. and Keller, J.B. (1961) The tranverse force on a spinning sphere moving in a viscous fluid. *Journal of Fluid Mechanic,* 11, 447-459.

Saffman, P.G. (1965) The lift on a small sphere in a slow shear flow.*Journal of Fluid Mechanic,* 22, 385-400.

Saffman, P.G. (1968) Corrigendum to “The lift on a small sphere in a slow shear flow.” *Journal of Fluid Mechanic,* 31, 624.

Saint, Venant (1871) Théorie du mouvement non permanent des eaux, avec application aux crues des rivières et à l'introduction des marées dans leurs lits. *Comptes Rendus des séances de l'Académie des Sciences*, 73, 237-240.

Schiller, L., and Naumann, A. (1935) A drag coefficient correlation. *Ver. Deut. Ing.,* 77, 318-320.

Segre, G. and Silberberg, A. (1962) Behaviour of macroscopic rigid spheres in Poiseuille flow Part 1. Determination of local concentration by statistical analysis of particle passages through crossed light beams. *Journal of Fluid Mechanic*, 14(1), 115-135.

Segre, G. and Silberberg, A. (1962) Behaviour of macroscopic rigid spheres in Poiseuille flow Part 2. Experimental results and interpretation. *Journal of Fluid Mechanic*, 14, 136-15.

Sequeiros, O.E., Spinewine, B., Beaubouef, R.T., Sun, T., Garcia, M.H., Parker, G. (2010) Bedload transport and bed resistance associated with density and turbidity currents. *Sedimentology,* 57, 1463-1490.

Shields, A. (1936) Anwendung der Ahnlichkeitsmechanik und der Turbulentzforschung auf die Geshiebebewegung. Mitteilungen der Preussischen Versuchsanstalt fur Wasserbau und Schiffbau 26, Berlin.

Simonin, O. (1991). Eulerian formulation for particle dispersion in turbulent two-phase flows. Proc. 5th Workshop *Two-phase flow predictions* Erlangen, 156-166.

Simpson, J.E (1972) Effects of the lower boundary on the head of a gravity current. *Journal of Fluid Mechanics,* 53(4), 759-768.

Simpson, J.E. and Britter, R.E. (1979) The dynamics of the head of a gravity current advancing over a horizontal surface. *Journal of Fluid Mechanics,* 94(3), 477-495.

Smith, D.J., Mclean, S.R. (1977) Spatially Averaged Flow Over a Wavy Surface. *Journal of Geophysical Research,* 82(12), 1735-1746.

Spalart, P.R. and Allmaras, S.R. (1992) A one-equation turbulence model for aerodynamic flows. *AIAA, Aerospace Sciences Meeting and Exhibit, 30th, Reno, NV, UNITED STATES,* 23, pp. 1992.

Stokes, G.G. (1851) On the effect of the inertial friction of fluids on the motion of pendulums, *Transactions of Cambridge Philosophical Society*, 9 (part II), 8–106.

Swamee, P.K., and Chandra Shakhar P.O. (1991) Drag coefficient and fall velocity of nonspherical particles. *Journal of Hydraulic Engineering,* 117(5), 660-667.

Tanaka, T. and Eaton, J.K. (2008) Classification of turbulence modification by dispersed spheres using a novel dimensionless number. *Physical Review Letters,* 101, 114502.

Tchen, C.M. (1947) Mean value and correlation problems connected with the motion of small particles suspended in a turbulent fluid, *Doctoral Thesis,* TU Delft, pp. 150.

Tomiyama, A., Sou, A., Zun, I., Kanami, N and Sakaguchi, T. (1995) Effects of Eötvös Number and Dimensionless Liquid Volumetric Flux on Lateral Motion of a Bubble in a Laminar Duct Flow. *Advances in Multiphase Flow,* Elsevier.

Tomiyama, A., (1998) Struggle with computational bubble dynamics. *3rd International Conference on Multiphase Flow,* Lyon, France.

Tomiyama, A., Tamai, H., Zun, I., and Hosokawa, S. (2002) Tranverse migration of single bubbles in simple shear flows. *Chemical Engineering Science,* 57, 1849-1858.

Toorman, E. (2003) Validation of macroscopic modeling of particle-laden turbulent flows. *Proceeding 6th Belgian National Congress on Theoretical and Applied Mechanics.*

Tsuji, Y. Morikawa, Y. and Shiomi, H. (1984) LDV measurements of an air-solid two-phase flow in a vertical pipe. *Journal of Fluid Mechanics,* 139, 417-434.

Tu, J.Y., and Fletcher, C.A. (1994) An improved model for particulate turbulence modulation in confined two-phase flows. *International communications in Heat and Mass Transfer,* 21(6), 775-783.

Ungarish, M. (2009) An introduction to gravity currents and intrusions. *Chapman and Hall,* 512 pages.

Van Driest, E.R. (1956) On Turbulent Flow Near a Wall. *AIAA Journal Special Supplement: Centennial Of Powered Flight,* 23(11), 1007-1011.

Van Rijn, L.C. (1984) Sediment Pick-Up Functions. *Journal of Hydraulic Engineering,* 110(10), 1494-1502.

Vasseur, P. and Cox, R.G. (1976) The lateral migration of a spherical particle in two-dimensional shear flows. *Journal of Fluids Mechanics,* 78(2), 385-413.

Wang, S.K., Lee, S.J., Jones Jr., O.C., and Lahey Jr., R.T. (1986) 3-D turbulence structure and phase distribution measurements in bubbly two-phase flows. *International Journal of Multiphase Flow,* 13(3), 327-343.

Weimer, P., and Slatt, R.M. (2007) Introduction to the petroleum geology of deepwater setting. In *AAPG Studies in Geology,* Tulsa, OK: American Association of Petroleum Geologists CD-ROM.

Wilcox, D.C. (1993) Turbulence Modelling for CFD, *DCW Industries Incorporated,* pp. 552.

Wolfstein, M. (1969) The velocity and temperature distribution of one-dimensional flow with turbulence augmentation and pressure gradient. *International Journal Of Heat and Mass Transfer,* 12, 301-318.

Xu, J.P., Noble, M., Eittreim, S.L., Rosenfeld, L. K., Schwing, F.B., and Pilskaln, C.H. (2002) “Distribution and transport of suspended particulate matter in Monterey Canyon, California.” *Marine Geology,* 181(1-3), 215-234.

Xu, J.P. (2010) Normalized Velocity profiles of field-measured turbidity currents. *Geology,* 38(6), 563-566.

Ye, J. and Rocco, M.C. (1991) Particle rotation in a Couette flow. *Physics of Fluids,* 4(2), 220-224.

Yin, C. Rosendhahl, L., Kaer, S.K., Sorensen, H. (2003) Modelling the motion of cylindrical particles in a nonuniform flow, *Chemical Engineering Science*, 58(1), 3489-3498.

Zhang, H.F. and Ahmadi, G. (2000) Aerosol particle transport and deposition in vertical and horizontal turbulent duct flows. *Journal of Fluid Mechanics,* 406, 55-80.

Appendix

A1. Turbulence Modulation

For the turbulence model-based approach, the turbulence modulation appears an additional dissipation term due to a hydrodynamic interaction force between the two phases in the two-equation turbulence model:

$$\frac{\partial}{\partial t}(\rho k) + Convection + Diffusion = Usual\ Sources\ and\ Sinks + S_k \quad \text{(A1.1)}$$

$$\frac{\partial}{\partial t}(\rho \varepsilon) + Convection + Diffusion = Usual\ Sources\ and\ Sinks + S_\varepsilon \quad \text{(A1.2)}$$

The sink term appearing in the turbulent kinetic energy of the fluid phase $S_{kf}$is given by

$$S_{kf} = \overline{F_p' u_f'} \quad \text{(A1.3)}$$

Where F_p is the momentum exchange between the two phases and is given by the

$$F_p = \frac{\tilde{\rho}}{t_p}(u_p - u_f) \quad \text{(A1.4)}$$

where $\tilde{\rho}$ is the concentration of the particle defined as the mass of particles per unit volume ($\tilde{\rho} = \alpha \rho_p$) and τ_p is the Stokes particle relaxation time is

$$t_p = \frac{d_p^2 \rho_p}{18 \mu_f} \quad \text{(A1.5)}$$

where ρ_p is the material density of the particle and μ is the dynamic viscosity of the fluid. The fluctuating momentum exchange term is

$$F_p^{'} = \frac{\tilde{\rho}^{'}}{t_p}(u_p^{'} - u_f^{'}) \quad \text{(A1.6)}$$

Hence, equation (A1.3) becomes

$$\overline{F_p' u_f'} = \frac{1}{t_p}\left[(u_p - u_f)\ \overline{\tilde{\rho}' u_f'} + \tilde{\rho}\left(\overline{u_f' u_p'} - \overline{u_f' u_f'}\right) + \overline{\tilde{\rho}' u_f'(u_p' - u_f')}\right] \quad \text{(A1.7)}$$

Neglecting the contributions due to the fluctuating concentration $\alpha^{'}$ (Chen & Wood, 1985), equation (A1.7) is simplified to the form as follows

$$\overline{F_p' u_f'} = \frac{\tilde{\rho}}{t_p}\left(\overline{u_f' u_p'} - \overline{u_f' u_f'}\right) \quad \text{(A1.8)}$$

The correlation $\overline{u_f' u_f'}$ is the turbulent kinetic energy ($\overline{u_f' u_f'} = 2k_f$) but the value of the correlation $\overline{u_f' u_p'}$ is not known and therefore needs to be modelled. The simplest model for determining the correlation $\overline{u_f' u_p'}$ is to assume dispersed phase velocity fluctuations are proportional to continuous phase velocity fluctuations.

$$u'_p = C(St)u_f' \quad \Rightarrow \quad \overline{u_p'.u_f'} = C(St)k_f \quad \text{(A1.9)}$$

Substitute equation (A1.9) into equation (A1.

$$S_{kf} = 2(C(St) - 1)\frac{\tilde{\rho}}{t_p}k_f \quad \text{(A1.10)}$$

where $C(St)$ is a function of turbulent Stokes number and has range $0 \leq C(St) \leq 1$. $C(St)$ has a value of 1 for very small particles and value of zero for very large particles. Therefore the turbulence modulation has maximum value for very large particle. Equation (A1.20) also indicates that the greater the particle volume fraction/particle density, the greater the turbulence modulation. The smaller the particle relaxation time is the greater the turbulence modulation is.

The sink term appearing in turbulent kinetic energy equation of the particle phase is given as

$$S_{kp} = \overline{-F_p' u_p'} = \frac{\tilde{\rho}}{t_p}\left(\overline{u_f' u_p'} - \overline{u_p' u_p'}\right) \quad \text{(A1.11)}$$

Here $\overline{u_p' u_p'}$ is the particle turbulent kinetic energy (k_p). If model (A1.9) is used, the following relation can be achieved,

$$u_p' u_p' = C(St)^2 u_f'^2 \Rightarrow \overline{u_p' u_p'} = 2k_p = C(St)^2 k_f \quad \text{(A1.12)}$$

Substitute (A1.9) & (A1.12) into (A1.11) gives

$$\overline{-F_p' u_p'} = 2\frac{\alpha_p}{t_p}C(St)(C(St) - 1)k_f \quad \text{(A1.13)}$$

The Mixture turbulence KE is the combination of the flow turbulence KE and the particle turbulence KE as follows

$$\rho_m k_m = \alpha_f \rho_f k_f + \alpha_p \rho_p k_p \quad \text{(A1.14)}$$

Therefore, the turbulence modulation for a mixture turbulence model is the combination of equations (A1.8) and (A1.9) which is

$$S_{km} = \frac{\alpha_p}{t_p}\left(2\overline{u_f^{'}u_p^{'}} - \overline{u_f^{'}u_f^{'}} - \overline{u_p^{'}u_p^{'}}\right) = -\overline{C_{cd}}\left(u_f^{'} - u_p^{'}\right)^2 \quad \text{(A1.16)}$$

Using relation (A1.9), equation (A1.16) becomes

$$S_{km} = 2\big(1 - C(St)\big)\frac{\tilde{\rho}}{t_p}k_f + 2\frac{\tilde{\rho}}{t_p}(C(St) - C(St)^2)k_f = 2\frac{\tilde{\rho}}{t_p}(1 - C(St)^2)k_f \quad \text{(A1.17)}$$

Equation (A1.17) implies a reduction in mixture turbulence when $C(St) > 0$. Replacing k_p in (A1.14) by equation (A1.12) to express k_f in terms of k_m as follows

$$\rho_m k_m = \big(\alpha_f\rho_f + \alpha_p\rho_p C(St)^2\big)k_f \quad => \quad k_f = \frac{\rho_m}{\left(\alpha_f\rho_f + \alpha_p\rho_p C(St)^2\right)}k_m \quad \text{(A1.18)}$$

Replacing k_f in equation (A1.15) by equation (A1.16) gives

$$S_{km} = 2\frac{\tilde{\rho}}{t_p}(1 - C(St)^2)\frac{\rho_m}{\left(\alpha_f\rho_f + \alpha_p\rho_p C(St)^2\right)}k_m = 2\frac{\tilde{\rho}}{t_p}(1 - C(St)^2)\tilde{k}_m \quad \text{(A1.19)}$$

The turbulent modulation in the turbulent dissipation rate ϵ of the fluid phase and the particle phase are defined as follows (Chen & Wood, 1985):

$$S_{\epsilon f} = 2\nu\frac{\partial u_f^{'}}{\partial x_k}\frac{\partial F_p^{'}}{\partial x_k} \quad \text{(A1.20)}$$

$$S_{\epsilon p} = -2\nu\frac{\partial u_p^{'}}{\partial x_k}\frac{\partial F_p^{'}}{\partial x_k} \quad \text{(A1.21)}$$

Substituting equation (A1.6) into equations (A1.20 – A1.21) and the dominant terms in the resulting expressions are

$$S_{\epsilon f} = 2\frac{\tilde{\rho}}{t_p}\left[\nu_f\,\overline{\frac{\partial u_f^{'}}{\partial x_k}\left(\frac{\partial u_f^{'}}{\partial x_k} - \frac{\partial u_p^{'}}{\partial x_k}\right)}\right] \quad \text{(A1.22)}$$

$$S_{\epsilon p} = 2\frac{\tilde{\rho}}{t_p}\left[\nu_p\,\overline{\frac{\partial u_p^{'}}{\partial x_k}\left(\frac{\partial u_p^{'}}{\partial x_k} - \frac{\partial u_f^{'}}{\partial x_k}\right)}\right] \quad \text{(A1.23)}$$

If relation (A1.9) is used onto (A1.22) and (A1.23), the following expressions are obtained

$$S_{\epsilon f} = 2\frac{\tilde{\rho}}{t_p}(1 - C(St))\left[\nu\overline{\frac{\partial u_f^{'}}{\partial x_k}\frac{\partial u_f^{'}}{\partial x_k}}\right] = 2\frac{\tilde{\rho}}{t_p}(1 - C(St))\epsilon_f \quad \text{(A1.24)}$$

$$S_{\epsilon p} = 2\frac{\tilde{\rho}}{t_p}C(St)(C(St) - 1)\left[\nu\overline{\frac{\partial u_p^{'}}{\partial x_k}\frac{\partial u_p^{'}}{\partial x_k}}\right] = 2\frac{\tilde{\rho}}{t_p}C(St)(C(St) - 1)\epsilon_p \quad \text{(A1.25)}$$

Since $\rho_m\epsilon_m = \alpha_f\rho_f\epsilon_f + \alpha_p\rho_p\epsilon_p$, we have

$$\rho_m\epsilon_m = \left(\alpha_f\rho_f + \alpha_p\rho_p C(St)^2\right)\epsilon_f \quad \text{(A1.26)}$$

Adding equations (A1.24) and (A1.25) yields the turbulence modulation term for the Mixture rate of turbulent dissipation equation

$$S_{\epsilon m} = 2\frac{\tilde{\rho}}{t_p}(1 - C(St)^2)\frac{\rho_m}{\left(\alpha_f\rho_f + \alpha_p\rho_p C(St)^2\right)}\epsilon_m = 2\frac{\tilde{\rho}}{t_p}(1 - C(St)^2)\tilde{\epsilon}_m \quad \text{(A1.27)}$$

Relation (A1.9) is a crude approach for modelling the fluid-particle correlation $\overline{u_f^{'}u_p^{'}}$. A more accurate approach is to model $\overline{u_f^{'}u_p^{'}}$ as a function of the fluid turbulent kinetic energy as follows

$$\overline{u_f'u_p'} = \gamma\overline{u_f'u_f'} \quad \text{(A1.28)}$$

$$\overline{u_p'u_p'} = \delta\overline{u_f'u_f'} \quad \text{(A1.29)}$$

where γ and δ are empirical parameters. Substituting (A1.27 – A1.28) into equations (A1.8), (A1.11) and (A1.16) gives

$$S_{kf} = \frac{\tilde{\rho}}{t_p}(\gamma - 1)\overline{u_f'u_f'} \quad \text{(A1.29)}$$

$$S_{kp} = \frac{\tilde{\rho}}{t_p}(\gamma - \delta)\overline{u_f'u_f'} \quad \text{(A1.30)}$$

$$S_{km} = -\frac{\tilde{\rho}}{t_p}(\delta - 2\gamma + 1)\overline{u_f'u_f'} \quad \text{(A1.31)}$$

For small Stoke number models, $\delta \sim \gamma^2$. Therefore,

$$k_m \propto -(\gamma - 1)^2\overline{u_f'u_f'} \quad \text{(A1.32)}$$

Parameter γ can be expressed using a Taylor series as follows

$$\gamma(St) = 1 - B_k St + \frac{B_k^2}{2!}St^2 + O(St^3) \quad \text{(A1.33)}$$

Substituting the first order term of (A1.33) into equation (A1.31) yield

$$S_{km} = -\frac{2\tilde{\rho}_s}{t_p} B_k^2 St\ \tilde{k}_m \tag{A1.34}$$

Equation (A1.34) shows that the turbulence modulation is proportional to the particle Stoke number.

Analysis above neglects the lower order terms of the turbulence modulation equation. If the lower order terms are included as well, equation (9) becomes

$$S_{km} = \left(\overline{u_f' F_p'} - \overline{u_p' F_p'}\right) \tag{A1.35}$$

Expanding (A1.35), we eventually arrived at the following expression:

$$S_{km} = \frac{\tilde{\rho}_s}{t_*}(\delta - 1)\left(\frac{\rho_m}{\tilde{\rho}_f + \delta\tilde{\rho}_s}\right)\left(U_{pi} - U_{fi}\right)D_{tm} \cdot \nabla C + \frac{2\tilde{\rho}_s}{t_*}\left(\frac{\rho_m}{\tilde{\rho}_f + \delta\tilde{\rho}_s}\right)(2\gamma - \delta - 1)k_m \tag{A1.36}$$

The second term on the right hand side of equation (A1.36) is the equivalent to equation (A1.31). The first term on the right hand side is the additional term that is neglected by Chen and Wood (1985). It describes a diffusion-like effect that depends on the concentration gradient. The corresponding turbulence modulation sink term in the turbulence rate of dissipation equation is

$$S_{\epsilon m} = \epsilon_m^2 / k_m \tag{A1.37}$$

Chen and Wood (1985) modelled γ to be an exponential function of particle Stoke number St:

$$\gamma_k = \frac{\overline{u_c' u_p'}}{\overline{u_c' u_c'}} = e^{-B_k St} \tag{A1.38}$$

$$\gamma_\epsilon = e^{-B_\epsilon St} \tag{A1.39}$$

where B_k = 0.0825 and $St = t_p / t_f^t$ is the particle Stoke number, defined as the ratio of the particle relaxation time to the eddy turnover time scale. The t_f^t is modelled as

$$t_f^t = \frac{0.165 k_m}{\varepsilon_m} \tag{A1.40}$$

Tu & Fletcher (1994) suggested a modification to the constant B_k in order take into account the effects of the mass loading. The constant B_k is divided by a parameter

$\dot{m}^n$ where $\dot{m}$ is the mass loading and n is a constant equal to 1 when $\dot{m}$ > 1 and 0 when $\dot{m}$ < 1.

Following Chen & Woods (1985), parameter δ is modelled as a function of particle Stoke number

$$\delta = \frac{1}{1+St} \quad \text{(A1.41)}$$

A2. Simulations Detail

Numerical Scheme

Table A2.1 Numerical schemes employed for each simulation

Items	Methods
Pressure-Velocity Coupling	SIMPLE (Patankar, 1980)
Spatial Discretization	
Gradient	Least Squares Cell Based
Pressure	PRESTO!
Momentum	Second Order Upwind
Volume fraction	QUICK
Turbulent kinetic energy	Second Order Upwind
Turbulent dissipation rate	Second Order Upwind
Transient Formulation	Second Order Implicit

Table A2.2 Convergence criteria

Equations	Absolute Criteria
Continuity	1e-5
x-velocity	1e-5
y-velocity	1e-5
k	1e-5
Epsilon	1e-5
Volume fraction	1e-5

UDF

(i) **Solid viscosity.** The mixture viscosity deviates from the fluid viscosity at high concentration. The power law of Ishii and Mashima (1984) is employed to calculate the mixture viscosity of high concentration flow accurately.

$$\mu_m = \mu_f \left(1 - \frac{\alpha_p}{\alpha_{pm}}\right)^{-2.5\alpha_{pm}} \quad \text{(A2.1)}$$

Where μ_f is the fluid viscosity, α_p is the particle volume fraction α_{pm} is the value of maximum packing number. Since $\mu_m = \sum_{k=1}^{n} \alpha_k \mu_k = \alpha_f \mu_f + \alpha_p \mu_p$, equation (A1.1) can be re-expressed as solid viscosity as follows:

$$\mu_p = \frac{\mu_f}{\alpha_p}\left(\left(1 - \frac{\alpha_p}{\alpha_{pm}}\right)^{-2.5\alpha_{pm}} - \alpha_f\right) \quad \text{(A2.2)}$$

(ii) **Particle mass sink**. A mass sink term is incorporated into the particle volume fraction equation at the bottom cell of the computational domain in order to model the particle deposition. The particle volume fraction equation is defined as (see equation (2.45) in the main text):

$$\frac{\partial}{\partial t}\left(\alpha_p \rho_p\right) + \frac{\partial}{\partial x_i}\left(\alpha_p \rho_p U_{mi}\right) = -\frac{\partial}{\partial x_i}\left(\alpha_p \rho_p U_{Mi}\right) + S_{mass} \quad \text{(A2.3)}$$

The mass sink term S_{mass} is defined here as $S_{mass} = \alpha_p \rho_p V_p / h_{cell}$, where V_p is the particle vertical velocity and h_{cell} is the height of computational cell at the bottom.

(iii) **Turbulence buoyancy production.** A standard Boussinesq gradient diffusion is employed to describe this process. For $k - \epsilon$ turbulence model, the term is defined as (see equation (2.29) in the text):

$$G_{bk} = -r_\rho \rho_f \frac{\mu_{tm}}{\sigma_t \rho_m} g_i \frac{\partial \alpha_p}{\partial y} \quad \text{(A2.4)}$$

The turbulent buoyancy in the turbulent rate of dissipation equation is

$$G_{b\epsilon} = C_{1\epsilon} \frac{\epsilon}{k} C_{3\epsilon} G_b \quad \text{(A2.5)}$$

The degree to which ϵ is affected by the buoyancy is determined by the constant $C_{3\epsilon}$. Henkes (1991) postulated that

$$C_{3\epsilon} = tanh \left|\frac{V_m}{U_m}\right| \quad \text{(A2.6)}$$

If $k - \omega$ turbulence model is used, the turbulence dissipation is modelled using a transport equation for the specific rate of dissipation ω defined as

$$\rho\frac{\partial\omega}{\partial t}+\rho U_j\frac{\partial\omega}{\partial x_j}=\frac{\partial}{\partial x_j}\left[(\mu+\sigma\mu_t)\frac{\partial\omega}{\partial x_j}\right]+\alpha\frac{\omega}{k}\tau_{ij}\frac{\partial U_i}{\partial x_j}-\ \beta\rho\omega^2 \qquad \text{(A2.7)}$$

where ω is defined as $\omega = k^{\frac{1}{2}}/l_t = \epsilon/k$. Since $\omega \sim 1/t_t$,

$$\frac{D\omega}{Dt}=\frac{D}{Dt}\left(\frac{\epsilon}{k}\right)=\ \frac{1}{k}\frac{D\epsilon}{Dt}-\ \frac{\omega}{k}\frac{Dk}{Dt} \qquad \text{(A2.8)}$$

Using this relation, the buoyancy term in the ω-equation can be shown to have the form of

$$G_{b\omega}=\frac{1}{k}\frac{D\epsilon}{Dt}-\ \frac{\omega}{k}\frac{Dk}{Dt}=(C_{\epsilon 3}-1)\left(\frac{\omega}{k}\right)G_b \qquad \text{(A2.9)}$$

(iv) Turbulence modulation. The Chen & Wood (1985) model is employed. Equations (A1.36) and (A1.37) outlined in the section A.1 are incorporated into turbulence model $k-\epsilon$ in FLUENT.

List of Simulations

Table A2.3 Simulations on flows investigated in Chapter 3

Folder Name	Flow	Mesh	Time step (s)	Turbulent Dispersion	Turbulent Modulation	Turbulent Model
G69_M1	G69	400 x 20	0.01	No	No	$k-\epsilon$
G69_M2	G69	800 x 40	0.01	No	No	$k-\epsilon$
G69_M3	G69	1200 x 60	0.01	No	No	$k-\epsilon$
G69_M4	G69	1600 x 80	0.01	No	No	$k-\epsilon$
G69_T005	G69	800 x 40	0.005	No	No	$k-\epsilon$
G69_T020	G69	800 x 40	0.02	No	No	$k-\epsilon$
G69_T050	G69	800 x 40	0.05	No	No	$k-\epsilon$
G69_TD	G69	800 x 40	0.01	Yes	No	$k-\epsilon$
G69_TM	G69	800 x 40	0.01	Yes	Yes	$k-\epsilon$
G69_KW	G69	800 x 40	0.01	No	No	$k-\omega$
G25	G25	800 x 40	0.01	No	No	$k-\epsilon$
G25_TD	G25	800 x 40	0.01	Yes	No	$k-\epsilon$
G25_TM	G25	800 x 40	0.01	Yes	Yes	$k-\epsilon$
G37_M1	G37	600 x 20	0.01	No	No	$k-\epsilon$
G37_M2	G37	900 x 30	0.01	No	No	$k-\epsilon$
G37_M3	G37	1200 x 40	0.01	No	No	$k-\epsilon$
G37_M4	G37	1500 x 50	0.01	No	No	$k-\epsilon$
G37_T005	G37	1200 x 40	0.005	No	No	$k-\epsilon$
G37_T020	G37	1200 x 40	0.02	No	No	$k-\epsilon$
G37_T050	G37	1200 x 40	0.05	No	No	$k-\epsilon$
G37_TD	G37	1200 x 40	0.01	Yes	No	$k-\epsilon$
G37_KW	G37	1200 x 40	0.01	No	No	$k-\omega$
G13	G13	1200 x 40	0.01	No	No	$k-\epsilon$
G13_TD	G13	1200 x 40	0.01	Yes	No	$k-\epsilon$
G13_KW	G13	1200 x 40	0.01	No	No	$k-\omega$
D37	D37	960 x 64	0.01	No	No	$k-\epsilon$
D37_TD	D37	960 x 64	0.01	Yes	No	$k-\epsilon$
D37_KW	D37	960 x 64	0.01	No	No	$k-\omega$

Table A2.4 Simulations on flows investigated in Chapter 5

Folder Name	Flow	Mesh	Time step (s)	Turbulent Dispersion
C500_M1	C500	800 x 20	0.01	Yes
C500_M2	C500	1200 x 30	0.01	Yes
C500_M3	C500	1600 x 40	0.01	Yes
C500_M4	C500	2000 x 50	0.01	Yes
C500_M5	C500	2400 x 60	0.01	Yes
C500_TS0005	C500	1600 x 40	0.0005	Yes
C500_TS0020	C500	1600 x 40	0.002	Yes
C500_TS0100	C500	1600 x 40	0.01	Yes
C500_TS0150	C500	1600 x 40	0.015	Yes
C500_TS0250	C500	1600 x 40	0.025	Yes
C500_TS0400	C500	1600 x 40	0.04	Yes
C500_TS0500	C500	1600 x 40	0.05	Yes
C500_TS0020(2)	C500	800 x 20	0.002	Yes
C500_TS0100(2)	C500	800 x 20	0.01	Yes
C500_TS0150(2)	C500	800 x 20	0.015	Yes
C500_TS0250(2)	C500	800 x 20	0.025	Yes
C500_TS0400(2)	C500	800 x 20	0.04	Yes
C500_TS0500(2)	C500	800 x 20	0.05	Yes
C027	C027	1600 x 40	0.005	No
C027_TD	C027	1600 x 40	0.01	Yes
C050	C050	1600 x 40	0.005	No
C050_TD	C050	1600 x 40	0.01	Yes
C100	C100	1600 x 40	0.005	No
C100_TD	C100	1600 x 40	0.01	Yes
C150	C150	1600 x 40	0.005	No
C150_TD	C150	1600 x 40	0.01	Yes
C200	C200	1600 x 40	0.005	No
C200_TD	C200	1600 x 40	0.01	Yes
C288	C288	1600 x 40	0.01	No
C288_TD	C288	1600 x 40	0.01	Yes
C388	C388	1600 x 40	0.01	No
C388_TD	C388	1600 x 40	0.01	Yes
C500	C500	1600 x 40	0.01	No
C500_TD	C500	1600 x 40	0.01	Yes
S58	S58	1600 x 40	0.01	No
S58_TD	S58	1600 x 40	0.01	Yes
UNS64	UNS64	1600 x 40	0.01	No
UNS64_TD	UNS64	1600 x 40	0.01	Yes
S71	S71	1600 x 40	0.01	No
S71_TD	S71	1600 x 40	0.01	Yes
S87	S87	1600 x 40	0.01	No
S87_TD	S87	1600 x 40	0.01	Yes
UNS84	UNS84	1600 x 40	0.01	No
UNS84_TD	UNS84	1600 x 40	0.01	Yes
S115	S115	1600 x 40	0.01	No
S115_TD	S115	1600 x 40	0.01	Yes
UNS109	UNS109	1600 x 40	0.01	No
UNS109_TD	UNS109	1600 x 40	0.01	Yes

A3. Flows Carrying Non-spherical Particles

Introduction

An investigation has been performed in order to investigate the effect of shape anisotropy on the sediment deposition of the lock-release - generated turbidity currents. Simple symmetrical non-spherical shapes such as oblate and problate spheroids are considered here. The deposit mass profile of flows carrying spheroid of different aspect is compared with that of flows carrying spheres alone. It was found that the effect of the spheroid on the deposition correspond well with the trend of settling velocity ratio as function of aspect ratio.

Theory

Spheroids are classified as oblate (E < 1) or problate (E > 1) – see below for the formulation of E. The shape of an oblate or problate spheroid is visualised in Figure A3.1. The size of a spheroid can be expressed using the particle diameter of a sphere with a volume equivalent to the spheroid in question (known as equivalent diameter d_e). The aspect ratio E of a spheroid is defined as

$$E = \frac{d_{\parallel}}{d_{\perp}} \tag{A3.1}$$

where $d_{\parallel}$ is the axial dimension of the particle and $d_{\perp}$ is the maximum dimension normal to the axis of symmetry. The volume of a spheroid is proportional to the product of the diameters of the three major axes, therefore the equivalent diameter is given by

$$d_e = d_{\perp}E^{\frac{1}{3}} = d_{\parallel}E^{-\frac{2}{3}} \tag{A3.2}$$

The Stokes correction for a spheroid Δ is defined as the ratio of the Stokes spheroid drag force to the Stoke sphere drag force for a fixed volume equivalent diameter, i.e.

$$\Delta = \frac{F_{D,spheroid}}{F_{D,Stoke}} \tag{A3.3}$$

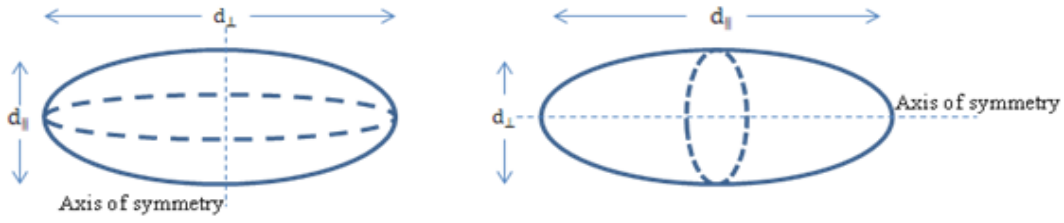

Figure A3.1 Schematic diagram of spheroid oblate (left) and problate (right).

Clift et al. (1978) give the formulae for analytical expressions derived by Oberbeck (1876) for the Stokes corrections for both oblate and problate spheroid - parallel (axial Stokes correction $\Delta_{\parallel}$) and spheroid - normal (normal Stokes correction $\Delta_{\perp}$) to the particle axis symmetry, as follows

$$\Delta_{\parallel,oblate} = \frac{\left(\frac{4}{3}\right)E^{-\frac{1}{3}}(1-E^2)}{E+\frac{(1-2E^2)\,cos^{-1}E}{\sqrt{1-E^2}}}\,;\ \Delta_{\perp,oblate} = \frac{\left(\frac{8}{3}\right)E^{-\frac{1}{3}}(E^2-1)}{E-\frac{(3-2E^2)\,cos^{-1}E}{\sqrt{1-E^2}}} \tag{A3.4}$$

$$\Delta_{\parallel,problate} = \frac{\left(\frac{4}{3}\right)E^{-\frac{1}{3}}(1-E^2)}{E-\frac{(2E^2-1)\,ln\left(E+\sqrt{E^2-1}\right)}{\sqrt{E^2-1}}};\ \Delta_{\perp,problate} = \frac{\left(\frac{8}{3}\right)E^{-\frac{1}{3}}(E^2-1)}{E+\frac{(2E^2-3)\,ln\left(E+\sqrt{E^2-1}\right)}{\sqrt{E^2-1}}} \tag{A3.5}$$

If random orientation is considered, the Stokes corrections are

$$\Delta_{oblate} = \frac{\sqrt{1-E^2}}{cos^{-1}E}E^{-\frac{1}{3}} \tag{A3.6}$$

$$\Delta_{problate} = \frac{\sqrt{E^2-1}}{ln\left(E+\sqrt{E^2-1}\right)}E^{-\frac{1}{3}} \tag{A3.7}$$

Figure A3.2 shows the plot of Stoke drag correction of oblate and problate spheroid based on equations (A3.4 – A3.7) as a function of aspect ratio. Reducing the aspect ratio lower than one (oblate spheroid) increases the axial Stokes correction $\Delta_{\parallel}$ exponentially but decreases the value of the normal Stokes correction $\Delta_{\perp}$ below one for aspect ratios between 0.7 and 1, and then increases $\Delta_{\perp}$ exponentially for aspect ratio smaller than 0.7. The value of the random Stokes correction lies between that of axial and normal Stokes corrections. Increasing the spheroid aspect ratio beyond one (prolate spheroid) slightly decreases the axial Stokes correction below one but slightly increases normal and random Stokes corrections.

Equations (A3.4 – A3.7) can be used to evaluate the ratio of the Stokes settling velocity of a spheroid to that of sphere with the same equivalent diameter. Figure A3.3 shows the plot of such ratio as a function of the spheroid aspect ratio for a spheroid falling axially, normally or randomly. Axial oblate spheroids experience a significant reduction in settling velocity (by almost 50% when E = 0.1). On the other hand, axial problate experiences a slight enhancement to the settling velocity. Randomly-oriented spheroids or normal oblate or normal problate spheroids all exhibits a settling velocity lower than that of a volume-equivalent sphere. Therefore, it can be concluded that aside from axial prolate spheroids, all spheroids settle slower than a sphere of equivalent volume.

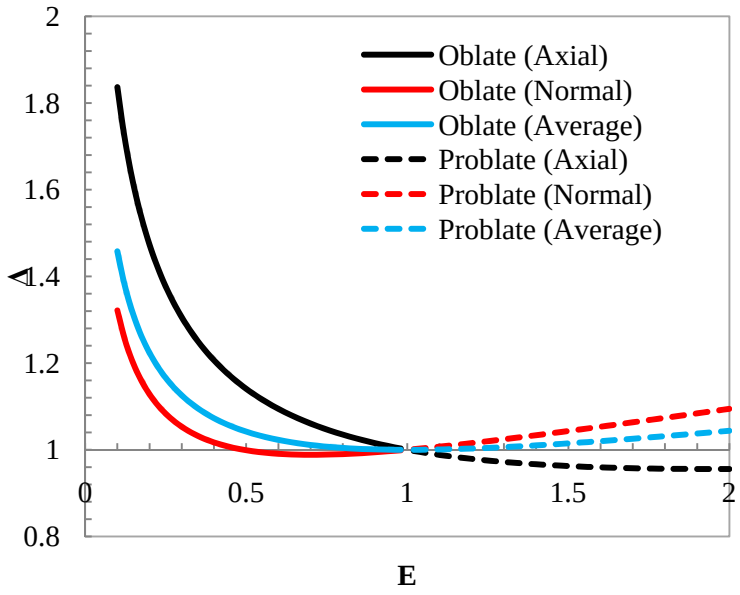

Figure A3.2 Plot of Stoke drag correction Δ as function of aspect ratio E for spheroid

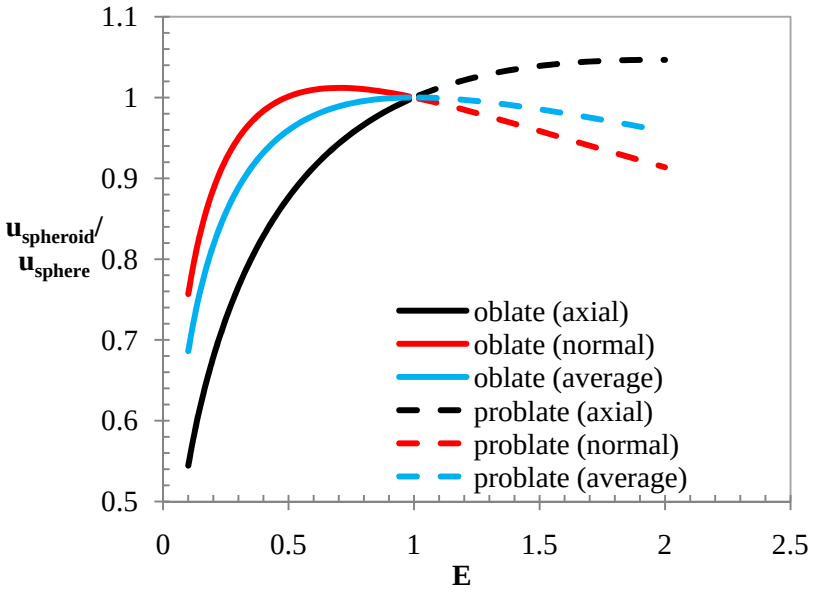

Figure A3.3 Plot of settling velocity as a function of spheroid aspect ratio

Simulations Results

The equations A(3.4 – 3.7) are incorporated into the FLUENT via UDF and two simulations were performed to model the effect of spheroids with aspect ratio E = 0.5 and E = 0.01 using the Mixture Model. The initial conditions of flows G37 (see Table 3.1 in the main text) were adopted. The results are compared against the simulations that assume all particles are spheres and the experimental data from Gladstone & Pritchard (2010).

Figure A3.4 shows that flows carrying oblate spheroids with aspect ratio = 0.5 experience an increase in the upstream deposition whereas flows carrying oblate spheroids with aspect

ratio = 0.01 experience a decrease in upstream deposition. These changes show that the effects of particle shape could be important in turbidity currents. Also, assuming that silicon carbide particles are spheres could be a poor approximation since the results agree better with the experiment when particle has a shape of an oblate spheroid with aspect ratio = 0.5.

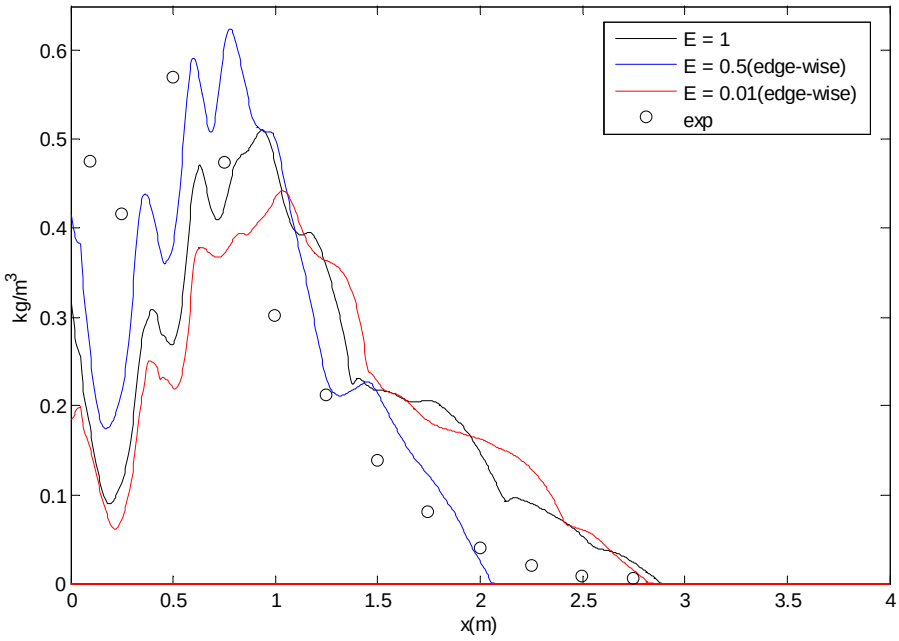

Figure A3.4 The Mixture Model prediction on the final deposit density of flows G37 carrying either sphere (black line), oblate spheroid with E = 0.5 (blue line) or oblate spheroid with E = 0.01 (green line). The circles are experimental data of Gladstone & Pritchard (2009).